Texture and Stress Characterization of a Copper Tube by Neutron, Synchrotron and Electron Diffraction

Doctoral Thesis
Dissertation
To be awarded the degree
Doctor of Engineering (Dr.-Ing.)

Submitted by
Nowfal A. Abdulrazzag Al-Hamdany
From Baghdad, Iraq

Approved by the Faculty of Natural and Materials Science
Clausthal University of Technology

Date of Oral Examination
30.03.2015

Chairperson of the Board of Examiners: Prof. Dr. Albrecht Wolter

Chief Reviewer: apl. Prof. Dr. rer. nat. Dr.-Ing. habil. Heinz-Günter Brokmeier

Reviewer: Prof. Dr.-Ing. habil Lothar Wagner

Abstract

Copper (Cu) was one of the first metals to be used by human beings (gold was the other) and was probably discovered around 6000 B.C. Cu is a very useful material with good properties like very gut thermal and electrical conductivity as well as corrosion resistance. The main applications of Cu and its alloys (like brass and bronze, etc.) are as thermal and electrical conductors, art works, beer tanks, musical instrument, coins, a building material, and is also a constituent of various metal alloys (e.g. Al, Fe, Ti alloys).

The present work deals with a DHP-Cu tube. Commercially pure Cu is available in several grades defined by the refining process, the impurities present and the oxygen content. One example of commercially pure Cu is DHP-Cu, which means a Cu variety with low phosphorus content. A typical application of DHP-Cu is as condenser, evaporator and heat exchanger tubes, for air conditioning for refrigeration as well as for plumbing pipes and steam tubes.

Rolling, extrusion and drawing are the preferred techniques for manufacturing seamless Cu tubes. Among other criteria, the quality of tube manufacturing can be determined from the tube eccentricity and ovality. Seamless tube production is a combination of both diameter and wall thickness reduction, this leads to a complex residual stress profile and variation in crystallographic texture around the circumference and through the wall thickness.

Experiments have been carried out by neutron-, synchrotron-, and electron diffraction to determine texture gradients and residual stress profiles. Neutron diffraction is non-destructive while the other methods need intense sample preparation. A main part of this work was the usage of the robot system at STRESS-SPEC (neutron diffractometer at FRM II) to handle large samples up to 12 kg. Due to the sample geometry (140 mm outside diameter and 10 mm average wall thickness) absorption and volume correction were necessary.

The texture was a combination of deformation and dominant recrystallization texture components, namely cube, rotated cube, copper, brass, S and Goss component. The {001}<100> cube component shows a variation of the orientation density around the circumference and a remarkable variation through the wall thickness while the copper component is nearly constant. Here, the temperature plays a major role.

The residual strains measured by the robot and by the XYZ-stage agree well; this indicates that the robot is reliable for strain measurements. The residual axial stress was tensile for the outer part of the copper tube and compressive for the inner part. The residual hoop stress has a similar distribution but with lower values. The residual radial stress has quite a low value.

Zusammenfassung

Kupfer (Cu) war eines der ersten Metalle, das von Menschen verwendet wurde (Gold war ein anderes). Es wurde ca. 6000 vor Christus entdeckt. Cu ist ein besonderes Metall mit hervorragenden Eigenschaften wie z.B. sehr guter thermischer und elektrischer Leitfähigkeit, sowie guter Korrosionsbeständigkeit. Hauptanwendungsgebiete von Kupfer und Kupferlegierungen wie Messing und Bronze sind elektrische und thermisch Leitungssysteme, Kunstgegenstände, Beer Backen, Musikinstrumente, Münzen, Rohrkonstruktionen und als Baumaterials unteranderem von Dachkonstruktionen. Darüber hinaus wird Kupfer als Legierungszuschlag in vielen Systemen verwendet (z.B. Al-, Fe-, Ti-Legierungen).

Die vorliegende Arbeit beschäftigt sich mit der Untersuchung eines DHP-Cu-Rohres. DHP-Cu ist kommerziell reines Cu mit geringem Phosphorgehalt. Typische Anwendungen für DHP-Cu sind die Verwendung als Kondensator-, Verdampfer- und Wärmetauscherrohre für Klimaanlagen, Kühlanlagen und auch für Sanitärrohrleitungen.

Die Haupttechniken zum Herstellen nahtloser Rohre sind diverse Walzverfahren, Strangpressen und Rohrziehen. Neben anderen Kriterien werden auch Exzentrizität und Ovalität der Rohre zur Beurteilung der Qualität verwendet. Die Nahtlosrohrproduktion ist eine Kombination aus Durchmesser- und Wanddickenreduzierung. Dies führt zu einem komplexen Eigenspannungsprofil und zur Variation kristallographischer Textur, sowohl um den Kreisumfang als auch über die Wanddicke als Funktion der Herstellungsparameter.

Die Bestimmung von Texturgradienten und Eigenspannungsprofile wurden mit Hilfe von Neutronen-, Synchrotron- und Elektronenbeugung durchgeführt. Je nach Strahlungsrat werden unterschiedliche Ortsauflösungen in der Probe realisiert. Das Hauptziel der Arbeit ist die Nutzung des Roboters am Neutronendiffraktometer STRESS-SPEC am FRM II. Dabei wurden Proben bis 12 kg zerstörungsfrei untersucht. Aufgrund der Probengeometrie (140 mm Außendurchmesser und 10 mm mittlere Wanddicke) wurde ein Verfahren zur Absorptions- und Volumenkorrekturen entwickelt. Ohne Roboter ist diese Messung nicht durchführbar.

Die Textur ist eine Kombination aus Verformungs- und Rekristallisationstextur-Komponenten, wie der Würfel-, der gedrehten Würfel-, der Kupfer-, der Messing-, der S- und der Goss-Lage. Über den Kreisumfang ist nur eine geringe Variation der Textur festgestellt worden. Dagegen zeigt die Würfellage eine ausgeprägte Variation über die Wanddicke. Hier spielt die Temperatur die wesentliche Rolle.

Das Kupferrohr zeigt im äußeren Bereich Zugspannungen und im inneren Bereich Druckspannungen, dabei sind die Radialspannungen nahezu null. Der Vergleich von Robotermessung und konventioneller Messung mit x-,y-,z- Tisch war außerordentlich positiv.

Acknowledgements

This thesis has been submitted in partial fulfillment of the requirements for a doctoral degree in the Faculty of Natural and Materials Science of Clausthal University of Technology in Germany. This research was carried out between October 2009 and January 2015 and was financially supported by the Deutscher Akademischer Austausch Dienst (DAAD) through A/08/96273.

I would like to express my sincere gratitude and wishes to my supervisor Prof. Dr. Heinz-Günter Brokmeier, for his patience, support, encouragement and guidance during the work.

I would like to acknowledge the Heinz Maier-Leibnutz Zentrum (MLZ) for being able to perform neutron diffraction at STRESS-SPEC. I would like to thank Dr. M. Hofmann, Dr. W. M. Gan, Dr. C. Randau, Dr. J. Rebelo-Kornmeier, M völler and K. Braun for helping me with STRESS-SPEC measurements.

I would like to acknowledge the Deutsches Elektronen Synchrotron (DESY) and Helmholtz-Zentrum Geesthacht (HZG) for being able to use Synchrotron radiation at the HEMS side station (P07b). I would like to thank Dr. N. Schell for his help.

I am grateful for beam time use at Stress-Spec (FRMII, Münich) and PETRAIII (Desy, Hamburg).

I am sincerely grateful and would thank colleagues at HZG (Helmholtz Zentrum Geesthacht); in particular Dr. V. Ventzke for characterizing my samples by SEM, S. Rieker for performing some mechanical test, F. Dorn for preparing samples for the microscope and Dr. J. Paul for checking my English.

I would also like to thank my colleagues Dr. E. Maawad, Dr. M. Z. Salih, Mr. B. Schwebke, Z.Y. Zhong, Mr. J. Schumann, and Mr. P. König for their kind help and fruitful discussions during experimental work.

Finally, I am indebted to my parents, brothers and sisters for their patience, encouragement to studying and their support.

Contents

1 Introduction and aims

1.1 Introduction

Seamless tubes essentially have two geometrical features which are eccentricity and ovality. Eccentricity and ovality give an indication of the quality and precision of the seamless tube manufacturing process. Such processing can impart inhomogeneous material flow around the circumference as well as through the wall thickness. In order to study the homogeneity of material flow during tube manufacture, crystallographic texture analysis has been used. Seamless tube manufacture consists of both cross-sectional area and wall thickness reductions. These lead to a complex variation of the through thickness residual stress state. To study the residual stresses a non-destructive method based on neutron diffraction has been used. In this work a DHP (Deoxidized High Phosphorus) copper tube with a diameter of 140 mm and an average wall thickness of 10 mm has been investigated.

For crystallographic texture analysis different types of radiation (thermal neutrons, hard X-rays, and electrons) have been used. Thermal neutrons are well known to be ideally suited for bulk texture analysis of relatively large sample volumes [1]. For most materials where the spherical sample method of Tobisch and Bunge [2] is used, no data correction for integrated peak intensities is needed. This is related to the high penetration power of thermal neutrons and a large beam cross section, and allows the average texture information of the whole test sample to be obtained. During sample tilting (χ) and rotation (φ) the gauge volume is constant for samples up to some cm in diameter. Consequently, the intensity variation $I_{hkl}(\alpha,\beta)$ in standard pole figure coordinates, α and β, only depends on the crystallographic texture and not on anisotropic absorption.

In the case of determining the local texture of semi-finished products, or of samples larger than the beam cross section, the above assumption no longer applies. When using slit systems or radial collimators, only part of a large sample is defined as the gauge volume. From neutron strain measurement it is known that the so called 90° arrangement is the best choice to get as close to a constant sample volume as possible during sample rotation. For texture analysis the 90° arrangement is not practical for most crystallographic plane reflections. This is because the diffraction volume changes as a function of tilting and rotation (χ and φ) and has a direct influence on the scattered intensity $I_{hkl}(\alpha,\beta)$ which must then be corrected.

The present investigation uses the STRESS-SPEC [3, 4] robot type Stäubli RX160 [5] to overcome the restrictions imposed when using an Eulerian Cradle. This allows us both to manipulate larger and heavier samples than with an Eulerian cradle and also to perform automatic mapping at a predetermined set of sample positions. The disadvantage is that the slit systems and radial collimators cannot be positioned close to the sample because of the size of the area required for robot movement. This increases the importance of the absorption and volume corrections compared to Eulerian cradle measurements. Moreover, one radial collimator is restricted to one only gauge volume, so that even a set of radial collimators will not be able to cover all the requirements of irregular shaped engineering samples. We thus decided to work without a radial collimator because not all radial collimator sizes were available.

In addition to thermal neutrons, Synchrotron (high energy X-rays) radiation is (because of its high penetration) used as a tool to investigate polycrystalline material. Synchrotron radiation (up to 200 keV) has a similar ability to thermal neutrons in that it is able to penetrate through materials. Thus Synchrotron radiation sources with their very high brilliance are becoming interesting for the investigation of crystallographic texture gradient within rather small gauge volumes [6]. High energy X-rays of 174 keV at HEMS (High Energy Materials Science) in DESY (Hamburg) were used to investigate the texture variation through the wall thickness of a DHP-copper tube at different positions around the circumference.

In order to understand the residual stress behavior of processed materials, the residual stress of the semi-finished product should also be studied. Thermal neutrons were used to characterize the residual stress within the DHP-copper tube. The residual stress was determined through the wall thickness at different positions around the circumference of a large tube segment (250 mm length). The STRESS-SPEC robot was used to continuously move the large tube segment so that all positions could be measured in one setup.

1.2 Aims and Objectives

- Illustrate the capability of the RX-160 robot for the texture mapping of a ring-shaped sample cut from a DHP-Cu tube using neutron diffraction.
- Calculate the volume and linear absorption corrections for the pole figures of the DHP-Cu tube obtained using neutron diffraction.
- Study the correlation between eccentricity/ovality and the texture variation around the circumference of the DHP-Cu tube using neutron diffraction.

- Illustrate the capability of the RX-160 robot in pole figure determination for large and heavy samples. A DHP-Cu tube segment of 250 mm length and 12 kg weight was investigated using neutron diffraction.
- Study the correlation between eccentricity/ovality and the texture gradient through the wall thickness at different positions around the circumference using synchrotron diffraction.
- Determine the texture gradient through the wall thickness using the EBSD technique.
- Illustrate the capability and reliability of the RX-160 robot for residual stress characterization of large samples.
- Study the residual stress at different positions within the wall thickness at different positions around the circumference.
- Determine the mechanical property variation through the wall thickness at different positions around the circumference. In this work the variation of Vickers hardness was determined.

2 Theoretical backgrounds

2.1 Commercial Pure Copper

In general, copper was one of the first metals used by human beings (gold was the other). Discovery of copper was probably around 6000 B.C. At that time, copper was found in the free metallic state [7]. Ancient people used it for fashion and weapons by forging the metal (cold forging). Pounding copper made it harder (strain hardening); this and its attractive reddish color made it valuable in early civilizations [8, 9]. Copper is one of the few colored metals, being salmon red. Its alloys range from reddish yellow through gold to pale yellow and white, (purple coloured alloys were known to alchemists as ‘Regulus of Venus’, consisting of 50% antimony 50% copper) [7].

Commercial pure is available in several grades defined by standards. The differences arise from the refining process, the impurities present and the oxygen content [7]. As an example of these commercial copper are:

1. Tough pitch, it is copper with oxygen contain between 0.02% to 0.06% by weight
2. Oxygen-free, it is high purity copper made by a refining operation which avoids the absorption of oxygen
3. Phosphorus dioxide (DHP-copper) is a deoxidized copper with a limited remaining amount of phosphorus

The chemical composition of DHP copper is (Cu ≥ 99.9% and P 0,015-0,04 %) [10]. Basic data on the DHP-copper are presented in the Table 2.1. In this work only the properties of DHP-copper will be presented.

Copper is a very useful material for human beings and used as a thermal and electrical conductor, a building material, and constituent of various metal alloys. Copper application areas cover a wide variety of different disciplines; examples are in architecture, automotive, electrical, tubes, pipes and fittings, fuel gas, industrial, sea water, machined products, computing and telecommunication [11]. The major uses of pure, unalloyed copper are based on its high electrical and thermal conductivity as well its good corrosion resistance. A typical Application of DHP-copper are in plumbing (plumbing pipes and fittings), electrical (heater element, wire connectors), building (air conditioner tubes, gas lines), automotive (air lines, oil lines) architecture (downspouts, roofing) and many other applications. [7].

Table 2.1 some properties of DHP-copper [7-12]

Property	Value
Symbol:	Cu
Atomic number:	29
Density at 20°:	8.94 g/cm^3
Space group:	Fm-3m
Lattice constant, a:	0.3608 nm
Melting temperature:	1083 °C
Linear coefficient of thermal expansion:	16.8*10^{-6} K^{-1} (20-100°C)
specific heat capacity:	386 J/kg.K (20°C)
Thermal conductivity:	305 W/mK (20°C)
Electrical conductivity:	43 m/(Ωmm^2) (0.042 %P)
Electrical resistivity:	0.022 Ωmm^2/m (20°C)
magnetic susceptibility:	-0.086*10^{-6} cm^3/g

Thermal conductivity is the property that characterizes the ability of a material to transfer heat. The thermal conductivity of DHP-copper is around 305 W/mK. Thermal conductivity is also changed significantly by even small additions of any other elements in solid solution. The added atoms (act as scattering centers) lowering the efficiency of electron motion. Thermal conductivity is also affected with respect to temperature changes as shown in figure 2.1. [7]

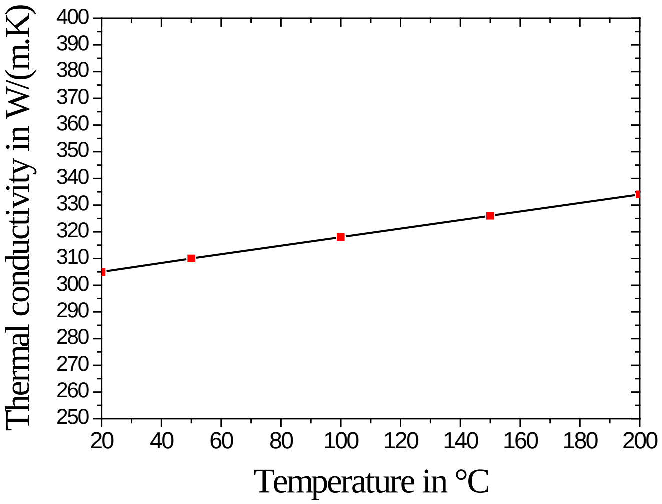

Figure 2.1 Change of thermal conductivity of DHP-copper with the temperature for 0,024% P [10].

In General, the high electrical conductivity of copper is only exceeded by that of silver, a major reason for the use of copper. Small amount of other elements as impurities and alloying element additions (Cd, Zn, Ni, Sn, Al, …) reduce the conductivity, often severely as indicated in figure 2.2. Elements which are added to copper lead to loss of conductivity and silver is notable as having no effect. Copper that contain phosphorus are not destined for electrical purpose [7].

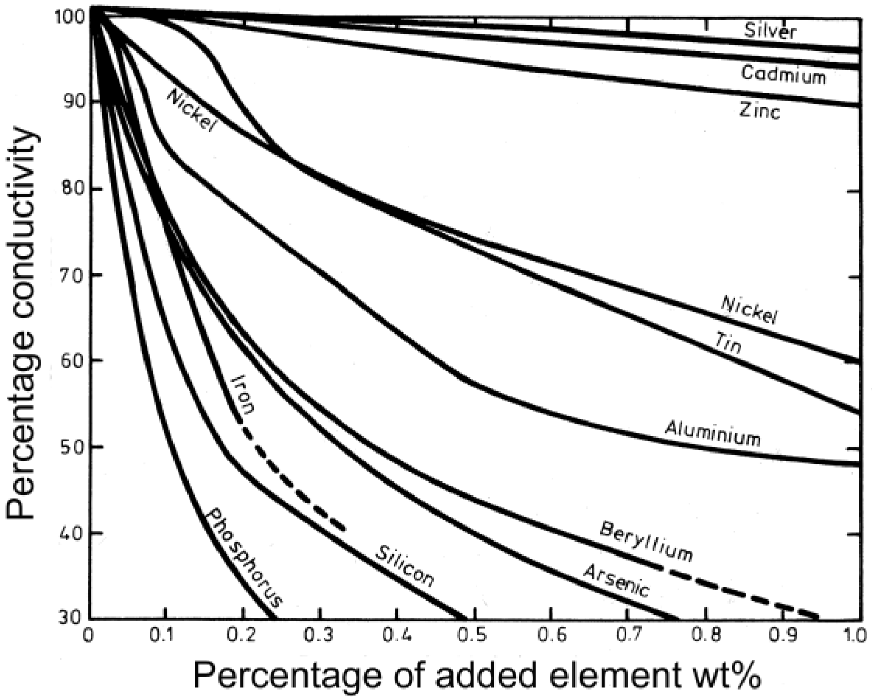

Figure 2.2 Effect of added elements on electrical conductivity of oxygen-free copper [7].

Mechanical properties of the DHP-copper depend on the crystallographic texture and compositions and degree of deformation. DHP-copper has excellent formability and wide range of strength/ductility values can be obtained. The elastic modulus of DHP-copper increases as a result of work hardening. The elastic modulus of DHP-copper is 110 GPa after annealing and reach up to 132 GPa after cold forming. The tensile strength values obtained by cold working of the three basic commercial types are similar from a practical standpoint. The strength of copper is increased by cold working which reduces its ductility as shown in figure 2.3. DHP-copper is also excellent for welding and brazing and is resistant to hydrogen [7]. Hardness of soft DHP-copper is around 40 on Vickers scale, up to 115 when it is cold formed [10].

Copper is not embrittled by sub-zero temperatures and strength is, in fact improved as the temperature decreases [7].

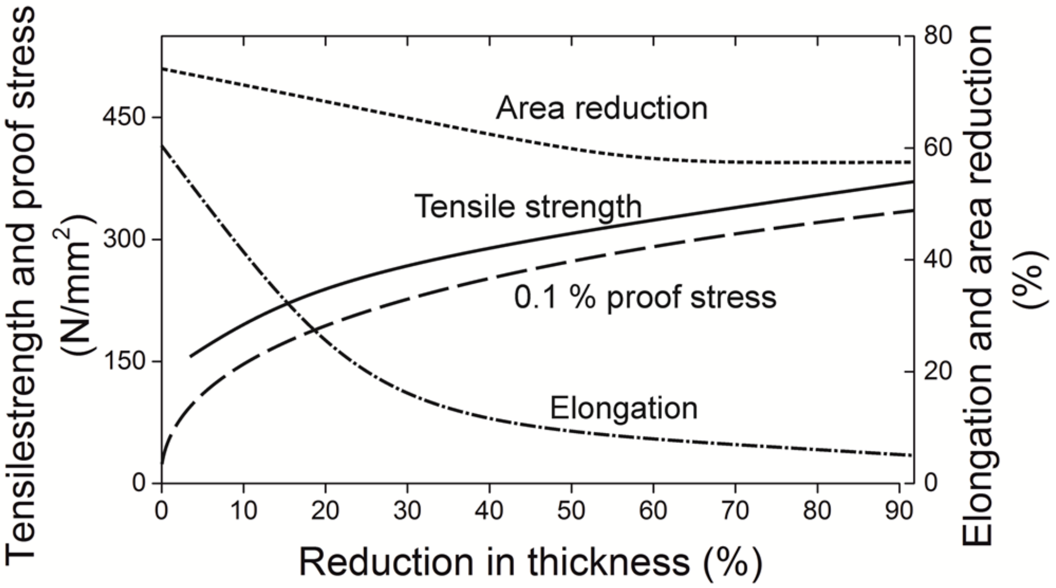

Figure 2.3 Effect of cold rolling on strength and ductility of high conductivity copper strip [7].

The orientation distribution of the crystals in a material is responsible for anisotropic properties in polycrystalline materials. The anisotropy plays a major role when considering the properties of polycrystalline materials, especially during deformation. Figure 2.4 shows an example of the directional distribution of the elastic moduli of a single copper crystal.

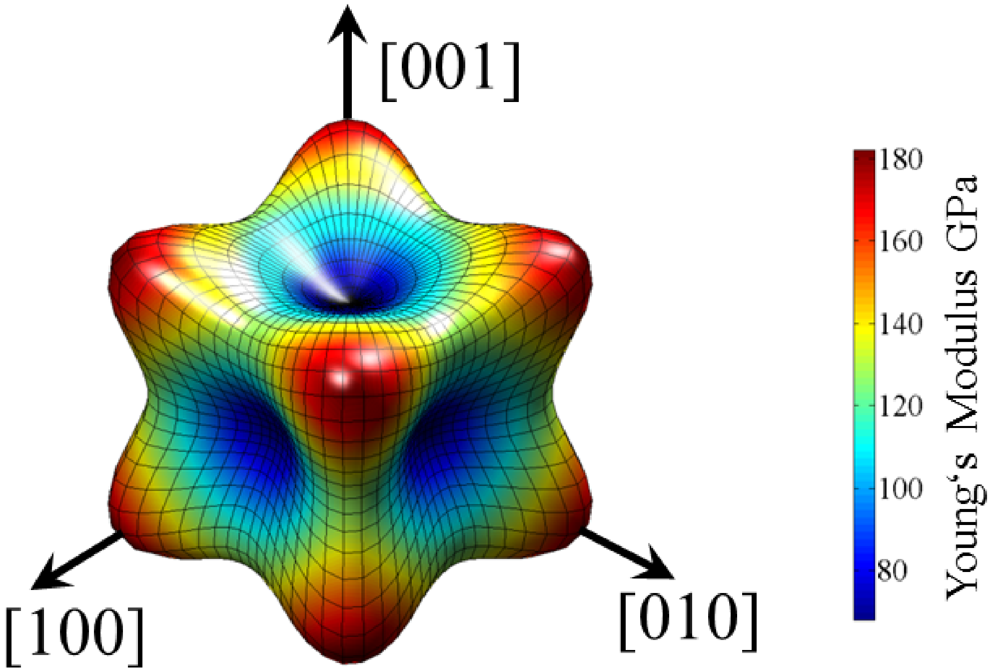

$E_{max\ (111)}$ =191,1 GPa, $E_{min\ (100)}$ = 66,7 GPa.

Figure 2.4 Orientation dependence of the modulus of elasticity (E) for Cu-single crystal [13]

2.2 Tube Forming

DHP-copper tubes and pipes are available in a wide variety of outside diameters and wall thicknesses, from small-diameter capillaries to tube with up to 300 mm outside-diameter pipe. To a certain extent, dimensions and tolerances for copper tube and pipe depend on the type of service for which they are intended [11]. There are many methods to produce tubes such as extrusion, drawing, rolling and etc.

2.2.1 Extrusion of tubes

Tube extrusion in general is as an industrial process that was invented around 1797 in England during the Industrial Revolution by Joseph Bramah. The invention was used to extrude long pipes from the molten lead. The first hydraulic press for vertical extrusion of lead tubes was developed in 1820 by Thomas Burr [14].

An important step forward was made in Germany in 1894 by Alexander Dick, when the first horizontal extrusion press was built for extruding metals with higher melting points than lead. The feature that made this possible was the use of a dummy block that separated the ram from the work billet [14, 15].

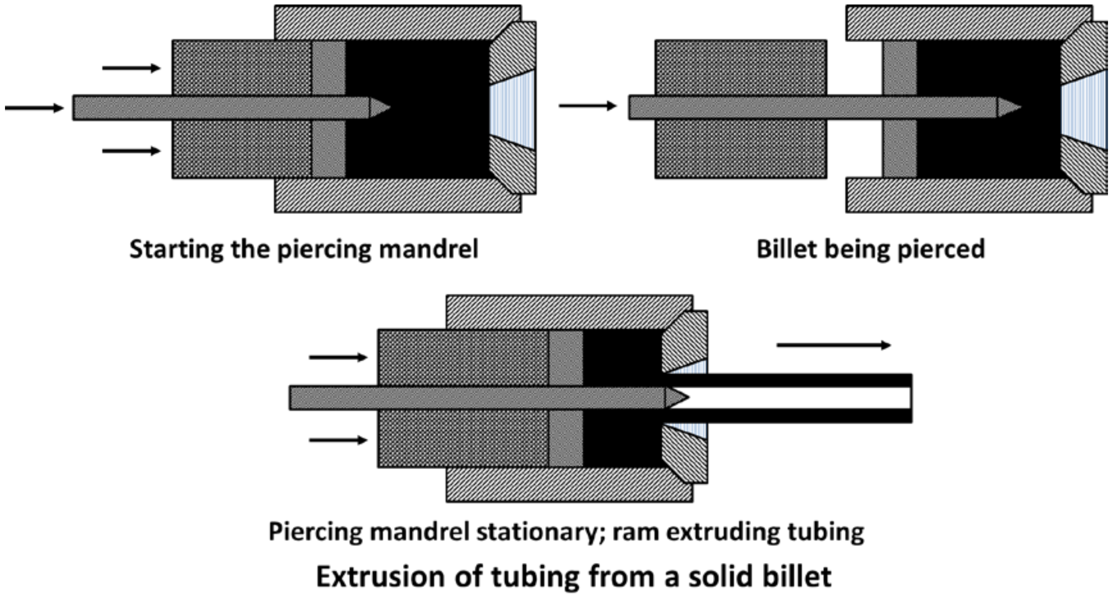

Figure 2.5 Forward extrusion of tube production [16]

In extrusion, the dies are located at one end of the container section of an extrusion press; the metal to be extruded is driven through the die by a ram, which enters the container from the opposite end to the die. Tubes are produced either by starting with a hollow billet or by a two-step operation in which a solid billet is first pierced and then extruded as shown in figure 2.5.

Extrusion pressure varies with alloy composition. Extrusion pressure also depends on billet temperature, extrusion ratio (the ratio of the cross-sectional area of the billet to that of the extruded section), speed of extrusion, and degree of lubrication. The flow of metal during extrusion depends on many factors, including copper content of the metal, amount of lubricant, and die design [17, 18].

2.2.2 Drawing of tubes

Cold drawing for DHP-copper tubes is done to the extruded or the pierced tubes to smaller sizes. With this type of machine, the metal is cold worked by pulling the tube through a die that reduces the diameter. Concurrently, wall thickness is reduced by drawing over a plug or mandrel that may be either fixed or floating as shown in figure 2.6 [14].

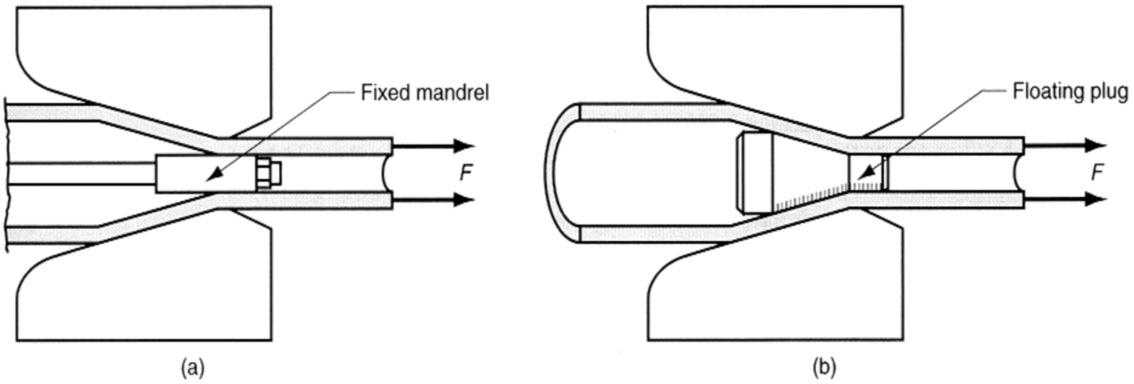

Figure 2.6 Tube drawing with mandrels (a) fixed mandrel and (b) floating plug [18].

Cold drawing increases the strength of the material and simultaneously reduces ductility. Outer diameter, inside diameter, wall thickness, and cross-sectional area all are smaller after drawing.

Tubes may be annealed at intermediate stages when drawing to small sizes because the metal work hardens during the process. However, copper and its alloys are so ductile that they frequently can be drawn to finished size without intermediate annealing [19].

2.2.3 Rolling of tubes

Another process to obtain seamless tubes are a variation of rolling called roll piercing. In this process, the billet or the round stock is rolled between two rolls, both of them rotating in the same direction with their axes at an angle of 4.5° to 6.5° as shown in figure 2.7. These rollers have a central cylindrical portion with the sides tapering slightly. There are two small side rolls which help in guiding the metal [17]. Because of the angle at which the rollers meet the billet it gets rotated and axially advanced, this aids billet piercing and results in a cylindrical shape [20]. The piercing plug assists in further opening the axial hole in the center of the billet, smoothes the wall of the hole, and controls the wall thickness of the formed tube [17].

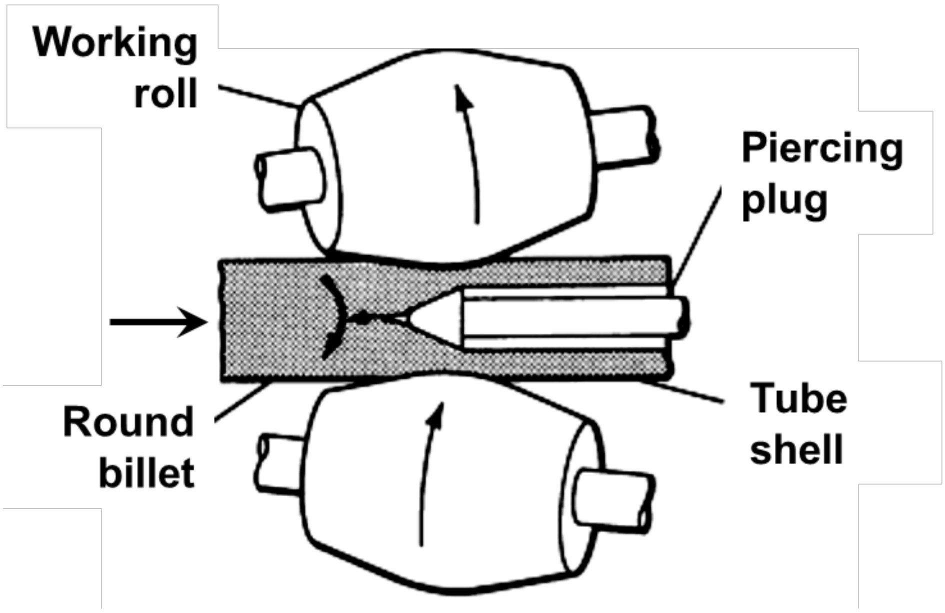

Figure 2.7 Schematic diagram of metal piercing. Arrows indicate direction of motion [17].

2.3 Eccentricity and Ovality

In spite of careful alignment of the centerline of the container, the tube and the mandrel during the tube manufacturing is almost impossible to avoid the eccentricity or the ovality [14]. Because of vibration of the mandrel, tolerance in positioning the die and the billet, and possible temperature inhomogeneities in the billet this step inherently results in a variation of the wall thickness (eccentricity and ovality) [21, 22].

The eccentricity U [23] of tubes is defined as the deviation of the wall thickness from an average value as shown in figure 2.8:

$$U = \frac{t_{max} - t_{min}}{t_{ave}} \times 100 \qquad (2\text{-}1)$$

With $t_{\max}$ and $t_{\min}$ as maximum and minimum wall thicknesses, respectively, and s_{ave} the average wall thickness.

The ovality or roundness tolerance R [23] is the deviation of the external cross-section from a perfect circular shape as shown in figure 2.8:

$$R = \frac{D_{max} - D_{min}}{D_{ave}} \times 100 \qquad (2\text{-}2)$$

D_{max} and D_{min} are the maximum and minimum outer diameters, respectively, and D_{ave} is the average outer diameter.

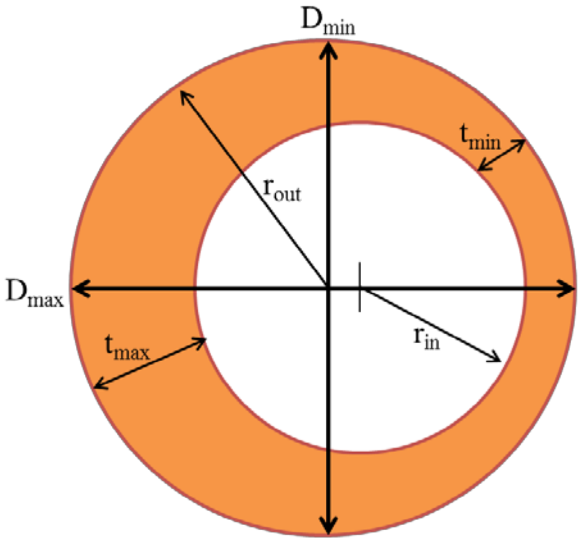

Figure 2.8 Schematic tube cross section emphasizing eccentricity and ovality.

For industrial tubes, the eccentricity for steel is typically in the range of 5 to 10% and for copper about 10%. Also industrial tubes typically show up to 1% ovality for carbon steel tubes and up to 3% for copper tubes [23].

2.4 Deformation mechanism of cubic metals

In Cubic metals the two basic mode of deformation are slip and twinning and the most significant material parameter with respect to the choice of the mode of deformation is the values of the stacking fault energy (γ_{SFE}). In this work only the deformation mode for face-centered cubic (fcc) and body-centered cubic (bcc) will be presented.

2.4.1 Deformation by slip

In general, bcc and metals deform by slip, as do fcc metals with medium to high values of γ_{SFE} such as copper (~ 80 mJm^{-2}) and aluminium (~ 170 mJm^{-2}). Plastic deformation of crystalline materials usually takes place by slip, which is the sliding of planes of atoms over one another as shown in figure 2.9 [24]. The planes on which slip occurs are called slip planes and the directions of the shear are the slip direction. These crystallographic planes and directions are characteristic for different crystal structures. If slip occurs on only part of a plane, there remains a boundary between the slipped and unslipped portion of the plane, which is called a dislocation. Slip occurs by movement of dislocations through the lattice. It is the accumulation of the dislocations that remain after slip that is responsible for the work hardening [25].

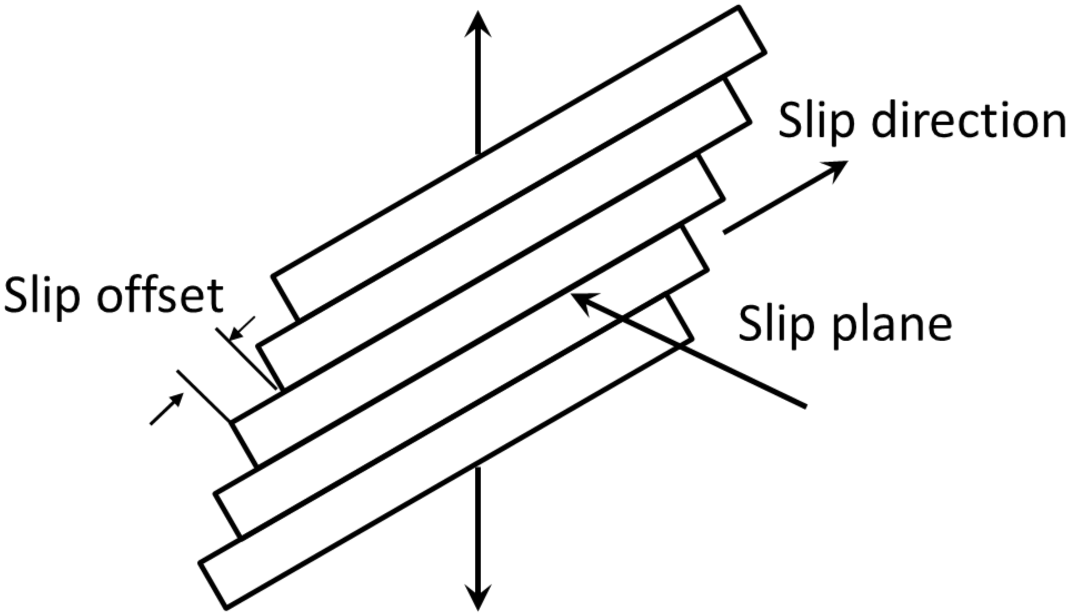

Figure 2.9 Slip by shear between parallel planes of atoms [24].

The slip system and direction for fcc and bcc common crystals are presented in the table 2.2. Almost without exception the slip directions are crystallographic directions with the shortest distance between like atoms or ions and the slip planes are usually the densely packed planes as shown in figure 2.10 [26].

At room temperature bcc metals slip on all three plane in commen <111> direction and term pencil glide [27].

Table 2.2 Slip directions and planes in cubic metal [27]

Structure	Slip direction	Slip plane
fcc	<110>	{111}
bcc	<111>	{110}, {112}, {123}, pencil glide

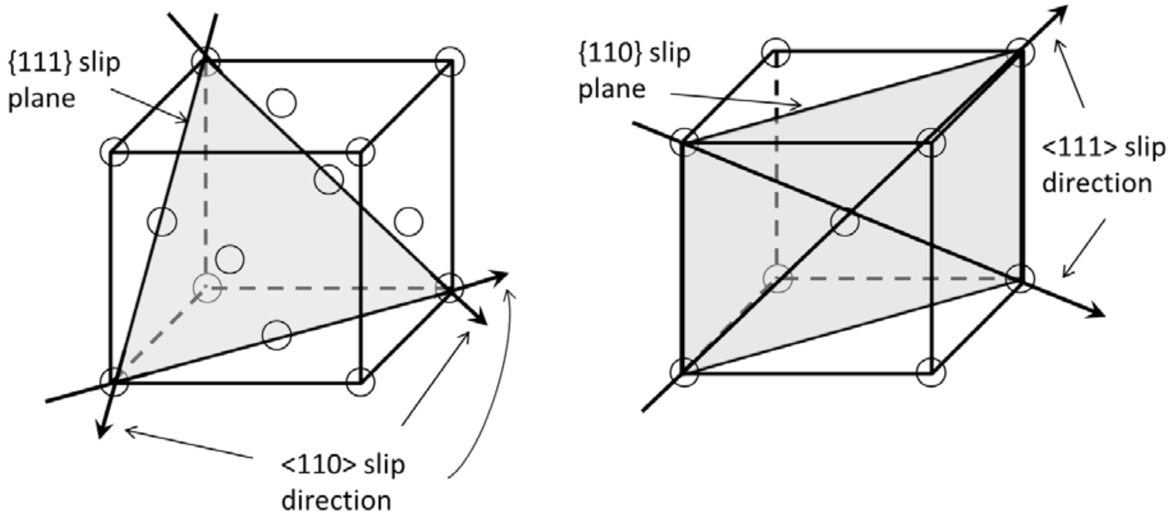

Figure 2.10 Diagram showing predominant slip systems in (left) fcc and (right) bcc [28].

2.4.2 Twinning

In general, twinning is a major deformation mechanism in fcc with low γ_{SFE}. It may also occur in fcc metals with high values of γ_{SFE} and in bcc metal if deformation occurs at low temperatures or high strain rates. Twins that form during recrystallization are called *recrystallized twins* and those that form during uniform shearing are *mechanical twins* [29].

Mechanical twinning, like slip takes place by shear. A twin is a region of crystal in which the orientation of the lattice is a mirror image of that in the rest of the crystal. Normally the boundary between the twin and the matrix lies in or near to the mirror plane [30, 31]. Table 2.3 shows the twinning system in metals with a cubic crystal structure.

Table 2.3 Twin directions and planes in cubic metal [27]

Structure	Twin direction	Twin plane
fcc	<112>	{111}
bcc	<111>	{112}

Both slip and twinning are deformation mechanisms that involve shear displacements on specific crystallographic planes and in specific crystallographic directions. However, there are important differences [24].

1. With slip, the magnitude of the shear displacement on a plane is variable, but it is always an integral number of the interatomic repeat distance *nb*, where *b* is the Burgers vector (The magnitude and direction of the lattice distortion associated with a dislocation). Slip occurs on

only a few of the parallel planes separated by relatively large distances. With twinning, on other hand, the shear displacement is a fraction of an interatomic repeat distance and every atomic plane shears relative to its neighboring plane.

2. The twinning shear is always directional in the sense that shear in one direction is not equivalent to shear in the opposite direction. Twinning in fcc crystal occurs by shear on the (111) plane in the [11-2] direction but not by shear in the [-1-12] direction. In fcc metals slip can occur on a (111) plane in either the [-110] or the [1-10] direction.

3. With slip the lattice rotation is gradual. Twinning reorients the lattice suddenly.

2.5 General introduction on crystallographic texture

Crystallographic texture is the orientation distribution of the crystallites of a polycrystalline sample with respect to a sample orientation. A lot of polycrystalline materials like metals, ceramics, rocks and some polymers, show preferred orientation of crystallites. Diffraction from powder samples with random texture gives rise to set of homogeneous concentric Debye-Scherrer rings which are related to the various reflecting lattice planes (hkl). If the sample has a pronounced texture, the rings display intensities variations which are express the presence of the texture in the measured volume [32].Texture is an essential feature in polycrystalline materials and has an influence on mechanical and physical properties such as strength, electrical conductivity, magnetic capability, light refraction and wave propagation, and particularly the anisotropy of these properties [33]. The texture may undergo evolution during casting, processing, deformation, welding, as well as heat treatment. The relation of the materials properties to this preferred orientation of the crystallites in certain sample directions is one of the main problems in materials science for the optimization of properties [34, 35].

2.5.1 Determination of the Orientation Distribution Function

A polycrystalline material consists of grains or crystallites which are separated from one another by grain boundaries. A complete description of the polycrystalline structure requires the specification of the orientation of the crystallographic axes of each grain as well as its form and its position within the sample. Such a description is usually much too complicated to be practicable. Polycrystalline structures are therefore usually described by certain statistical distribution functions such as the mean grain size, the grain size distribution, or the main grain shape. One of these statistical parameters is the orientation distribution function of the material. It is obtained by neglecting the form and the position of the crystallites, thus taking into account only the orientation of the crystallographic axes with respect to sample axes.

Mathematical descriptions on texture characterization and measurement technology have been systematically done by, Prof. H.J. Bunge, in his books or published papers [36-38]. For describing the orientation distribution two of coordinate systems are introduced. These two coordinate systems are related to each other with an orientation (*g*) as following:

$$K_A \to g \to K_B \tag{2-3}$$

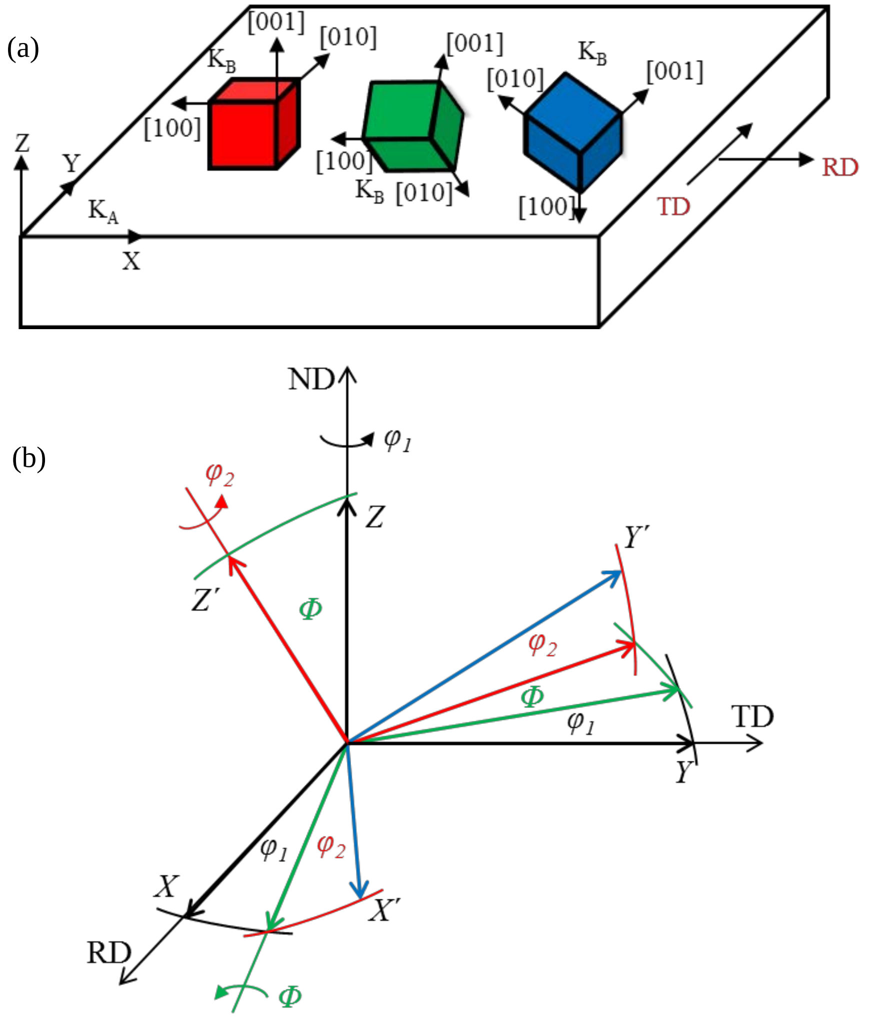

Figure 2.11 Two methods for representing the orientation g, (a) Miller indices and (b) Euler angle, a coordinate system is presented as Z-axis and its X-Y plane for the sample; Z' and X'-Y' plane for crystal [36].

As the coordinate system is fixed in the sample, $K_A = (X, Y, Z)$, the exterior shape is generally used, e.g. rolling, transverse, and normal directions in case of rolled sheet. The second coordinate system for each crystal is defined, $K_B = (X', Y', Z')$, which is fixed within the crystal-lattice, e.g. [100], [010] and [001] in case of cubic crystallography, *i.e.* the K_A is transformed by g into the K_B as shown in figure 2.11a.

The orientation g can be presented in some different ways, for example, by Miller-indices ($h\ k\ l$) [$u\ v\ w$] or by Euler angles $\{\varphi_1, \Phi, \varphi_2\}$. The indices ($h\ k\ l$) stand for a crystallographic plane whose plane normal is parallel to plate-normal direction and [$u\ v\ w$] and is the crystallographic direction parallel to the rolling direction (for the case of a rolled plate) [36].

The Euler angles are defined by rotation angles around 3 fixed axes (see figure 2.11b), by which the crystal coordinate system becomes matched with the sample coordinate system. The crystal coordinate system is firstly rotated about the Z-axis through the angle φ_1, then about the X'-axis (in its new orientation) through Φ and, finally, once again around the Z'-axis (in its new orientation) through the angle φ_2 [36].

If one denotes by dV the totality of all volume element of the sample which possess the orientation g within the element of orientation dg, and by V the total sample volume, then an orientation distribution function (ODF) $f(g)$. In this case the orientation distribution function of the volume, is defined by [37]

$$f(g)dg = \frac{1}{V}\, dV \tag{2-4}$$

$$g = \{\varphi_1, \Phi, \varphi_2\} \tag{2-5}$$

$$dg = \frac{1}{8\pi^2} \sin\Phi \; d\Phi \; d\varphi_1 d\varphi_2 \tag{2-6}$$

In the above formula, the orientation distribution function (ODF) $f(g)$is given as the multiples of the random distribution (mrd) *i.e.*

$$\int_{random} = \oint f(g)dg = 1 \tag{2-7}$$

ODFs cannot be measured directly by means of diffraction techniques but need to be calculated from measured pole density distribution functions ($P_{hkl}(\alpha,\beta)$, pole figures), called pole figure inversion. Usually, a larger number of pole figures is determined and used to calculate an ODF than is mathematically necessary. With cubic crystal structures 3 and hexagonal crystal structures 5-6 pole figures are suffice [33, 36]. A pole figure represents the probability of lattice plane poles in different sample directions. The probability is contoured on a sphere, relative to sample coordinate and projected on a plane, using equal area or stereographic projection. Pole figures can be directly measured by some diffraction techniques, e.g. laboratory X-ray, neutron and synchrotron diffraction facilities. However, the coverage of such measurements is sometimes incomplete which mean that not the whole pole figure can be recorded. This further reduces the texture information available in such pole figure. More importantly, the pole figures provide the orientation distribution in 2-dimension so that several orientations may be overlapped on a pole figure position and the rotation around the poles cannot be considered because the degree of freedom remains open in its description. These are the reasons why ODF is preferred for a quantitative representation and analysis [33].

In order to display the three-dimensional ODF, a representation in an appropriate three-dimensional frame is required, thus several suitable orientation spaces have been introduced, namely Euler space, cylindrical angle/axis space and Rodrigues space. Among them, the Euler space is most often used to represent macrotexture data. One can represent the ODF in a reduced Euler space, when the crystal and sample symmetries are considered. The whole Euler space is given in the range of $0° \leq \varphi_1 \leq 360°$, $0° \leq \Phi \leq 180°$ and $0° \leq \varphi_2 \leq 360°$, without consideration on the symmetry [36].

The mathematical methods for ODF calculation has been described by many authors, Bunge and Roe [36, 39] introduced the series expansion method and Matthies [40] used the WIMV (Williams-Imhof-Matthies-Vinel) method. In the present work the series expansion method by Bunge is used. In Bunge's formalism, a pole figure is expanded in a series of spherical harmonic function;

$$P_{hkl}(\alpha,\beta) = \sum_{l=0}^{l_{max}} \sum_{v=1}^{N(l)} F_l^v\,(hkl) \cdot \dot{k}_l^v(\alpha,\beta) \tag{2-8}$$

$$F_l^v(hkl) = \int_{\alpha=0}^{\pi/2} \int_{\beta}^{2\pi} P_{hkl}\,(\alpha,\beta) \cdot \dot{k}_l^v(\alpha,\beta) \sin\alpha\, d\alpha d\beta \tag{2-9}$$

Where, l is the series expansion degree, F are the pole figure coefficients, and $\dot{k}$ are the symmetrized spherical harmonic functions. The F coefficient can be calculated by integration of the experimentally determined pole density distribution using pole figure inversion. For this the normalized pole figure intensities are used;

The above equations show how the unknown *C* coefficients of the orientation distribution function can be calculated from the known *F* coefficients. Once the *C* coefficients are known, the ODF can be expanded into a series of generalized spherical harmonics;

$$f(g) = f(\varphi_1, \Phi, \varphi_2) = \sum_{l=0}^{l_{max}} \sum_{\mu=l}^{M(l)} \sum_{v=l}^{N(l)} C_l^{\mu v} \cdot \ddot{T}_l^{\mu v}(\varphi_1, \Phi, \varphi_2) \qquad (2\text{-}10)$$

$$F_l^v(hkl) = \frac{4\pi}{2l+1} \sum_{\mu=1}^{M(l)} C_l^{\mu v} \cdot \dot{k}_l^{*\mu}(hkl) \qquad (2\text{-}11)$$

In the Eq. 2-8 to 2-11, the symbol ‘*’ denotes the complex conjugate, and the dots over the harmonic functions denote the symmetrization of the functions. *M(l)* and *N(l)* are the number of independent values for each expansion degree *l*, after the sample- and crystal symmetrizations, respectively. All summations in the above equations are controlled by the index *l* which means that the truncation error is merely determined by the maximum value of *l*. In general, for cubic materials the order of the series expansion is limited to *l* = 22 or, for sharper textures, to *l* = 34, which yields sufficiently accurate results with an acceptable computational effort [36, 37].

The orientation distribution function (texture) can be presented be ideal locations (texture components). The description of the orientation distribution function (ODF) by texture components provides a strong reduction in the total representation of the orientation distribution information. The Determination of the main texture components, however, can be very useful, for example, certain texture components can be assigned to specific deformation processes. Determination of texture components can be made from both the ODF or made directly from the pole figures [41]. But as mentioned before, when determining the texture components of pole figures it should be noted that several components may be superimposed on a Pole figure position.

2.6 Fundamentals of texture measurement

To calculate the ODFs experimental data are needed as input for the mathematical procedure. Experimental textural data can be obtained by many methods. In this part the fundamentals of texture measurements by x-ray, synchrotron, neutron and electron will be presented.

2.6.1 Texture measurement by x-ray method

Texture measurement by x-ray diffraction was first used by (Wever) [42] to investigate preferred orientations in polycrystalline metals by evaluating the inhomogeneous intensity distribution along the Debye-Scherrer rings. Decker *et al.* [43] and Norton [44] have introduced the texture goniometer and the use of Geiger counters to record the pole figures directly. Many aspects of pole figures goniometry have been discussed in some detail by Schultz [45, 46]. Bragg's law [47] for monochromatic radiation is used. It has two conditions, a lattice plane *hkl* scatters if it is in scattering position between incident and diffracted x-rays. The second condition is that lattice planes with a spacing d_{hkl} obey the law

$$n\lambda = 2d_{hkl}\sin\theta \tag{2-12}$$

Where 2θ is the angle between incident and diffracted beams, and λ is the monochromatic x-ray wavelength and n an integer defining the order of diffraction.

For an x-ray source one generally relies on an x-ray tube with a particular metal as the anode material for producing a wavelength spectrum with high intensity of $K\alpha$ and $K\beta$ from the anode element see table 2.4. For x-ray tube, the $K\beta$ component in the spectrum can be reduced by applying an absorption filter. Single crystal monochromators are preferred for producing truly monochromatic radiation [48].

Table 2.4 Characteristics of various X-ray tubes and appropriate filters [33]

Wavelength λ (nm)			Kβ-filter			
Anode material	**Kα**	**Kβ**	**Material**	**Edge λ (nm)**	**Thickness for Kβ /Kα 1:500(nm)**	**Loss in Kα (%)**
Cr	0.22909	0.20848	V	0.22690	17	51
Fe	0.19373	0.17565	Mn	0.18964	18	53
Co	0.17902	0.16208	Fe	0.17433	19	54
Cu	0.15418	0.13922	Ni	0.14880	23	60
Mo	0.07107	0.06323	Zr	0.06888	120	71
Ag	0.05609	0.04970	Rh	0.05338	90	73
			Pd	0.05092	92	74

Two methods of analysis are generally used: determination of texture can be done on a sample of large thickness and with a plane surface on which x-rays are reflected (*reflection*) or using a thin slab of thickness *t* which is penetrated by x-rays (*transmission*) as shown in figure 2.12.

The goniometer moves the detector with respect to the x-ray beam (rotation 2θ) with an Eulerian Cradle; the sample is positioned relative to the x-ray beam defined by the rotation angle Φ and the tilting angle χ as shown in figure 2.12. The χ circle is generally symmetrical between incoming and diffracted beam, ω is the deviation from the bisecting position. The 2θ and ω axis coincide [33].

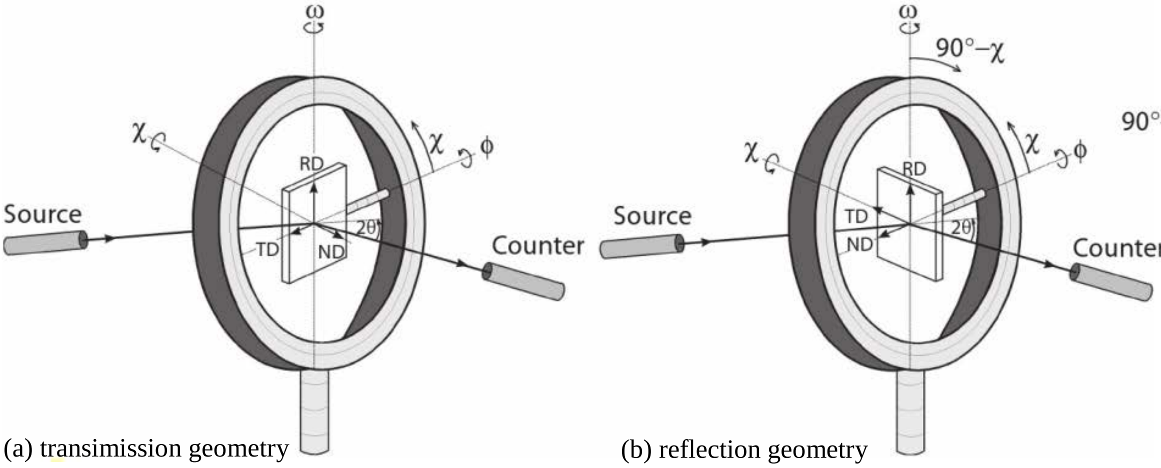

(a) transimission geometry (b) reflection geometry

Figure 2.12 Diffraction in a four-circle texture goniometer with definition of the instrument angles [33].

In order to measure an unknown crystal orientation in practical applications, the sample is systematically rotated in a texture goniometer about well-defined angles in such a way that all possible lattice planes are successively brought into the reflection condition and the reflected intensities are recorded as a function of these rotation angles. The rotation angles are directly related to the pole figure angles α (radial) and β (azimuthal), so that the reflected intensities can readily be represented in a pole figure. Although the limiting value for α in the Bragg-Brentano focusing condition is obtained when both the incident and reflected beams are parallel to the sample surface, so that $\alpha_{max} \leq 90°$, there are several aspects that usually limit α_{max} to values of 60°-85°[33].

In stepper motor driven goniometers, the pole figures are mostly scanned on equidistant concentric circles of constant α in steps of typically 5° both in α and β (Figure 2.13). For a complete pole figure this results in (α x β) = 19 x 72 = 1368 points. At counting times of typically one second per point this yields a total measuring time of less than 30 min per pole figure. For very sharp textures, the standard 5° X 5° grid may be too coarse and finer grids, e.g. 1° x 1°, are required [33].

A pole figure is scanned by measuring the diffracted intensity at different (*α, β*) settings. This can either be done in stepwise manner or by recording the average intensity continuously over an angular range from one setting to the next.

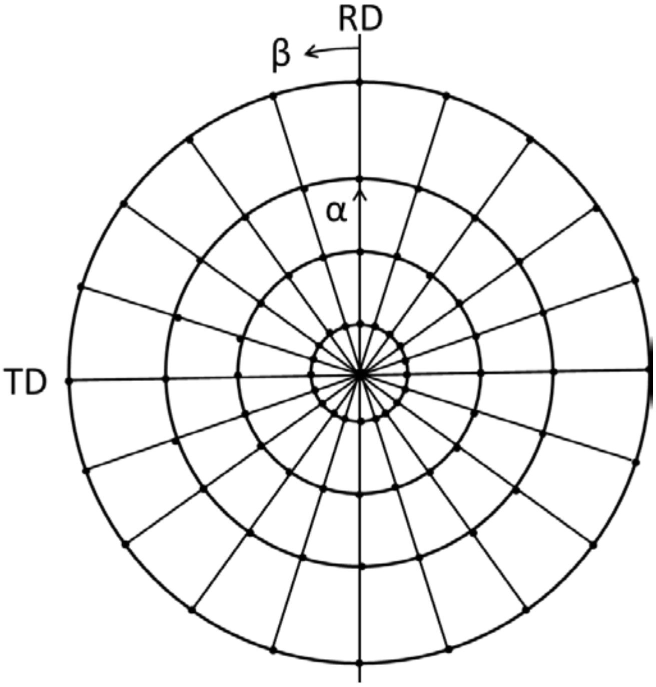

Figure 2.13 Circular, equal angle scanning grid for pole figure measurements (note that for clarity the scanning schemes are shown in steps of 20°) [33].

2.6.2 Texture measurement by synchrotron radiation

Synchrotron beam is the electromagnetic radiation emitted when electro-charged particles usually electron or positron in storage ring, moving at velocities close to the speed of light, are forced to change direction by magnetic field. The synchrotron radiation is emitted in at tangent to the particles' orbit [49].

Synchrotron radiation yield a much greater penetration depth, up to the order of centimeters because of its high energy, compared to values of about 100 µm for laboratory x-ray sources. This allows global texture of big samples to be measured. However, measurements can also be performed on a local basis in the interior of large bulk specimens [32]. Synchrotron radiation has also high spatial resolution and excellent brilliance.

For texture analysis in fine grained polycrystalline samples by means of the powder diffraction method with synchrotron radiation, a narrow beam of monochromatic x-rays is required. To achieve monochromatic radiation, the beam first passes through a monochromator crystal that selects the desired wavelength in the range of 0.01 nm- 0.1 nm. Finally, the monochromatic beam is collimated to the desired size and falls onto the investigated sample, where the Debye-Scherrer patterns are generated in transmission geometry [33].

For 2D detectors provide digitized intensities with high spatial resolution within a few seconds. The usage of 2D detectors contribute to remarkable reduction of the measuring time and more angular resolution, since some complete Debye-Scherrer rings are simultaneously collected during radiating a sample.

For the texture measurement the sample needs to be rotated by an angle ω and in each setting a diffraction pattern has to be recorded. After appropriate correction the texture can be calculated from analysis of the intensity variation along the Debye-Scherrer rings [33].

Interesting application of synchrotron radiation may include [50]:

- Non-destructive local texture measurements
- High resolution texture analysis
- Investigation of texture gradient
- *In situ* texture measurement of texture transformations
- Determination of misoientation and characterization of grain boundaries including boundary plane
- Internal strain in selected local volumes

2.6.3 Texture measurement by neutrons diffractions

The first texture measurements by means of neutron diffraction were performed in 1953 by Brockhouse [51] at Chalk River National Laboratory. In the 1960s, this technique was further developed by Tobisch and coworkers (e.g. Kleinstück and Tobisch [52], Tobisch *et al.* [53]; Kleinstiick *et al.* [54]); the advantages of neutron diffraction for texture analysis have been demonstrated. Nowadays, the application of neutron diffraction for texture analysis is well established [55-62].

Most neutron diffraction texture studies are done at reactors which produced a constant beam of thermal neutrons. Few facilities use pulsed neutrons, e.g. at spallation sources. A disadvantage of neutrons is that the flux is very low, compared even to conventional x-ray generators, and thus long counting times are required [33].

The neutron detector is set to the corresponding Bragg angle 2θ for the selected lattice planes $\{hkl\}$ (angle dispersive method). The pole densities of that lattice plane in different sample directions are scanned with a goniometer by rotating the sample around two axes, Φ and χ , corresponding to the pole figure angles β and α, to cover the entire orientation range. The main difference between neutron and x-ray diffraction is the much lower, almost negligible, absorption of neutrons by matter as presented in table 2.5 [1].

Table 2.5 Comparison of penetration depth d1/2 (in cm) [61]

Material	Neutrons (λ= 1.00 Å)	X-rays (λ= 1.54 Å)	X-rays (λ= 0.124 Å)
Mg	6.10	0.0140	3.40
Al	7.67	0.0053	1.5
Cu	0.85	0.0015	0.20
Ti	1.61	0.0011	0.60
Pb	2.10	0.0003	0.03

Therefore, large samples, usually several centimeters in size, can be analyzed using transmission geometry [62]. Roughly spherical samples after Tobisch and Bunge [2] are completely sufficient for neutron experiments [63]. In contrast to x-ray experiments, where the x-ray beam must not leave the sample surface, for neutron diffraction experiments the sample must not leave the neutron beam. Then, no intensity corrections are necessary and complete pole figures, i.e. up to $\alpha = 90°$, can be obtained in one scan. The number of grains encountered is much larger, usually by 4-5 orders of magnitude, which means that grain statistics are much better [60, 62].

For analysis of too thin specimens, e.g. sheet material, a cubic or a cylindrical shape samples may be produced by stacking several pieces cut from the sheet and then glued together. For most materials cubic and cylindrical samples give the same accuracy as spherical sample [62].

The texture measurement is performed on a standard four-circle diffractometer. An Eulerian cradle which can be rotated around the co-axis is mounted on the four-circle diffractometer.

The cradle allows the sample to be rotated about two angles χ and Φ. The principal axes are shown in Figure 2.14 [1].

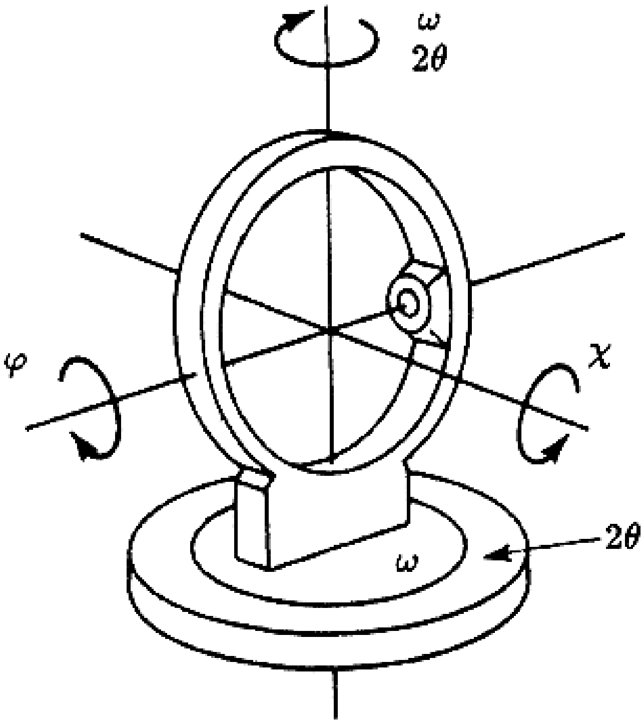

Figure 2.14 Principal axes of a four-circle diffractometer [1].

2θ is twice the Bragg angle θ which is determined by the crystallography of the material. The ω axis is coincident with the 2θ axis and defines the angle between the diffraction vector and the plane of the χ circle. The two angles (ω, 2θ) are also used for standard powder diffraction work (two-circle diffractometer). Hence, the other two angles χ and Φ correspond to the pole figure angles α and β and are used for the pole figure measurement. The sample is positioned at the center of the diffractometer. Before the pole figures can be measured, the 2θ positions of the Bragg-reflections must be determined, a selection of the suitable Bragg-reflections for a pole figure measurement has to be made, and a selection of the background positions is necessary [1].

2.6.4 Texture measurement by Scanning Electron Microscope (SEM)

Local orientation can also be measured with the scanning electron microscope (SEM). The interaction of the electron beam with outer surface layer of the sample produce two types of diffraction patterns from which the orientation can be determined, electron channeling pattern and electron back-scattering diffraction (EBSD). EBSD is more commonly used for texture analysis [64].

For EBSD pattern are generated by backscatter diffraction of a stationary beam of high-energy electrons from a volume of crystal material approximately 20 nm deep in the specimen, times the projected area of the incident beam [64]. The specimen should be tilted by angles of typically >60° [65] as shown in figure 2.15. The main effect of tilting the specimen is to reduce the path length of electrons which have been backscattered by lattice planes as they enter the specimen. Thus allowing a far greater proportion of these electrons to undergo diffraction and escape from the specimen (having lost virtually none of their energy) before being absorbed. Electron backscatter diffraction (EBSD) is a technique which is becoming almost universally used to obtain local orientation information [33].

The steps necessary to produce an EBSD pattern in an SEM are:

- Tilt the specimen so that its surface makes an angle >60° with the horizontal
- Turn off the scan coils to obtain a stationary beam
- Place a recording medium or device in front of the tilted specimen to capture the diffraction pattern.

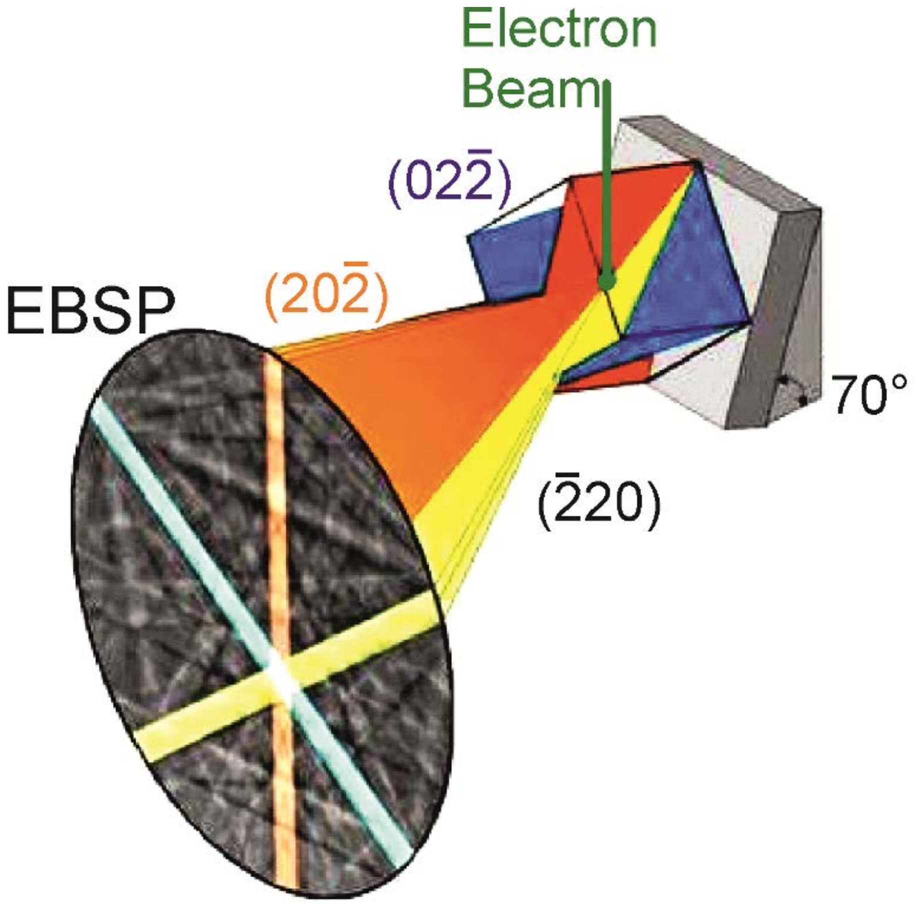

Figure 2.15 Principle of EBSD pattern formations [66].

Since the back scattered electrons emerge from a very thin surface layer of the sample (on the order of few nm), the technique requires a completely flat surface that is as free of defects as possible. It is essential to remove the damaged surface layer created during mechanical polishing. For metals electropolishing has proven to be useful [64].

In order to make orientation measurements from EBSD patterns it is essential to identify the following parameters [67], which are illustrated on Figure 2.16:

- The coordinates of the pattern centre, PC.
- The specimen-to-screen distance L on Figure 2.16.
- The relationship between reference directions in the microscope X_m Y_m Z_m specimen X_s Y_s Z_s and screen/pattern x y z

These parameters depend on the relative positions of the camera and specimen within the microscope.

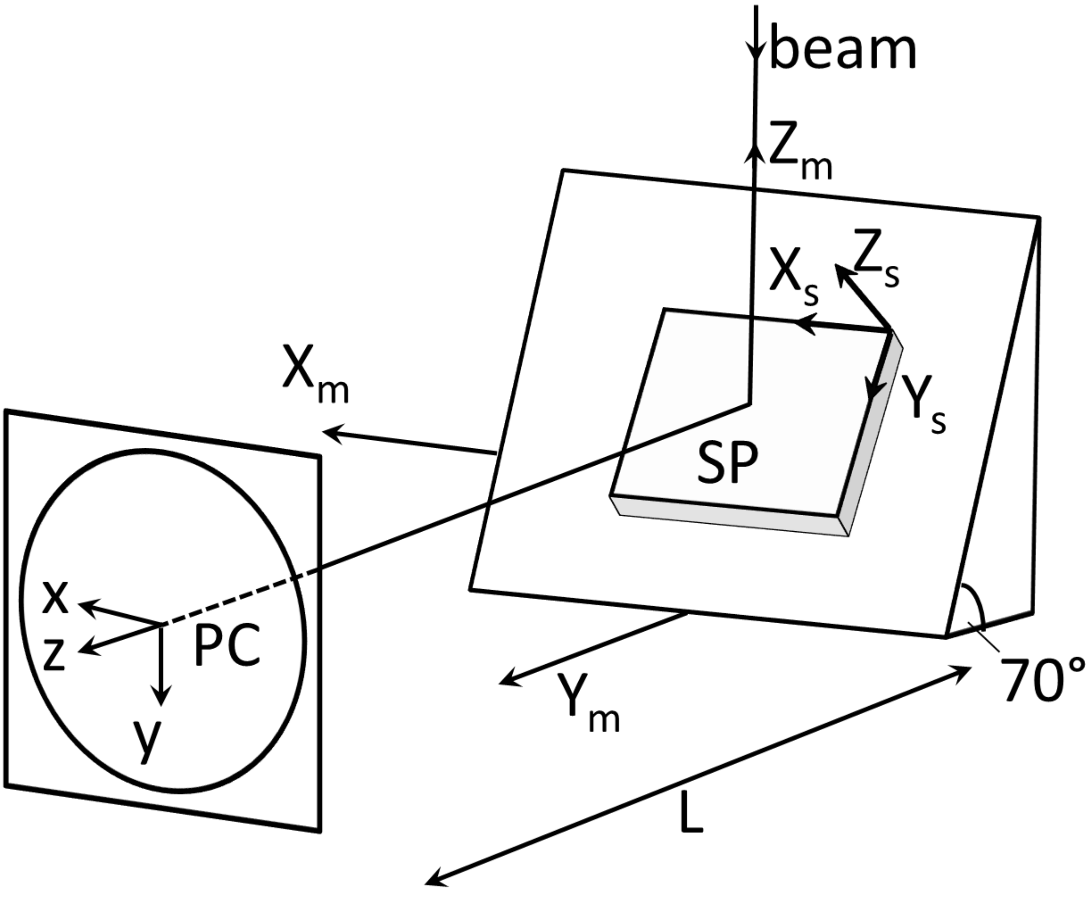

Figure 2.16 Parameters required for EBSD orientations measurements: pattern source point on the specimen, *SP*, pattern centre on the recording screen, *PC*, specimen-to-screen distance *L*, and three sets of orthogonal axes, *x y z* (screen/pattern axes), X_S Y_S Z_S (specimen axes) and X_m Y_m Z_m (microscope axes) [33].

A map of the sample is prepared which shows the grain boundaries. Then the operator locates the grain of interest and obtains a diffraction pattern. The interpretation of EBSDs can be done on the photographic film, on an analog video screen, or on a digital image. The angle between bands- and sometimes their width (which is inversely proportional to d) and the intensity are used to index the pattern and determine the crystal orientation. This information directly provides the Euler angles [64].

The entire procedure has been automated. The sample is translated with a high precision mechanical stage in increments as small as 1 μm, or even smaller. Different sample locations are reached by beam deflection. At each position an EBSD pattern is recorded with a phosphor screen. Back scattered electrons are converted to light, this signal is transferred by a lens system or fiber optics into a CCD or analog camera. The digital EBSD is entered into a computer and indexed on-line in matter of seconds [33, 64].

2.7 Intensity correction of integrated peak intensity after neutron diffraction

In bulk texture analysis thermal neutrons are well known for their excellent penetration of comparably large sample volumes [62]. For most materials where the spherical sample method after Tobisch and Bunge [2] is used no data correction of integrated peak intensities is needed. This is related to the high penetration power of thermal neutrons and a large enough beam cross section that the average texture information of the whole test sample is obtained. During sample tilt and rotation the gauge volume is constant for samples up to some cm in diameter for each measured intensity $I_{hkl}(\alpha,\beta)$. In the case of local texture measurements of large samples, such as semi-finished products, this assumption is no longer true. Any texture measurement, independent which volume methods is used, is very sensitive to changing gauge volume during sample tilting and rotation. Looking at the intensity formula (see eq. 2-13) of a scattered Bragg reflection one can clearly see the importance of volume correction (V). But also a *hkl* dependent absorption correction (A_{hkl}) is necessary if the sample is larger than the beam cross section as in case of semi-finished products. K is a constant related to all sample independent contributions, N_{hkl} includes all parts of the measured phase and $P_{hkl}(\alpha,\beta)$ is the crystallographic texture.

$$I_{hkl}(\alpha,\beta) = KN_{hkl}A_{hkl}VP_{hkl}(\alpha,\beta) \tag{2-13}$$

In the past some work has been done to implement absorption correction to correct measured pole figures [68, 69]. Luzin and Brokmeier, have corrected pole figure data from different types of tubes for incomplete pole figure measurements using the Schultz method [45, 46].

The key problem in non-destructive investigation of texture gradients is the changing gauge volume during sample movement and consequently different absorption factors for each pole figure point $P_{hkl}(\alpha,\beta)$ [4]. The absorption correction can play an important role on the quality of quantitative textures in case of complex sample geometries, of high absorption coefficient or for multi-phase systems with different absorption properties. Montesin *et al.,* [70] presented the intensity correction of X-rays pole figure measurements of wires. Mücklich and Klimanek [71] studied the experimental errors in quantitative texture analysis directed to experimental pole figures. They concentrated on statistical errors and physical errors including absorption and extinction corrections. Nikolayev and Walther [72] calculated the absorption correction factors for pole figures of cylindrical samples measured by neutron time of flight technique. Volz *et al.* [73] measured the effect of strong neutron absorption on the crystallographic texture of cold rolled foils of Dysprosium and Erbium with different thicknesses (152 μm, 229 μm and 686 μm). The samples were measured by neutron time of flight diffraction.

2.8 Texture in copper

The deformation textures of fcc metals are determined primarily by the stacking fault energy (γ_{SEF}). For example, for both aluminum with γ_{SEF} ~ 170 mJm^{-2} and copper with γ_{SEF} ~ 80 mJm^{-2}, slip is the deformation mode and the rolling texture, after large reduction, are very similar to that of figure 2.17. It is usually to refer to the texture of metal with high values of γ_{SEF} referred to as PURE METAL TEXTURE (or copper type)to distinguish it from the ALLOY TYPE TEXTURES (or silver or brass type)characteristic of materials with low values of γ_{SEF} [27, 74]. In this work we will describe only the PURE METAL TEXTURE.

The 111 and 200 pole figures for 96.6% cold rolled electrolytic copper are shown in figure 2.18. On the pole figure in figure 2.18 are the ideal orientations, {112}<111>, {110}<112>, {123}<412>, that are commonly used to describe the texture by many studies [74-91]. Nowadays the latter of these has been largely replaced by the slightly different orientation {123}<634>.

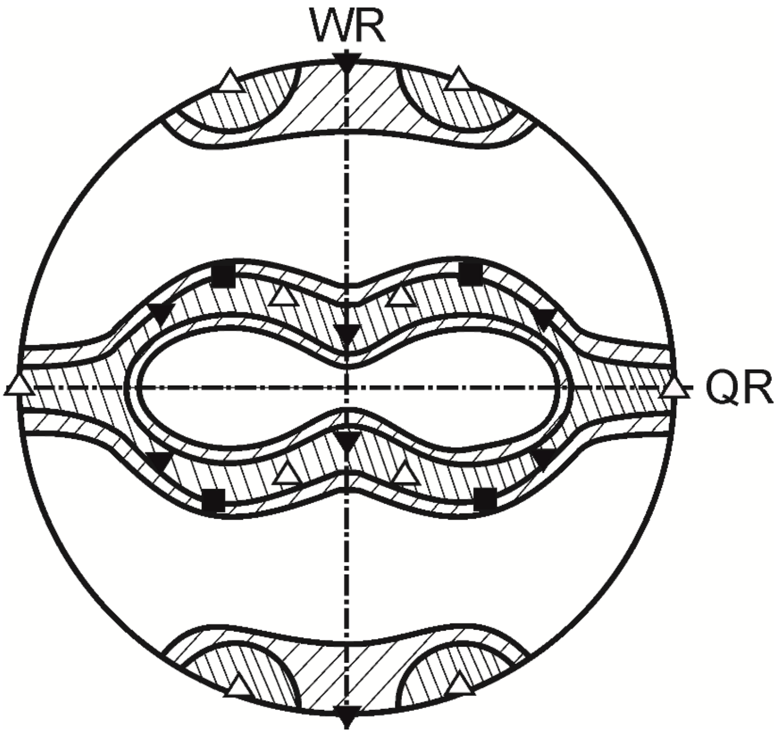

Figure 2.17 (111) Pole figure of 98 % cold rolled electrical copper [41]

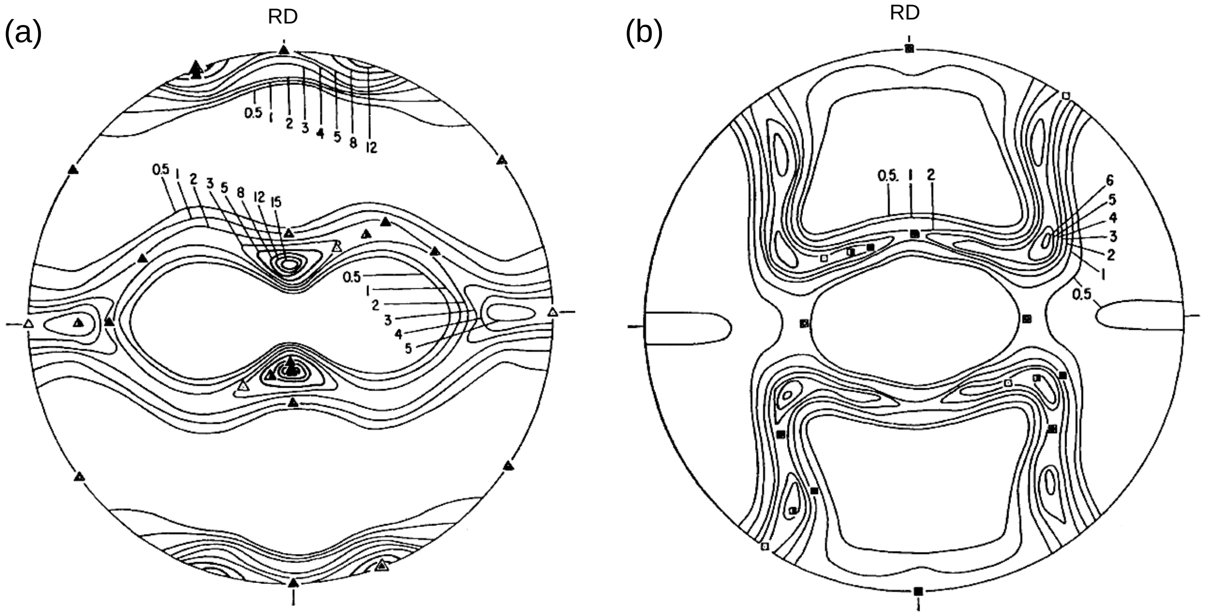

Figure2.18 Rolling texture of electrolytic copper after 96.6% reduction in thickness at 25°C. (a) (111) pole figure, (b) (200) pole figure [74].

Examination of figure 2.18 shows that no combination of these orientations corresponds to all of the high intensity regions and therefore a description of the texture in terms of these ideal components is unsuitable. More information is given by describing the texture as a spread of orientations from {112}<111> through {123}<634> to {110}<112> but such a description does not specify the crystallographic nature of the orientations within the spread [27].

A better description of the texture is provided by the ODF as shown for the 90% cold rolled copper in figure 2.19 [75]. The most important observation is that the texture is now represented by a continuous tube of orientation which runs from {110}<112> (Brass) at Φ=45°, φ_2=90°, φ_1=35° through {123}<634> (S) at Φ=37°, φ_2=63°, φ_1=59° to {112}<111> (Copper) at Φ=35°, φ_2=45°, φ_1=90°. A schematic representation of the tube is given in figure 2.20 where one of the two braches has been omitted for the sake of clarity [27].

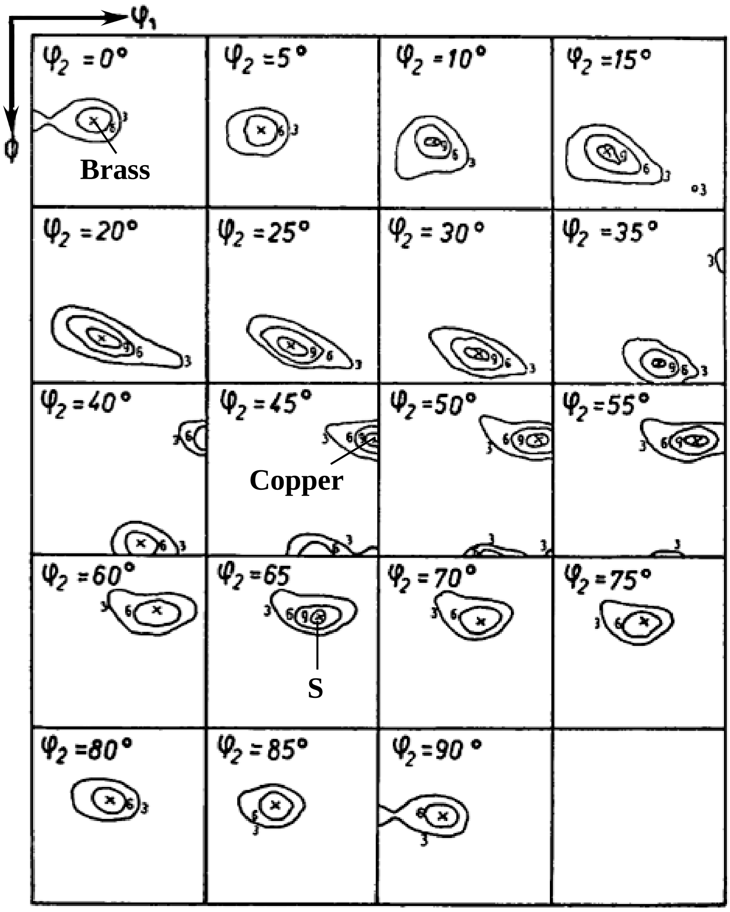

Figure 2.19 The ODF of the crystallites in copper for 90% cold rolling [77]

The omitted branch is that observed in the sections φ_2= 0° – 45°. The tube shown in figure 2.20 can also be described in terms of its axis or skeleton line. By convention the axis of the tube shown is called the β-fibre and many studies of rolled fcc metals report data only in the form of orientation density along this fiber [74-91]. A second fiber, the α-fiber can be seen in figures 2.19 and 2.20 where it extends from {110}<001> (Goss) at Φ = 45°, φ_2 = 90°, φ_1 = 0° to {110}<112> (Brass) at Φ = 45^o ,φ_2 = 90^o , φ_1 = 35^o.

A number of the common texture components have acquired simple names and symbols given in table 2.6 which also gives details of the Euler angles of the main texture components of rolled fcc metals.

Table 2.6 Texture components in rolled fcc metals [76].

Component, symbol	{hkl}	<uvw>	φ_1	Φ	φ_2
Copper, C	112	111	90	35	45
S	123	634	59	37	36
Brass, B	011	211	35	45	90
Goss, G	011	100	0	45	90

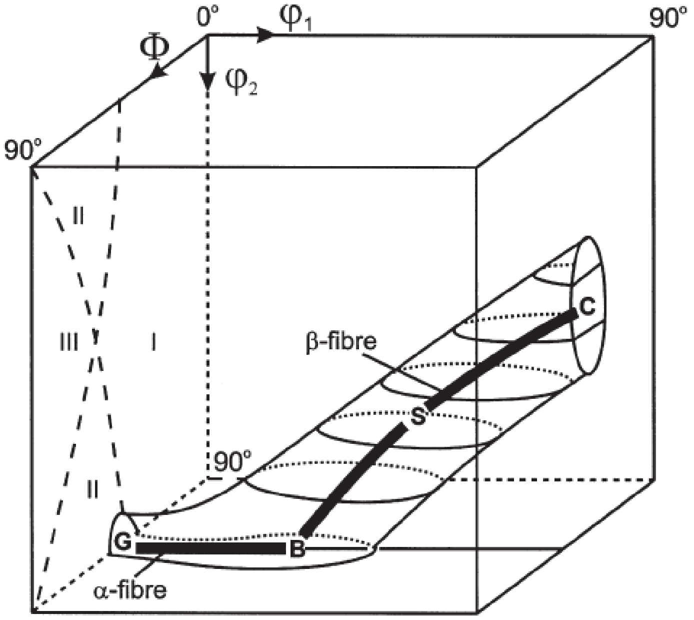

Figure 2.20 Schematic representation of the fcc rolling texture in the first subspace of three dimensional Euler angle space [76].

The deformation textures of materials deformed by uniaxial processes such as tension, wire drawing, extrusion etc., are fibre textures and the results are most commonly expressed as inverse pole figures. For fcc metals the texture is described simply as a double fibre texture with <111> and <100> parallel to the loading axis in the case of tensile deformation as shown in figure 2.21. While in compression a <110> texture is most frequently reported [74, 92-95].

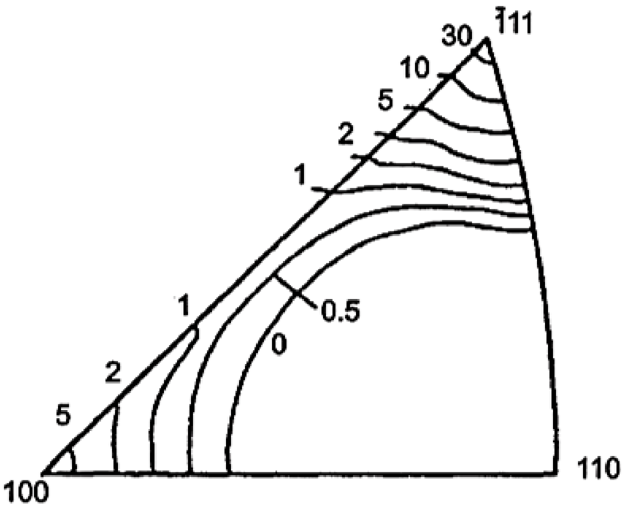

Figure 2.21 Inverse pole figure for cold drawn aluminum wire [93].

Textures resulting from recrystallization can have a remarkably sharp (100)[001] orientation- the so-called cube texture- or a combination of other types of orientations entirely different from the cube orientation, depending upon the deformation texture. In general, if the rolling texture is of the pure metal-type, cube texture is produced by recrystallization [96-108]. Usually there is a minor component of (122)[21-2] orientation [74], which arises from annealing twins of the cube grains. Figure 2.22 shows cube texture in a heavily rolled and recrystallized Cu sheet. A fully developed cube texture may approach the perfection of a pseudo-single crystal. Conditions favoring the development of a sharp cube texture are: (1) a small penultimate grain size, (2) a heavy total reduction, and (3) a high annealing temperature.

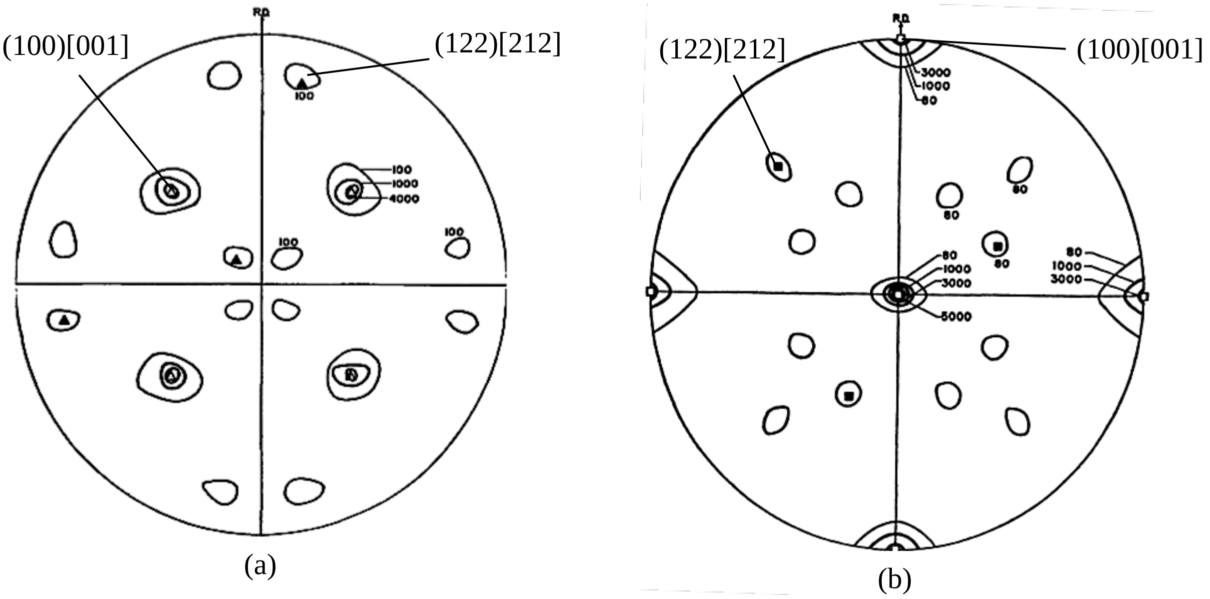

(a)

(b)

Figure 2.22 Recrystallization texture of electrolytic tough-pitch copper, rolled 96 % and annealed 5 min at 200° C, as shown by (a) (111), and (b) (200) pole figures. Intensity in arbitrary units [74].

If the stacking fault energy is sufficiently low, minor components that correspond to the twins of this orientation are also present. The strong cube texture of copper is eliminated by quite small amounts of many alloying elements, e.g. Al 5%, Be 1%, Cd 0.2%, Mg 1.5%, Ni 4.2%, P 0.03%, Sb 0.3%, Sn 1%, Zn 4% [27]. It will be recognized that for the most part these alloying elements reduce the stacking fault energy and change the nature of the deformation texture. The rotated cube around the rolling direction Rot C_{RD} {013}<100> was described as recrystallization twins. This has been observed in Cu during static and dynamic recrystallization. Formation is explained by chains of recrystallization twins up to 4th and higher generations [99]. The process may stop when recrystallization twins reach a specific preferred orientation and sometimes the twin texture component (rot C_{RD}) is much stronger than the cube components [99]. Figure 2.23 shows the most common components in fcc metal presented in triclinic sample symmetry for $\varphi_2 = 0^{\circ}$ and $\varphi_2 = 45^{\circ}$.

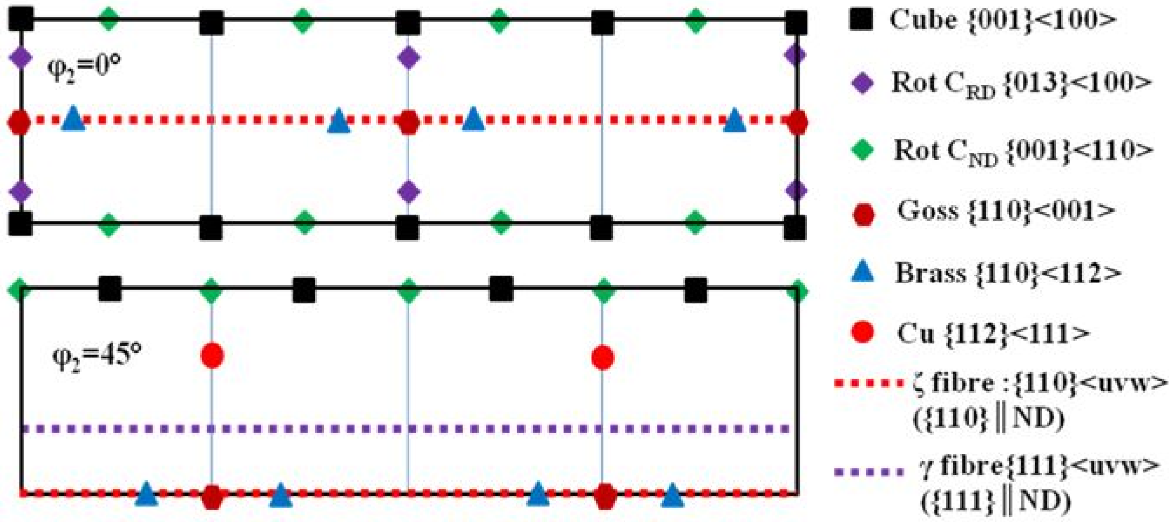

Figure 2.23 Texture components and components positions using triclinic as sample symmetry for sections (φ_2=0° and φ_2=45°) for the copper tube

2.9 Fundamentals of texture inhomogeneity through the thickness

Texture inhomogeneity is an essential feature in deformed polycrystalline materials. The texture inhomogeneity (type and degree) is affected by the technological parameters such as the coefficient of friction, geometry of the deformation gap, and the rate and temperature of deformation.

These texture inhomogeneities can be measured after several deformation processes, such as in wires (surface to center parts), rolled sheet (surface to mid plane) and tubes (outer, mid-plane to inner wall). Wires exhibit ideal fiber textures at the core part (<111>or <100> in fcc and <110> in bcc) but the texture inhomogeneity increases at the surface. It is known that friction affects the surface of a rolled sheet, and the *l/h* ratio characterizing the roll geometry (*l*: the projection length of contact between roll and material, *h*: the mean thickness of sample) lead to inhomogeneity of the intermediate layers. An analysis of the texture in particular layers of a sheet (surface, intermediate layer, center) can permit the observation of the formation of preferred orientation at a well-defined state of stress and strain [109]

Previous experimental works [109-117] show clearly that texture in cold deformed and annealed metals and alloys after plastic working is inhomogeneous. The essential feature of the textural inhomogeneity is the different mechanical and physical properties between the different layers of the deformed metal (through-thickness change). Less important changes of texture along the width and length of a rolled sheet and along the length of uniaxial deformed materials may also be observed.

Schläfer and Bunge [110] have calculated the ODF variation from neutron diffraction pole figures of a cold drawn wire at different distances from the central axis. The texture changes from axially symmetric at very center of the wire to a near rolling type texture close to the surface. Bertheloot *et al.* [111] showed that drawn and extrusion tubes have significant texture variation at the inner and outer walls. They have reported that the textures in drawn tubes were affected by drawing geometry. Truszkowski *et al.* [112] analyzed the texture in different layers of a sheet metal (surface, intermediate layer and center) to observe the effect of technological perimeters on the type and degree of through thickness texture inhomogeneity in rolled sheet in fcc metals. They carried out the experiments on aluminum, silver and 70/30 brass. They clearly showed that the sensitivity of metals and alloys to form an inhomogeneous texture is caused by their flow characteristics: yield strength and the work hardening exponent. High values of yield strength and the work hardening exponent will tend to hinder shear deformation and consequently hinder the occurrence of inhomogeneity. Wiedzbanowski and Jasieński [113] compared experimental results with modeling of the texture inhomogeneity between the surface and the center layer of(aluminum and 70/30 brass plates. Engler *et. al*.[85] investigated the inhomogeneity in 95% cold rolled and in recrystallized highly purity copper sheet by means of x-ray diffraction. Duggan *et al.* [114] presented a simple model of rolling deformation to predict both plane strain and inhomogeneous rolling conditions that lead to variation in texture components between the surface and the subsurface for copper rolled at 77 K. Hong *et al.* [115] studied the deformation texture of the surface layer and the center layer and the recrystallization texture of the surface layer for the 93% cold rolled copper sheet. Cho *et al.* [109] investigated with X-ray Diffraction (XRD) and Electron Backscatter Diffraction Analysis (EBSD) the texture variation through the thickness during tube drawing and they used FE analysis to study texture evolution during the tube drawing process. Sarkar *et al.* [116] studied the friction effect on through-thickness texture evolution during rolling for AA5182 and 5754 Aluminum alloys. Choi *et al.* [117] predicted an inhomogeneous texture development through the thickness direction in hot-rolled Al-5wt%Mg alloy sheets using the finite element analysis with a visco-plastic self-consistent polycrystal model.

2.10 Introduction about residual stresses measurements by neutron diffraction

Materials and components of technological and industrial interest can present residual stresses (RS), which are those remaining in a material in the absence of any external force. Residual stresses can arise at any moment during the life of a component, due to production and manufacturing processes, thermal or mechanical treatments and operational use. Knowledge of the spatial and directional distribution of residual stresses is very important in order to evaluate their influence on the material. When they add to the external loads they can accelerate the fatigue process, hence inducing an earlier failure of the component and reducing the life of the component [118].

The macrostresses just described are of type I because they vary continuously over large distances (see figure 2.24). This is in contrast to residual stresses which vary over the grain scale (type II or intergranular stresses) or the atomic scale (type III). In these cases, the misfitting regions span microscopic or submicroscopic dimensions. Low level type II stresses nearly always exist in polycrystalline materials simply from the fact that the elastic and thermal properties of differently oriented neighboring grains are different. More significant grain scale stresses occur when the microstructure contains several phases or phase transformations take place. The type III category typically includes stresses due to coherency at interfaces and dislocation stress fields [118].

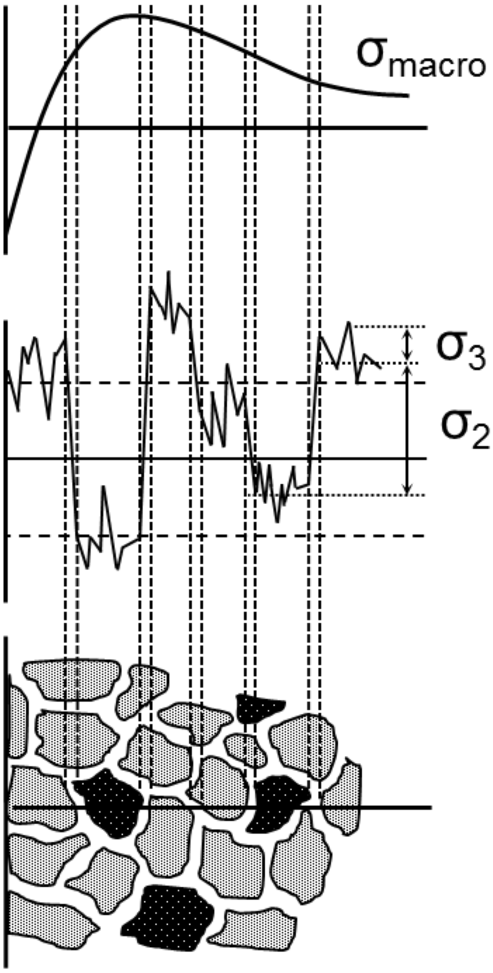

Figure 2.24 Residual stress fields can be categorized according to characteristic length scales $l_{0,I}$, $l_{0,II}$, and $l_{0,III}$ over which they self-equilibrate: for type I, $l_{0,I}$ represents a considerable size fraction of component; for type II, $l_{0,II}$ is comparable to grain dimensions, while for type III, $l_{0,III}$ is less than grain diameter [118].

Various methods have been used to evaluate residual stresses (RS), some of which are destructive and some nondestructive. Mechanical techniques based on the use of a strain gauge are destructive because the component needs to be drilled or cut. Among the non-destructive techniques, some are based on acoustic or magnetic effects, whereas Bragg diffraction is the basis of stress determination when using x-ray or neutron beams [119].

The major difference between the last two techniques is that x-rays from traditional sources can only be used in the surface region (a depth of a few micrometers), due to strong absorption in the materials, whereas neutrons can penetrate several millimeters or centimeters and hence their use constitutes the most direct technique for measuring strains inside massive materials or components [119].

The principle of strain measurement by neutron diffraction is shown in figure 2.25. In a typical neutron diffraction experiment [120-122] (see figure 2.26) a collimated neutron beam, of wavelength λ, is diffracted by the polycrystalline sample (with a take-off angle of 2θ), passes through a second collimator and reaches the detector. The slits of the two collimators define the ‘gauge’ volume, the cross section of which can be as small as 1 x 1 mm^2 and, in special cases, even smaller.

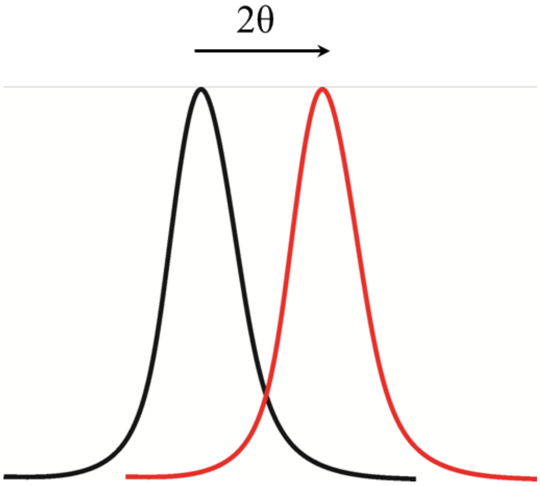

Figure 2.25 The principle of strain measurement by diffraction technique

The interplanar distance d_{hkl} (where *hkl* are the Miller indices of the investigated lattice planes) can be evaluated by using the Bragg law (see equation 2-12). The corresponding lattice strain is defined as [121]

$$\varepsilon^{hkl} = \frac{(d_{hkl} - d^0_{hkl})}{d^0_{hkl}} = \frac{\sin\theta^0_{hkl}}{\sin\theta_{hkl}} - 1 \qquad (2\text{-}13)$$

Where d^0_{hkl} is the hkl-interplanar distance in a stress-free material.

In practice the technique consists of precisely measuring the angular position of the Bragg peak for the stress-free and stressed material. From the observed shift one can obtain the value of the lattice strain [120].

Knowledge of the interplanar distance d_0 in the stress-free sample is necessary in order to determine the strain at any given point of a sample, as shown in equation 2-13. Determining d_0 with the highest possible accuracy is very important because each error in d_0 implies systematic errors in the strain value.

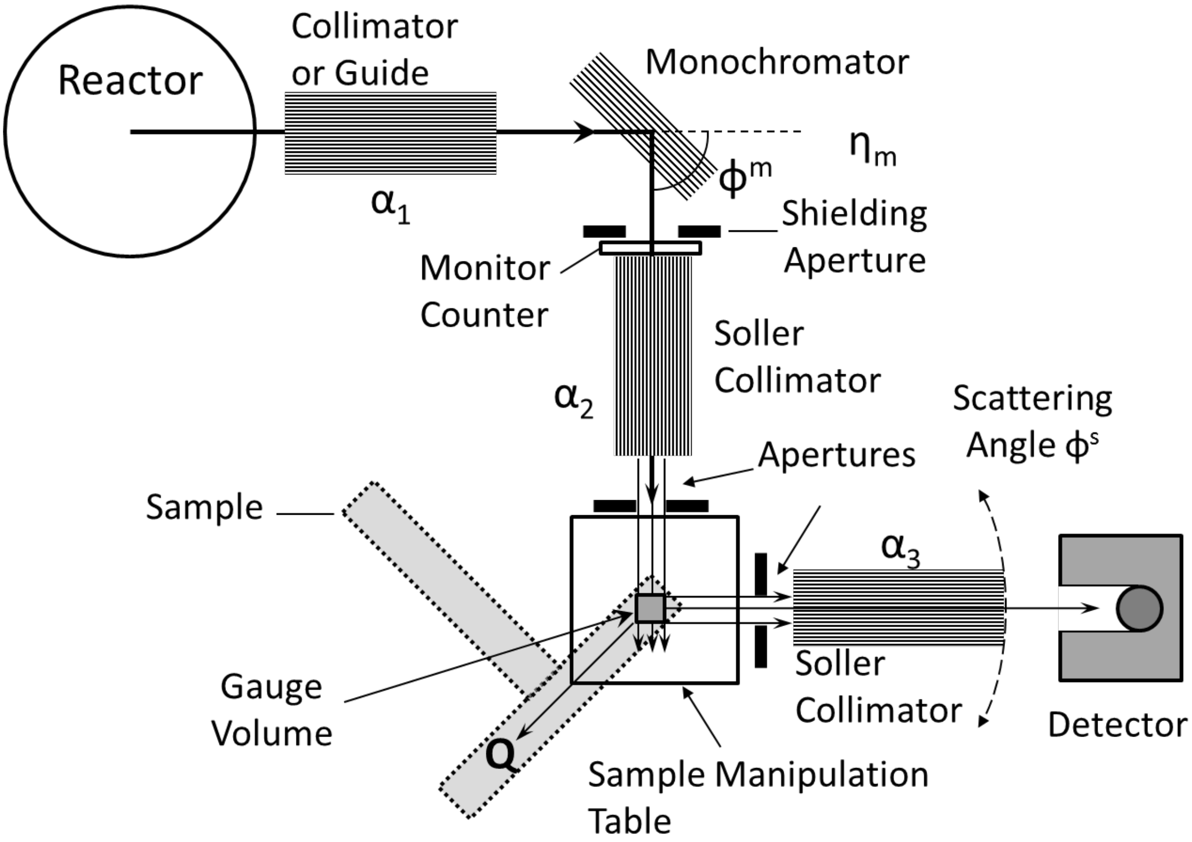

Figure 2.26 Schematic layout of standard two axis instrument for strain measurement of reactor neutron source [120].

Methodological problems, however, do not allow a clean and safe determination of d_0, although various methods are commonly used. A very commonly used method consists of measuring the interplanar distance inside a sample obtained from the investigated material that has been subjected to an appropriate thermal treatment in order to relieve the residual stress. A standard annealing is performed by heating the sample for several hours at half the melting temperature. However, one cannot be sure that all the internal stresses are relaxed [120, 123].

d_0 evaluation is also performed by measuring the interplanar distance in a region of the sample that is assumed stress-free, because it is considered not to have been affected by the process inducing the residual stresses. Also powders from the investigated materials are used to measure the reference distance d_0, assuming the powder granulates to be small enough that stresses are relaxed. Often annealing treatments are also performed on the powders. Another method for d_o measurement that does not suffer from metallurgical problems connected to a reference sample, but require a high number and high accuracy of the measurements, is based on the integrals of the stresses and of their moments, which are zero in any system in equilibrium. Numerical codes making use of iterative procedures are used in these cases. These methods, however, may suffer from practical limitations, such as the impossibility of having access to any desired direction, due to the geometry of the sample, or to restrictions on the available measuring time. Owing to the importance of the problem, many efforts at introducing new methods are under way in numerous laboratories [120-123].

Using diffraction it is only possible to determine the lattice strain for a given (*hkl*) plane spacing in the direction of the bisector of the incident and diffracted beams. In order to calculate the stress (or strain) tensor at a sampling gauge location at least six independent measurements of strain in different directions $\varepsilon\{\varphi, \psi\}$ are required [120].

$$\varepsilon_{\varphi\psi} = \alpha_1^2\varepsilon_{xx} + \alpha_2^2\varepsilon_{yy} + \alpha_3^2\varepsilon_{zz} + 2\alpha_1\alpha_2\varepsilon_{xy} + \alpha_2\alpha_3\varepsilon_{yz} + \alpha_3\alpha_1\varepsilon_{zx} \qquad (2\text{-}14)$$

where the direction cosines α_1, α_2 and α_3 are defined by

$$\alpha_1 = \sin\psi\cos\varphi$$

$$\alpha_2 = \sin\psi\sin\varphi$$

$$\alpha_3 = \cos\psi \qquad (2\text{-}15)$$

The six unknowns ε_{xx}, ε_{yy} , ε_{zz}, ε_{xy} , ε_{yz} and ε_{zx} (equation (2-14)) are all the elements of the ε tensor (it is symmetrical, so $\varepsilon ij = \varepsilon ji$). In principle the strains along six independent directions are required in order to solve equation (2-14); but a larger number of directions is considered in practice in order to have reliable results. By diagonalizing the strain tensor ε the principal strain axes *OX´ Y´ Z´* and the principal strains ε^D along them may be found.

In an elastically isotropic model (with Young's modulus *E* and Poisson's ratio *ν*) the principal stresses $\sigma_{\mathrm{xx}}^{\mathrm{D}}$, $\sigma_{\mathrm{yy}}^{\mathrm{D}}$, $\sigma_{\mathrm{zz}}^{\mathrm{D}}$ are related to the strains by

$$\sigma_{xx} = \frac{E_{hkl}}{(1+\nu_{hkl})(1-2\nu_{hkl})}\left[(1-\nu_{hkl})\varepsilon_{xx} + \nu_{hkl}\left(\varepsilon_{yy} + \varepsilon_{zz}\right)\right]$$

$$\sigma_{yy} = \frac{E_{hkl}}{(1+\nu_{hkl})(1-2\nu_{hkl})}\left[(1-\nu_{hkl})\varepsilon_{yy} + \nu_{hkl}(\varepsilon_{xx} + \varepsilon_{zz})\right]$$

$$\sigma_{zz} = \frac{E_{hkl}}{(1+\nu_{hkl})(1-2\nu_{hkl})}\left[(1-\nu_{hkl})\varepsilon_{zz} + \nu_{hkl}\left(\varepsilon_{yy} + \varepsilon_{xx}\right)\right] \qquad (2\text{-}16)$$

Owing to the anisotropy of elastic properties in crystalline materials, the values of E and ν at a microscopic level depend on the lattice planes (*hkl*) considered. Thus the neutron elastic constants must be known or can be determined experimentally [120].

The diffraction elastic constants (DECs) are defined as [123-124].

$$\left(\frac{1}{2}\,S_2\right)_{hkl} = \frac{1+\nu_{hkl}}{E_{hkl}}$$

$$(S_1)_{hkl} = -\frac{\nu_{hkl}}{E_{hkl}} \tag{2-17}$$

Where ν_{hkl} and E_{hkl} are Poisson's ratio and Young's modulus, respectively, referred to the considered diffraction plane *hkl*.

2.11 Peak shift due to surface effect

It was apparent from the earliest attempts to measure strain near the surface of a sample, or at an interface between two materials, that anomalous shifts in Bragg peak angles may occur that could not be attributed to stresses and strains. These shifts arise from the fact that when the sample partly fills the gauge volume, the position of the effective centroid of the sample gauge volume (SGV) is not at the center of the instrument gauge volume (IGV). To distinguish strain and position errors, we say that surface effect arises due to spurious near-surface strain and spurious near-surface location, referred to more concisely as spurious strains and spurious location. When the IGV is not fully immersed inside the material, the centroid of the partial immersed (SGV) should be calculated as shown in figure (2.27) [120].

To calculate the correct location of the centroid of the SGV the following correlation should be used [120]:

1. If less than the half of the nominal gauge volume is inside the sample $-D \le d_{sr} \le 0$ or equivalent $0 \le Z \le D$ then equation 2-18 should be used Where D is half of the diagonal of the nominal gauge volume and d_{sr} is the distance between the instrument reference point and the sample surface.

$$|d_{cs}| = \frac{\left[(2+aZ)\cdot e^{-aZ} - (2-aZ)\right]}{a\left[e^{-aZ} + aZ - 1\right]} \tag{2-18}$$

Where $Z = D + d_{sr}$ and $a = 2\mu / \sin\theta$ and μ is the linear absorption coefficient.

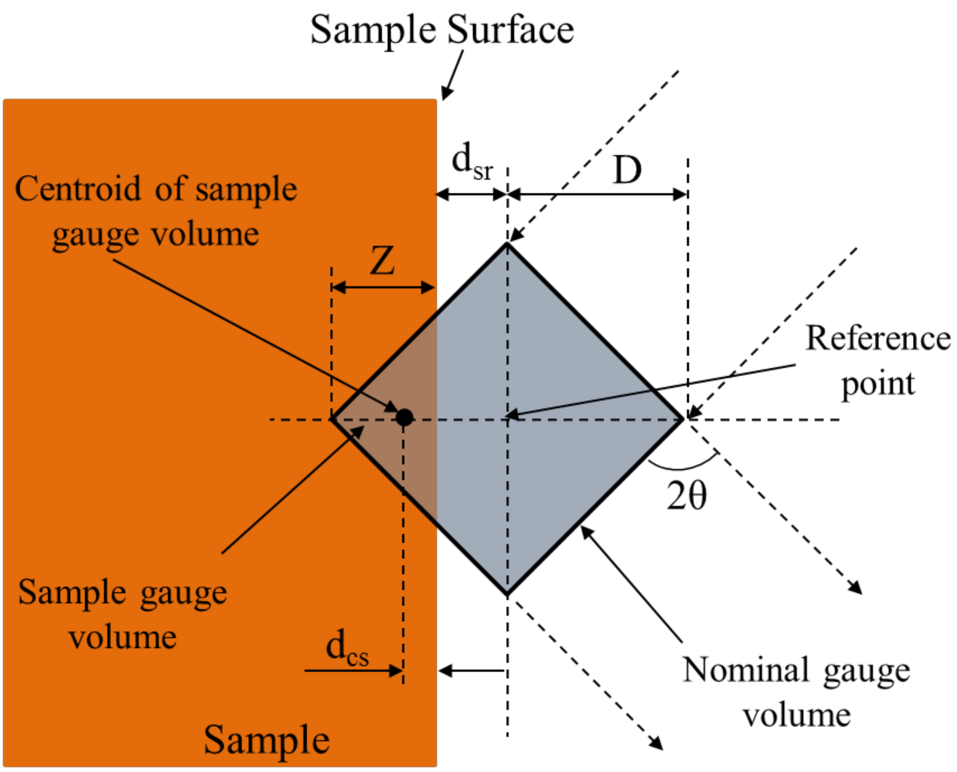

Figure 2.27 Schematic illustration showing the sample gauge volume and its centroid [122]

2. If more than the half of the nominal gauge volume is inside the sample $0 \leq d_{sr} \leq -D$ or equivalent $D \leq Z \leq 2D$ then

$$|d_{cs}| = \frac{[(2+aZ)\cdot e^{-aZ} - (2-aZ+2aD) + (2aD-2aZ-4)\cdot e^{-ad_{sr}}]}{a[(e^{-aZ} - aZ+1) + 2(aD - e^{-ad_{sr}})]} \tag{2-19}$$

The magnitude of the anomalous shift in measured angle, and thus the related spurious strain, is dependent on the configuration and type of the instrument used. The effect is most easily understood in the case of a simple monochromated, continuous-beam, two-axis diffractometer with a single detector. If one imagines the case of perfect resolution (i.e., no angular or wavelength spread in the incident or diffracted path), then there would be no anomalous shift since the detector would respond only at the correct Bragg scattering angle.

Two effects can give rise to spurious strain from surface effects, the first arising because of a wavelength spread across the incident beam on the IGV, and the second because the instrument has imperfect angular resolution. The former means that the part of the IGV that is filled by the SGV determines the relevant wavelength profile, causing a shift in the mean wavelength distribution and is only properly averaged when the IGV is completely filled. The second effect, termed here the positional discrimination effect (PDE), means that the signal recorded by the detector is dependent on where within the IGV the diffracting grains are positioned, that is, on the position of the SGV in the IGV. If the scattering event occurs within the IGV at a position farthest from the monochromator, it will be measured as occurring at a lower angle by the detector than if it occurs within the IGV nearest the monochromator. Consequently, in the former case one obtains a negative anomalous shift in the angle corresponding to a spurious tensile strain [120].

3 Material description and experimental procedure

3.1 Material description

The test sample was an industrial seamless DHP-copper tube of 140 mm outer diameter, 10 mm wall thickness and 1 m length. By using the digital vernier caliper the thicknesses of DHP-copper tube have been measured every 15° around the perimeter. The wall thicknesses of the DHP-copper tube varied from 10.36 mm (maximum thickness) at 0° to 9.57 mm (minimum thickness) at 180° as shown in figure 3.1. The diameter of the DHP-copper tube varied from 140.2 mm (maximum diameter) to 139.2 mm (minimum diameter). The eccentricity and ovality of the copper tube are (7.92% and 0.57%) respectively. For industrial copper tube the value for the eccentricity is up to about 10 % and the ovality is up to 3% [23, 125].

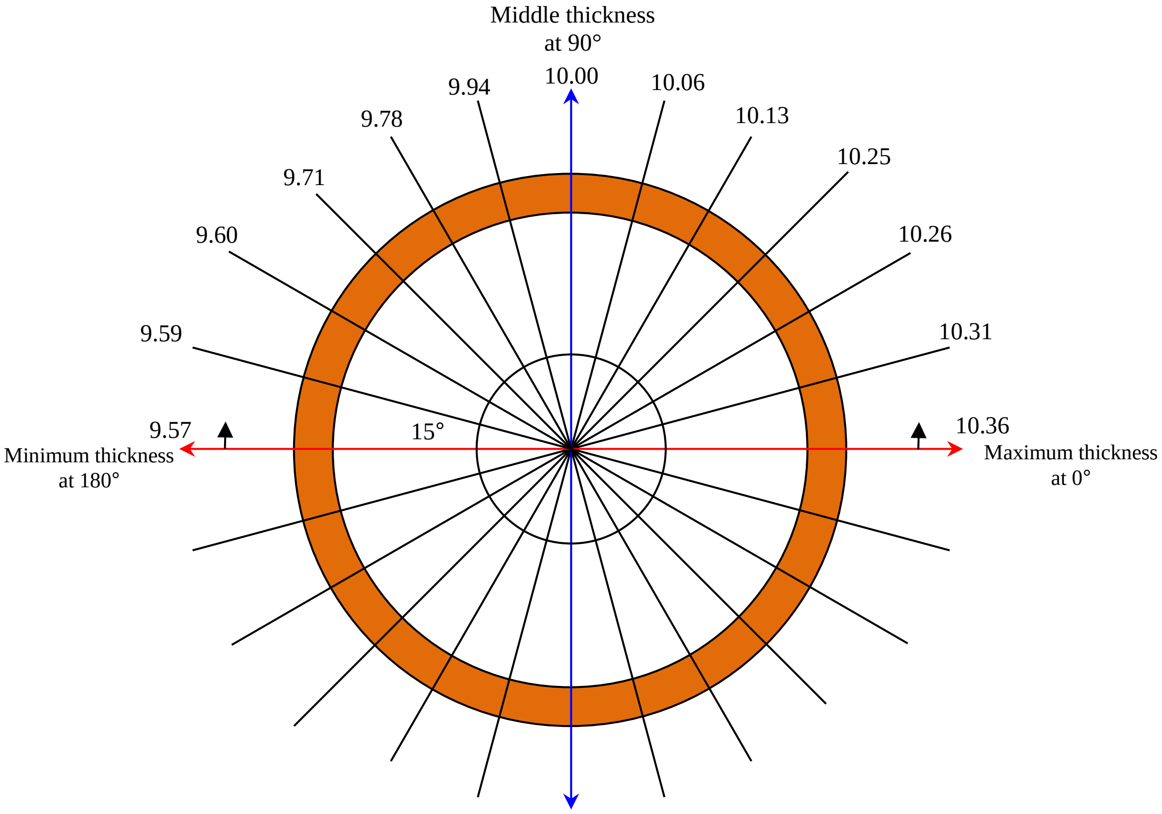

Figure 3.1 Thickness values around the perimeter from 0° (maximum thickness) to 180° (minimum thickness) for the copper ring (all dimensions in mm)

The chemical composition has been measured in the material science and engineering department at TU-Clausthal using electric discharge spectroscopy (Spectro Analytical Instrument, GmbH). The chemical composition of the material is Cu: 99.972%, Al: 0.005%, Ni: 0.0016%, Pb: 0.0041% and P: 0.0168%.

3.2 Microstructure measurement and grain size determination

Two sets of samples were cut from the copper ring in different planes (axial-radial and hoop-radial planes). For every plane three samples were cut from the copper ring at different positions minimum, middle and maximum thickness. The samples then mounted in epoxy resin for grinding and polishing.

The grinding process was done using six different silicon papers of different grade (320, 500, 800, 1200, 2500 and 4000). During grinding the grinding machine had a rotational speed 150 rpm and a force of 10 N on the sample was used. The grinding time was 2 min for every silicon paper grade and water was used for cooling.

The polishing process was made by using two different grades of diamond/based paste (Diamond pastes (3 µm and 1 µm) on a polishing pad of type (MOLTEC). The diamond pastes were applied on the polishing pad and an oil based lubricant was used for cooling. The final polishing stage with oxide polish suspension (< 0,05 µm) was used on polishing pad of type (CHEMTEC) with water cooling. The rotational speed of the polishing machine was 150 rpm and the force on the sample was 10 N. The polishing time was 3 min for every polishing step. The polished surfaces were etched using a solution of 50 ml water and 50 ml HNO_3 for 5 sec [126]. The microstructures were observed using a Leica DMI 5000M imaging device (optical microscope) starting from the outer to the inner diameter.

The grain sizes from optical microscopy were determined by the intercept method. Straight lines (all the same length) were drawn through each micrograph of the grain structure as shown in figure 3.2. The grains intersected by each line segment were counted, the line length was then divided by an average of the number of grains intersected, taken over the entire line segment. The average grain diameter (L_g) was found according to equation (3-1) [126]:

$$L_g = L_T/PM \tag{3-1}$$

Where: L_T: is the total length of the drawn lines, P: is the total number of grain boundary intersections and M. is the magnification.

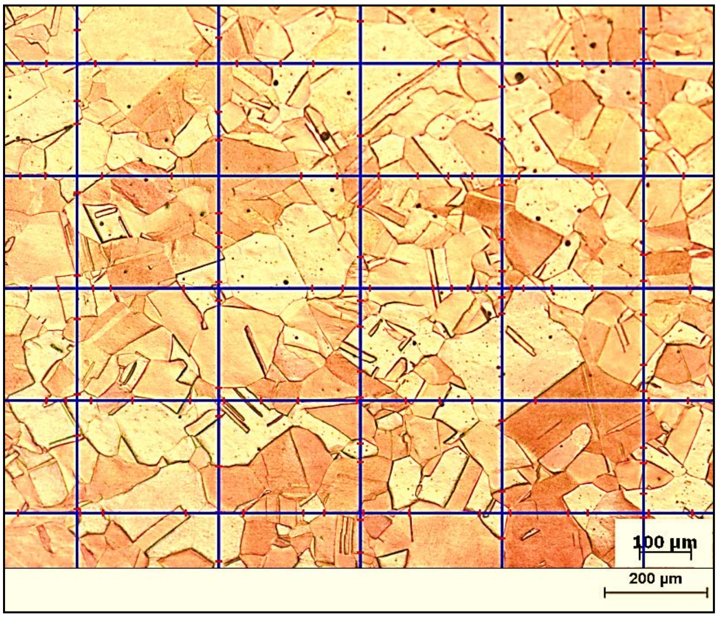

Figure 3.2 linear intercept method for grain size determination

3.3 Texture investigations by neutron diffraction at STRESS-SPEC

Neutrons diffraction has been used to measure the pole figures at different positions around the circumference of the DHP-Copper ring cut from the tube to observe the texture variation around the circumference. Because of the irregular shape of the DHP-Cu ring, the volume and the absorption correction for the pole figures measurements are essential.

Three cubic samples from different positions (minimum, middle and maximum thicknesses) have been measured to compare the result obtained from corrected pole figures after volume and absorption correction

Also three pole figures at one position in a large tube segment (250 mm length) have been measured to illustrate the capability of the RX160 robot.

All pole figure measurements by neutron diffraction were carried out on STRESS-SPEC [3, 4] at the Research Neutron Source Heinz Maier-Leibnitz (FRM II). STRESS-SPEC is located at a thermal beam port and contains three flexible monochromators: Ge, bent Si and Pyrolytic graphite. These three monochromators are installed in monchromators castle as shown in figure 3.3 and the movements of the monchromators can be controlled by STRESS-SPEC software. STRESS-SPEC is equipped with a ^{3}He area detector with dimensions of 300 X 300 mm^2. By varying the detector angle a total range of 2θ between 30° and 120° can be covered. That means, related to the wavelength range, d-values from 4.8 to 0.6 Å can be investigated by this area detector. Figure 3.3 shows the schematic view of the experimental area with robot system. Using two Huber circles it is also possible to rotate the robot and the detector around the scattering point [3, 4].

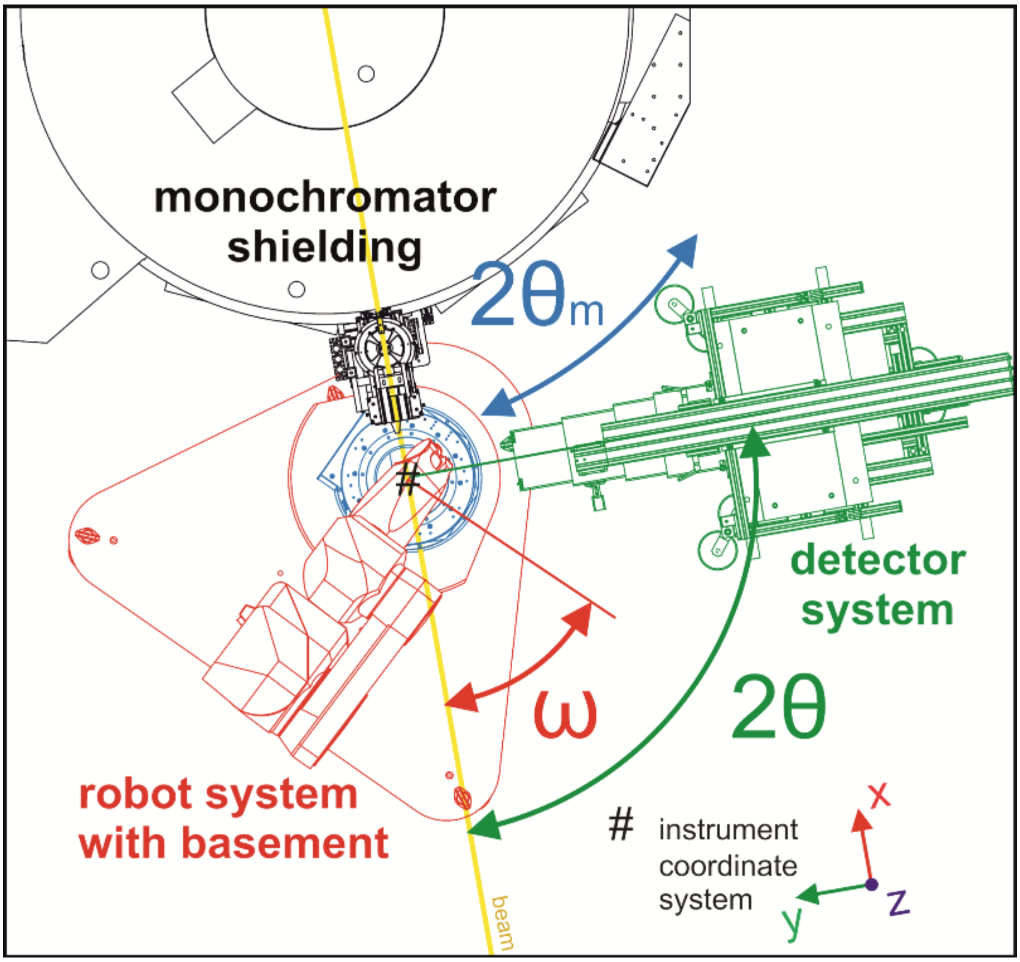

Figure 3.3 Schematic view of the experimental area at STRESS-SPEC [127].

The standard equipment for pole figure measurement at STRESS-SPEC is an Eulerian cradle type Huber 512 with an asymmetric φ-table arrangement to gain more space for the sample environment. Due to the need of sample tilt and rotation, texture mapping is strongly limited in movement as well as limited in sample weight as shown in figure 3.4a. Some investigations have been done to adjust samples with complex geometries, such as large tubes, shafts, turbine blades, etc. [4, 5] with manual sample positioning and automatic pole figure scanning. To overcome these limitations an industrial Stäubli RX160 robot combined with a laser tracker positioning system has been developed [4, 5]. Figure 3.4b shows the robot arm and the free space for movement. The working range for strain scanning and texture mapping is within a circle of 500 mm radius (safety radius) and the present limitation is given by a nominal load of 20kg. The big brother Stäubli RX170 with a nominal load of 30kg can only be used for low Bragg angles due to limited space availability at STRESS-SPEC. This robot arm has 6 degrees of freedom for sample movement, can reach points inside a spherical volume with a maximum radius of 1710 mm and has a repeatability of ± 0.05 mm [4, 5].

The instrument software at STRESS-SPEC supports two methods of pole figure scanning. Firstly, a step scan mode, which allows running sample rotation φ in constant steps $\Delta\varphi$ from 0° to 360°, as shown in figure 3.5a with a constant grid of 5°X5°. At any tilt angle the χ step width in $\Delta\varphi$ can be adapted to the texture sharpness. The area detector allows any step width in $\Delta\chi$ for data evaluation. Equal angular scans as well as equal area scans are possible. Secondly, continuous scanning along φ can be implemented. A schematic illustration of the continuous scanning method is shown in figure 3.5b.

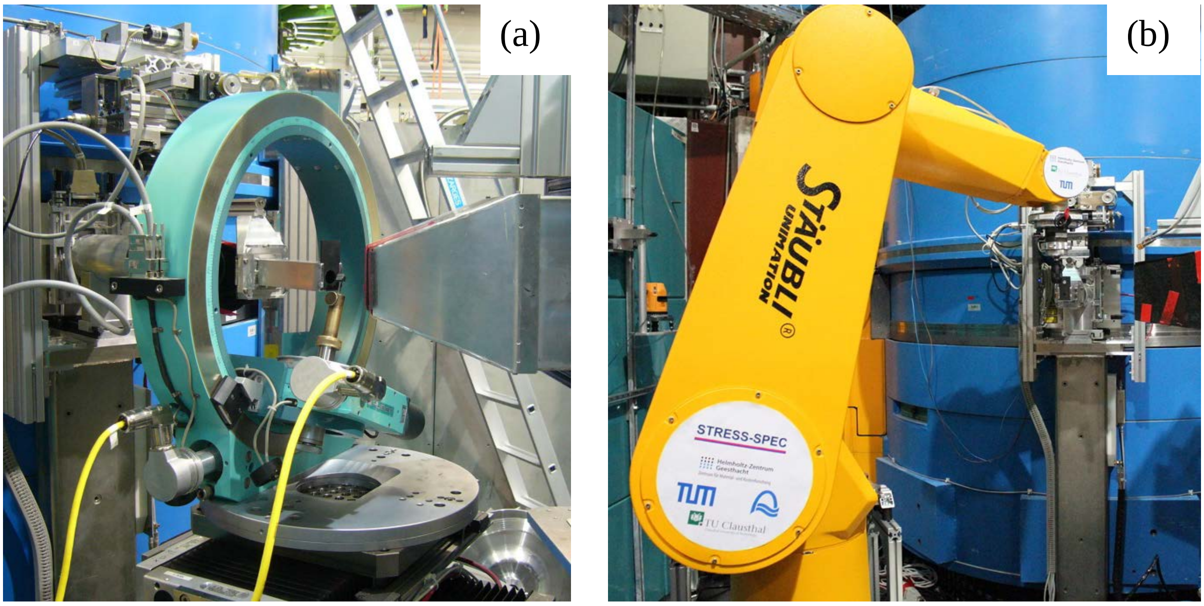

Figure3.4 (a) a conventional Eulerian cradle and (b) a Stäubli RX160 robot at STRESS-SPEC.

Continuous scanning has the advantage of eliminating positioning time and for STRESS-SPEC the total counting time can be reduced by 30%. Furthermore, continuous rotation guarantees that all crystallites contribute which is not the case for most pole figure scanning routines in other diffractometers but has the disadvantage that data is averaged over grid size in φ [4].

The robot that was used for the pole figure measurement using neutron diffraction consists of:

1. Texture measurement of DHP-Cu ring.
2. Texture measurement of cubes cut from the DHP-Cu tube.
3. Texture measurement of tube segment.

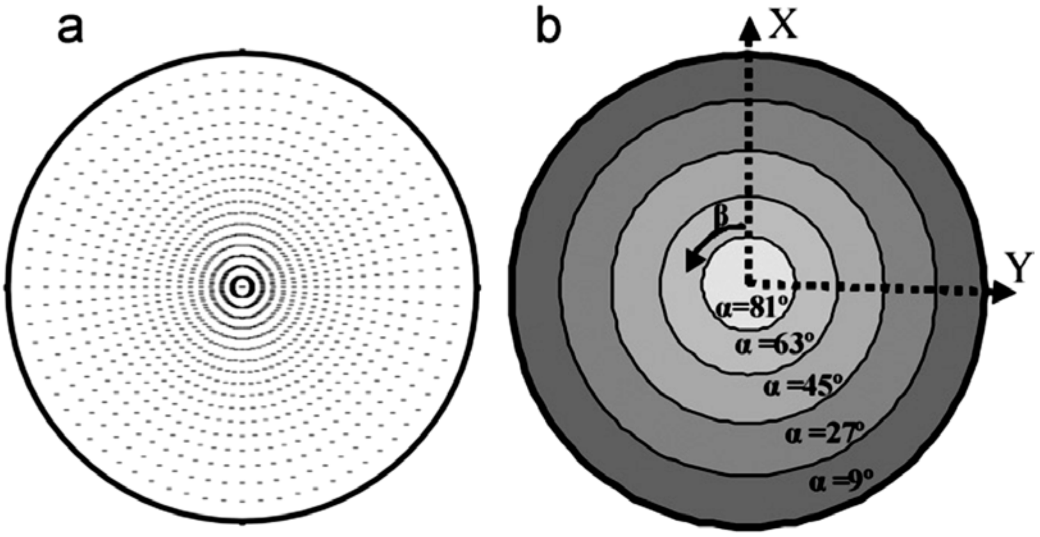

Figure 3.5 Schemes of pole figure scan with (a) discrete method using an equal angular 5°X5° and (b) with discrete steps in χ (0°–90°) and continuous scanning of φ (0°–360°) [4].

3.3.1 Texture investigation around the circumference of a ring cut from DHP-Cu tube

The DHP-Cu ring was cut from the 1 m tube had a length of 11 mm. The values of the thickness around the perimeter from 0° to 180° are shown in figure 3.1.

The experimental procedures for the pole figure measurement of the DHP-Cu ring consists of four steps:

- -Three dimensional scanning of the sample including sample holder and defining the coordinates for all sample positions where pole figures measurements will be performed.
- -Sample adjustment on the robot arm and importing the (sample position) coordinates from the first measuring session.
- Pole figure measurement using a continuous scanning mode in φ-rotation by the robot.
- Automatic adjustment to the next sample position and repeated pole figure measurement.

3.3.1.1 Three dimensional sample scanning of DHP-Cu ring for pole figure measurements

For the robot experiment the sample with sample holder have been scanned in 3D. The device we used was a CimCore Infinite portable coordinate measuring arm equipped with an integrated laser head type V4i Percetron Scanner and the Geomagic Studio software. The ScanWorks sensor uses solid state, non-contact, laser-based technology. The scanner captures the profiles generated by the interaction of a projected laser and the target topography using triangulation. The accuracy was tested by a calibration scan using a matte grey standard sphere of 25.4 mm diameter. The whole calibration scan consists of measurements in 5 different directions. For texture analysis the obtained accuracy of 110 µm is sufficiently precise to get the centers of rotation for pole figure mapping [128].

The scanning process was started by moving the integrated laser head manually around the object sample plus sample holder. Numerous line scans were performed with the laser head perpendicular to the surface and continuously recording the reflections giving a cloud of points. The data collection rate was 23,040 points/sec. The Geomagic studio allows direct viewing of the cloud of points during scanning. Thereafter the 3D picture of the Cu-ring and the sample holder (see fig. 3.6) is created from the cloud of points. In the next step the coordinates for all sample positions where pole figure measurements will be done are defined (e.g. point A - see fig. 3.6). By using a small in house developed mathematical library, the numerical values for the sample positions (X, Y, Z, RX, RY and RZ with respect to robot plate) can be extracted from Geomagic Studio software and implemented into the robot software [128]. The sample is mounted in the sample holder which is then placed on the robot arm.

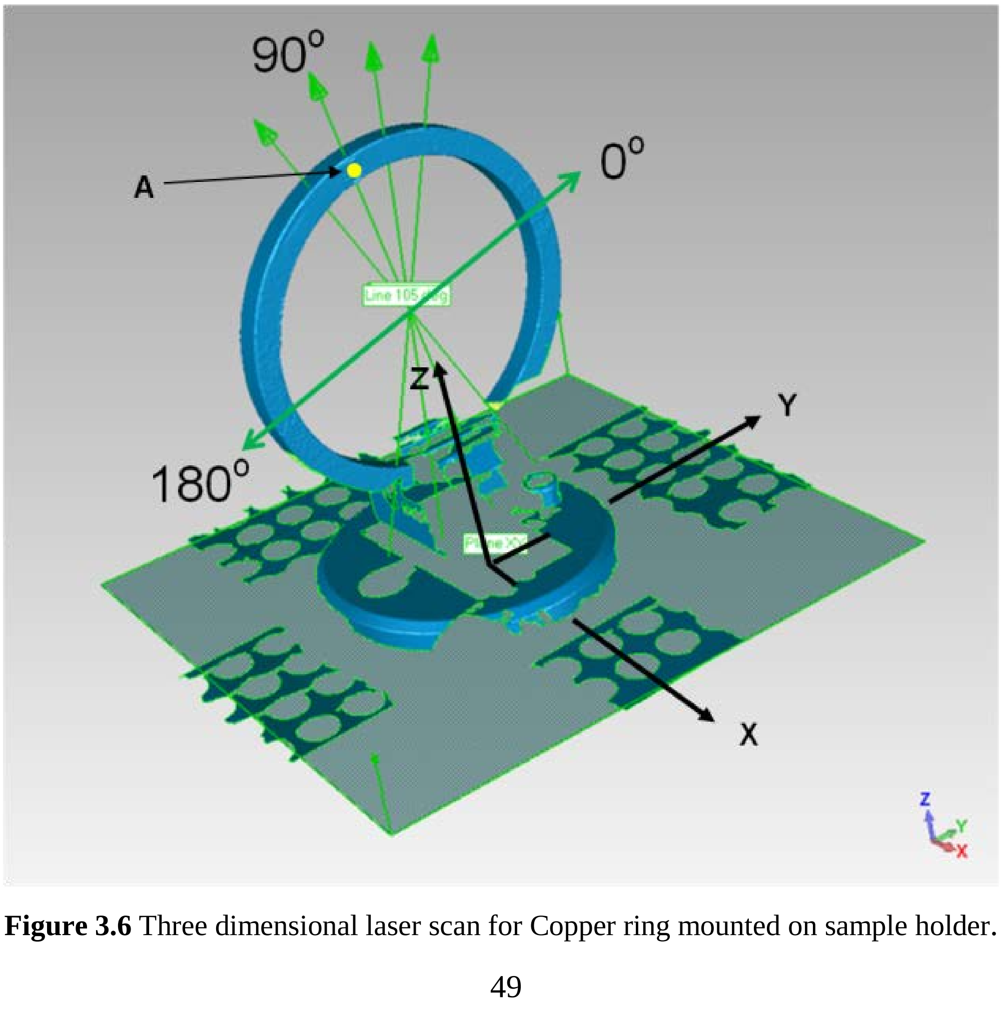

Figure 3.6 Three dimensional laser scan for Copper ring mounted on sample holder.

3.3.1.2 Pole figure measurement of DHP-Cu ring by the robot

The pole figure measurements were carried out using a neutron wavelength of 1.565 Å obtained using a Ge (311) monochromator. A Ge monochromator is favorable for texture measurements because the vertical focusing of Ge monochromator makes it is possible to get high resolution over a wider region of scattering angles.

As already pointed out the robot was used because of the space limitation of the existing Eulerian cradle (Huber 512). Tilt and rotation in the Eulerian cradle was not possible for rings larger than 13 cm in diameter. Depending on the 2θ angle and the sample detector distance of 850 mm the sample was tilted up to six times in χ. For each χ-position a continuous scanning along φ followed by automatic data collection every 5° was performed so that complete pole figures were obtained [128]. Figure 3.7a shows the tilting and rotation axes.

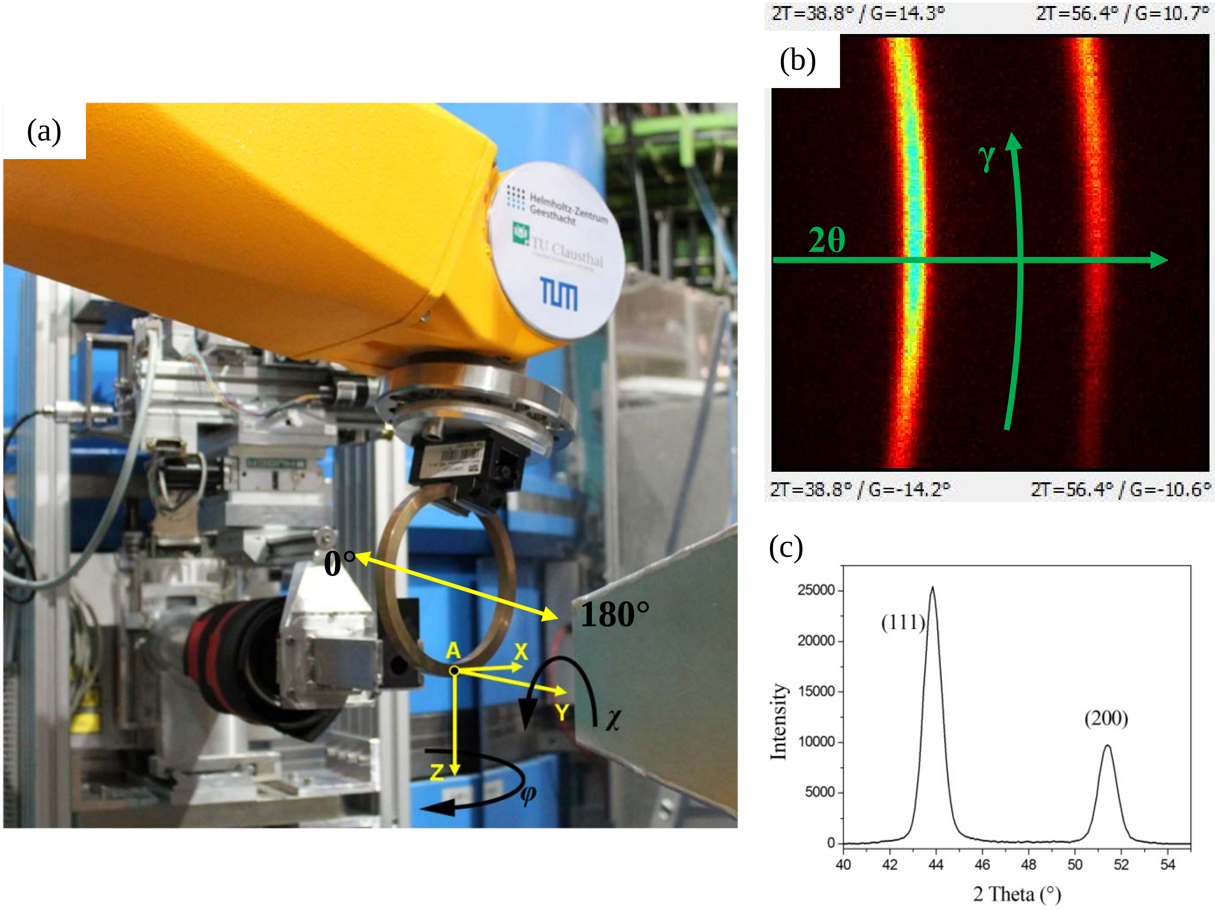

Figure 3.7 (a) Copper ring with the sample holder mounted on the robot arm [128] (b) 2D diffraction image (c) The sum of diffraction patterns of Cu (111), and (200) reflections.

The exposure time for each detector image (5° rotation in φ) was 10 sec. In order to get three pole figures for a quantitative texture description via calculation of the orientation distribution function (ODF), one needs two detector positions because of limited detector area and large diffraction angles as shown in figure 3.7b,c. Values of 2θ = 47° for Cu (111) and Cu (200) and 2θ = 75° for Cu (220) were used.

Due to the limited beam time the texture gradient around the circumference was measured at every 15°. Because of the limited range of the robot we had to measure the texture gradient from 0° to 180° in four sessions in two independent beam time periods. Each session consisted of up to four sample positions like 0°, 15°, 30° and 45° for the first session. The robot is able on one hand to make complete pole figure measurements and on the other hand perform automatic positioning for texture mapping. The texture at 105° was measured during both beam time periods and compared in order to adjust for changes caused by uncertainties in instrument alignment [128].

Beside the limited range of the robot, the biggest disadvantage of this method is the robot area which has to be free of any installations. Therefore the slit systems are far away from the gauge volume. The circular primary slit made of boron carbide was 15 mm in diameter to get the average information of the tube wall (global texture), a secondary slit was not used.

The software package StressTextureCalculator (STeCa) [129] has been used to extract pole figure data from area detector data using the mathematical formalism of Bunge and Klein [130].

3.3.1.3 Volume correction

As already mentioned, a volume correction is needed if the effective volume changes during sample tilting and rotation [68]. Because the irradiated gauge volumes during tilting and rotation have a complex shape, a 3D software package (Gambit 2.4.6: it is a software package designed to help analysts and designers build and mesh models for computational analyzes and scientific applications) was used to determine the gauge volume for any pole figure points following the same steps in χ tilting (six positions) and φ rotation (72 positions). Key inputs for the program to calculate $V_{hkl}(\alpha,\beta)$ are the cross section of the circular primary beam ($\o$=15 mm), the opening detector window dimensions (75 mm×75 mm) and the Cu-ring dimensions (diameter 140 mm and 10 mm wall thickness, assuming perfect symmetry) [128].

The irradiated gauge volume for each point in the pole figure was calculated by taking into account the beam size, detector window size and the tube dimensions.The gauge volume also depends on the detector angle so the volume correction pole figures for Cu (111) and (200) which are related to the detector angle 47° as well as for Cu (220) with 75°. The two volume correction pole figures are calculated in a 5x5 grid ($\Delta\alpha = 5°$ and $\Delta\beta = 5°$) [128].

3.3.1.4 Absorption correction

The interaction between radiation and matter results in an attenuation of the beam intensity along its path through the sample [131]. In case of transmission through a sample with thickness t, the incident intensity I_0 is attenuated according to:

$$I = I_0 \exp(-\mu t) \tag{3-2}$$

Here, μ is the linear absorption coefficient (given in cm^{-1}) which depends on the material investigated and the radiation used [132]. Using tabulated values [133] the linear absorption coefficient was calculated to be μ= 0.237 cm-1. The primary beam was considered as a line passing through the center of the primary slit. The path length $t_{hkl}(\alpha,\beta)$ was estimated from the neutron beam within the tube wall (primary beam and the scattered beam). Due to the high penetration of thermal neutrons, absorption is not very high. Because the path lengths are complex during sample tilting and rotation, a 3D software package (Gambit 2.4.6) was used to get the path length for any pole figure points following the same steps in χ tilting (six positions) and φ rotation (72 positions). As the path length depends on the scattering angle, one needs to perform absorption correction for the for Cu (111) and (200) pole figures with detector angle 47° as well as for Cu (220) with 75°. The two anisotropic absorption factors ($exp(-\mu t)$) pole figures are calculated in a 5x5 grid [128].

3.3.1.5 Texture investigations of cubes cut from the DHP-Cu tube

Quasi-cubic samples of dimensions (10 × 10 × 11) mm^3 were cut from the copper ring at 0°, 90° and 180° (maximum, middle and minimum thickness respectively).

A sample changer magazine with up to 12 slots for storing samples was integrated with the robot system, as shown in Figure 3.8. This sample changer system is based on standard tool changer from (PTM Präzisionstechnik GmbH) and a conventional three jaw chuck. The three samples were glued on vanadium pins and mounted in the jaw chucks before the measuring was started. The total sample change and positioning time was about 5 min which is relatively fast compared to a manually change.

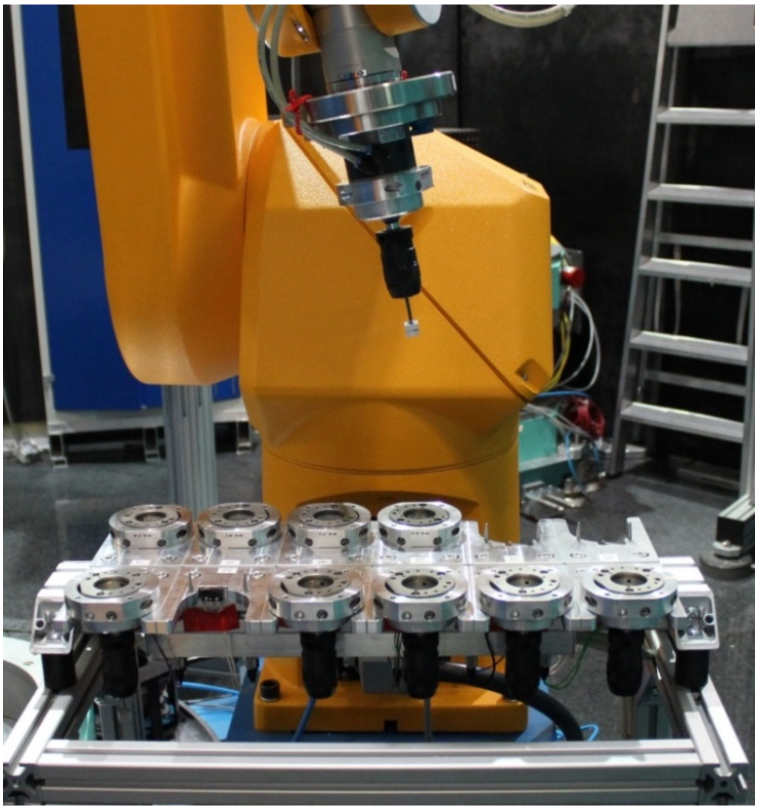

Figure 3.8 Robot arm and the sample changer magazine with 12 slots for storing samples

A neutron wavelength of 1.565 Å obtained using a Ge (311) monochromator was used. According to the area detector, the *2θ* angle and the sample detector distance the samples were tilted six times in *χ*. For each *χ*-position a continuous scanning along *φ* was performed. The primary slit was 20 mm diameter and no secondary slit was used, the exposure time was 10 sec. The sample detector distance was 850 mm.

Three pole figures (111), (200) and (220) were measured with two detector positions (*2θ* = 47° and *2θ* = 75°). The software package StressTextureCalculator (STeCa) [129] has been used to extract pole figure data from area detector data using the mathematical formalism of Bunge and Klein [130].

3.3.2 Texture investigations of tube segment

A copper tube segment of 250 mm in length was cut from the 1 m DHP-Cu tube. For the copper segment the same experimental procedure as the Cu-ring has been followed except that only one point in the center of the wall thickness at 90° position was measured.

3.3.2.1 Three dimensional laser scanner of tube segment for pole figure measurements

For the tube segment work, the sample and sample holder (see figure3.9a) were 3D scanned. As mentioned earlier, the device we used was a CimCore Infinite portable coordinate measuring arm equipped with an integrated laser head type V4i Percetron Scanner and the Geomagic Studio software.

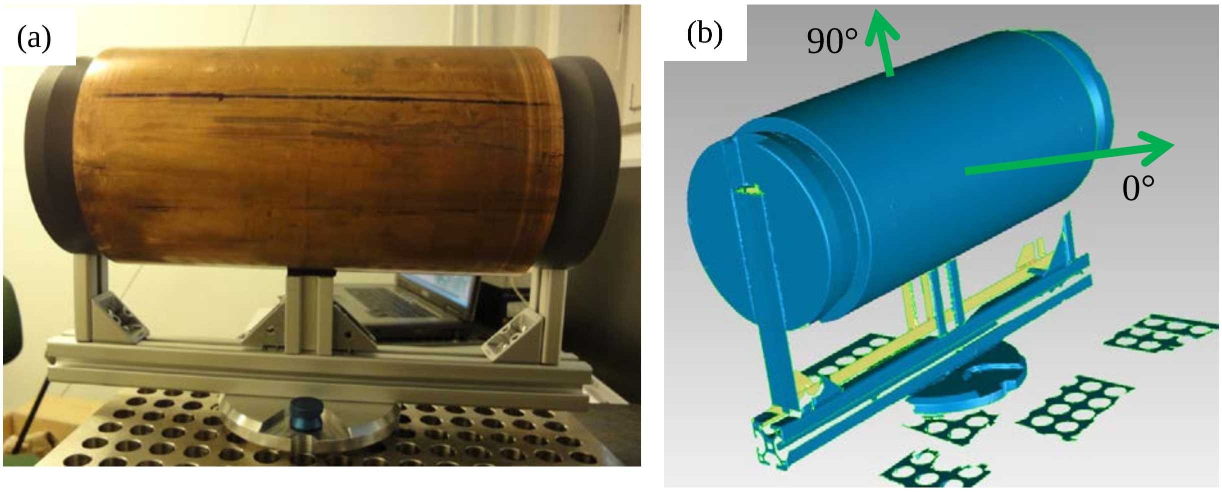

Figure 3.9 (a) Cu-tube segment mounted on the sample holder (b) Three dimensional laser scan for Copper tube segment mounted on sample holder for texture configuration [128]

The scanning process was started by moving the integrated laser head manually around the object sample plus sample holder. Numerous line scans were performed with the laser head perpendicular to the surface and continuously recording the reflection giving a cloud of points. The Geomagic studio allows direct viewing of the cloud of points during scanning. Thereafter the 3D picture of the Cu-tube segment and the sample holder (see fig. 3.9) are created from the cloud of points. In the next step the sample position coordinates where pole figure measurement will be performed are defined. By using a small in house developed mathematical library, the numerical values for the sample position (X, Y, Z, RX, RY and RZ with respect to robot plate) can be extracted from the Geomagic Studio software and implemented in the robot software [128].

3.3.2.2 Pole figure measurements of tube segment by the robot

The 250 mm copper tube segment with the sample holder was mounted on the robot arm as shown in figure 3.10a. The weight of the tube and the sample holder is 12 kg. The pole figures measurements were carried out using a neutron wavelength of ($\lambda_{PG(004)}$ =1.55 Å) and ($\lambda_{PG(006)}$ =1.03 Å) obtained using a pyrolytic graphite (PG) monochromator. The PG monochromator offers the highest neutron flux between the three monochromators in STRESS-SPEC but only for limited number of wavelengths, and moderate resolution which is only used for texture measurements [4].

Depending on the *2θ* angle and the sample detector distance of 1065 mm the sample was tilted five times in χ. For each χ-position a continuous scanning along φ followed by automatic data collection every 5° was performed.
The exposure time for each detector image (5° rotation in φ) was 2 minutes. In order to get three pole figures for quantitative texture description via calculation of the orientation distribution function (ODF), one detector position was enough to get three reflexes. A value of 2θ = 47° was used and due to the dual wavelength arrangement three pole figures can be obtained with one set-up, Cu (111) and Cu (200) with 1.55 Å, and Cu (220) with 1.03 Å as shown in fig 3.10 b,c. The circular primary slit made of boron carbide was 5 mm in diameter and a radial collimator (5x5 mm^2) was used as a secondary slit.

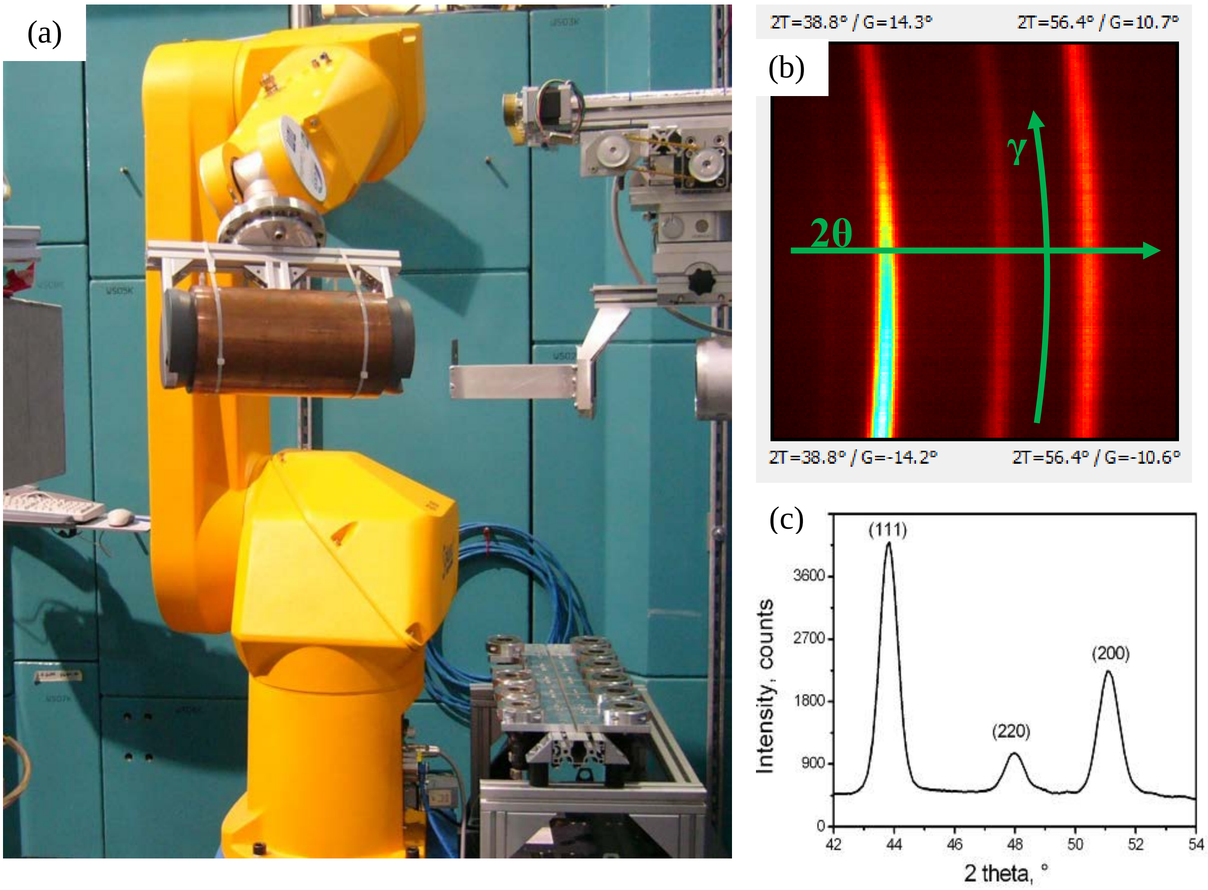

Figure 3.10 (a) Copper tube with the sample holder mounted on the robot arm (b) 2D diffraction image (c) The sum of diffraction patterns of Cu (111), (220) and (200) reflections.

For local texture measurements the slit systems normally for strain scanning can be utilized. The primary slit system in STRESS-SPEC before the sample allows variation of the incident beam size from ϕ = 1 mm to ϕ = 25 mm. For the out coming beam a radial collimator can be put in front of the detector for better gauge volume definition and background reduction. Three radial collimators are available at STRESS-SPEC having an FWHM of 1, 2 and 5 mm, respectively. Gauge volumes for local texture measurements are typically in the range of $1 \times 1 \times 1\ \text{mm}^3$ to $5 \times 5 \times 5\ \text{mm}^3$ [4].

The software package StressTextureCalculator (STeCa [129]) has been used to extract pole figure data from area detector data using the mathematical formalism of Bunge and Klein [130].

3.4 Texture investigation by synchrotron diffraction

The synchrotron pole figure measurements were made at the High Energy Materials Science Beamline (HEMS) P07 at storage ring PETRA III at DESY, Hamburg. The main energy of 100 keV is tunable in the range 35 to 200 keV. HEMS has high brilliance which results in high flux and high resolution [6]. P07 beamline consists of two hatches the main station and the side station. In this work all the measurement have been done in the side station P07B. Figure 3.11 shows the principle set up using the monochromatic beam in the P07B.

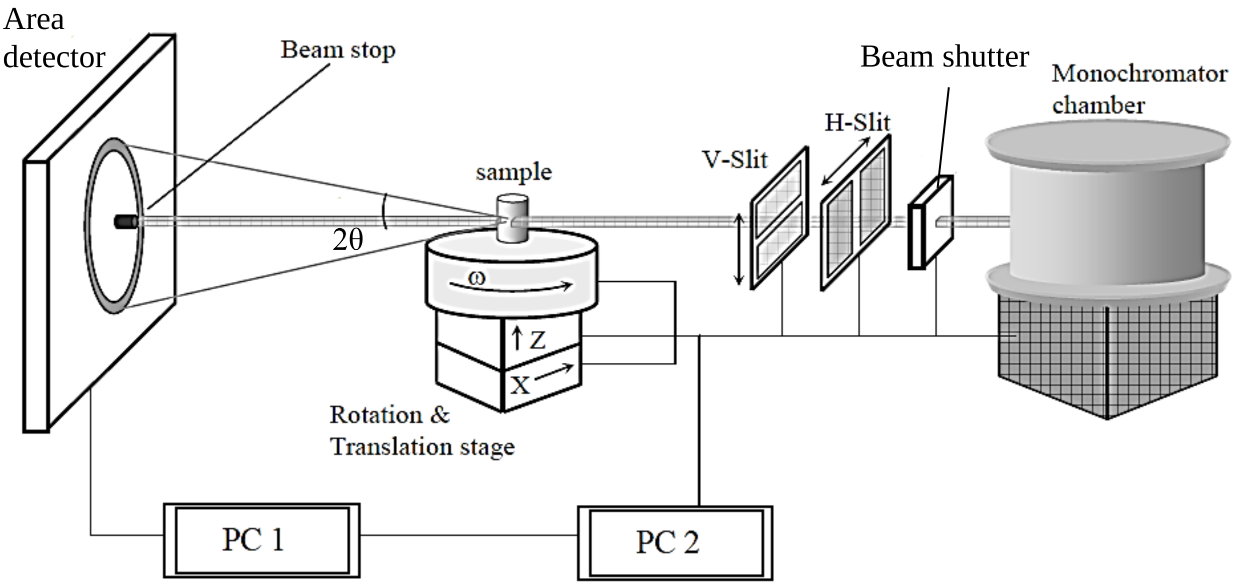

Figure 3.11 Beam line setup for texture measurement at P07 side station in HEMS@ DESY. PC 1 is responsible for reading data from the area detector, PC 2 is connected and controls all. X and Z are perpendicular to the direction of the incident beam [49].

The primary white beam from the wiggler enters the experimental station through a high vacuum pipe. The desired wavelength of the beam is selected by a Si(111) or Si(220) single crystal monochromator in the monochromator chamber under vacuum. According to the crystal structure of the monochromator two wavelengths can be obtained from each single crystal. Firstly, the wavelengths that can be obtained via the Si(220) relate to energies of about 87 keV and 174 keV and secondly, wavelengths obtained from Si(111) are related to energies of about 57 keV and 114 keV. The setup of the wavelengths can be controlled from the P07 main station.

The beam size is controlled by vertical and horizontal slit systems which can be up to 0.5×0.5 mm^2. The intensity of the incident beam can be reduced by a copper filter. The sample is positioned on the ω-rotation stages. The rotation stage was mounted on a XZ-stage, which allows for translation of the sample in sample-height (Z) and perpendicular to incident beam (X) directions. Therefore continuous measurements at different sample positions are possible. At a stationary sample position only lattice planes ($h\ k\ l$) that are inclined by an angle of 90° to the incident beam satisfy Bragg's condition, and the corresponding Debye-Scherrer rings are generated with an opening angle of 2θ.

Three quasi rectangular samples were cut from the DHP-Cu tube at positions of maximum (0°), middle (90°) and minimum (180°) thickness, the dimensions are shown in table 3.1.

Table 3.1 Samples Dimensions

Sample name	thickness(mm)	a(mm)	b(mm)	Measured Points
Min. thickness	9.57	5.16	4.72	5
Mid. thickness	10.00	5.85	4.85	5
Max. thickness	10.36	5.85	4.25	5

A sample was fixed on a steal pin and mounted on the sample stage (ω-rotation stage) so the arrow (rolling direction) points in the direction of the detector, as shown in figure 3.12. An x-ray beam of energy 174 keV (wavelength of 0.07105 Å) with a size of 0.5×0.5 mm^2 was used for local texture measurements. The distance between the sample and the two dimensional Mar345 detector was 1168 mm. Generally, one of two detectors can be installed in P07B depending on the user requirements. Firstly, Mar345 with resolution 0.1 mm or 0.15 mm and maximum diameter of 345 mm and secondly a Perkin Elmer (PE) detector with resolution of 0.2 mm and diameter of 416 mm, the read out of the PE detector is much higher than the mar345.

The azimuthal rotation (phi motor) was driven from -90° to 90° in steps of 5° with an exposure time of 4 seconds for every phi step. Debye Scherrer rings for a number of reflections were recorded [6].

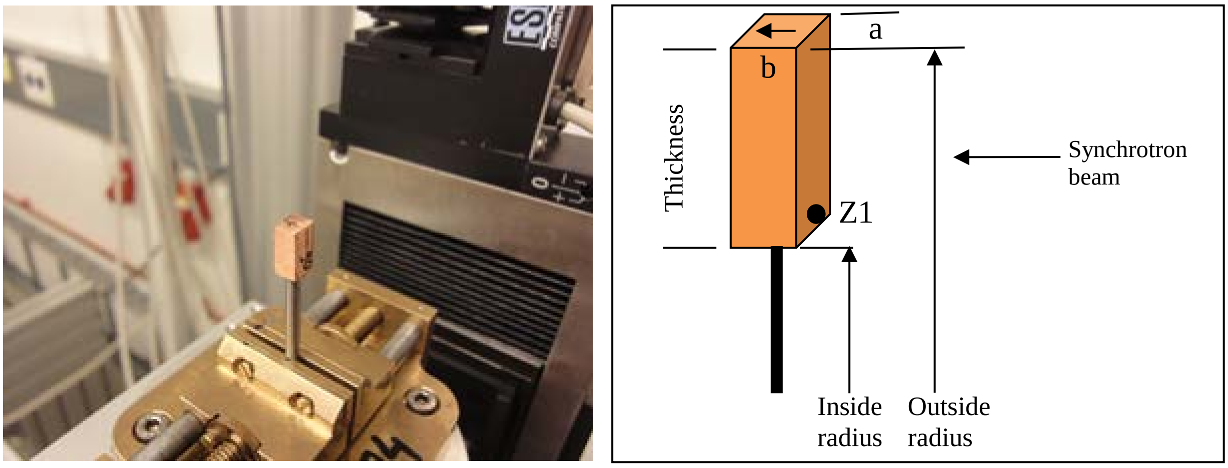

Figure 3.12 Copper sample cut from ring (left) Cu sample fixed on sample stage (right) schematic draw of Cu sample

The instrument software at P07B supports two methods for pole figure scanning. Firstly, a step scan mode, which allows running sample rotation ω in constant steps $\Delta\omega$ from 0° to 180°. The step width in $\Delta\omega$ can be adapted to the texture sharpness. The area detector allows any step width in $\Delta\gamma$ (0° - 360°) for data evaluation. Secondly, continuous scanning along ω can be implemented. Continuous rotation guarantees that all crystallites contribute but has the disadvantage to average over the grid size in ω. According to the small scattering angle of synchrotron one can get complete Deby Scherrer rings for a number of reflections. Figure 3.13a,b show the 2D image from the area detector (Mar345) and its diffraction pattern. A Debye-Scherrer ring ($h\ k\ l$) in the single detector image covers only one circle in ($h\ k\ l$) pole figure as shown in figure 3.14. The coverage can be extended by rotating the sample around the ω-axis. Therefore, a texture measurement is carried out with ω-rotation and detector images are collected after each ω-rotation-step. On a practical point, the rotation axis must be precisely fixed to the center of the measured volume, otherwise the center shifts during the rotation [41, 134].

As shown in figure 3.14 there is a blind area in the pole figure, even though the sample is rotated 180° around the ω-axis. However, this blind area is generally very small because the θ-values for interesting Debye-Scherrer rings ($h\ k\ l$) are smaller than 3° in most metallic materials using high energy beams.

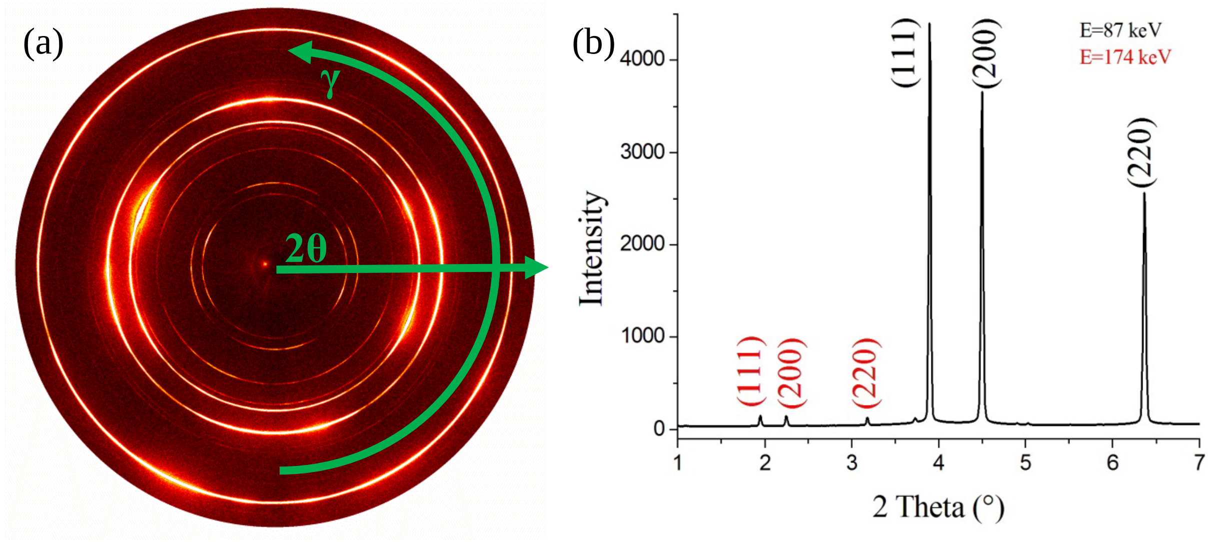

Figure 3.13 (a) Detector image from the copper tube (b) diffraction pattern related to the detector image

In order to take into account possible through thickness-inhomogeneities of the samples, pole figure measurements of the copper tube were carried out at five different positions from the inside radius to the outside radius, namely for the depth parameters Z. (Here the parameter Z1 indicates the inside radius and Z5 the outside radius of the tube).

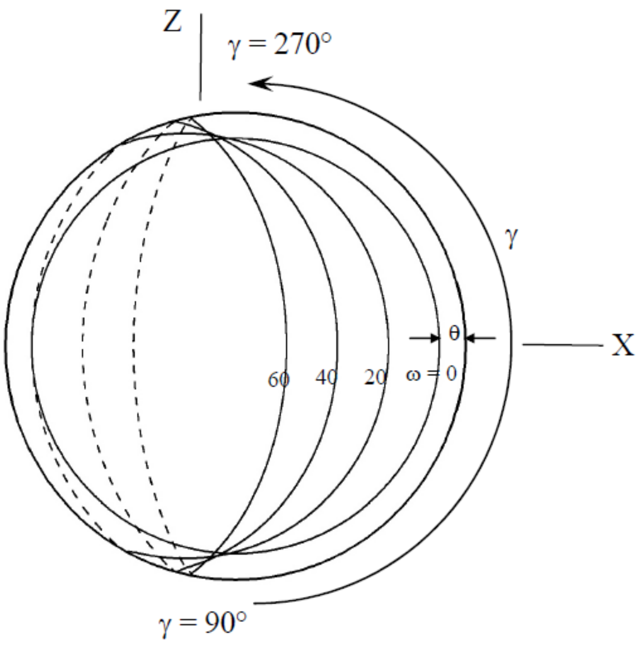

Figure 3.14 Representation of a pole figure using Debye-Scherrer rings captured at different ω-rotation angles. A solid line in the pole figure are corresponding to Debye-Scherrer ring in range from γ = 90° to 270°. Moreover, for emphasizing the blind area effect, θ = 10° and equal area projection are applied to this figure [135].

In the following, the data evaluation procedures for quantitative texture analysis are briefly introduced. This evaluation is made using an in-house software package. The evaluation consists of five steps [49]:

Step 1.

The center position of the detector image and the positions of Debye-Scherrer rings (*h k l*) are determined using Fit2d, developed at ESRF (European Synchrotron Radiation Facility) [136]. Fit2d offers a possibility for correcting a spatial distortion of the detector image, for example, if the detector leans towards one direction. In many practical cases the texture information can be extracted reasonably without this correction, it has an important meaning when some Debye-Scherrer rings are very closely spaced or partially overlapped. The correction is made with reference to a 2D image from a stress free and texture free material like LaB_6 or Al_2O_3 using the same experimental setup.

Step 2.

Calculation of diffraction pattern from 2D image averaged over 1° leads to 360 diffraction patterns for every detector image and total of 13320 when the ω-rotation-step is 5°. This step is also can be done by the Fit2d program.

Step 3.

From the diffraction patterns only the intensities are collected from the interesting Debye-Scherrer rings with background correction. For each different (*h k l*) a reduced file is written separately. Then, the intensities in the reduced files can be corrected according to the variation of sample volume, called volume correction, during the ω-rotation. The volume correction is based on the fact that higher diffraction intensities are induced from larger irradiation volume which is not the case for cylinder shaped samples. However, in case of sheet samples this is important because the beam path lengths are continually varied during the sample rotation. The absorption correction can be also made according to differences in the beam path.

Step 4.

The data obtained from the above steps are expressed by laboratory coordinate in terms of the angles describing the sample position and diffraction geometry, (ω and γ) respectively. The laboratory coordinates should be converted into the pole figure angles {α, β} for representing pole figure, pole distance α and azimuth angle β as shown in figure 3.15.

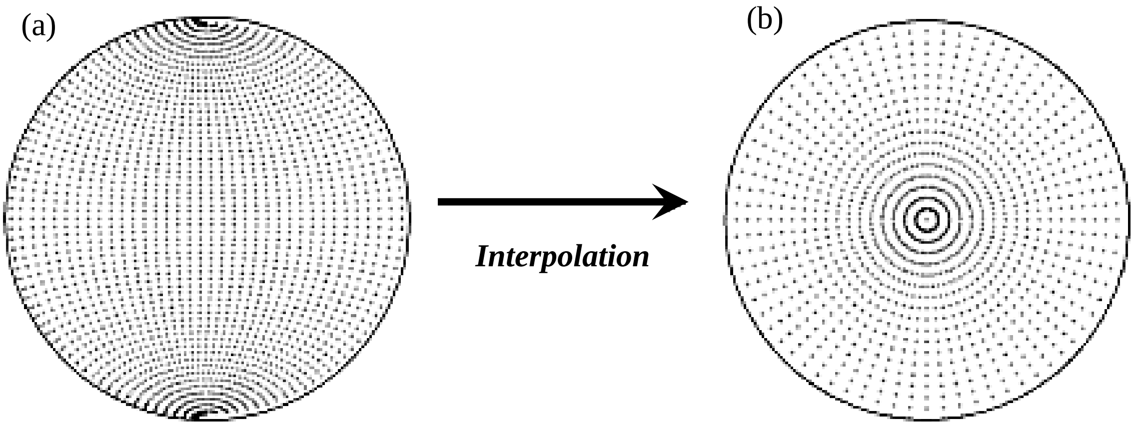

Figure 3.15 The data points represented on a pole figure; (a) measured points presented in regular (ω, γ) with 5° × 3° steps and (b) after interpolation in regular (α, β) with 5° × 5° steps [49].

Step 5.

The pole figure should be expressed in one of the standard regular distributions in α, β for ODF calculation, e.g. 5° × 5° or even finer grids. Figure 3.15 shows an example of the data points represented in a pole figure. The measured data points are distributed according to regular (ω, γ) angles, while the interpolated one has a regular distribution on the (α, β) grid. Usually intensity along 'γ' is collected at every 1°, however, 3° of γ-step is applied in figure 3.15 (a) for easy graphical representation.

3.5 Texture measurement by EBSD

A sample was cut from the minimum thickness of the DHP-Cu tube. The plane surface which has been prepared for the measurement was 10 x 9.57 mm^2 and 4 mm long in the axial direction. The plane of the measurement was the radial-hoop. For Sample preparation, the final polishing step for scanning electron microscopy was conducted with commercial polishing solution of Al_2O_3 powder.

A scanning electron microscope (JEOL JSM-6490LV) operated with a tungsten cathode and additionally equipped with an EBSD detector (EDAX TSL OIM) was used for constructing the EBSD map. For the CCD camera, a 4 × 4 binning was used. 9 EBSD maps were constructed, every map having dimension of 0.955 X 0.955 mm^2. For every EBSD map the kikuchi patterns were captured in step of 0.2 µm. For every detector picture (Kikuchi pattern) the exposure time was 0.2 seconds, the energy was 25 keV and a 120 µm aperture was used. The working distance was 16 mm.

Figure 3.16 shows how the measurements were carried out. After identifying the material and phases (lattice parameters, space group) a Kikuchi pattern (see figure 3.16b) from the defined area (see figure 3.16a) will be collected by the backscattered detector. Every Kikuchi pattern is continuously indexed (see figure 3.16c). After indexing the discrete orientation (see figure 3.16d) can be plotted on the selected pole figure. The measurement starts from the outer diameter to the inner diameter. Using the above setting the period to collect one EBSD map was 15 hours for a total of 263580 data points.

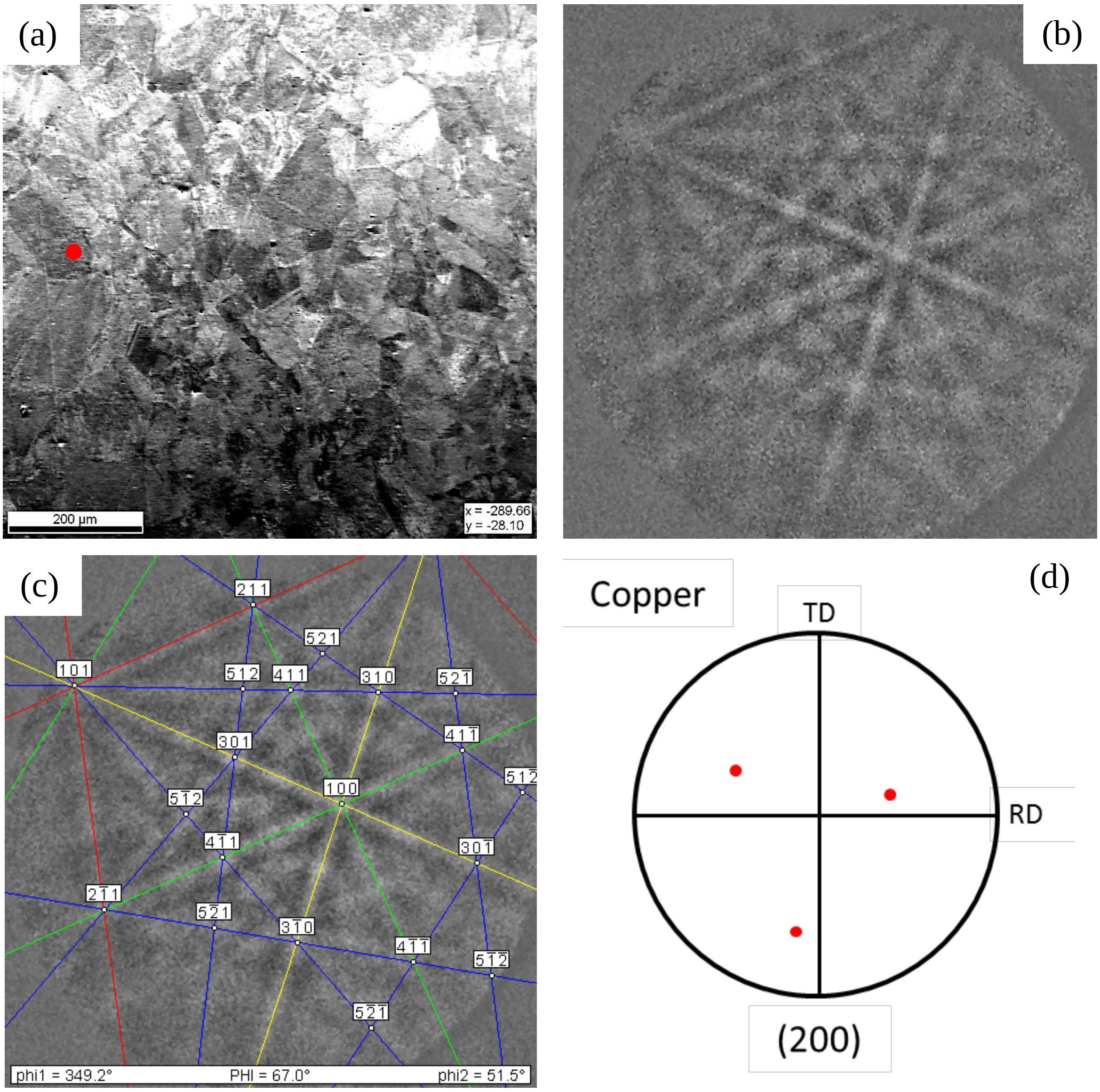

Figure 3.16 (a) backscattered image of copper sample cut from the minimum thickness of the DHP-Cu tube that is mounted in front of the EBSD detector (b) Kikuchi diffraction pattern of the material at the red mark (c) automatic indexing of Kikuchi pattern (d) discrete (200) pole figure.

3.6 Strain measurement by neutrons

A copper tube with length of 250 mm was cut from the 1 m DHP-Cu tube. The chemical composition of the material is Cu: 99.972%, Al: 0.005%, Ni: 0.0016%, Pb: 0.0041% and P: 0.0168%., and the values of the thickness around the perimeter from 0° to 180° are shown in figure 3.1.

The strain measurement were performed by using the robot and the XYZ-stage to compare the two instruments and to illustrate the capabilities and reliability of the RX160 robot in residual stress analysis of engineering samples, and also to characterize the through wall thickness residual stress variation along the circumference between the maximum to minimum wall thickness positions.

3.6.1 Strain measurement by neutron using the robot

3.6.1.1 Measuring d_0 for the stress free sample

A small sample was cut from the ring with dimension 5 × 5 × 5 mm^3. The cut sample was fixed on a vanadium pin and installed in a sample holder. Then the sample holder was installed on the robot arm. The d_0 measurements were carried out using a neutron beam with a wavelength of 1.53 Å obtained via Si (400) monochromator. A rectangular primary slit 2 × 2 mm^2 and a radial collimator of FWHM = 2 mm as a secondary slit were used. A sample to detector distance of 1065 mm was used and primary slit to sample distance was 50 mm. To measure the peak position of Cu (311) for d_0 measurement the detector position was 89.6°. The exposure time was 5 min while the sample was rotating.

The software package StressTextureCalculator (STeCa [129]) has been used to extract the peak positions from the area detector data.

3.6.1.2 Three dimensional laser scanning of tube segment for strain measurement

For the strain measurement by the robot, the sample and sample holder have been 3D scanned. The device we used was a CimCore Infinite portable coordinate measuring arm which is described in section 3.3.1.1.

The scanning process was started by moving the integrated laser head manually around the sample plus sample holder. Numerous line scans were performed with the laser head perpendicular to the surface and continuously recording the reflection giving a cloud of points. The Geomagic studio allows direct viewing of the cloud of points during scanning.

Thereafter the 3D picture of the Cu-tube and the sample holder (see fig. 3.17) is created from the cloud of points. In the next step the coordinates for all sample positions where strain measurements will be done are defined. By using a small in house developed mathematical library, the numerical values for the selected points (X, Y, Z, RX, RY and RZ with respect to robot plate) can be extracted from the Geomagic Studio software and implemented in the robot software.

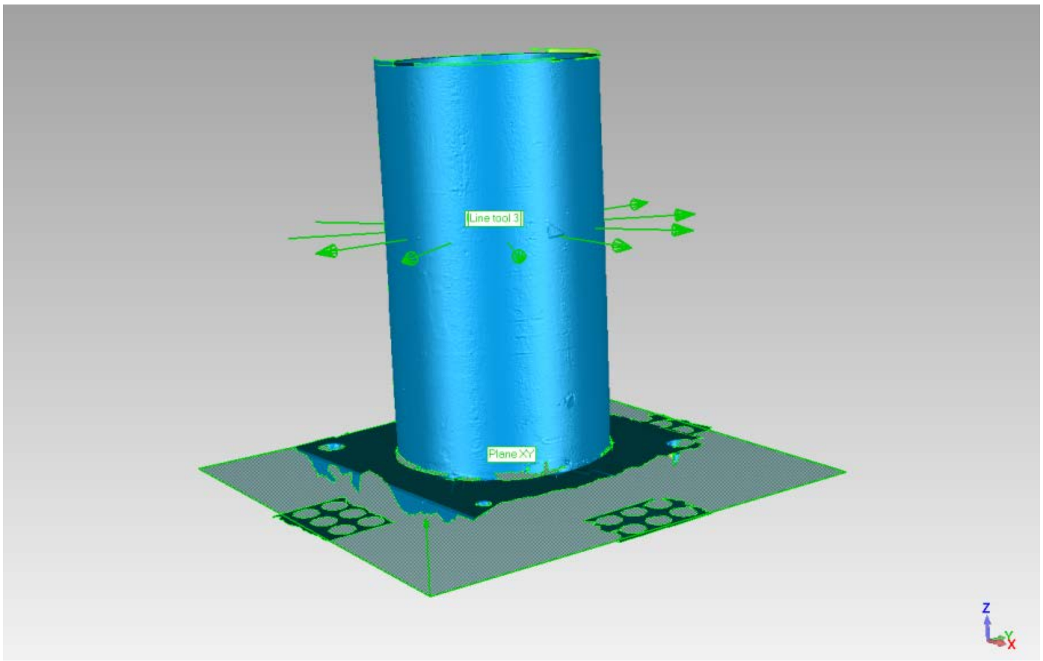

Figure 3.17 Three dimensional laser scan for Copper tube mounted on sample holder strain configuration

3.6.1.3 Strain measurement by the robot

After 3D laser scanning of the sample geometry and extraction of the coordinates of the measuring positions, the copper tube segment with sample holder (weight 15 kg) were installed on the robot arm as shown in figure 3.18. The strain measurements were carried out on STRESS-SPEC [3, 4] using a neutron wavelength of 1.53 Å obtained via a Si (400) monochromator. A rectangular primary slit of 2 × 2 mm^2 made of cadmium and a radial collimator of FWHM = 2 mm as a secondary slit were used.

A sample to detector distance of 1065 mm was used and the primary slit to sample distance was 50 mm. To measure the peak position of Cu (311) for strain measurement the detector position was 89.6°. This 2θ angle provides a practically equal shaped gauge volume in all measuring direction for the axial, hoop and radial orientations.

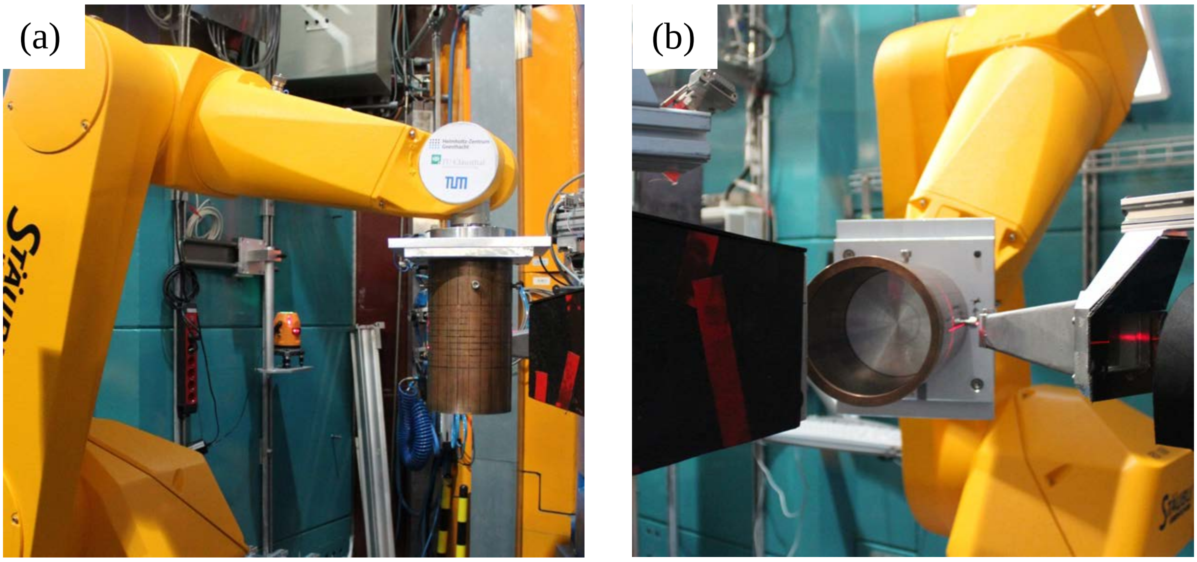

Figure 3.18 Copper tube with the sample holder mounted on the robot arm (left) radial and hoop configuration (right) axial configuration

The robot was programmed according to the selected points obtained by 3D laser scanning to move the copper tube automatically in a range of 0° to 180° around the circumference in steps of 30°. For every position 6 through thickness measurements were made for each direction (radial, hoop and axial). The exposure time for every measuring point was 5 min. Figure 3.19 presents a schematic set up for the radial, hoop and axial residual strain measurements

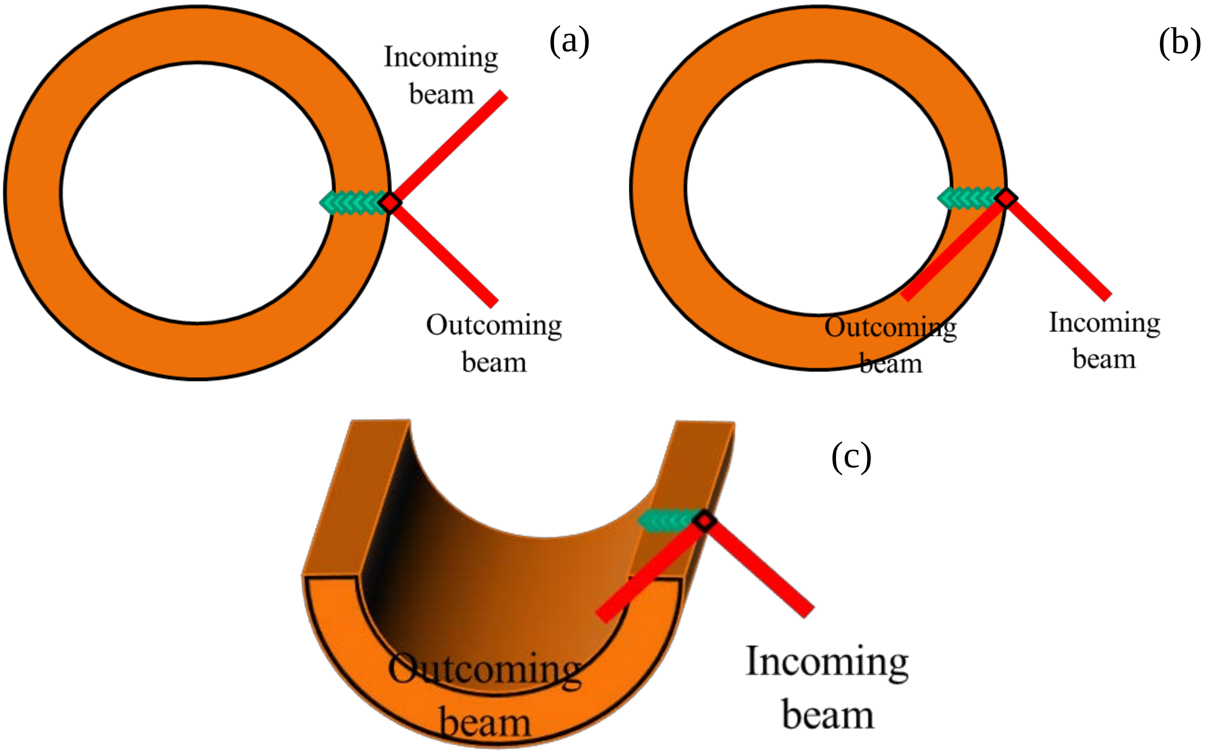

Figure 3.19 Schematic Set up for (a) radial strain measurement (b) hoop strain measurement (c) axial strain measurement.

Residual Strain measurements were performed in axial, hoop and radial directions a minimum of 125 mm away from the tube ends to avoid measurement in regions that had relaxed.

The precise location of the surface has been extracted from the 3D laser scan and has been checked by a surface scan of the neutron beam to calculate the centroid position from the intensity profile.

The software package StressTextureCalculator (STeCa [129]) has been used to extract the peak positions from area detector data.

3.6.2 Strain measurement by neutrons using the XYZ-table

3.6.2.1 Measuring d_0 for the stress free sample

A small sample cut from the tube with the dimensions 5 × 5 × 5 mm^3. The cut sample was fixed on a vanadium pin and installed in a sample holder. Then the sample holder was installed on the XYZ-table. The strain measurements were carried out using a neutron beam with a wavelength of 1.55 Å obtained via a Si (400) monochromator. A rectangular primary slit 2 × 2 mm^2 and a radial collimator of FWHM = 2 mm as a secondary slit were used. A sample to detector distance of 1065 mm was used and the primary slit to sample distance was 50 mm. To measure the peak position of Cu (311) for d_0 measurement, the detector position was 90.6°. The exposure time was 5 min.

The software package StressTextureCalculator (STeCa [129]) has been used to extract the peak positions from area detector data.

3.6.2.2 Strain measurement by the XYZ-table

The copper tube with sample holder was installed on the XYZ table as shown in figure 3.20. The strain measurements were carried out on STRESS-SPEC [3, 4] using a neutron wavelength of 1.55 Å obtained via a Si (400) monochromator. STRESS-SPEC is equipped with an area detector of 300 X 300 mm^2. A rectangular primary slit 2 × 2 mm^2 and a radial collimator of FWHM = 2 mm as a secondary slit were used.

A sample to detector distance of 1065 mm was used and the primary slit to sample distance was 50 mm. To measure the peak position of Cu (311) for strain measurement, the detector position was 90.6°. The XYZ-stage was programmed so that strain measurements in the radial and hoop directions were made at the 0°, 90° and 180° positions around the circumference in one run. Then the configuration of the tube was changed to measure the axial direction for the positions 0°, 90° and 180° as shown in figure 3.20. For every position 8 steps through the thickness were measured for every direction (radial, hoop and axial). The exposure time for measurement was 2 min.

Residual Strains measurements were performed in axial, hoop and radial directions a minimum of 125 mm away from the tube ends to avoid measurement in regions that had relaxed.

The precise location of the surface has been extracted by calculating the centroid position from the intensity profile after a surface scan by the neutron beam.

The software package StressTextureCalculator (STeCa [129]) has been used to extract the peak positions from area detector data.

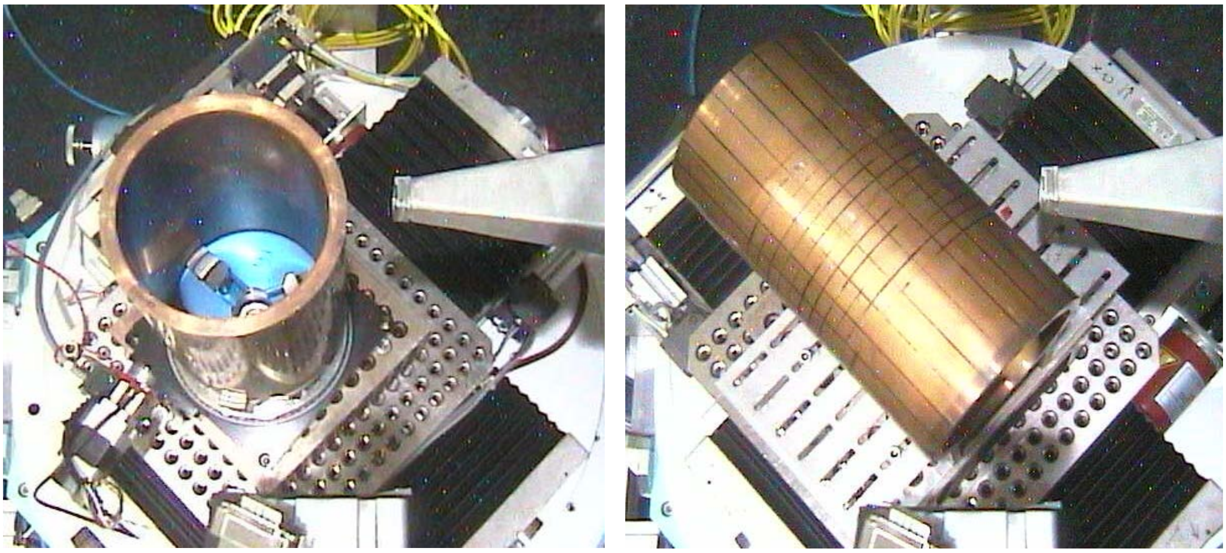

Figure 3.20 Copper tube with the sample holder mounted on the XYZ table (left) radial and hoop configuration (right) axial configuration

3.7 Mechanical properties

3.7.1 Tensile test

The tension test is widely used to provide basic design information on the strength of materials and as an acceptance test for material specifications. In the tension test a specimen is subjected to a continually increasing uniaxial tensile force with simultaneously monitoring of the specimen elongation [17, 137].

A tensile sample of cylindrical shape with the dimension shown in table 3.3 was machined from the copper tube from the longitudinal direction as shown in figure 3.21. The tensile test was performed using a Schenck Trebel RM100 machine with speed 0.5 mm/min. A laser extensometer from Fiedler Optoelektronik was used to measure the elongation in the sample.

The stress (σ) in the stress strain curve is the average longitudinal stress in the tensile specimen. It is obtained by dividing the load (P) by the original cross-sectional area (A_0) of the specimen.

$$\sigma = \frac{P}{A_0} \tag{3-3}$$

The strain (ε) used for the engineering stress-strain curve is the average linear strain, which is obtained by dividing the gage length of the specimen (L), by its original length (L_0).

$$\varepsilon = \frac{\Delta L}{L_0} = \frac{L - L_0}{L_0} \tag{3-4}$$

Table 3.3 Dimensions of tensile test sample

$\mathbf{d_0}$	$\mathbf{d_1}$	$\mathbf{L_0}$	$\mathbf{L_C}$	$\mathbf{L_t}$
5 mm	M8	25 mm	30 mm	50 mm

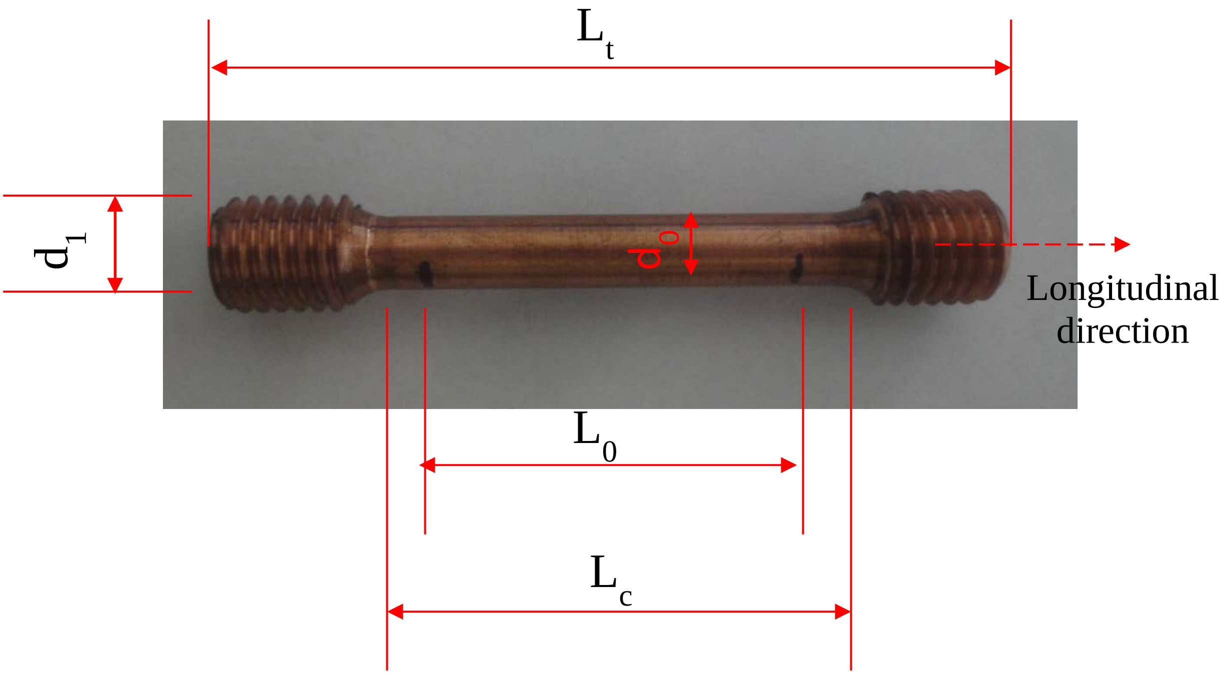

Figure 3.21 Tensile sample cut from the DHP-Cu tube

The elongation (A) is used to describe the ductility. The conventional calculation of elongation is obtained from the engineering strain at fracture (ε_f). Elongation usually is expressed as percentage.

$$A = \varepsilon_f = \frac{L_f - L_0}{L_0} \qquad (3\text{-}5)$$

The shape and magnitude of a metals' stress-strain curve depend on its composition, heat treatment, prior history of plastic deformation, the strain rate, temperature and the type of stress imposed during the testing. The parameters which are used to describe the stress-strain curve of metal are the tensile strength, yield strength or yield point, and percentage elongation. The first two are strength parameters; the last is a measure of ductility [17, 137].

3.7.2 Hardness test

Hardness is one of the important mechanical properties of materials, the resistance to indentation indicates the strength, and is thus sensitive to heat treatment. Hardness generally implies resistance to penetration. There are a number of hardness testing methods; however, the most commonly used are the Brinell, Rockwell and Vickers (Diamond Pyramids) methods. In this work Vickers methods has been used [17, 137]. The Vickers hardness (*HV*) test can be used for all metals and has one of the widest scales among hardness tests.

The *HV* number is determined by the ratio *F/A* where *F* is the force applied to the diamond shaped indenter (in newtons) and *A* is the surface area of the resulting indentation (in square millimeters). *A* can be determined by the equation (3-5):

$$A \approx \frac{d^2}{2\sin(136°/2)} \qquad (3\text{-}5)$$

Where *d* is the average length of the diagonals (*d1* and *d2*) left by the indenter (see figure 3.22) in millimeters. Hence,

$$HV = \frac{F}{A} \approx 0.1891\frac{F}{d^2} \qquad (3\text{-}6)$$

The Vickers hardness was measured at different positions around the circumference (minimum, middle and maximum thicknesses). At each through wall thickness position a Vickers hardness test was performed by using a Struers Durmain Hardness measuring instrument. A load of 0.1 N of force was applied for 10 seconds. The hardness test was repeated three times and the average was taken for each point. The measurements were started from the inside diameter towards the outside diameter.

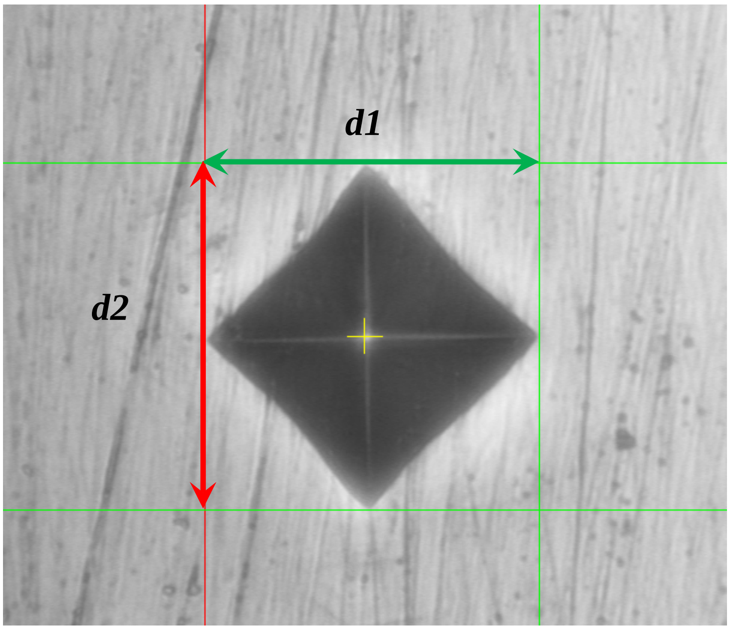

Figure 3.22 Indenter profile of the diamond-pyramid, *d1* and *d2* are the diagonals left by the indenter

4. Results and Discussions

4.1 Microstructure and mechanical properties

Optical microstructures of DHP-copper tube at different wall thickness (maximum, middle and minimum) are shown in figure 4.1 for the axial-radial plane and figure 4.2 for the hoop-radial plane. The optical microstructures through the whole wall thickness of DHP-copper tube at different wall thickness (maximum, middle and minimum) starting from outer diameter are shown in Appendix 1. The microstructures of DHP-copper tube at different wall thickness are equiaxed recrystallized grains that containing annealing twins as shown in figures 4.1 and 4.2, which is the expected microstructure for the annealed DHP-copper [10]. Twinned crystals will easily form above the recrystallization temperature because of the low stacking fault energy (SFE). The frequency of the twins is determined primarily by the stacking fault energy and is greatest in low SFE materials like 70:30 brass [138]. Coarse grains larger than 200 µm can be seen at the inner surfaces and central portion of the wall surrounded by small grains as shown in Appendix 1.

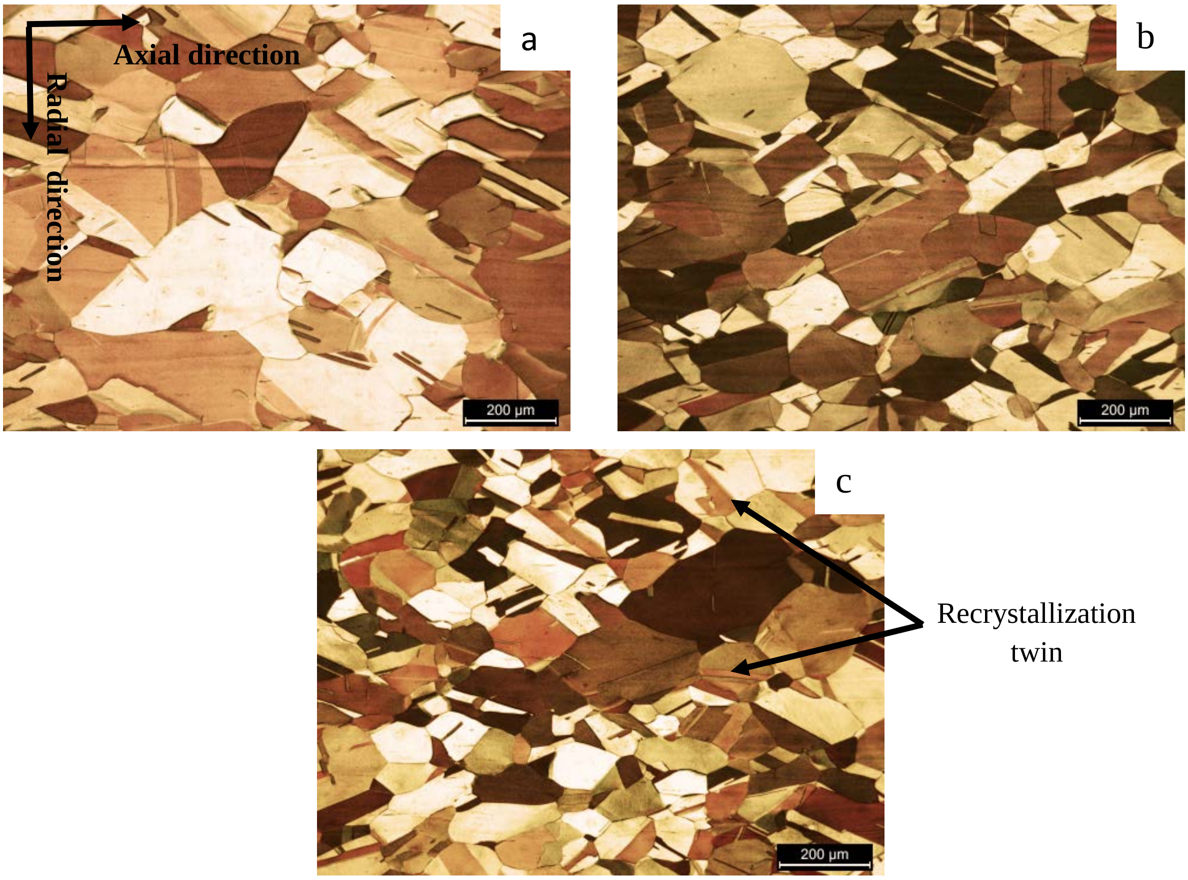

Figure 4.1 Micrographs of DHP-copper tube for axial-radial plane at three different positions around the circumference (a) maximum, (b) middle and (c) minimum wall thicknesses

The average grain sizes have been calculated from all the micrographs that have been obtained at the different wall thicknesses. For the axial-radial plane, the average grain size at the maximum wall thickness is 83 µm, and at the minimum wall thickness is 78 µm. For the hoop-radial plane, the average grain size at the maximum wall thickness is 77 µm and at the minimum wall thickness is 66 µm.

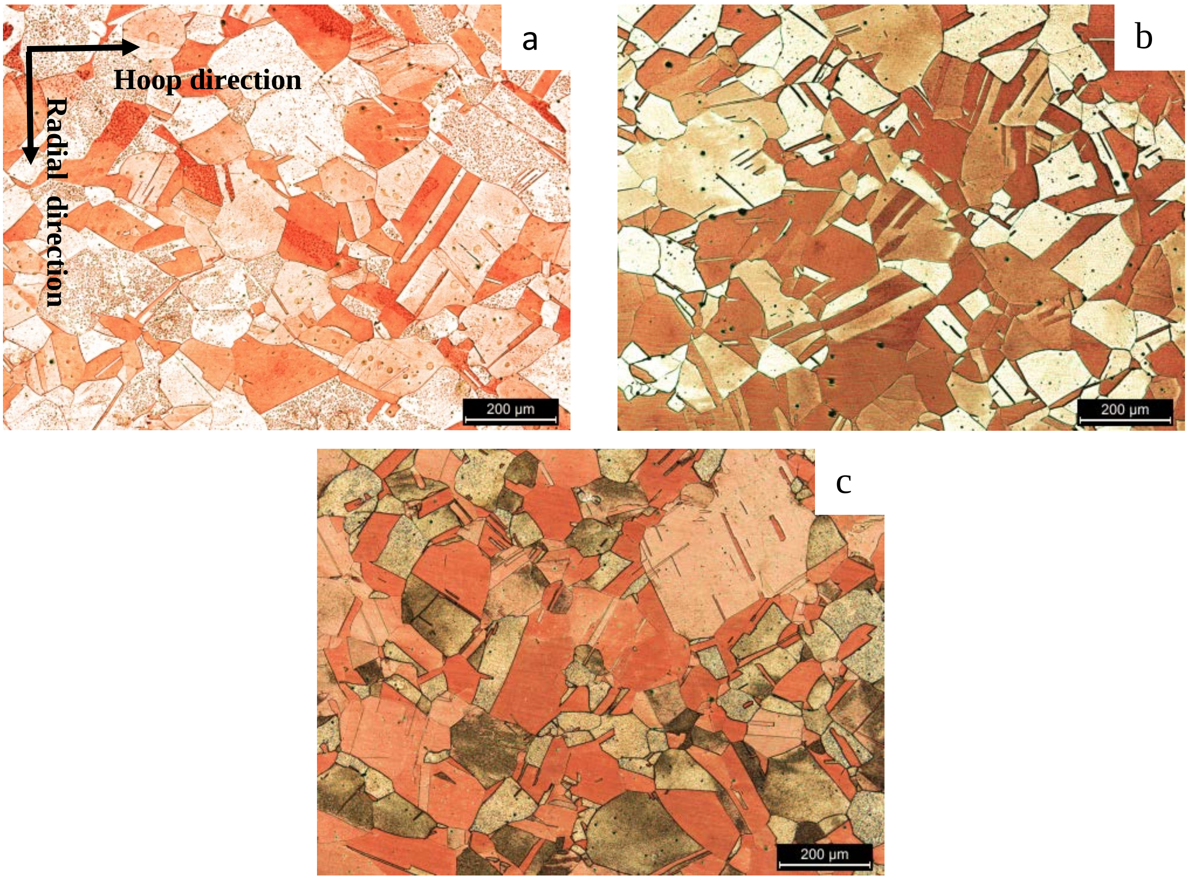

Figure 4.2 Micrographs of DHP-copper tube for hoop- radial plane at three different positions around the circumference (a) maximum, (b) middle and (c) minimum wall thicknesses

Figure 4.3 shows the stress-strain curve for a sample cut from the copper tube in the axial direction. The stress-strain curve shows very small work hardening which results in the difference between the yield stress ($YS_{0.2}$) and the ultimate tensile stress (UTS) being very small.

The mechanical properties of DHP-copper tube including the yield stress ($YS_{0.2}$), ultimate tensile stress (UTS), elongation (A) and modulus of elasticity (E) are given in table 4.1. The mechanical properties fit quit well with the German Copper Institute catalog for DHP-Cu type tube R250 [54].

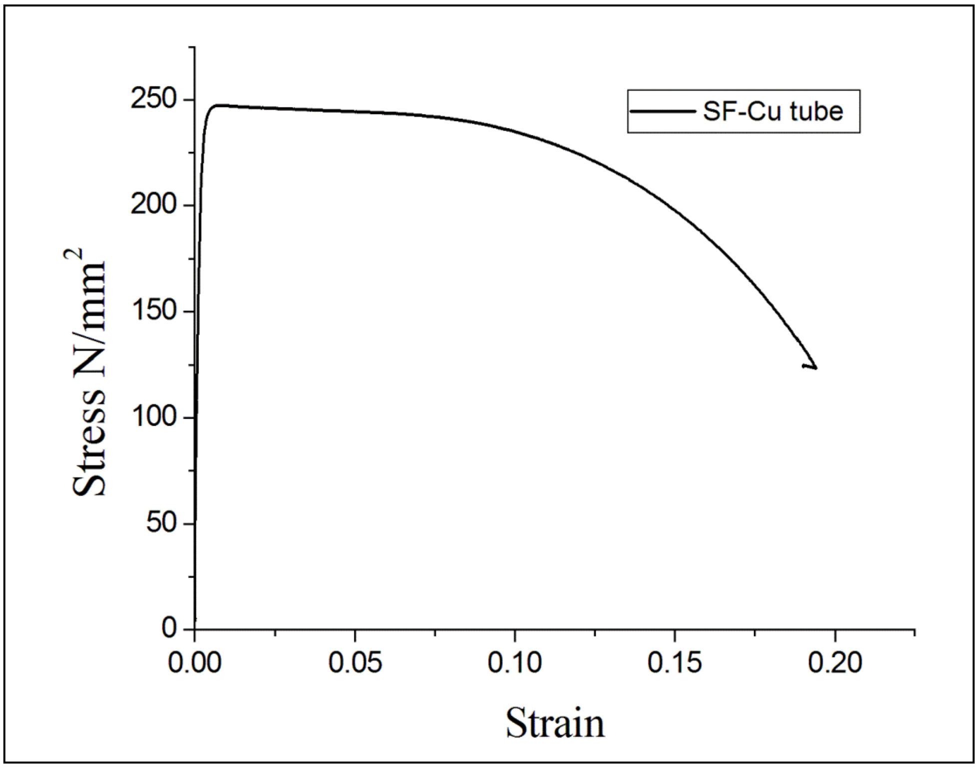

Figure 4.3 Stress-strain curve of DHP-Cu tube

Table 4.1 Mechanical properties of DHP-Cu tube

Properties	**YS$_{0.2}$(N/mm^2)**	**UTS(N/mm^2)**	**A %**	**E(kN/mm^2)**
values	240	250	20	114

The fracture surface of the DHP-Cu tensile sample is a classic cup and cone fracture as shown in figure 4.4a. Within the necking area, microvoids nucleate at regions of localized strain discontinuity, such as that associated with second-phase particles, inclusions, grain boundaries and dislocation pile-up [139, 140]. As the load continues, these microvoids expand and join together to create a crack with its plane perpendicular to the axis of the tensile force being applied. As this crack grows, a shear plane at approximately 45° to the tensile direction develops around specimen edge and merges with the existing crack, resulting in the classic cup and cone fracture surfaces as demonstrated in figure 4.4b.

Investigation under higher magnifications by SEM shows a ductile fracture surface consisting of many ductile dimples or microvoids as shown in figure 4.5.

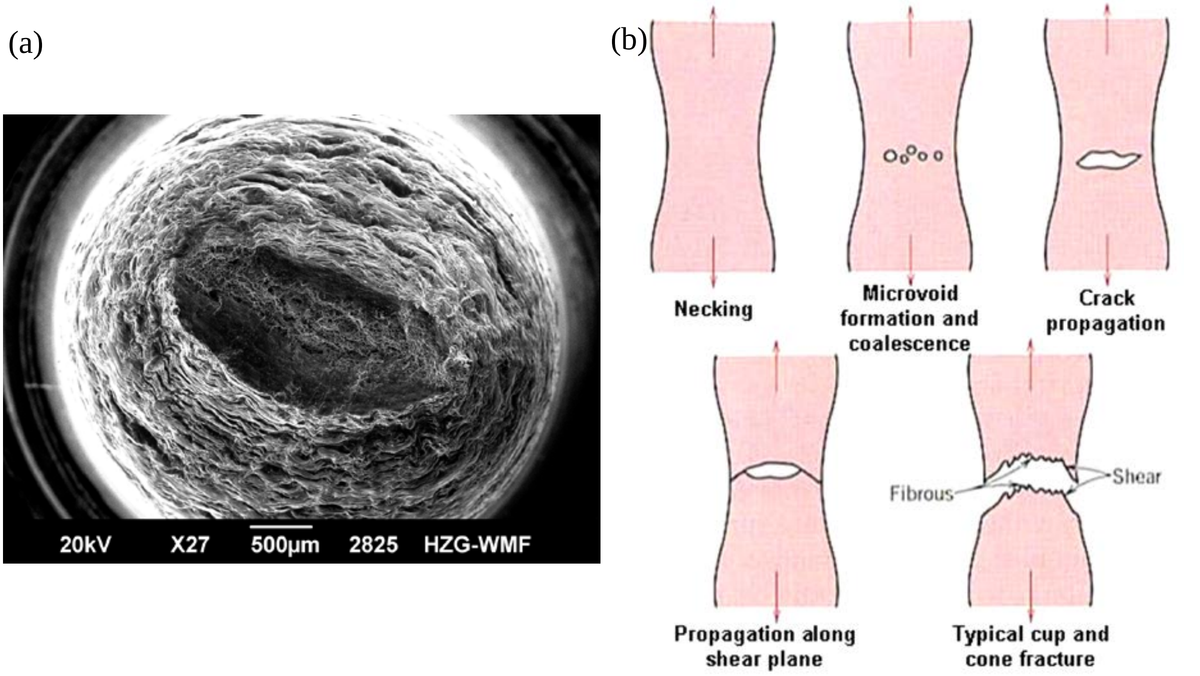

Figure 4.4 a) Cup fracture surface of DHP-Cu tensile sample, b) Cup and cone fracture mechanism [141].

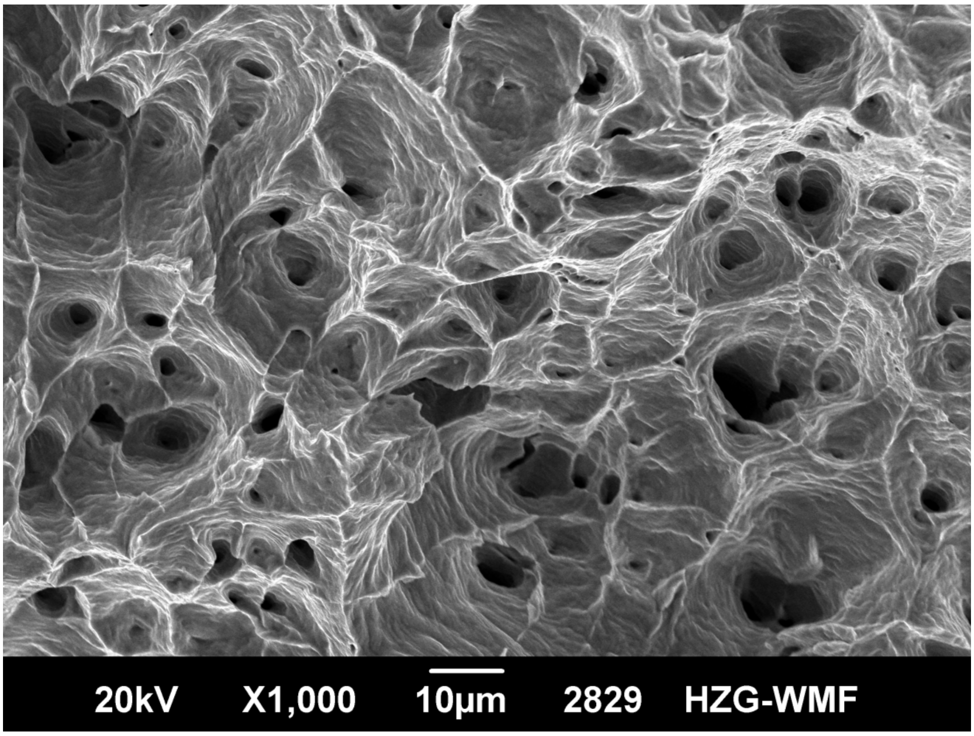

Figure 4.5 Ductile fracture surface consisting of many ductile dimples and microvoids

Figure 37 shows the hardness values through the wall thickness for different positions around the circumference (positions of minimum, middle and maximum wall thickness). The hardness values have been measured from the inside diameter (ID) to the outside diameter (OD). The hardness remains nearly constant. The variation of hardness at the minimum wall thickness is between 98 HV and 107HV, 99 HV to 105HV at the middle thickness and between 95 HV and 105HV at the wall maximum thickness. The hardness values depend on the copper tube heat treatment [23, 142]. These values fit quite well with the catalog of the German Copper Institute for DHP-Cu type tube R250 [10]. Vickers Hardness can be a good tool to evaluate the mechanical properties through the wall thickness.

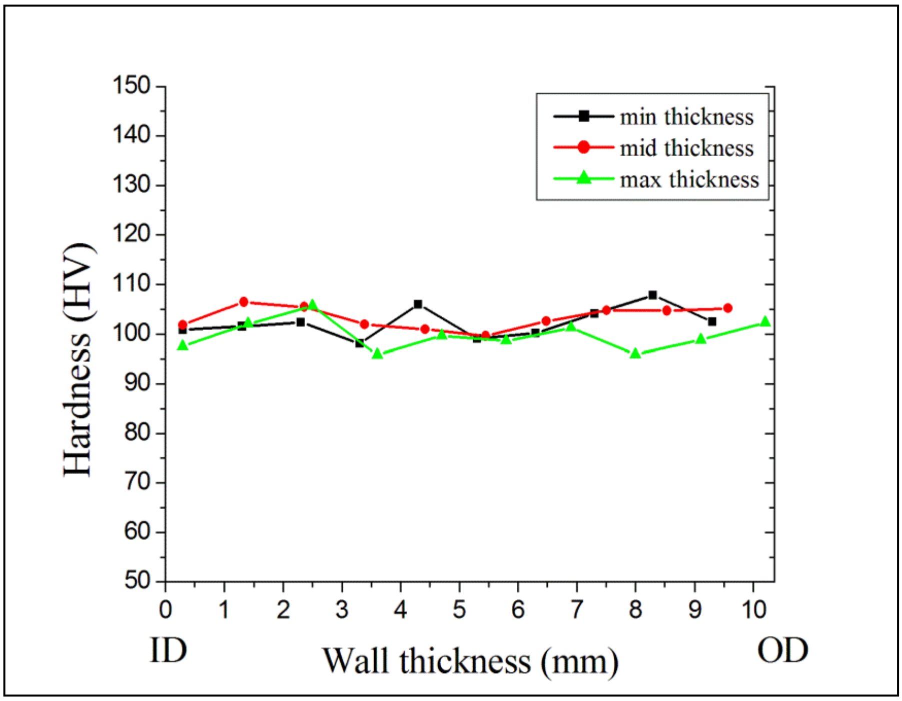

Figure 4.6 Through-thickness hardness variation of the copper tube at different circumferential positions

4.2 Texture variation around the DHP-Cu ring measure by neutrons

The texture variation has been calculated from pole figure measurements at different positions around the circumference of the DHP-Cu ring. Because the irregular shape of the investigated sample (ring shape) the measured pole figure should be corrected for volume and absorption corrections. The corrected pole figures and ODFs have been compared with pole figures and ODFs from cubic sample cut from the tube at the same circumferential positions. This comparison can give a good indication about how were the volume and absorption corrections.

4.2.1 Pole figures before and after intensity correction

The normalized raw data pole figures of Cu (111), (200) and (220) only with background correction are shown for circumference positions 0° (maximum wall thickness), 90° (middle wall thickness) and 180° (minimum wall thickness) in figure 4.7. The other positions are presented in appendix 2.

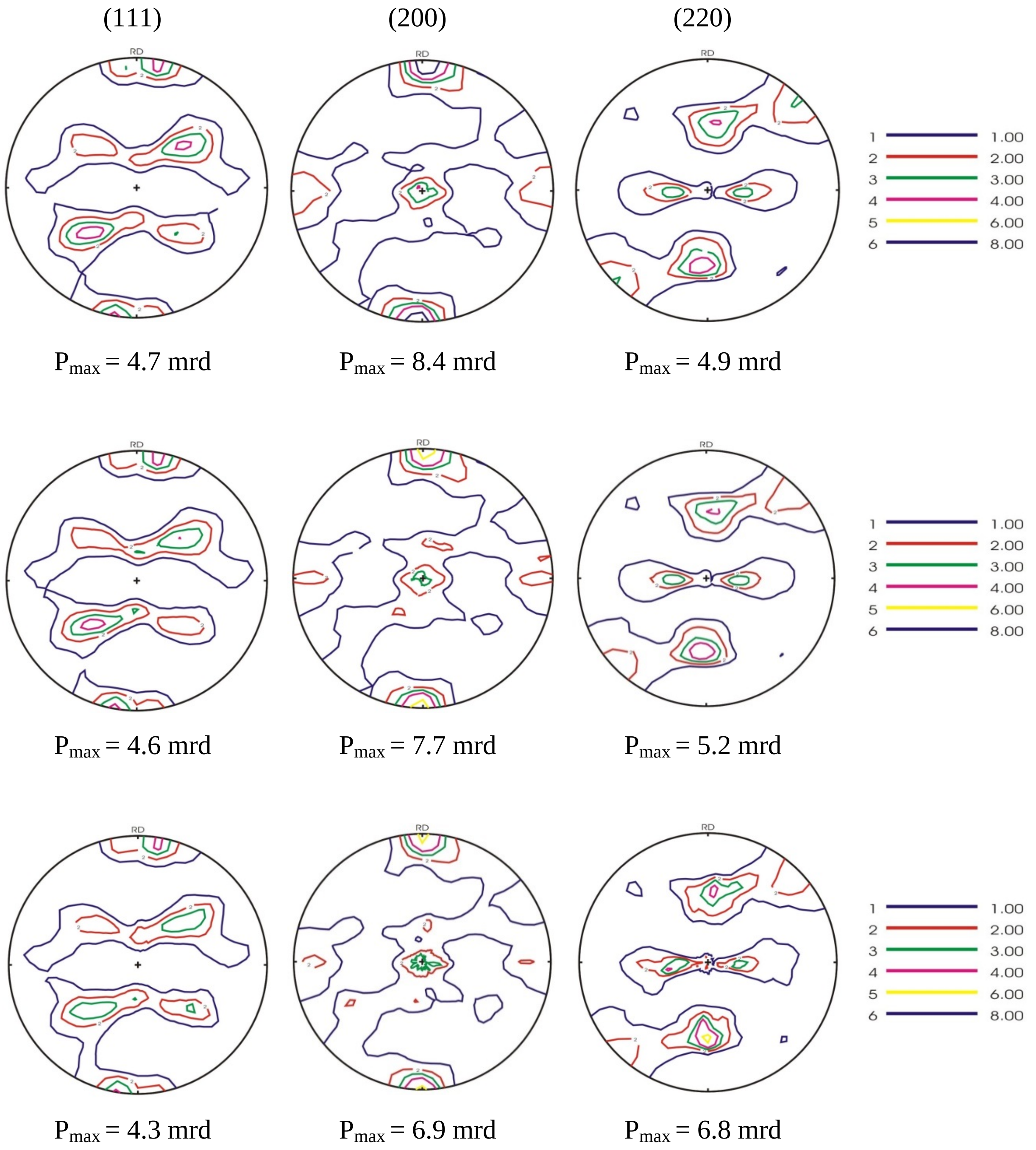

P_{max} = 4.7 mrd P_{max} = 8.4 mrd P_{max} = 4.9 mrd

P_{max} = 4.6 mrd P_{max} = 7.7 mrd P_{max} = 5.2 mrd

P_{max} = 4.3 mrd P_{max} = 6.9 mrd P_{max} = 6.8 mrd

Figure 4.7 (111), (200) and (220) pole figures as measured by the Robot before correction for Cu-ring in top (0°-maximum wall thickness), middle (90°-middle wall thickness) and bottom (180°-minimum wall thickness) figures.

One can see clearly asymmetric pole figures, which can result from i) asymmetric material flow during tube processing, ii) a variation of the gauge volume during pole figure measurement and iii) from anisotropic absorption. The ovality and the eccentricity of the tube clearly indicate asymmetric material flow [128].To correct the pole figures in fig. 4.7 and in appendix 1, the gauge volume and the anisotropic absorption change during tilting and rotation have been calculated. Figure 4.8 shows the two volume correction one for a 47° detector angle ((111) and (200) pole figures) and the second for a 75° detector angle ((220) pole figure). The pole figures have a regular (5x5) grid ($\Delta\alpha = 5°$ and $\Delta\beta = 5°$), a regular grid is required for most software packages for ODF calculation (ODF orientation distribution function). Due to the fact that a radial collimator was not used the gauge volume varies from 1511 mm^3 to 6527 mm^3 for the 47° detector angle and from 1501 mm^3 to 6390 mm3for the 75° detector angle.

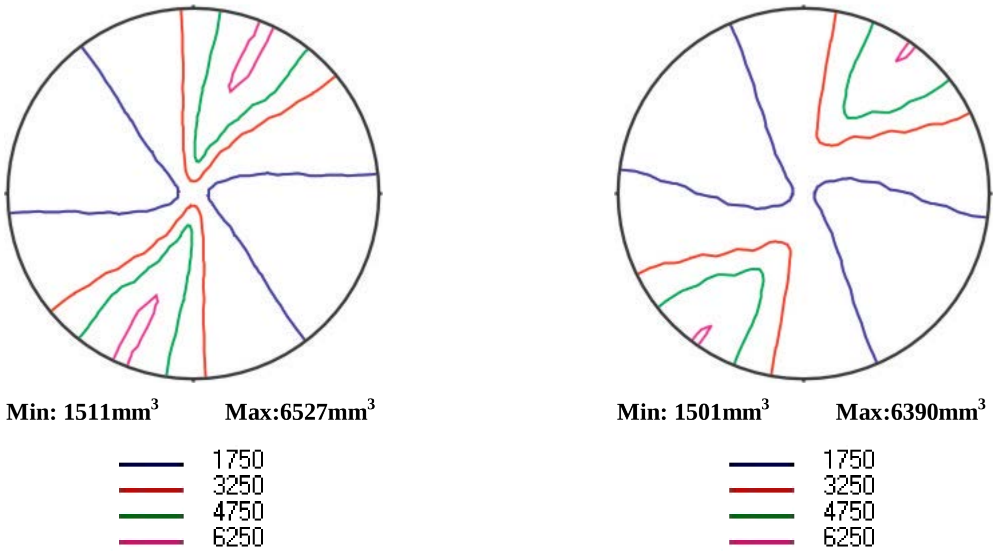

Figure 4.8 Pole figures taking into account the constant volume correction for Cu (111) and Cu (200) (left) Cu (220) right

After calculation of the beam paths, the anisotropic factor (*exp(-μt)*) pole figures for a 47° detector angle ((111) and (200) pole figures) and for a 75° detector angle ((220) pole figure) were determined and are shown using 5x5 grid ($\Delta\alpha = 5°$ and $\Delta\beta = 5°$) in figure 4.9. Due to a missing radial collimator the gauge volume varies from 0.454 to 0.752 for the 47° detector angle and from 0.517 to 0.723 for the 75° detector angle [128].

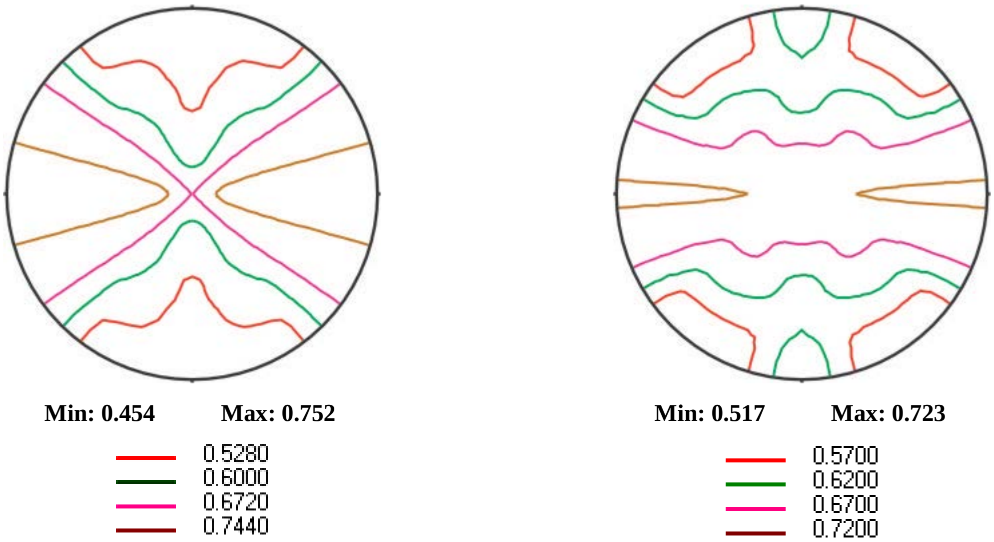

Figure 4.9 Pole figures taking into account the anisotropic absorption correction for Cu (111) and Cu (200) (left) Cu (220) right

By dividing the raw data pole figures (fig. 4.7) with correction pole figures (fig. 4.8 and 4.9) one can clearly see the dominating influence of the volume correction, see figure 4.10 and appendix 2. An enhancement of the pole figure symmetry can be seen in figure 4.10 and appendix 2 when compared with figure 4.7. Without the correction a much higher shear would be assumed than is really the case. In figure 4.7 the anisotropic pole density of the (111) planes resulting from variations of the irradiated volume and absorption can be seen.

For example, at the middle wall thickness the texture sharpness decreases from 4.6 mrd (multiples of random distribution) to 4.3 mrd for the Cu (111) pole figure and from 7.7 mrd to 6.4 mrd for the Cu (200) pole figure, while remaining nearly constant for the Cu (220) pole figure [128].

To control the goodness of the corrections, Copper cubes have been cut and analyzed from the same positions. In figure 4.11 one can see a good agreement between both sets of pole figures [128]. In general, it was proposed by Linssen, Mengelberg and Stüwe that the sample symmetry of seamless tubes is no longer orthorhombic. According to the geometry of the manufacturing process one can only expect one mirror plane, which is defined by the tube axis and the radius. Together with centrosymmetry this leads to monoclinic sample symmetry 2/m [143].

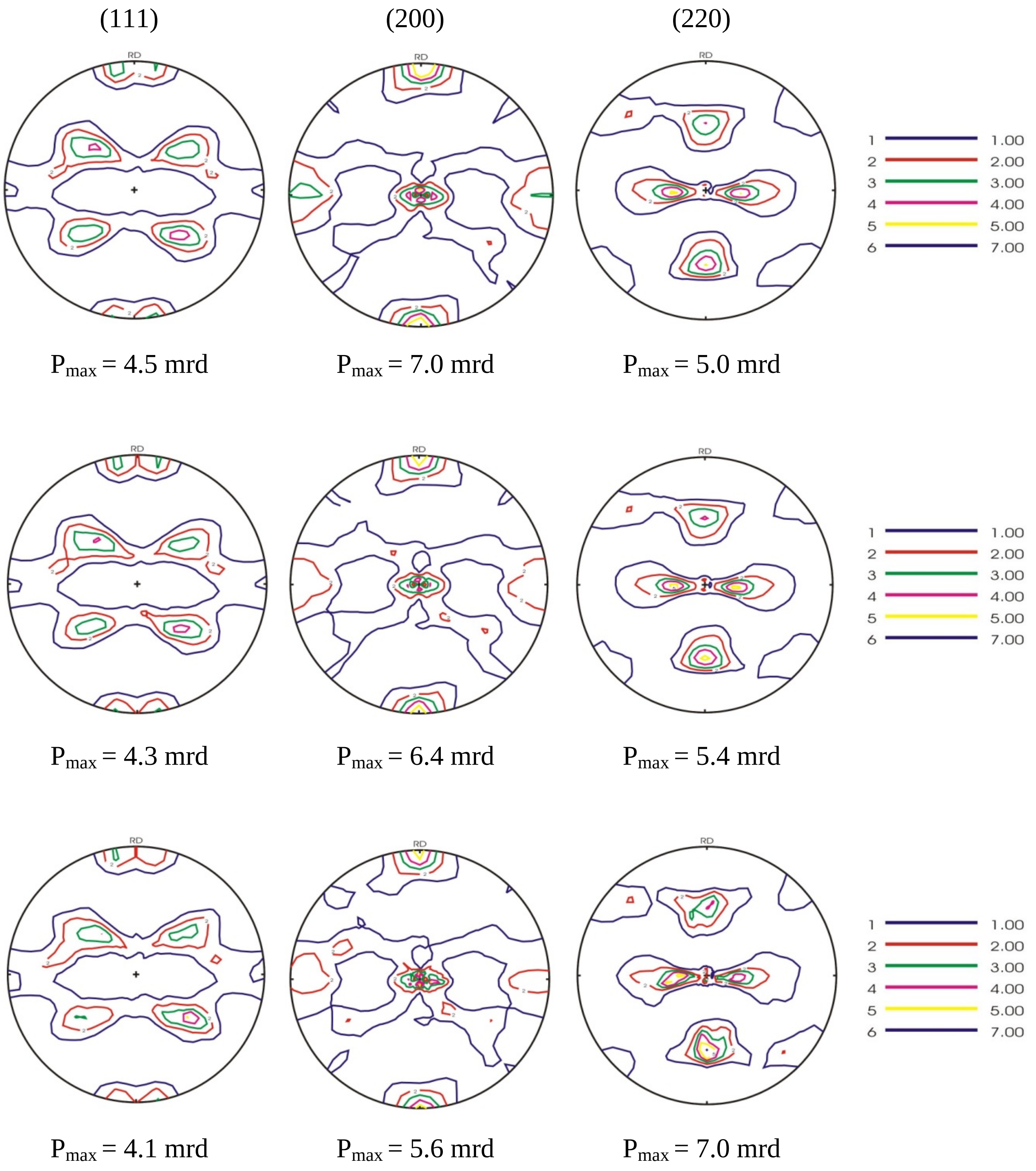

Figure 4.10 (111), (200) and (220) pole figures after volume and anisotropic absorption correction for Cu-ring in top (0°-maximum wall thickness), middle (90°-middle wall thickness) and bottom (180°-minimum wall thickness) figures.

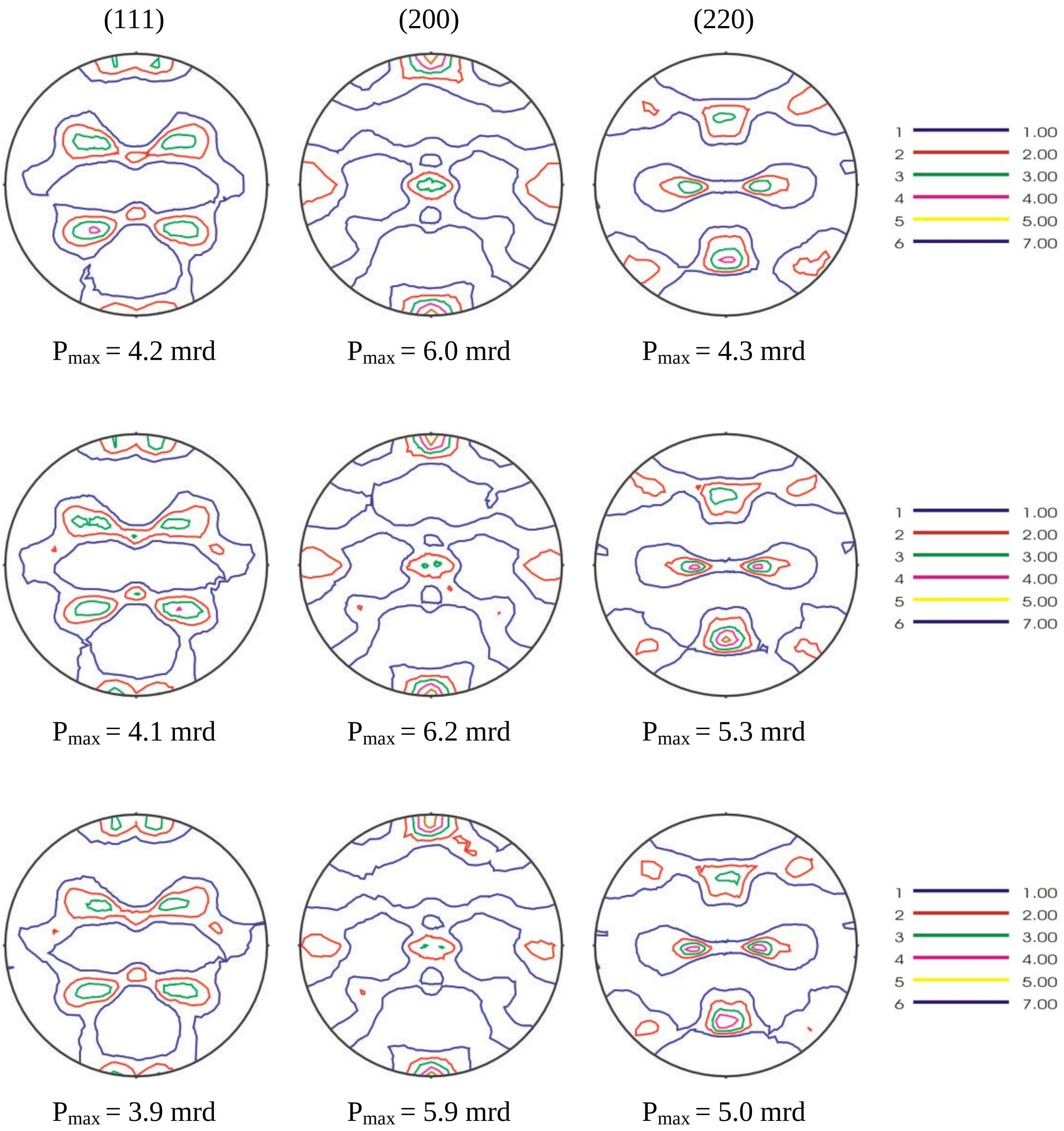

Figure 4.11 (111), (200) and (220) pole figures of the cubes cut from copper ring in top (0°-maximum wall thickness), middle (90°-middle wall thickness) and bottom (180°-minimum wall thickness) figures.

4.2.2 Quantitative texture variation around the circumference

The orientation distribution functions for the ring sample were calculated by the iterative series expansion method using three pole figures (111), (200) and (220). Degree of series expansion was Lmax=23. Due to the fact of lower sample symmetry the ODF-calculation was done with triclinic sample symmetry. In the sections φ_2=0° and φ_2=45° most of the texture components are visible, see figures 4.12 and 4.13 (the ODF sections at the different wall thickness around the Cu-tube circumference are presented in appendix 2).

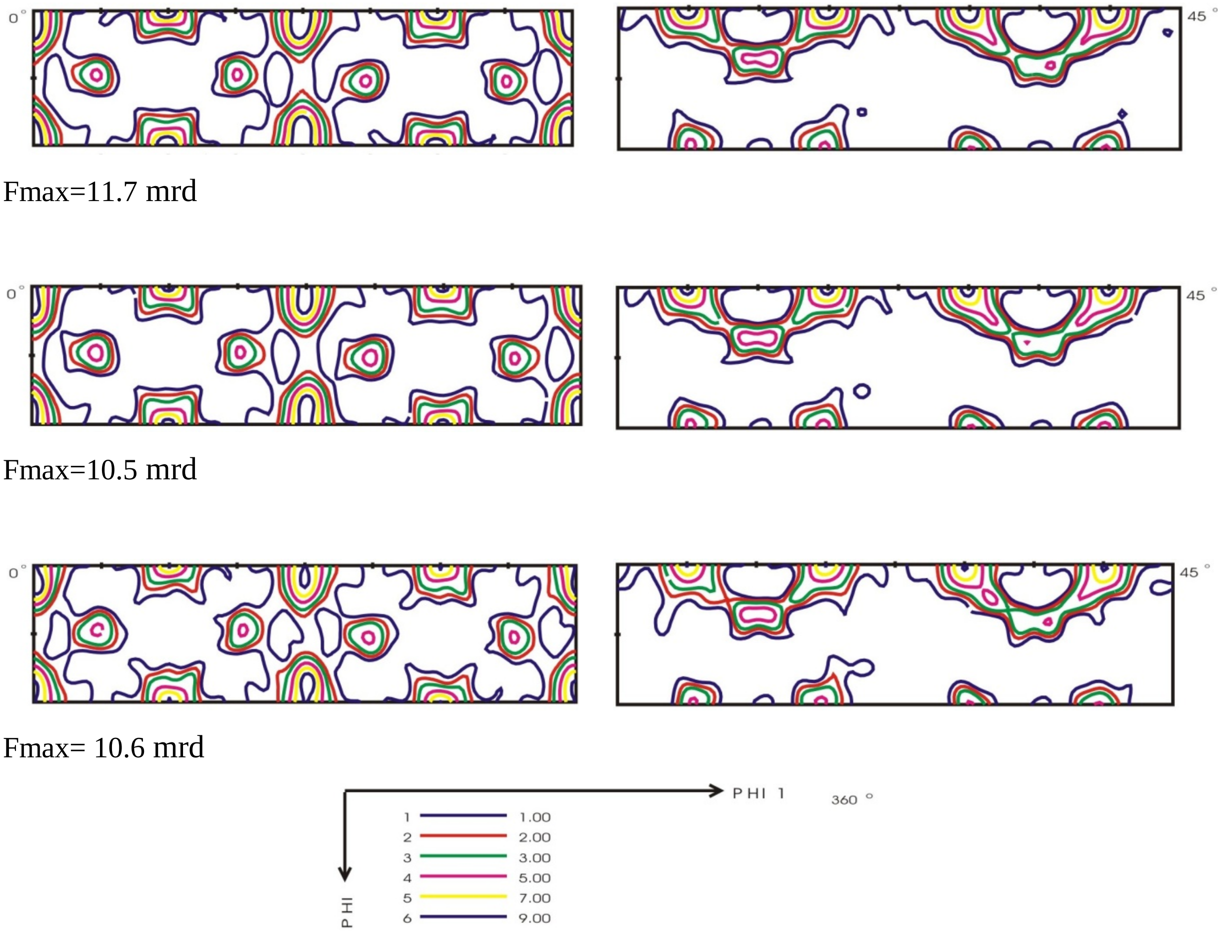

Fmax=11.7 mrd

Fmax=10.5 mrd

Fmax= 10.6 mrd

Figure 4.12 ODF of the copper ring after volume and absorption corrections in the top (0°-maximum wall thickness), middle (90°-middle wall thickness) and bottom (180°- minimum wall thickness) figures.

Firstly one can see a good agreement between the corrected non-destructive investigations and the cube sample measurements. Secondly the weakening of the orthorhombic symmetry is not very strong.

To explain the texture information, ideal texture components and texture fibers in the orientation space are presented in figure 2.10. The texture is characterized by 6 components namely the cube {001}<100>, rotated cube C_{RD} {013}<100>, Goss{110}<001>, copper {112}<111>, brass {110}<112>, and S {123}<643> as described by Lücke [99].

The copper, brass and S components also known as *β*-fibre are related to the deformation process of the tube formation [74-76], while cube, rot C_{RD} and Goss components are recrystallization based texture components [96-99]. Rot C_{RD} was described as recrystallization twins. This has been observed in Cu during static and dynamic recrystallization. Their formation is explained by chains of recrystallization twins up to 4th and higher generations [99]. The process may stop when recrystallization twins reach a specific preferred orientation and sometimes the twin texture component (rot C_{RD}) is much stronger than the cube components [101].

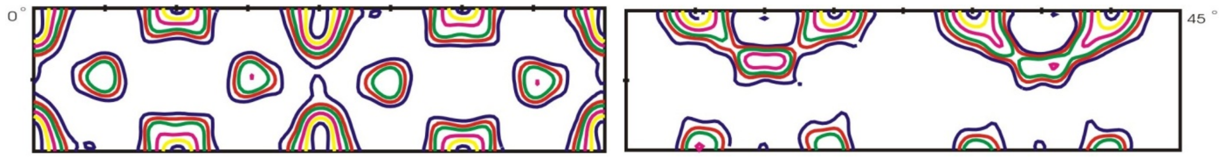

Fmax= 10.6 mrd

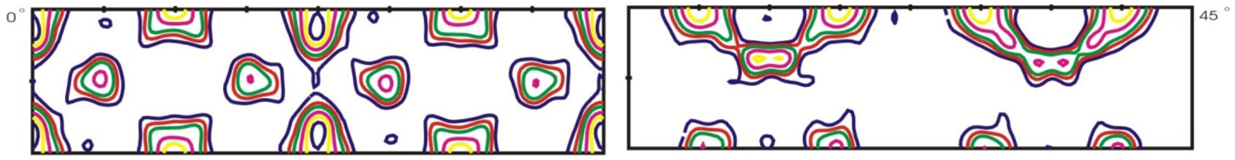

Fmax= 10.5 mrd

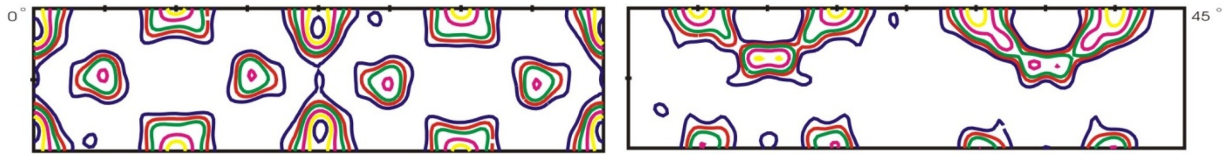

Fmax= 10.5 mrd

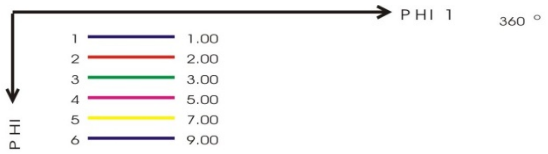

Figure 4.13 ODF of the cubes cut from the copper ring in the top (0°-maximum wall thickness), middle (90°-middle wall thickness) and bottom (180°- minimum wall thickness) figures.

Looking only on the cube component (φ_2 = 45°) (see figure 4.12 and 4.13) no variation between φ_1=45°, φ_1=135°, φ_1=225°, φ_1=315° is visible, which means that grains with cube component follow the orthorhombic sample symmetry. While the copper component shows the expected monoclinic sample symmetry from tube processing [128].

Of basic interest is the relation between texture variation around the circumference and the tube ovality and eccentricity. In figure 4.14 the variation of the strength of cube and copper component are shown. One can see that for the Cu component no variation exists while the cube component shows a slight variation with highest strength at maximum thickness [128].

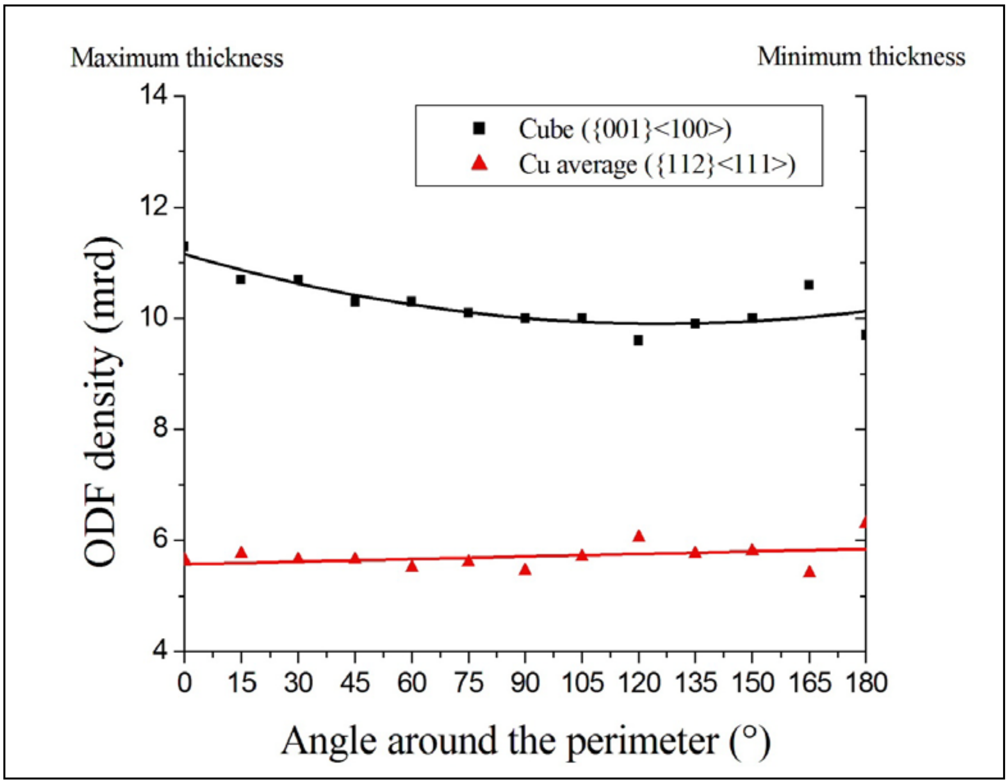

Figure 4.14 Orientation densities of Cube and copper average texture components along the circumference of the copper ring

4.3 Texture of tube segment

Incomplete pole figures for the large tube segment of 250 mm length (12 kg weight) have been measured using the robot. Figure 4.15 shows the (111), (200) and (220) pole figures for the centre of the wall at 90° (middle wall thickness).

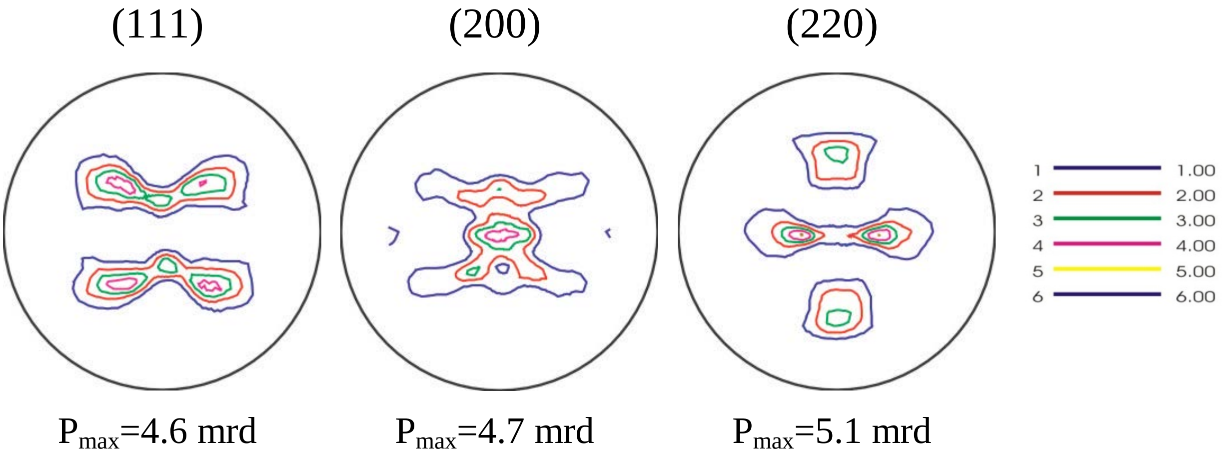
(111) (200) (220)

P_{max}=4.6 mrd P_{max}=4.7 mrd P_{max}=5.1 mrd

Figure 4.15 Experimental incomplete (111), (200) and (220) pole figures for the centre of the wall at 90° (middle wall thickness).

Incomplete pole figures were measured because of high absorption when the beam reached its longest path in the tube. Some important texture information at the outer part of the pole figures is missing, as is often the case for standard texture analysis using laboratory X-ray equipment. The ODF was calculated by the iterative series expansion method using the incomplete (111), (200) and (220) pole figures. The degree of series expansion was Lmax=23. The sample symmetry of the ODF-calculation was triclinic [128]. Recalculation of complete pole figures from the ODF has been performed as shown in figure 4.16.

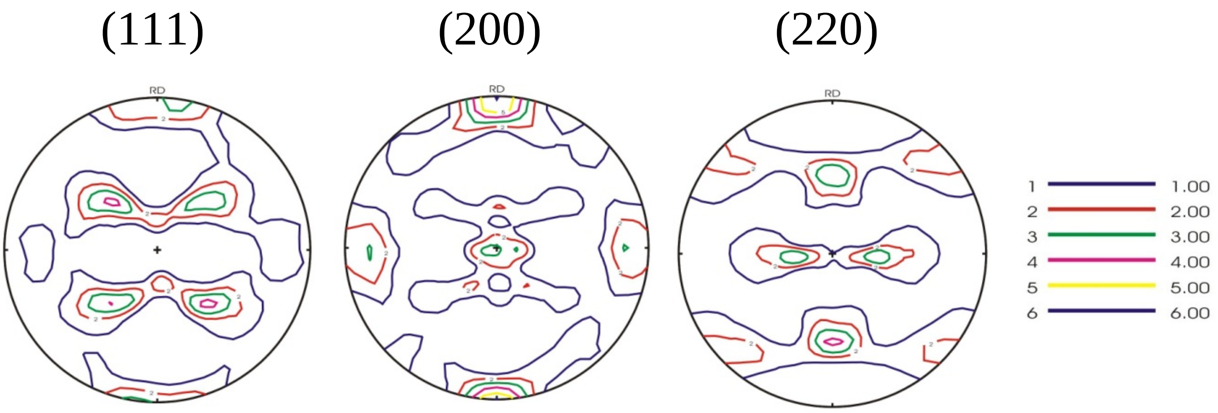

P_{max}=4.3 mrd P_{max}=6.1 mrd P_{max}=4.4 mrd

Figure 4.16 Recalculated (111), (200) and (220) pole figures for the centre of the wall at 90° (middle wall thickness).

In general, as was proposed by Linssen, Mengelberg and Stüwe the sample symmetry no longer has orthorhombic symmetry after tube processing. According to the geometry of the tube manufacturing process, one can only expect one mirror plane, which is defined by the tube axis and the radius. Together with centrosymmetry this lead to monoclinic sample symmetry 2/m [143].

Figure 4.17 shows the ODF sections of the copper tube segments from the center of the wall thickness at 90°. The texture of the Copper tube segment is characterized by the following texture components Cube {001}<100>, C_{RD} {013}<100>, Goss{110}<001>, Copper {112}<111>, Brass {110}<112>, and S {123}<643>. Copper-, Brass- and S-components represent the β-fiber. A β-fibre is present which runs from copper component (φ_2=45°) over the S component to the brass component (φ_2=90°).

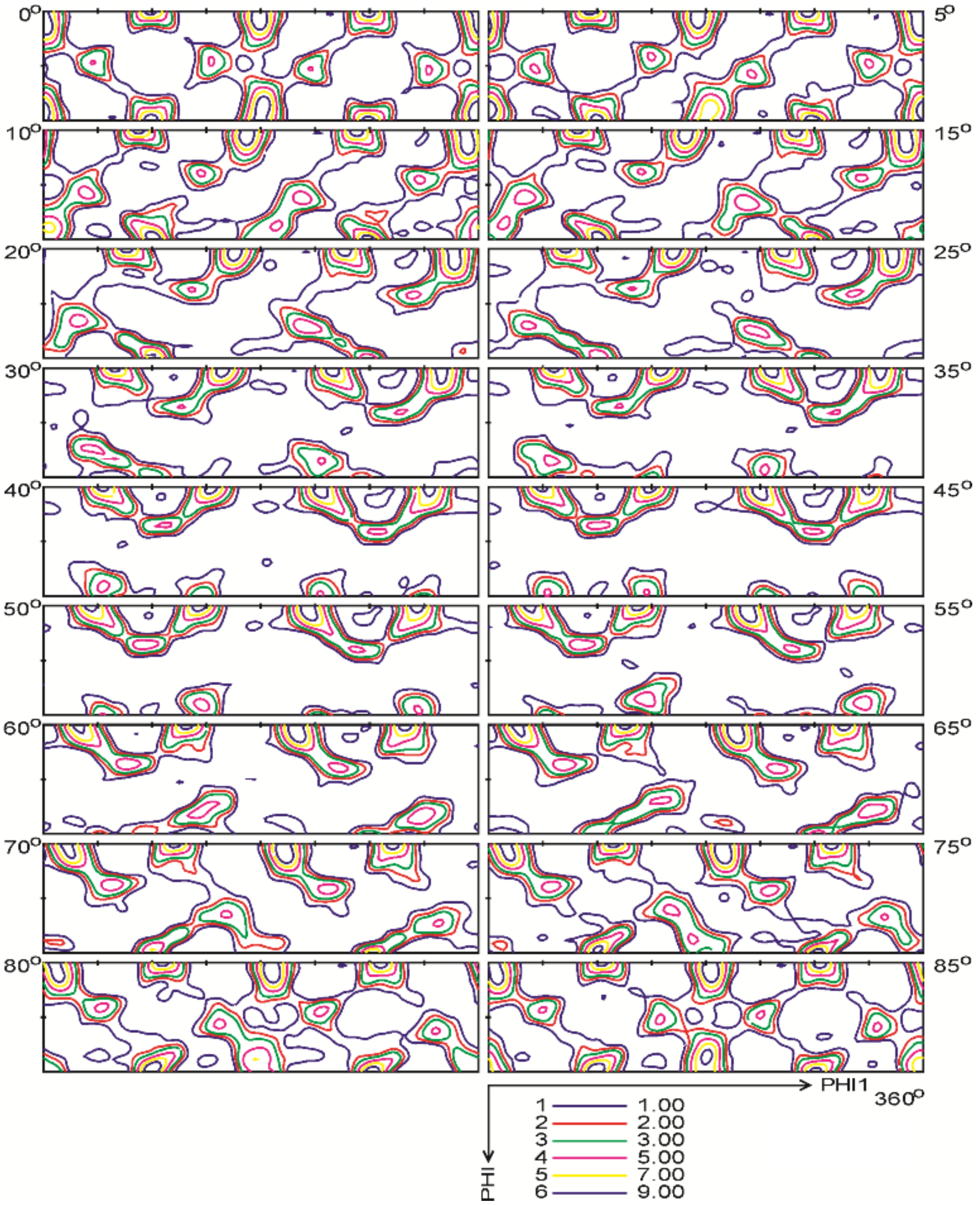

Figure 4.17 ODF for the center of the wall at 90° (middle wall thickness) calculated from the incomplete (111), (200) and (220) pole figures with Lmax 23 and triclinic sample symmetry.

In the case of cold rolled fcc materials with high stacking fault energy (γ_{SFE}) like pure copper and Cu alloys with only low levels of alloying elements the typical texture component is the copper type texture {112}<111> [74-76]. Moreover, preferred orientations along the β-fibre describe the deformation texture. The recrystallization texture of pure copper is mainly composed of the cube orientation [96-99]. The microstructure and crystallographic texture of the copper tube are typical of hot deformation and indicates that some recrystallization occurred during and after extrusion.

4.4 Texture variation through the wall thickness

For the texture variation through the wall thickness of the DHP-Cu tube, the pole figures have been measured by using a hard X-ray beam (synchrotron). Figure 4.18 shows the (111), (200) and (220) pole figures for the first position (Z1: inside diameter) through the wall thickness of the copper tube at three different positions around the circumference (minimum, middle and maximum wall thicknesses).

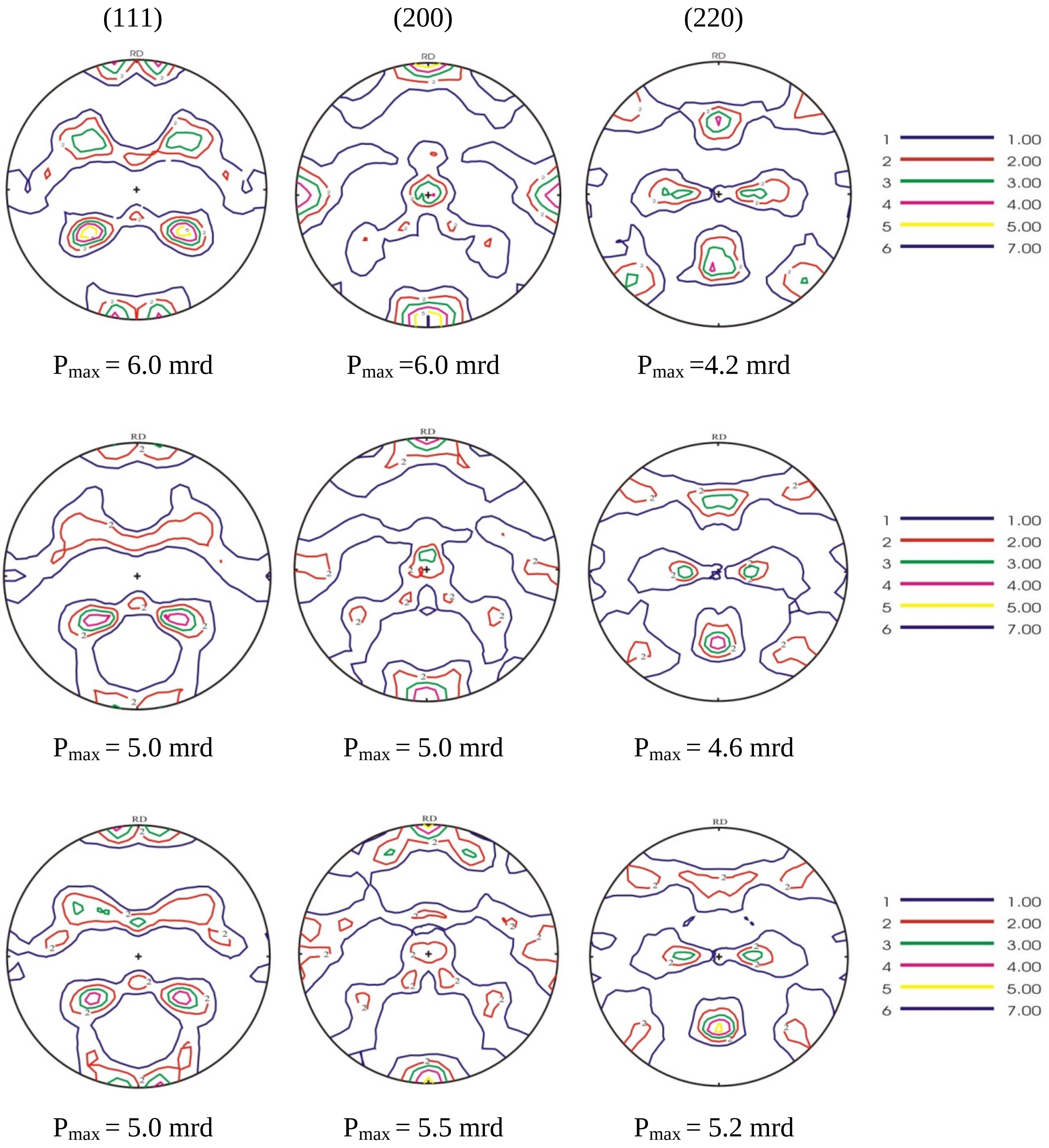

Figure 4.18 (111), (200) and (220) pole figures of the cubes cut from copper ring in the top (0°-maximum wall thickness), middle (90°-middle wall thickness) and bottom (180°- minimum wall thickness) figures for the first position (Z1: inside diameter) through the wall thickness.

In general, it was proposed by Linssen, Mengelberg and Stüwe that the sample symmetry of seamless tubes is no longer orthorhombic. According to the geometry of the manufacturing process one can only expect one mirror plane, which is defined by the tube axis and the radius. Together with centrosymmetry this lead to monoclinic sample symmetry 2/m [143]. Also this symmetry must be assumed for samples taken asymmetrically out of a sheet (texture variation through thickness) [37]. Appendix 3 shows the (111), (200) and (220) pole figures through the thickness for the maximum, middle and minimum wall thicknesses.

The orientation distribution functions for the ring sample were calculated by the iterative series expansion method using three pole figures (111), (200) and (220). The degree of series expansion was Lmax=23. Due to the fact of lower sample symmetry the ODF-calculation was done with triclinic sample symmetry.

In the sections φ_2= 0° and φ_2= 45° most of the texture components are visible, (see figure 4.19) one can see that the weakening of the orthorhombic symmetry is not very strong. To explain the texture information, ideal texture components and texture fibers in orientation space are presented in figure 2.10.

The texture is characterized by 6 components namely the cube {001}<100>, rotated cube C_{RD} {013}<100>, Goss{110}<001>, copper {112}<111>, brass {110}<112>, and S {123}<643> as described by Lücke [99]. Copper, brass and S component, also known as β-fibre are related to the deformation process of the tube formation [74-76], while cube, rot C_{RD} and Goss [96-99] are recrystallization based texture components. Rot C_{RD} was described as recrystallization twins and has been observed in Cu during static and dynamic recrystallization. Its formation is explained by chains of recrystallization twins up to 4th and higher generations [99]. The process may stop when recrystallization twins reach a specific preferred orientation and sometimes the twin texture component (rot C_{RD}) is much stronger than the cube components [99].

Looking only at the cube {001}<100> component (φ_2 = 45°) no variation between φ_1=45°, φ_1=135°, φ_1=225°, φ_1=315° is visible, this means that grains with a cube {001}<100> component follow the orthorhombic sample symmetry. While the Cu {112}<111> component (φ_2 = 45°) shows the expected monoclinic sample symmetry between Cu I at φ_1=90°, Cu II at φ_1=270° from tube processing as shown in figure 4.19.

Z1- Minimum wall thickness

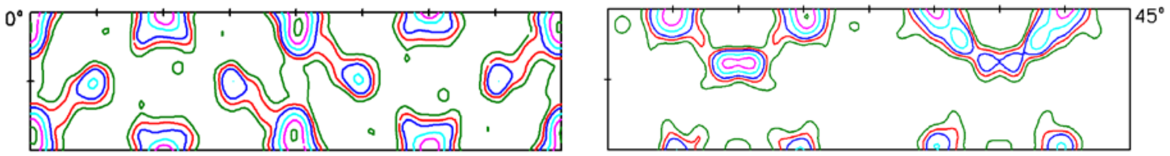

F_{max} = 9.81 mrd

Z1- Middle wall thickness

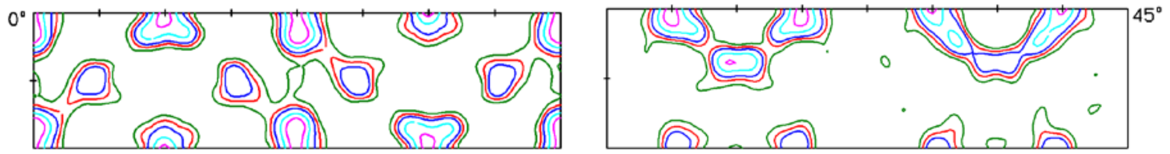

F_{max} = 9.16 mrd

Z1- Maximum wall thickness

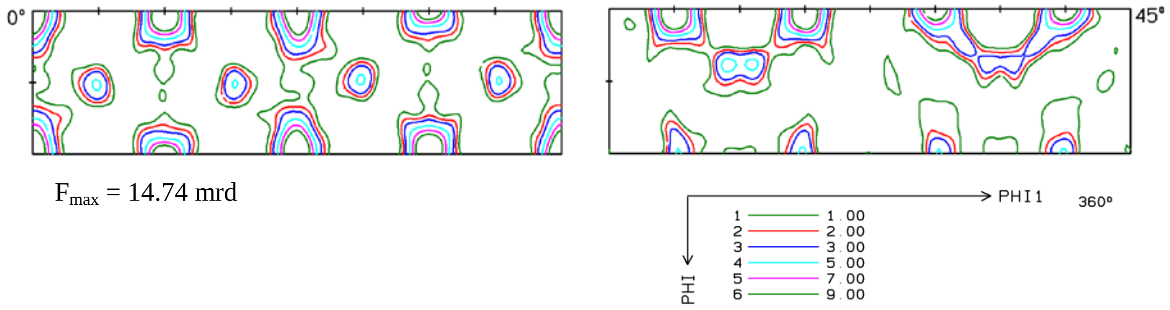

F_{max} = 14.74 mrd

Figure 4.19: ODF for the first layer (Z1) through the wall thickness of the copper tube in three different positions (minimum, middle and maximum thicknesses) sections (φ_2=0° and φ_2=45°)

As shown in figure 4.20 the cube {001}<100> component has a remarkable variation of the orientation density through the thickness with higher texture sharpness near the outside radius in the different wall thicknesses (maximum, middle and minimum). The average copper {112}<111> component is nearly constant. This copper tube can be described as hot deformed, i.e. recrystallization occurs during and after extrusion. The texture strength of the average copper components varies between 3.9 mrd and 6.4 mrd (mrd – multiples of random distribution). The stronger cube component varies between 6.3 mrd and 21.1 mrd.

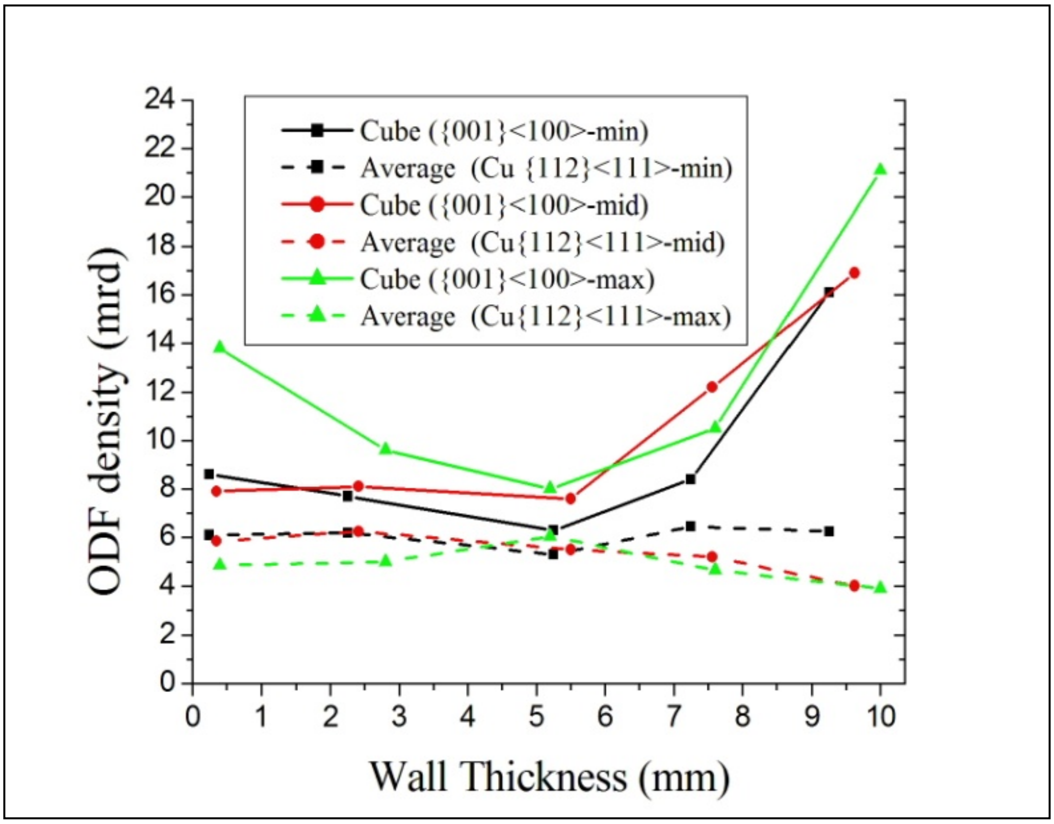

Figure 4.20: Cube and average copper components starting from inside diameter for the minimum, middle and maximum thickness

The global texture variation around the Circumference can be calculated by two methods. First, the average of the through thickness texture gradient for different positions (minimum, middle and maximum wall thicknesses) can be calculated as shown in figure 4.21. Second, the global texture can be measured by neutron diffraction using a large enough beam cross section that average texture information from the whole test sample is obtained (see figure 4.11).

A comparison of the pole figure and the orientation distribution functions between the two methods has been made. Qualitatively both pole figures calculated from synchrotron radiation and pole figures measured by neutron diffraction have similar components as shown in figures 4.17 and 4.6 and the sample symmetry of both pole figures are no longer orthorhombic. According to the geometry of the manufacturing process one can only expect one mirror plane, which is defined by the tube axis and the radius. Together with centrosymmetry this lead to a monoclinic sample symmetry 2/m [143]. Quantitatively there are small differences between the sharpness of the pole figures. The pole figures measured by synchrotron radiation have a higher intensity. This is due to the fact that the neutrons measures the whole sample (average the information over the whole thickness) while the pole figures of the synchrotron radiation are the average of only 5 through thickness pole figures.

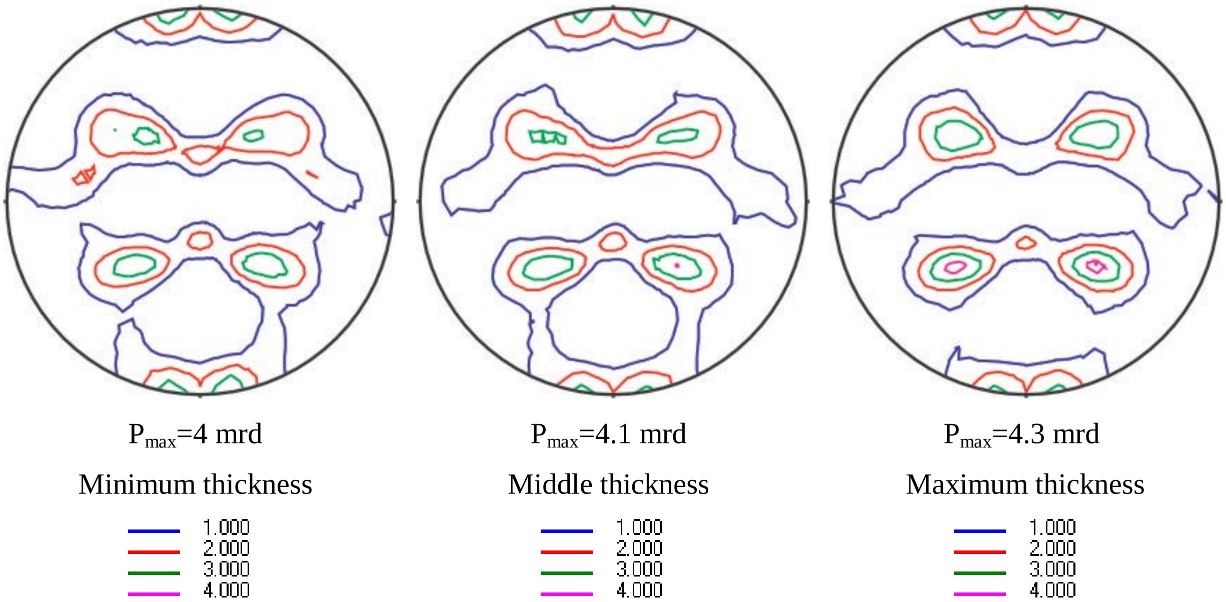

P_{max}=4 mrd
Minimum thickness

P_{max}=4.1 mrd
Middle thickness

P_{max}=4.3 mrd
Maximum thickness

Figure 4.21: Average of (111) pole figures for different wall thickness (minimum, middle and maximum thickness) measured by synchrotron diffraction for copper tube

The orientation distribution functions for the global texture of the ring sample were calculated by the iterative series expansion method using three pole figures (111), (200) and (220). The degree of series expansion was Lmax=23. Due to the fact of lower sample symmetry the ODF-calculation was done with triclinic sample symmetry.

For both methods, the global texture is characterized by 6 components namely the cube {001}<100>, rotated cube C_{RD} {013}<100>, Goss{110}<001>, copper {112}<111>, brass {110}<112>, and S {123}<643> .

For the ODFs calculations, qualitatively results obtained from both the synchrotron radiation measurements and the neutron measurements have the same texture components shown in figures 4.22 and 4.23. Quantitatively tables 4.2 and 4.3 show the differences between the components obtained from synchrotron radiation measurements and from neutron measurements. This indicates that the cube texture is overestimated when determined from the average of five layers.

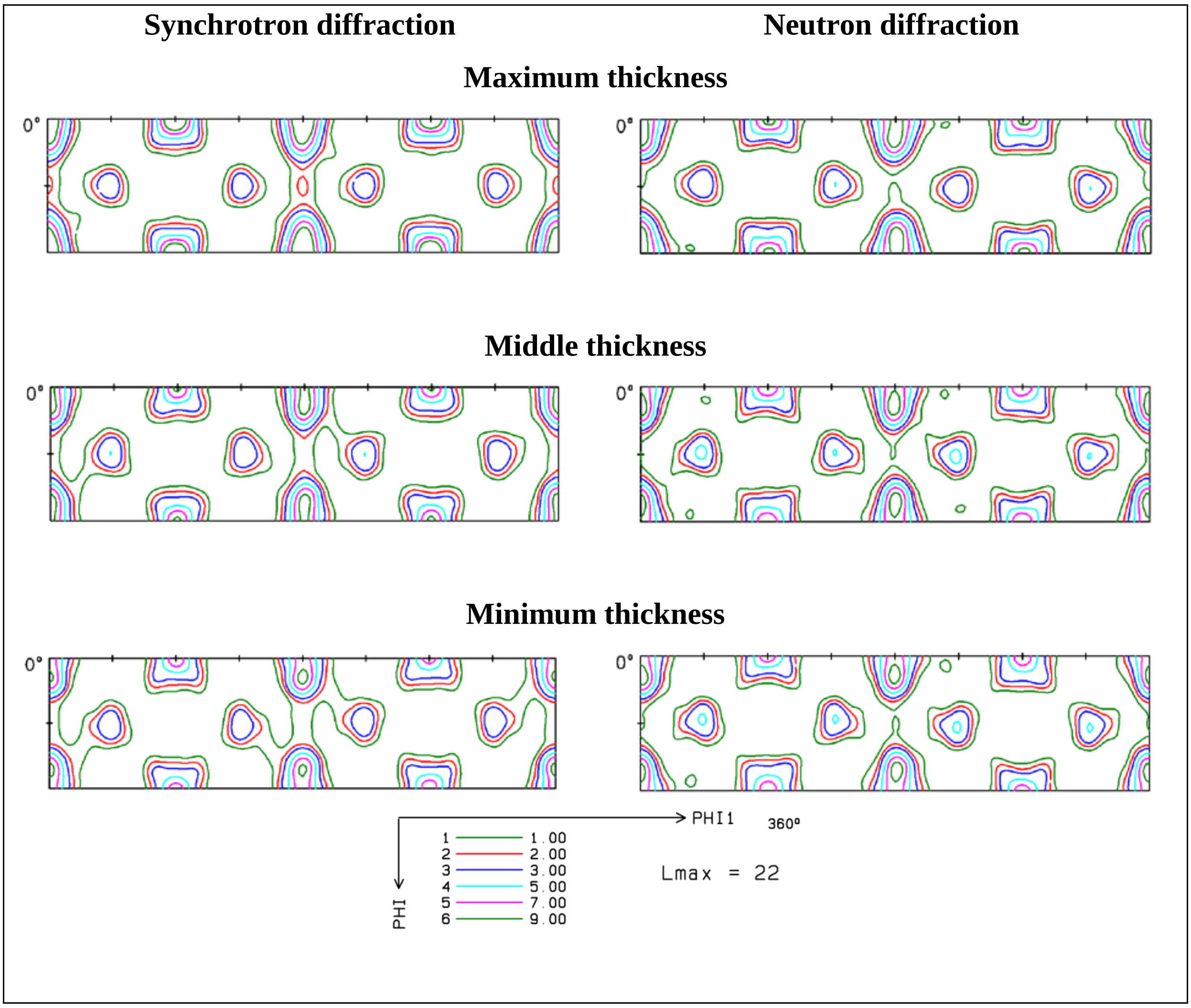

Synchrotron diffraction **Neutron diffraction**

Maximum thickness

Middle thickness

Minimum thickness

Figure 4.22: ODF's of the copper tube from different wall thicknesses with triclinic sample symmetry and Lmax= 22, section (φ_2=0°) measured from average pole figures obtained by synchrotron radiation and from global pole figures obtained by neutron diffraction.

Of basic interest is the relationship between textural variation around the circumference and the extent of tubes ovality and eccentricity. The variation of textural component strengths are given in tables 4.2 and 4.3. One can see that the {001}<100> cube component shows a variation with the highest strength at maximum wall thickness, independent of measuring technique (x-rays or neutrons), and that the {112}<111> Cu component has a slight variation with highest strength at minimum thickness. These variations (also differences in the texture sharpness) can be seen for both methods used to determine the global texture. As mentioned earlier, this is due to the fact that the neutrons measure the whole sample (and average the information over the whole thickness) while the pole figures from the synchrotron radiation scattering are the average of only 5 through-thickness pole figures.

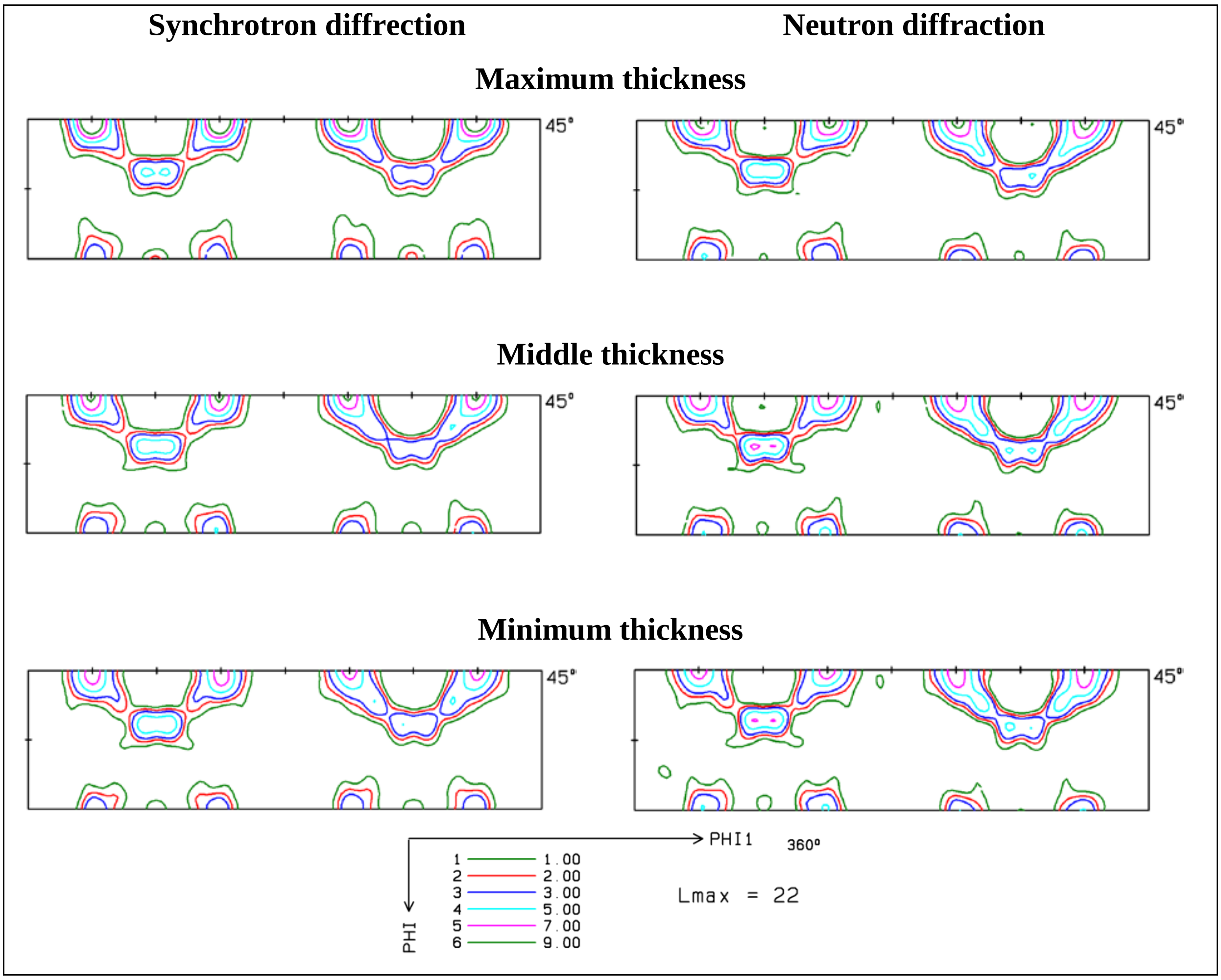

Figure 4.23: ODF's of the copper tube from different wall thicknesses with triclinic sample symmetry and Lmax =22, section (φ_2=45°) measured from average pole figures obtained by synchrotron radiation and from global pole figures obtained by neutron diffraction.

Table 4.2: Global texture components for different positions around a copper ring calculated by the average through thickness texture components, all units in (mrd)

Name	Cube	Rot C_{RD}	Cu I	Cu II	Cu average
{hkl}<uvw>	**{001}<100>**	**{013}<100>**	**{112}<111>**	**{112}<111>**	
(φ_1,Φ,φ_2)	**(0,0,0)**	**(0,15,0)**	**(90,35,45)**	**(270,35,45)**	
Max thickness	**12.7**	**11.6**	**5.4**	**4.1**	**4.75**
Mid thickness	**9.8**	**10.6**	**6.5**	**4.6**	**5.55**
Min thickness	**8.4**	**9.7**	**7.3**	**5**	**6.15**

Table 4.3: Global texture for different positions around a copper ring measured with neutrons, all units in (mrd).

Name	**Cube**	**Rot C_{RD}**	**Cu I**	**Cu II**	**Cu average**
{hkl}<uvw>	**{001}<100>**	**{013}<100>**	**{112}<111>**	**{112}<111>**	
(φ_1,Φ,φ_2)	**(0,0,0)**	**(0,15,0)**	**(90,35,45)**	**(270,35,45)**	
Max thickness	**9.7**	**11.2**	**6.1**	**5.2**	**5.65**
Mid thickness	**8.8**	**11.3**	**6.4**	**5.1**	**5.75**
Min thickness	**8.4**	**11**	**6.5**	**5.3**	**5.9**

4.5 Texture variation through the wall thickness measured by EBSD

The quality of EBSD measurement can be judged by the so-called “confidence Index” (CI), this is a measure of the unambiguity of indexing the Kikuchi band. The Confidence Index (CI) varies from 0 to 1, the larger the number the better the quality of the EBSD map [64]. The confidence index CI values for the 9 maps measured along the minimum wall thickness are presented in table 4.4.

Table 4.4: map number and positions through the wall thickness and its confidence indexes.

Map number	**Wall thickness (mm)**	**CI**
1	0.98	0.69
2	2.03	0.72
3	3.024	0.81
4	4.024	0.76
5	5.024	0.79
6	6.024	0.5
7	7.024	0.59
8	8.024	0.45
9	9.024	0.39

An EBSD map of the first position is shown in figure 4.24. Each color has its own crystallographic plane in the direction perpendicular to the map plane (radial-hoop plane) which it is the extrusion direction in this sample for example the red color grains have the {001} and the extrusion direction. The other maps are shown in Appendix (4).

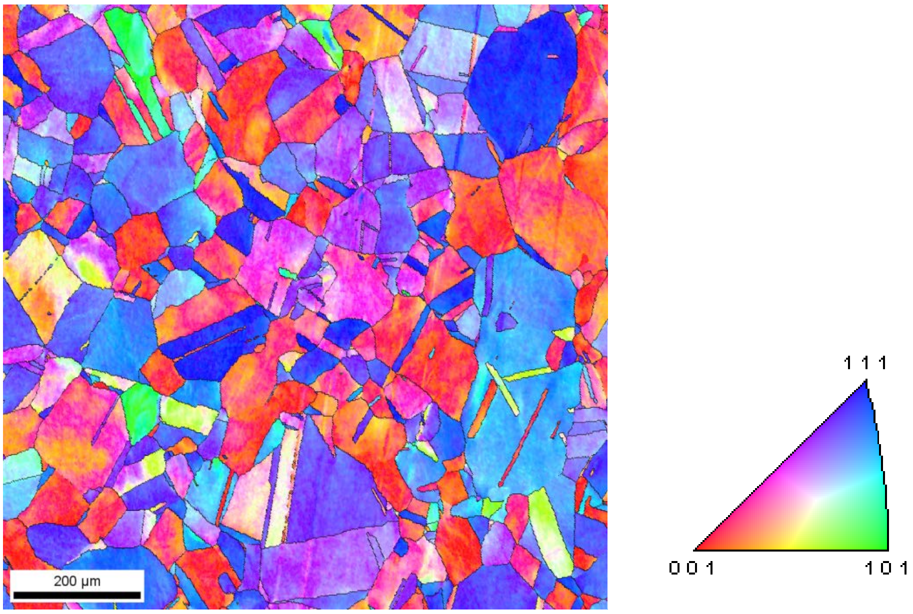

Figure 4.24: EBSD map number 1at 0.98 mm from the outer surface

During the map construction by the SEM scan the orientation of every measurement point was recorded. The MTEX [144, 145] software package was used to construct the data from the EBSD map in Eulerian space. The orientation distribution function of the EBSD map number 1 is presented in figure 4.25 using triclinic sample symmetry. Section φ_2=0° and φ_2=45° was selected to present the ODFs of every EBSD map because most of the texture components are visible. The cube {001}<100> component (φ_2 = 45°) has a visible variation between φ_1=45°, φ_1=135°, φ_1=225°, φ_1=315°. This means grains with {001}<100> cube component no longer have an orthorhombic sample symmetry which is not the case for the neutron and synchrotron measurements. The Cu {112}<111> component (φ_2 = 45°) shows the expected monoclinic sample symmetry between Cu I at φ_1=90°, Cu II at φ_1=270° from tube processing as shown in figures 4.25 and Appendix (4). The Brass component also shows no more orthorhombic sample symmetry as was the case for neutron and synchrotron measurements. The texture components sharpness by EBSD measurement is lower than the sharpness of the neutron and synchrotron measurements. There is an asymmetry in sharpness and position of the texture components indicated by EBSD measurements. This asymmetry is related to the bad grains statistic. The (111), (200), (220) and (311) pole figures for every EBSD map from the ODF were also calculated using MTEX. Figure 4.26 shows the calculated pole figure for the EBSD map number 1. The calculated pole figures show no monoclinic sample symmetry although monoclinic is the expected symmetry for the tube manufacturing process. The pole figures of the other maps are presented in Appendix 4. Because of the large grain size and low grain statistics the texture gradient measurement by EBSD has been not continued.

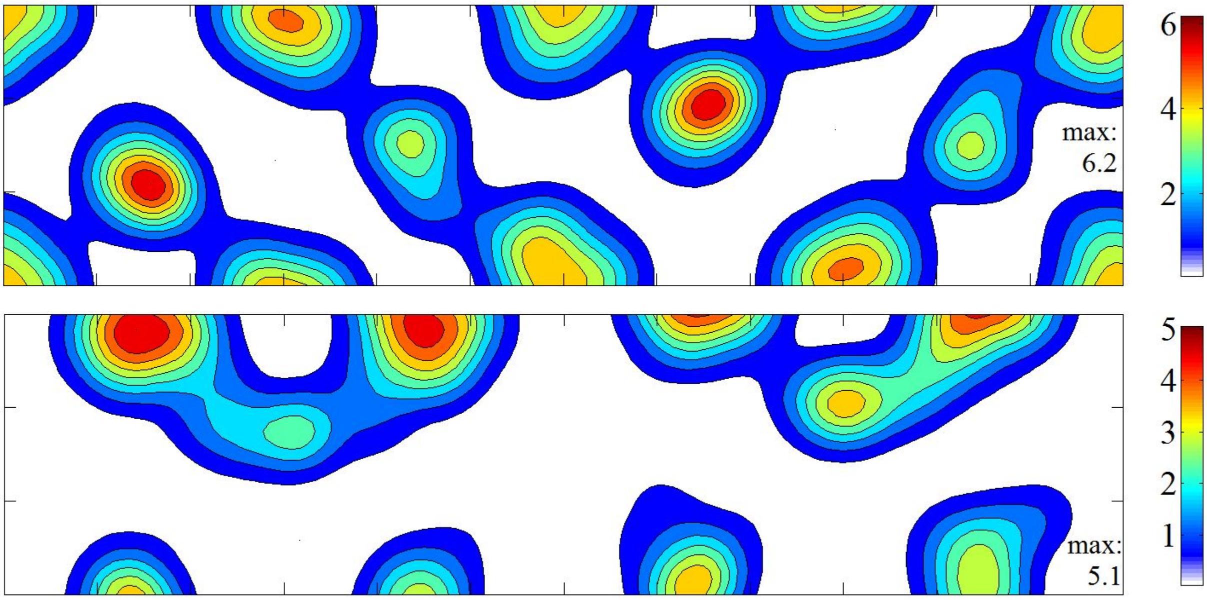

Figure 4.25: ODF of the EBSD map number 1at 0.98 mm from the outer surface using triclinic as sample symmetry (top) φ_2=0° (bottom) φ_2=45°.

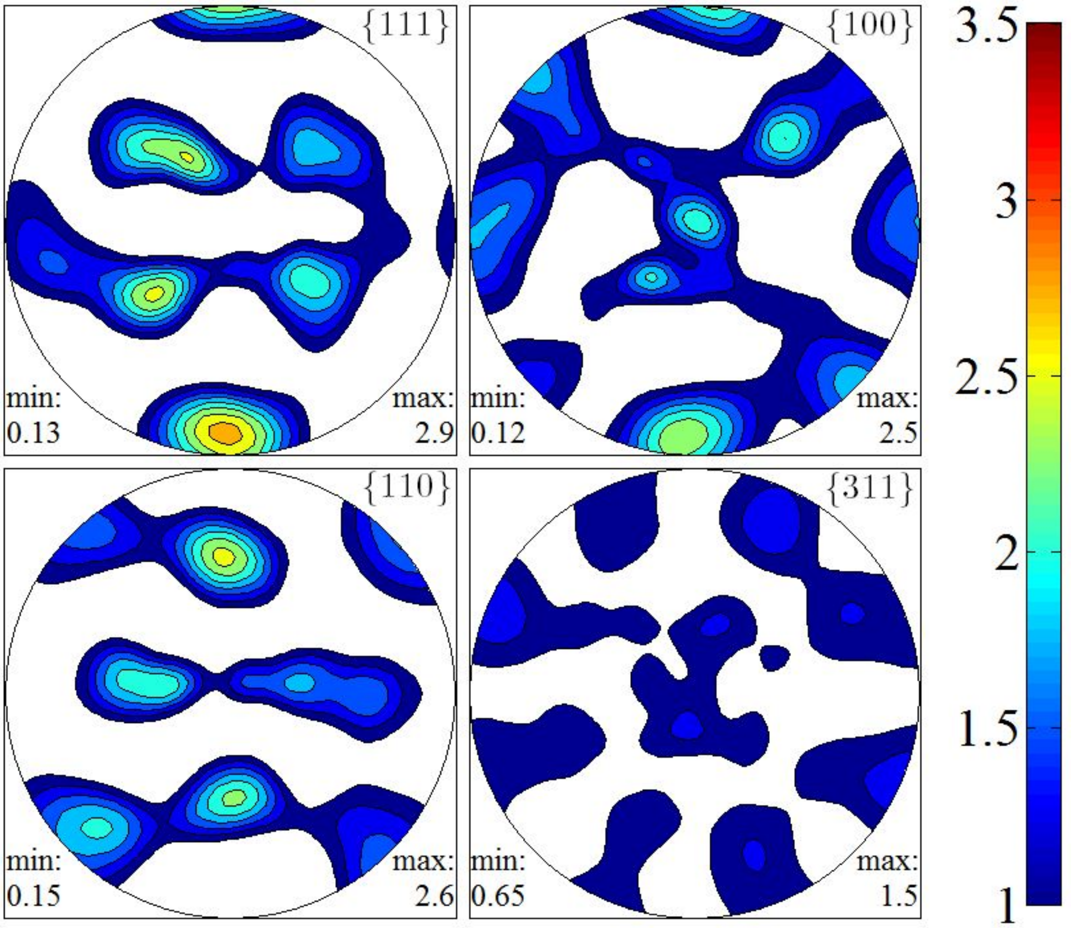

Figure 4.26: The calculated pole figures of the EBSD map number 1at 0.98 mm from the outer surface using triclinic sample symmetry.

4.6 Strain variation through the thickness and around the circumference measured by neutrons

Diffraction image has been collected for every measuring point. The diffraction patterns have been constructed and the peak positions have been extracted for every measuring point and for the stress free sample by using STeCa [129] via Gaussian fitting.
The strain values have been calculated according to equation 2.13 and the residual stresses have been calculated according to Hook's law (equation 2.16). The strains measured by the robot have been compared with the strains measured by the XYZ-stage to exam the reliability of the robot in the strains measurements.

4.6.1 Comparison between strains measurement by the robot and by the XYZ stage

It is very important to have an accurate spatial value for residual stress analyses of engineering components. To illustrate the capabilities and to check the reliability of the results from the RX160 robot for residual stress analysis, a comparison has been made between the strains measured by the robot and by the XYZ stage.

For the robot measurements, entry scans were performed to correct the surface point extracted from the 3D laser scan. In this case the sample surface is scanned in small steps of 0.5 mm cross the gauge volume. The intensity profiles from the entry scan should be then fitted and from this the position of the surface can be defined. The entry scan for the radial and hoop strain measurements have been performed as shown in figure. 4.27. The differences between the extracted points from the 3D laser scan and the entry scan are between 0.1 mm to 0.6 mm.

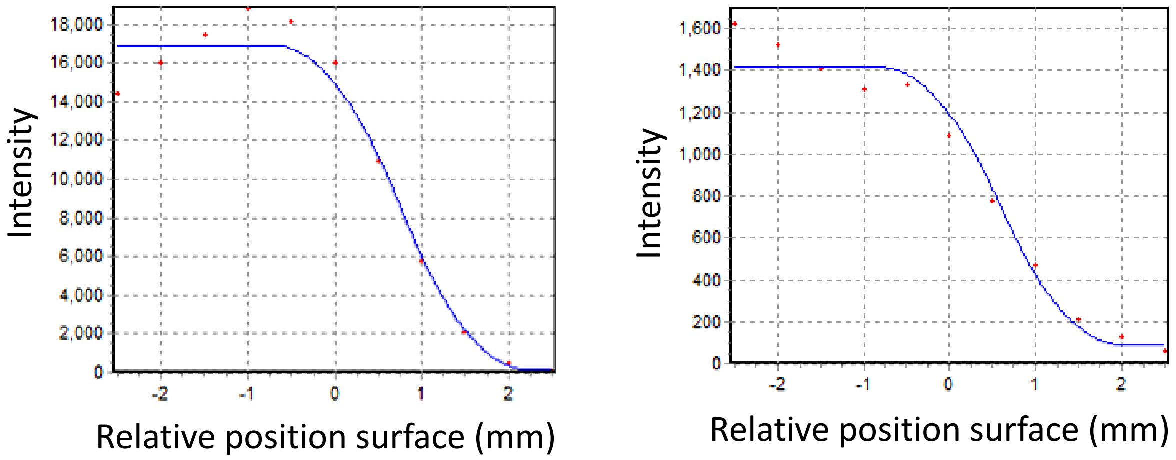

Figure 4.27 Intensity profile after entry scan using the robot system for (left) radial measurement (right) hoop measurements at 90° (middle wall thickness)

As a drawback, the spatial and value of the strain is falsified at the outer and inner surfaces for all sample positions around the circumference. When the sample gauge volume (SGV) is not fully immersed by the instrument gauge volume (IGV) and a wavelength gradient is present in the primary beam the diffraction peak can be shifted [120]. The sample positions have been corrected by calculating the center of gravity of the sample gauge volume for every surface position using equations 2-18 and 2-19 [120]. The pseudo peak shifts were corrected using a model developed by Šaroun *et. al* [146]. This model covers a broad variety of instrument arrangements including flat mosaic and bent perfect crystal monochromators, narrow slit, solar and radial collimator.

Figures 4.28 to 4.30 compare the measurements made by the robot and the XYZ table for the axial and radial strains at different wall thicknesses (maximum, middle and minimum). As expected, small differences in tube alignment can affect the results for nominally identical points. Both the axial and radial strains measured by the robot and XYZ table fit quite well. The strain measurement by the robot is reliable. The axial strain varies from tension at outer diameter to compression at the inner diameter. The radial strain varies from compression at the outer diameter to tension at the inner diameter.

Figure 4.31 compares the hoop strain at different wall thicknesses. The differences in strain values and behavior between the two instruments come from the different exposure times. The exposure time for the hoop strain using the XYZ table was 2 min which it is not long enough. This means that the robot can be used to measure the residual strain in the copper tube with reliable results.

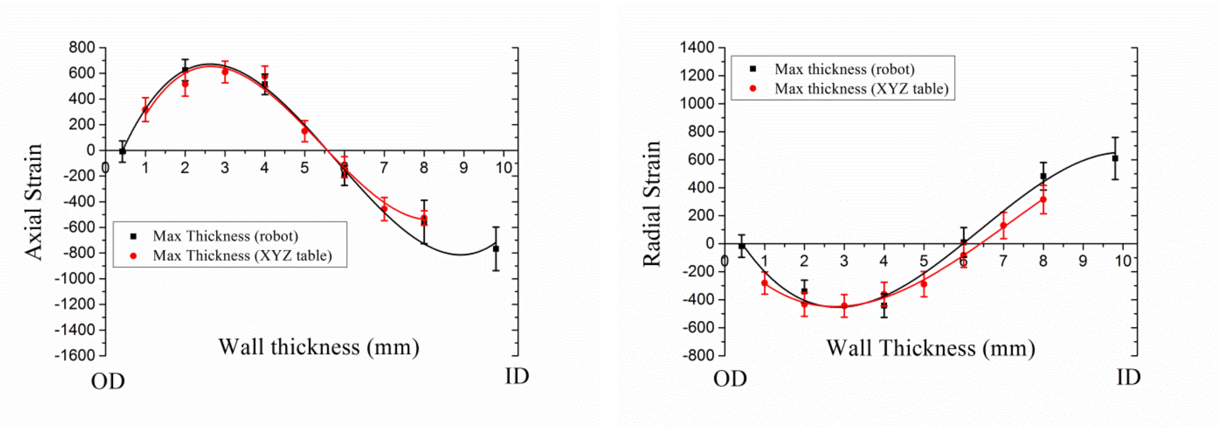

Figure 4.28 Comparision between the measurements made by the robot and the XYZ table at the maximum wall thickness for the (left) axial strain and (right) radial strain

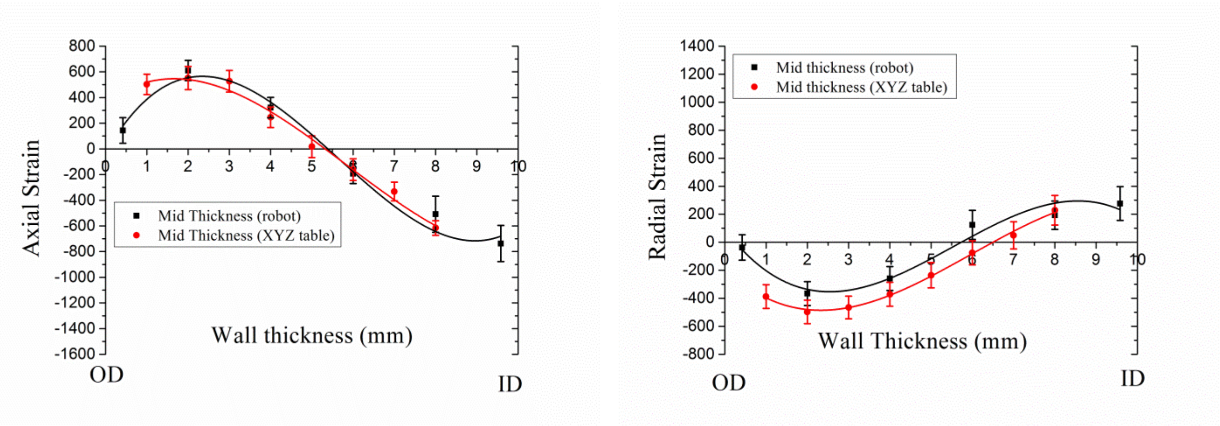

Figure 4.29 Comparision between the measurements made by the robot and the XYZ table at the middle wall thickness for the (left) axial strain and (right) radial strain

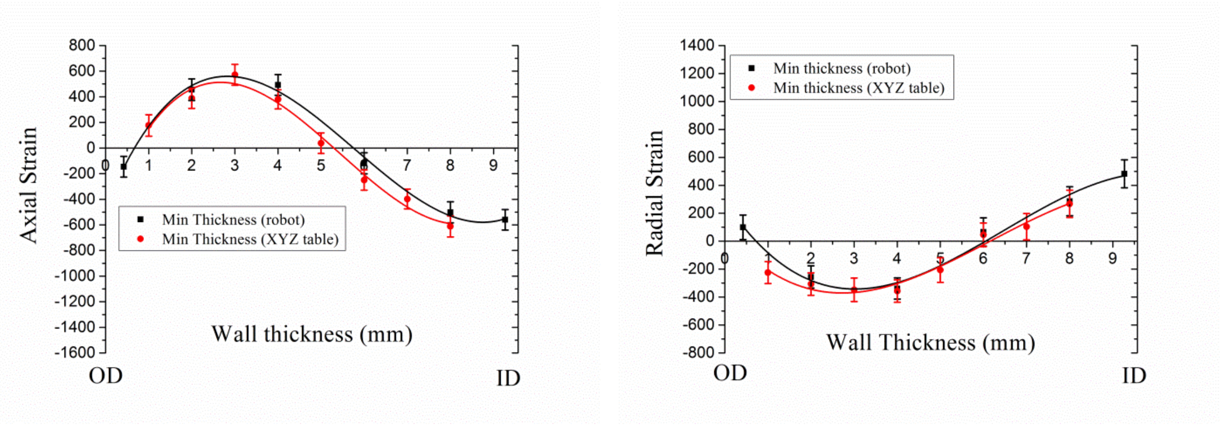

Figure 4.30 Comparision between the measurements made by the robot and the XYZ table at the minimum wall thickness for the (left) axial strain and (right) radial strain

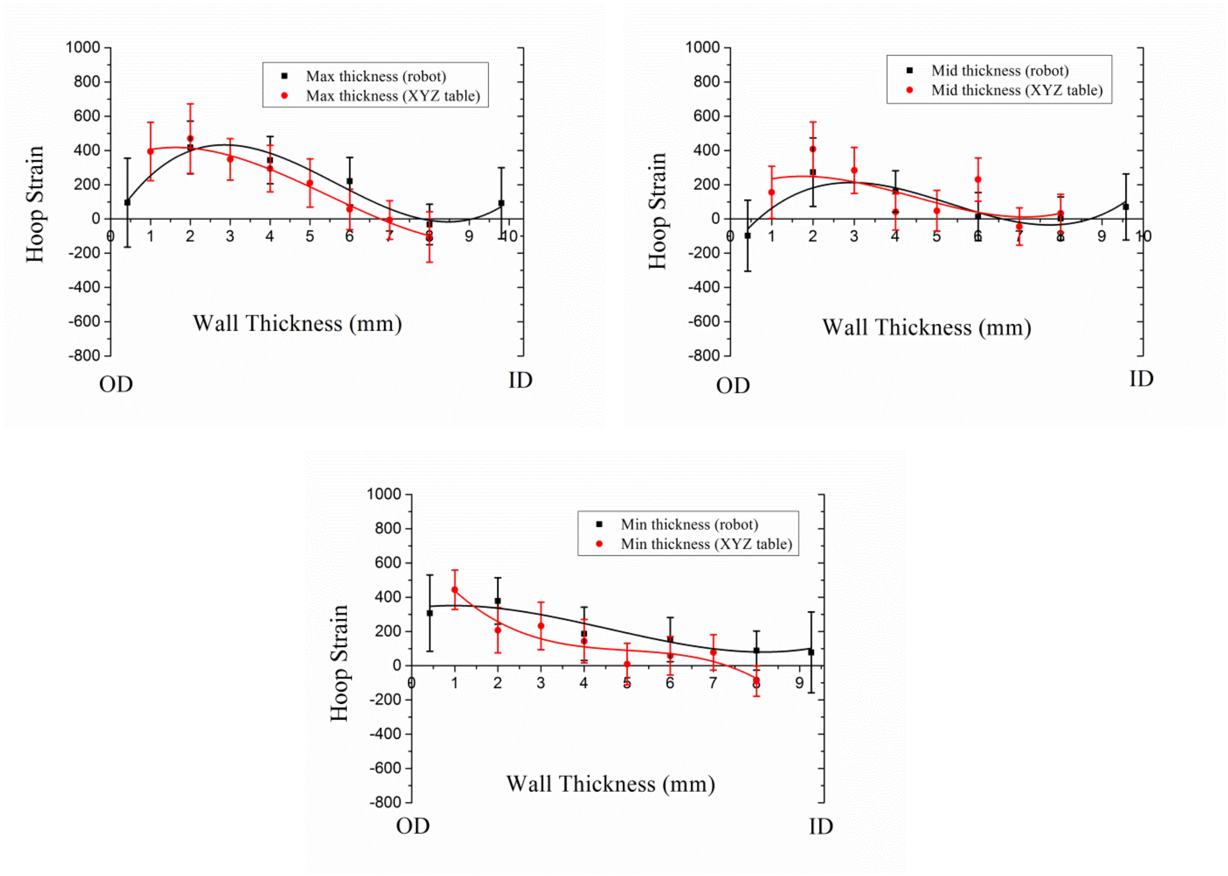

Figure 4.31 Comparision between the measurements made by the robot and the XYZ table at different wall thickness for the hoop strain

4.6.2 Residual stress variation

To understand the residual stresses of the final product, the residual stresses of the semi-finished product should also be studied. Knowledge of the spatial and directional distribution of residual stresses is very important in order to evaluate their influence on the material. During processing, the tube undergoes plastic deformation, generating residual stresses. Theses stresses remain after removal of the external load or after processing [118]

In general, tube production consists of both cross-sectional area and wall thickness reduction. This generates a complex residual stress pattern that can affect the mechanical and fatigue behavior of the final tube. The production of highly precise tubes has two main manufacturing problems, the anisotropy around the circumference and the anisotropy through the wall thickness. Eccentricity influences the circumferential material flow during the tube manufacturing processes.

In horizontal extrusion, the plug is kept in a fixed position inside the die by a rod. However, it must be noted that due to gravity and the elasticity of the supporting rod the plug can move slightly in a vertical direction.

The residual stresses have been calculated according to the equation (2-17). The Young's modulus and the Poisson's ratio for the plane Cu(311) are E_{311}=121.8897 GPa and ν_{311}=0.354. The numerical value of E_{311} and ν_{311} was calculated from the Xec program written by H. Wern [147]. The Kröner model was used to calculate E_{311} and ν_{311}.

The calculated axial residual stress profile of the copper tubes measured by the robot at the maximum, the middle and the minimum wall thickness are given in figure 4.32. The Figure shows the calculated stress profiles through the wall ('OD': outside diameter and 'ID': inner diameter). The residual axial stress shows a gradient with tensile stress at the outer surface and a compressive state at the inner surface of the tube which is in agreement with other publications [21-23, 148-150]. The residual hoop stress shows the same behaviour but with lower stress values as shown in figure 4.33. The radial stress shows quite a small stress at the different wall thicknesses as shown in figure 4.34. The experimental values show negligible difference between the maximum, the minimum and the middle wall thickness

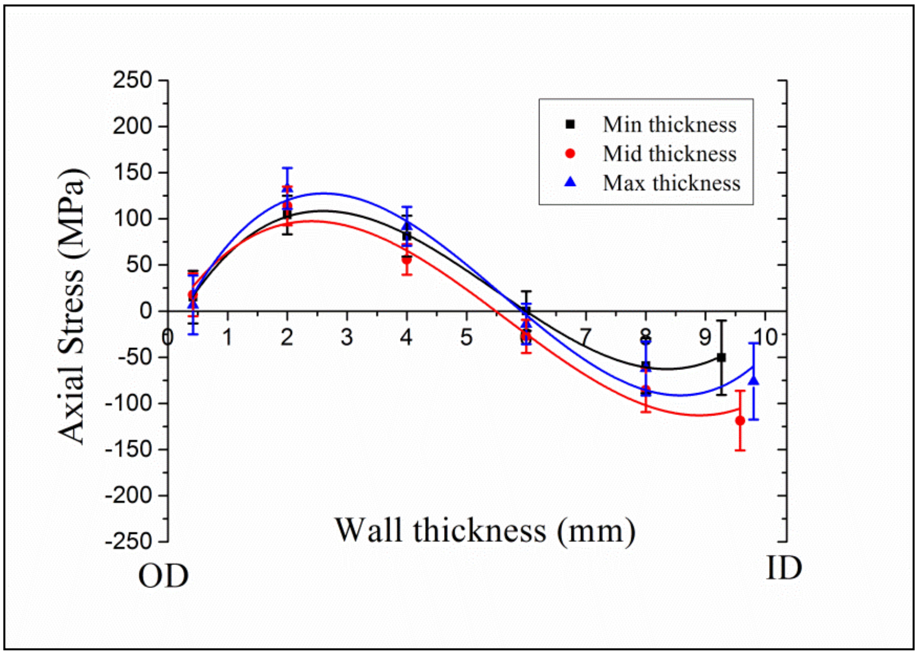

Figure 4.32 Axial residual stress for the Cu-tube at different wall thickness

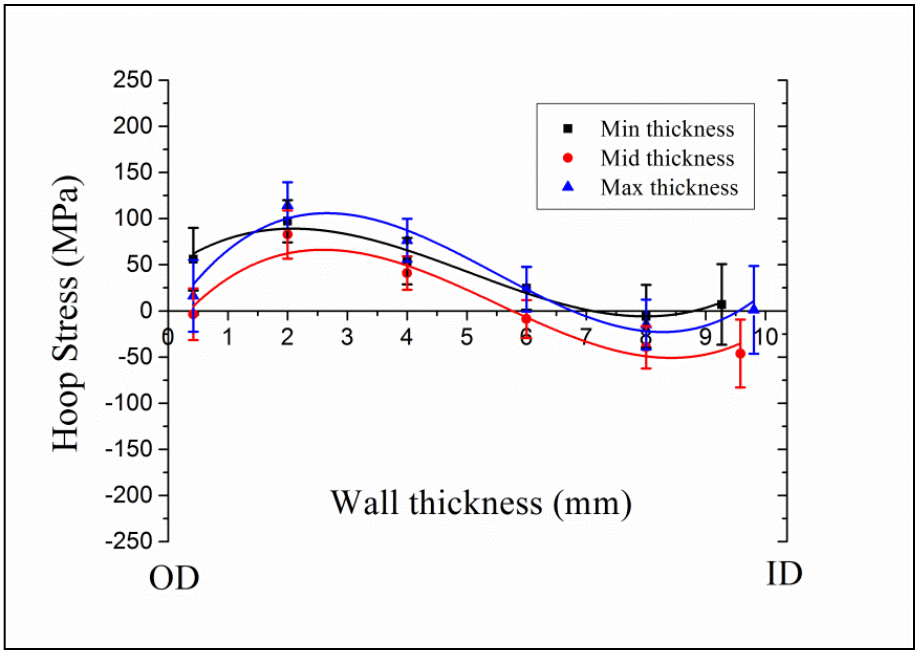

Figure 4.33 Hoop residual stress for the Cu-tube at different wall thickness

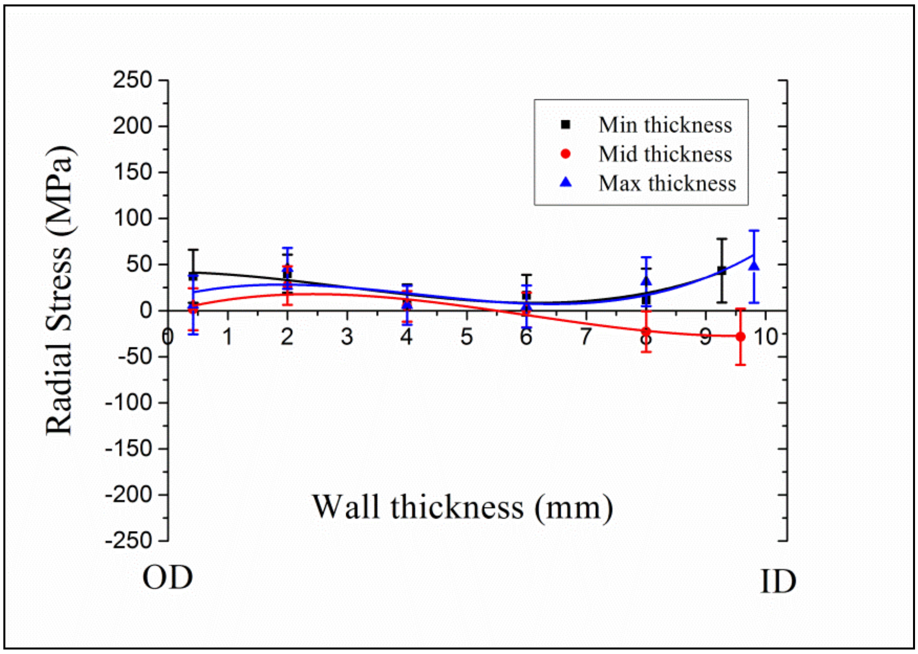

Figure 4.34 Radial residual stress for the Cu-tube at different wall thickness

The three principle residual stresses maps for the copper tube from 0° (Maximum thickness) to 180° (minimum thickness) are presented in figures (4.35 to 4.37). The axial residual stresses at the outer surface of the copper tube are tensile with the highest stress being 2 mm from the outer surfaces. This observation was the same for all positions measured around the circumference. The maximum axial residual stress (134.77 MPa) was at a 60° angular position from the position of maximum wall thickness (0°). The state of the residual axial stress changes from tensile at the outer part of the copper tube to compression at the inner part of the tube with the highest compressive stresses at the inner surface. The maximum compressive axial stress is (-203.9 MPa) was at the 30° angular position from the position of maximum wall thickness (0°) as shown in figure 4.35

The residual hoop stresses behave similar to the residual axial stresses. They are tensile at the outer surface of the copper tube and switch to compressive stresses at the inner surface. The residual hoop stresses have lower values compared to the residual axial stress. The highest residual hoop stress was 2 mm from the outer surface and this was the same for all positions measured around the circumference. The maximum tensile hoop residual stress (136 MPa) was at an angular position of 150°. The maximum compressive hoop stress was (-82.64 MPa) at the 60° angular position as shown in figure 4.36

In figure 4.37 we can see that the residual radial stress has quite small values at different positions around the circumference and through the wall thickness.

Seamless tube production is a combination of diameter reduction and wall thickness reduction and this leads to a complex residual stress profile. In general, the higher the reduction in wall thickness the lower the tensile stress at the outer surface and the higher the compression stress at the inner surface. Higher reductions in cross-sectional area will lead to higher compressive residual stresses at the inner surface and lower tensile residual stress over a larger volume of material in order to balance the stresses [148].

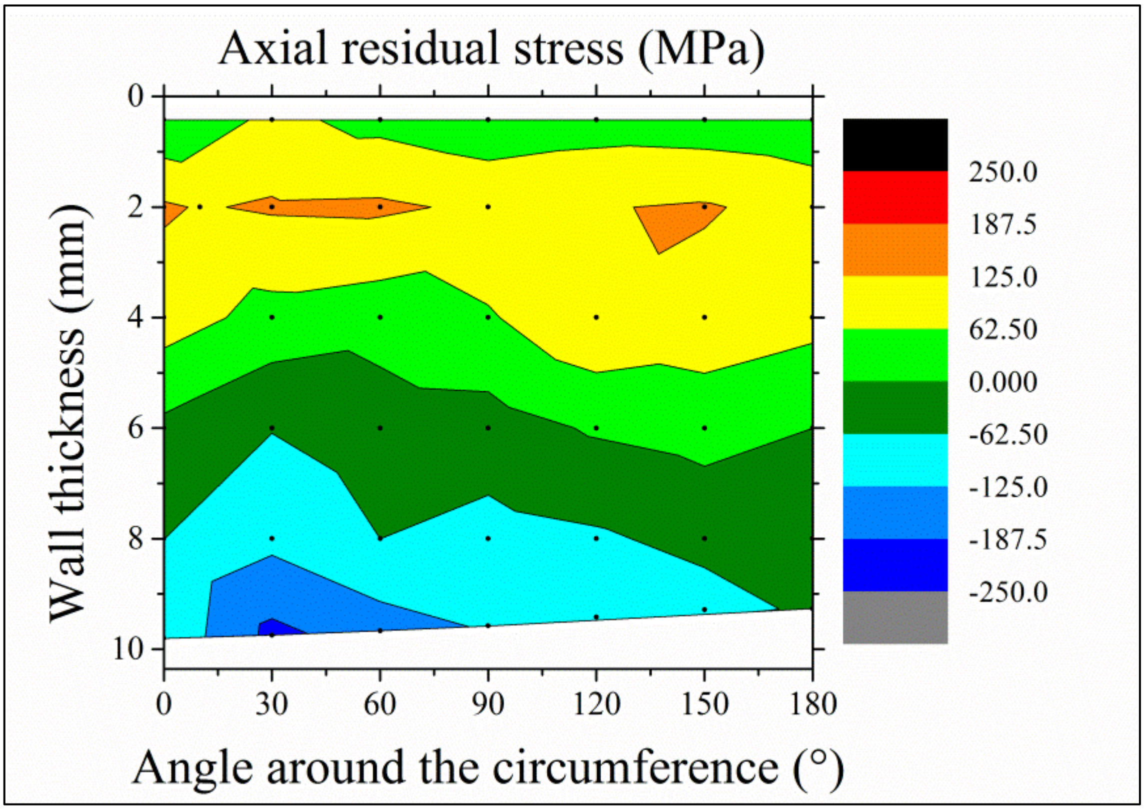

Figure 35: Residual axial stress map for the Cu-tube from 0° to 180°.

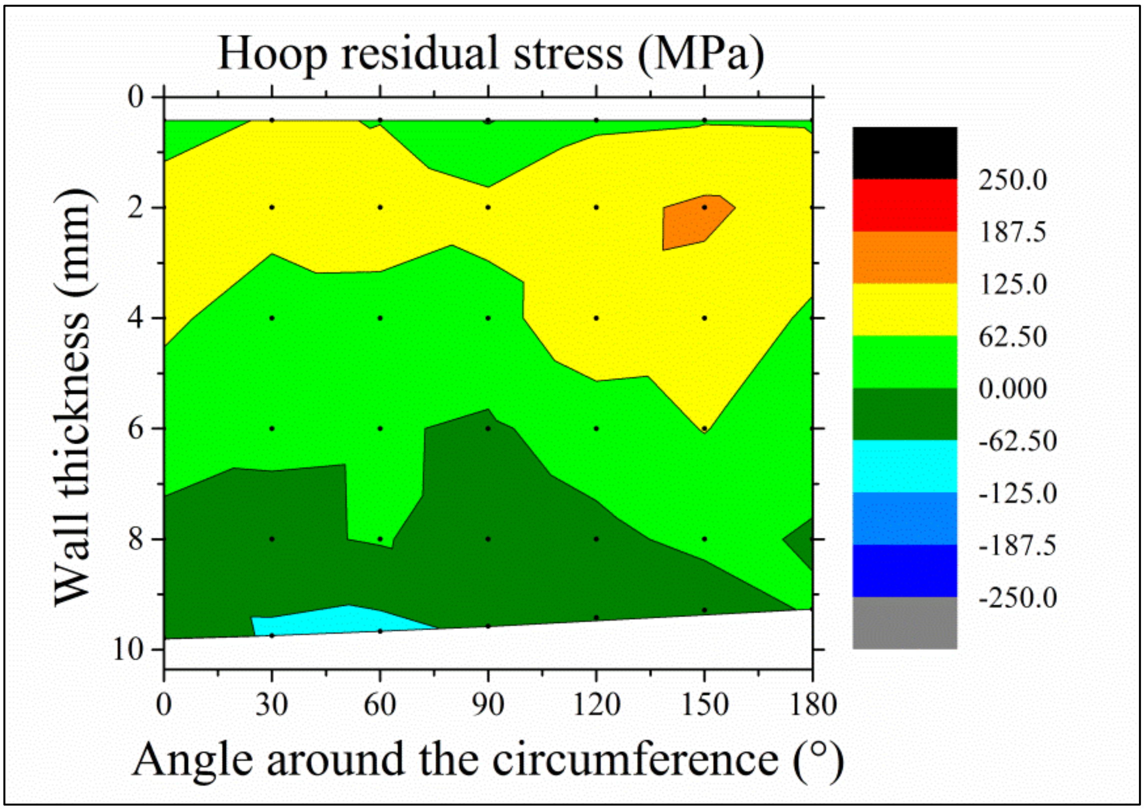

Figure 36: Residual hoop stress map for the Cu-tube from 0° to 180°.

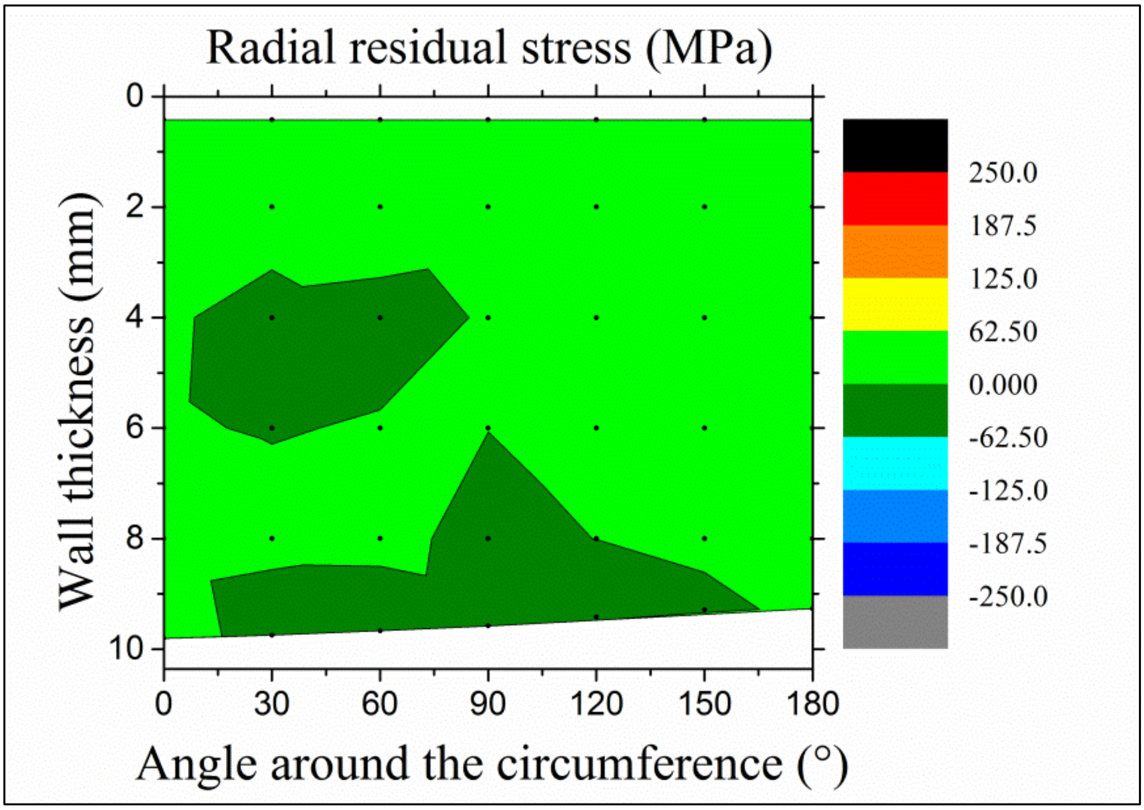

Figure 37: Residual radial stress map for the Cu-tube from 0° to 180°.

5 Conclusions

1. Combining neutron diffraction and the Stäubli RX160 robot provided a good method for automated non-destructive characterisation of the texture gradient around the tube circumference. The robot combines sample positioning and pole figure measurement, which is not possible with any other techniques.
2. Implementation of such a robotic technique in neutron diffraction makes it possible to handle large and heavy samples, which is not possible with an Eulerian cradle.
3. For the DHP-Cu ring, the robot allows measurements through an angular range of about 45° around the ring circumference in one run. This limitation is related to the geometry of the measured sample.
4. In the absence of secondary slit or radial collimator, volume and absorption corrections are important for pole figure analysis of an irregular-shaped sample like the ring.
5. Cu-ring measurements were compared with those from a cubic sample that had been cut from the tube. The results showed good agreement.
6. The combined high penetration power of neutrons and sample manipulation by the Stäubli RX160 robot are advantageous for residual strain measurements. Strain measurements obtained using a XYZ-stage and the robot showed a good agreement and proves that the robotic technique is reliable for strain measurements.
7. A great advantage is that all three strain directions can be measured with one experimental set up. It is not necessary to manually change the sample alignment.
8. The microstructure consisted of recrystallized equiaxed grains with twined grains. For the axial-radial plane, the average grain size at the maximum wall thickness was 83 µm, and at the minimum wall thickness was 78 µm. For the hoop-radial plane, the average grain size at the maximum wall thickness was 77 µm and was 66 µm at the minimum wall thickness.
9. The hardness remained nearly constant along the wall thickness of the investigated copper tube.
10. The texture components of the investigated copper tube consist of: copper {112}<111>, brass {110}<112>, and S {123}<643>, which are part of so called (β-fiber) deformation components. The dominant texture components are the cube component {001}<100> and the rotated cube component {013}<100>. Both components indicate a high state of recrystallization. Also a weak Goss {110}<001>

was observed. The copper tube can be described as being hot deformed (recrystallization occurring during and after extrusion).

11. For the investigated copper tube only a small variation of the {001}<100> cube component around the circumference was obtained (with the highest strength at maximum tube thickness). The orientation density of the {001}<100> cube component shows a remarkable variation in the through-thickness direction. The {112}<111> copper component is nearly constant around the circumference and through the wall thickness.
12. The axial residual stress was tensile for the outer part of the copper tube and compressive in the inner part. The residual hoop stress has a similar distribution but with lower values. The residual radial stress has quite a low stress state. Seamless Tube production is a combination of diameter reduction and wall-thickness reduction and this leads to a complex residual stress profile.

References

[1]. H.-G. Brokmeier, Neutron diffraction texture analysis of multi-phase system, Textures and Microstructures 10, p. 325, 1989.

[2]. J. Tobisch and H.-J. Bunge, The spherical sample method in neutron diffraction texture determination, Texture 1, p. 125, 1972.

[3]. M. Hofmann, R. Schneider, G. A. Seidle, J. Rebelo-Kornmeier, R.C. Wimpory, U. Garbe, H.-G. Brokmeier, The new materials science diffractometer STRESS-SPEC at FRM-II, Physica B 385-386, p. 1035, 2006

[4]. H.-G. Brokmeier, W.M. Gan, C. Randau, M. Völler, J. Rebelo-Kornmeier, M. Hofmann, Texture analysis at neutron diffractometer STRESS-SPEC, Nucl. Instrum. and Methods.Phys. Res. Sect. A642, p. 87, 2011.

[5]. H.-G. Brokmeier, C. Randau, W.M. Gan, M- Hofmann, T. Lippmann, N. Schell, The robot concept at STRESS-SPEC for the characterization or semi-finished products. Mater. Sci. Forum. 652 p. 197, 2012.

[6]. H.-G. Brokmeier, C. Randau,W. Gan, M. Hofmann, T. Lippmann, N. Schell, Investigation of texture gradients of semi-finished products by neutrons and photons Mater. Sci. Forum 702-703, p. 499, 2012.

[7]. E.G. West, Copper and its alloys, Halsted Press, Chichester 1982.

[8]. V Sedlacek, Non-ferrous metals and alloys, Elsevier, Amsterdam, 1986.

[9]. M. Thompson, Base Metals Handbook, CRC press, Boca Raton, 2006.

[10]. http://www.kupferinstitut.de/front_frame/pdf/Cu-DHP.pdf

[11]. J. R. Davis (editor), Copper and copper alloys, ASM International, Metal Park, Ohio, 2001.

[12]. Cu : http://www.webelements.com/

[13]. T. Manns, B. Scholtes, Eine Software zur Berechnung diffraktionselastischer Konstanten aus Einkristalldaten. HTM J. Heat Treatm. Mat. 65, 75-84, 2010.

[14]. M. Bauser, G. Sauer and K. Siegert, Aluminium Fachbuchreihe Strangpressen, Aluminium-Verlag, Düsseldorf, 2001.

[15]. M. P. Groover, Fundamentals of Modern Manufacturing: Materials, Processes, and Systems, John Wiley & Sons, USA, 2010.

[16]. http://www.copper.org/publications/newsletters/innovations/how/howdo_tube.html

[17]. G. E. Dieter, Mechanical metallurgy, McGraw-Hill, London, 1988.

[18]. H. Tschaetsch, Metal Forming Practise: processes-machines-tools, Springer, Berlin, 2006.

[19]. P. N. Rao, Manufacturing technology: foundry, forming and welding, Tata McGraw-Hill, New Delhi, 1998.

[20]. B. Li, S. H. Zhang, H. Q. Zhang, and G. L. Zhang, Microstructure and properties of copper tube during three-roll planetary rolling, J. Mater. Eng. Perform. 17, p. 499, 2008.

[21]. T. Pirling, A. Carradò, S. Brück and H. Palkowski, Neutron imaging of drawn copper tube: comparison with finite element model, Metall. and Mater. Trans. A, 39A, p. 3149, 2008.

[22]. T. Pirling, A. Carradò and H. Palkowski, Residual stress distribution in seamless tubes determined experimentally and FEM, Procedia Engineering 10, p. 3080, 2011.

[23]. A. Carradò, D. Duriez, L. Barrallier, S. Brück, A. Fabre, U. Stuhr, T. Pirling, V. Klosek, and H. Palkowski, Variation of residual stresses in drawn copper tube, Mat. Sci. Forum 571-572, p. 21, 2008

[24]. W. F. Hosford, Mechanical behavior of materials, Cambridge University Press, New York, 2010.

[25]. J. Rösler, H. Harders and M.Bäker, Mechanical behavior of engineering materials: metal, ceramics, polymers and composites, Springer, Berlin Heidelberg, 2007.

[26]. R. E. Samllman and R. J. Bishop, Modern physical metallurgy and materials engineering: science, process, application. Butterworth Heinemann, Oxford, 1999.

[27]. F.J. Humphreys and M. Hatherly, Recrystallization and related annealing phenomena, Elisvier, Amsterdam, 2004.

[28]. C. R. Brooks, Heat treatment, structure and properties of nonferrous alloys. ASM, Ohio, 1982.

[29]. W. D. Callister, Jr. and D. G. Rethwisch, Fundamentals of materials science and engineering an integrated approach, John Willey and Sons, INC. United states, 2008.

[30]. A. M. Russel and K. L. Lee, Structure-property relations in nonferrous metals, John Willey and Sons, INC. United states, 2005.

[31]. R. W. Hertzberg, Deformation and fracture mechanics of engineering materials. John Willey and Sons, INC. United states, 1996.

[32]. J. A. Szpunar and S. T. Davies, Application of synchrotron radiation to texture experiments, Proc. of 7th International Conference on Textures of Materials (ICOTOM 7), Netherlands Society for Materials Science, p.845, 1984.

[33]. V. Randle and O. Engler, Introduction to texture analysis: macrotexture, microtexture and orientation mapping, CRC press, Boca Raton, 2000.

[34]. H.-R. Wenk and P. Van Houtte, Texture and anisotropy, Rep. Prog. Phys. 67, p. 1367, 2004.

[35]. U. F. Kocksc, C. N. Tomé and H.-R. Wenk, Texture and anisotropy, Cambridge University press, Cambridge, 2000.

[36]. H.-J. Bunge, Texture analysis in materials science: mathematical methods, Butterworths, London, 1982.

[37]. H.-J. Bunge and C. Esling, Quantitive texture analysis, DGM infformationsgesellschaft, Oberursel, 1986.

[38]. H.-J. Bunge, Physical versus mathematical aspects in texture analysis, Textures and Microstructures 25, p. 71, 1996.

[39]. R.-J Roe, Description of crystallite orientation in polycrystalline materials III, general solution to pole figure inversion, J. Appl. Phys. 36, p. 2024, 1965.

[40]. S. Matthies, On the basic element of and practical experience with the WIMV algorithm- an ODF reproduction method with conditional ghost correction, Proc. of 12th International Conference On Textures Of Materials (ICOTOM 12), p.37, 1998.

[41]. G. Wassermann. & J. Grewen, Texturen metallischer Werkstoffe, Springer Verlag, Berlin, 1962.

[42]. F. Wever, Über die Walzstruktur kubisch kristallisierender Metalle, Z. Phys. 28, p. 69, 1924.

[43]. B. F. Decker, E. T. Asp and D. Harker, Preferred orientation determination using a Geiger counter xray diffraction goniometer, J. Appl. Phys. 19, p. 388, 1948.

[44]. J. T. Norton, A technique for quantitative determination of texture of sheet metals, J. Appl. Phys. 19, p. 1176, 1948.

[45]. L. G. Schulz, A direct method of determining preferred orientation of a flat reflection sample using a geiger counter x-ray spectrometer, J. Appl. Phys. 20, p.1030, 1949 a.

[46]. L. G. Schulz, Determination of preferred orientation in flat transmission samples using a geiger counter x-ray spectrometer, J. Appl. Phys. 20, p. 1033, 1949 b.

[47]. W. L. Bragg, The diffraction of short electromagnetic waves by crystal, Proceedings of the Cambridge Philosophical Society 17, p. 43, 1913.

[48]. B. D. Cullity, Element of x-ray diffraction, Addison-Wesley publishing company, Inc., Reading, 1956.

[49]. S.Yi Investigation on deformation behavior and the texture evaluation in magnesium wrought alloy AZ31, Dissertation, TU-Clausthal, 2005.

[50]. S. Garbe, H. F. Poulsen and D. J. Jensen, Local texture analysis using high energy synchrotron radiation, Proc. of 11th International Conference On Textures Of Materials (ICOTOM 11), International Academic Publishers, China, p.100, 1996.

[51]. B. N. Brockhouse, The initial magnetization of nickel under tension, Can. J. Phys. 31, p. 339, 1953.

[52]. K. Kleinstück, and S. Tobisch, Die Methode der Texturuntersuchung mittels Neuronenbeugung und ihre besonder Anwendungsvorteile, Kristall und Technik 3, p. 455, 1968.

[53]. J. Tobisch, M. Betzl and P. Reichel, Ein automatisch gesteuertes Neutron-Texturgoniometer, Experimentellr Technik der Physik 17 , p. 391, 1969.

[54]. K. Kleinstück, S. Tobisch, M. Betzl, A. Miicklich, D. Schlafer and U. Schläfer, Texturuntersuchung von Metallen mittels Neutronenbeugung, Kristall und Technik 11, p. 409, 1976.

[55]. H.-J. Bunge, H. R. Wenk and J. Pannetier, Neutron diffraction texture analysis using a 2θ- position sensitive detector, Textures and Microstructures, 5, p. 153, 1982

[56]. S. Szpunar, Texture studies using neutron diffraction, J. Mat. Sci. 19, p. 3467, 1984.

[57]. H.-J. Bunge, Advantages of neutron diffraction in texture analysis, Textures and Microstructures 10, p. 265, 1989.

[58]. H.-R. Wenk, Standard project for pole-figure determination by neutron diffraction, J. Appl. Crystallogr. 24, p. 920, 1991.

[59]. H.-G. Brokmeier, Texture analysis by neutron diffraction, Mater. Sci. Forum 157-162, p. 59, 1994

[60]. H.-G. Brokmeier, Neutron diffraction texture analysis, Phys. B., 234-236, p. 977, 1997.

[61]. H.-G. Brokmeier and S. Yi, Texture and texture analysis in engineering material, ed. by W. Reimer, A. R. Pyzalla, A. Schreyer and H. Clemens, Willy-VCH Verlag GmbH & Co. KGaA, Weinheim, Ch.3, p.57, 2008.

[62]. H.-G. Brokmeier, Advances and application of neutron texture analysis, Texture and Microstructure 33, p. 13, 1999.

[63]. H.-G. Brokmeier and D. Ostwaldt, Influence of the sample shape on the global-texture determined by neutron diffraction, proc. Of 11th International Conference on textures of materials (ICOTOM 11), International Academic Publishers, Beijing, p. 75, 1996

[64]. A. J. Schwartz, M. Kumar and B. L. Adams, Electron Backscatter diffraction in material science, Kluwer Academic- Plenum Publishers, New York, 2000.

[65]. J. A. Venables and R. Bin-Jaya, Accurate microcrystallography using electron back-scattering patters, Philos. Mag. 35, p. 1317, 1977

[66]. http://www.ifw-dresden.de/en/institutes/ikm/departments/micro-and-nanostructures/available-methods/ebsd/

[67]. .V. Randle, Microtexture determination and its applications, The Institute of Materials, London, 1992.

[68]. V. Luzin and Brokmeier, Attenuation correction in neutron texture experiment, Mat. Sci. Forum 408-412, p. 191, 2002.

[69]. H.-G. Brokmeier, Non-destructive characterization of tube segments by means of neutron diffraction, Proc. of ICOTOM 12.ed J.A. Szpunar, NRC research press Ottawa, p. 86, 1999.

[70]. T. Montensin, J.J. Heizmann, A. Vadon, Absorption corrections for x-ray texture measurement of any shape sample, Textures and Microstructures 14-18, p. 567, 1991.

[71]. A. Mücklich and P. Klimanek, Experimental errors in quantitative texture analysis from diffraction pole figures, Mat. Sci. Forum 157-162, p. 275, 1994.

[72]. D. I. Nikolayev and K. Walther, Absorption correction for non-standard geometry for pole figure measurements, Mat. Sci. Forum 157-162, p. 381, 1994.

[73]. H.M. Volz, S.C. Vogel, J.A. Robert, A.C.Lawson, D.J. Williams, L.L. Daemen, Effect of strong neutron absorption on texture and diffraction data analysis, Mat. Sci. Forum 495-497, p. 199, 2005.

[74]. H. Hu, Texture of metals, Texture 1, p. 233, 1974.

[75]. H.-J Bunge J. Tobisch and W. Sonntag, The development of rolling texture in copper measured by neutron diffraction, J. Appl. Crystallogr. 4, p. 303, 1971.

[76]. J. Hirsch and K. Lücke, Mechanism of deformation and development of rolling texture in polycrystalline fcc metal-I description of rolling texture development in homogeneous CuZn alloys, Acta metall. 36, p. 2863, 1988.

[77]. A. Mücklich, J. Tobiscch, K. Kleinstück and K. Henning, Investigation of rolling texture of some fcc metals, Proc. of 4th International Conference On Textures Of Materials (ICOTOM 4), The metal society Cambridge, p.237, 1976.

[78]. J. Hirsch, K. Lücke and H. Mecking, Comparison of experimental and theoretical rolling texture of fcc metals, proc. Of 7th International Conference on textures of materials (ICOTOM 7), Netherlands Society for Materials Science, p. 83, 1984.

[79]. K. Sekine. H. Fukutomi and T. Kamijo, Warm rolling textures of commercial purity aluminum and aluminum alloy containing zirconium, proc. Of 7th International Conference on textures of materials (ICOTOM 7), Netherlands Society for Materials Science, p. 139, 1984.

[80]. H. Hammelrath, J. F. Bulter, Jr., D. Juul-Jensen, T. Leffers, H. Hu and K. Lücke, An ODF study of the deformation and recrystallization textures of rolled and channel-die compressed high purity copper, Textures and Microstructures 13, p. 165, 1991.

[81]. H. Hammelrath, J. F. Bulter, Jr., H. Hu and K. Lücke, Deformation and recrystallization texture of rolled and channel-die compressed high purity copper, Textures and Microstructures 14-18, p. 629, 1991.

[82]. C. Maurice, J. H. Driver and L. S. Tóth, Modeling high temperature rolling textur of fcc metals, Textures and Microstructures 19, p. 211, 1992.

[83]. O. Engler, J. Palacios, W. Schäfer, E. jansen, K. Lücke and G. Will, Comparison of results of texture measurements obtained by x-ray and by neutron diffraction. Textures and Microstructures 21, p. 195, 1993.

[84]. O. Engler, C. Pithan and K. Lücke, Rolling texture developed in Cu-Mn-Alloys, Mater. Sci. Forum 157-162, p.679, 1994.

[85]. P. Wagner, N. Akdut, K. Lücke and G. Gottstein, Influence of grain boundary orientation on deformation and texture development in rolled {112}<111> Cu-bicrystals, Mater. Sci. Forum 157-162, p.865, 1994.

[86]. S.Benum, O. Engler and E. nes, Rolling texture in twin roll cast commercial purity aluminum, Mater. Sci. Forum 157-162, p.913, 1994.

[87]. E. Jansen, W. Schäfer, A. Kirfel and J. Palacios, On the longtime stability of a copper rolling texture analysed by neutron diffraction pole figures, Mater. Sci. Forum, 278-281, p.502, 1998.

[88]. O. Engler, Deformation and texture of copper-manganese alloys, Acta mater. 48, p.4827, 2000.

[89]. E. Jansen, W. Schäfer, A. Kirfel and J. Palacios, On the development of copper texture-Neutron diffraction control over a period of 12 Years, Mater. Sci. Forum 443-444, p.239, 2004.

[90]. A. A. Gazder, F. D. torre, C. F. Gu, C. H. J. Davies and E. V. Pereloma, Microstructure and texture evolution of bcc and fcc metals subjected to equal channel angular extrusion, Mat. Sci. and Eng. A 415, p. 126, 2006.

[91]. T. Leffers, The brass-type texture-how close are we to understand it?, Mater. Sci. Forum 702-703, p.216, 2012.

[92]. D. Merz and G. Wassermann, Bildung von Verformungtexturen in heterogenen Legierungen, Z. Metallkde., 56, p. 516, 1956.

[93]. M. Hatherly, W. B. Hutchinson, An introduction to textures in metals, Institution of Metallurgists, London, 1979.

[94]. H. Gertel-Kloos, H.-G. Brokmeier, and H. J. Bunge, Texture development in extruded Al-cu composite, Mater. Sci. Forum 157-162, p.685, 1994.

[95]. N. Inakazu, Y. Kaneno and H. Inoue, Fiber texture formation and mechanical properties in drawn fine copper wire, Mater. Sci. Forum 157-162, p.715, 1994

[96]. G. Gottstein, Recent aspects in the understanding of recrystallization texture, Proc. of 4th International Conference On Textures Of Materials (ICOTOM 4), the metal society Cambridge, p.93, 1976.

[97]. J. Szymanski, Annealing texture of rolled aluminum crystals, Proc. of 4th International Conference On Textures Of Materials (ICOTOM 4), the metal society Cambridge, p.425, 1976.

[98]. K. H. Virnich, G. Köhlhoff, K. Lücke and J. pospiech, Texture transformation during primary recrystallization of rolled copper sheets as function of annealing time, Proc. of 4th International Conference On Textures Of Materials (ICOTOM 4), the metal society Cambridge, p.475, 1976.

[99]. K. Lücke, The formation of recrystallization textures in metals and alloys, proc. Of 7th International Conference on textures of materials, Netherlands Society for Materials Science, p. 195, 1984.

[100]. E. Nes, J. Hirsch and Lücke, On the origin of the cube recrystallization texture in directionally solidified aluminum, proc. Of 7th International Conference on textures of materials (ICOTOM 7), Netherlands Society for Materials Science, p. 663, 1984.

[101]. O. Daaland, p.-E. Vatne, S. E. Neass and E. Nes, On the growth rate of cube-, rotated cube – and rotated goss-grain in commercial aluminum alloys, Mater. Sci. Forum 157-162, p.115, 1994.

[102]. B. J. Duggan, K. Lücke, G. Köhlhoff and C. S. Lee, Studies of annealing in cold rolled copper, Mater. Sci. Forum 157-162, p.121, 1994

[103]. C. T. Necker, R. D. Doherty and A. D. Rollet, Cube texture generation dependence on formation in cold rolled OFE copper, Mater. Sci. Forum 157-162, p.1021, 1994.

[104]. H. E. Vatne, O. Daaland and E. Nes, On the formation of cube texture in aluminum, Mater. Sci. Forum 157-162, p.1087, 1994.

[105]. F. Basson and J. H. Driver, The lattice reorientation of cube and near-cube orientated fcc crystal during plane strain compression, Mater. Sci. Forum 273-275, p.313, 1998.

[106]. Y. B. Park, Y. H. Kim and B. I. Kim, Formation of the cube band and it evolution during recrystallization, Proc. of 12th International Conference On Textures Of Materials (ICOTOM 12). NRC research press 2, p. 830, 1999.

[107]. B. Hutchinson, The cube texture revisited, Mater. Sci. Forum 702-703, p.3, 2012.

[108]. F. X. Lin, W. Pantleon, T. Leffers and D. J. Jensen, Effect of initial parameters on the development of cube texture during recrystallization of copper, Mater. Sci. Forum 702-703, p.398, 2012.

[109]. J. H. Cho, S. J. Park, S.H. Choi and K. H. Oh, Deformation texture of cold drawn Al6063 Tube, Mater. Sci. Forum 408-412, p 565, 2002.

[110]. U. Schläfer and H. J. Bunge, Cyclic textures in Aluminum wires, Texture, 1, p. 31, 1972.

[111]. L. Bertheloot. P. Van Houtte, and E. Aernoudt, Texture development in tube drawing, Proc. of 4th International Conference On Textures Of Materials (ICOTOM 4), p.64-73, 1976

[112]. W. Truszkowski, J.król, and B. Major, Inhomogeneity of rolling texture in fcc metals, Metall. Trans. A, 11A, p.749. 1980.

[113]. K. Wiedzbanowski and Z. Jasieński, Some results of rolling texture heterogeneity, Scripta Metall. 16, p. 653, 1982.

[114]. B. J. Duggan, C. S. Lee and R. E. Smallman, On the inhomogeneous rolling texture transition, Mater. Sci. Forum 157-152, p. 659, 1994.

[115]. S.-H. Hong, H.-T. Jeong, C.-H. Choi, D. N. Lee, Deformation and recrystallization textures of surface layer of copper sheet, Mat. Sci. and Eng. A 229, p. 147, 1997.

[116]. J. Sarkar, S. Cao, Shigeo Saimoto, Friction effect on through-thickness texture evoluation during rolling, Mater. Sci. Forum 495 - 497, p. 567, 2005.

[117]. S.-H. Choi. Y. S. Song, B. J. Kim, H.-W. Kim and S.-B. Kang. Simulation of texture evolution during hot rolling deformation in fcc materials, Key Eng. Mat., 345-346, p. 869, 2007.

[118]. P. J. Withers and H. K. D. H. Bhadeshia, Residual stress Part 1 – Measurement techniques, Mater. Sci. and Technol. 17, p. 355, 2001.

[119]. G. Albertini, G. Bruno, A. Carradò, F. Fiori, M. Rogante and F. Rustichelli, Determination of residual stresses in materials and industrial components by neutron diffraction, Meas. Sci. Technol. 10, p. R56, 1999.

[120]. M. T. Hutchings, P. J. Withers, T. M. Holden and T. Lorentzen, Introduction to the characterization of residual stress by neutron diffraction, CRC Press Taylor & Francis Group, Boca Raton, 2005.

[121]. A.J. Allen, M.T. Hutchings, C.G. Windsor and C. Andreani, Neutron diffraction methods for the study of residual stress fields, Adv. Phys. 34, p. 445, 1985.

[122]. M. T. Hutchings, Neutron diffraction measurement of residual stress fields: overview and points for discussion, NATO Science Series 216, p. 3, 1992.

[123]. V. Hauk, Structure and residual stress analysis by nondestructive methods, Elsevier, Amsterdam, 1997

[124]. A.N. Ezeilo and G. A. Webster, Advance in neutron diffraction for engineering residual stress measurements, Texture and Microstructure 33, p. 151, 1999.

[125]. A. Butts, Copper, the science and technology of the metal, its alloys and compound, Reinhold Publishing Corporation, New York, 1954.

[126]. ASM, Metallograph and microstructure Vol. 9, ASM international, 1992.

[127]. C. Randau, H.-G Brokmeier, W. M. Gan, M. Hofmann, M. Völler, W. Tekouo, N. Al-hamdany, Improved sample manipulation at the STRESS-SPEC neutron diffractometer using an industrial 6-axis robot for texture and strain analyses, Nucl. Instrum. and Methods.Phys. Res. Sect. A, doi:10.1016/j.nima.2015.05.014, 2015

[128]. N. Al-hamdany, H.-G. Brokmeier, C. Randau, W. Gan, and M. Völler, Texture gradient studies of a Cu-tube by the robot at STRESS-SPEC, Cryst. Res. Technol., 49, p. 888, 2014.

[129]. C. Randau, U. Garbe, H.-G. Brokmeier, StressTextureCalculator: a software tool to extract texture, strain and microstructure information from area-detector measurements, J. Appl. Crystallogr. 44, p. 641, 2011.

[130]. H. J. Bunge, H. Klein, Determination of high resolution pole figures with area detector, Z. Metallkunde 87, p. 465, 1996.

[131]. H Humber, Intensity correction, resolving power and statistical relevance in pole figure measurement. In: H. J. Bunge (ed) Experimental Techniques of Texture analysis. DGM Oberusel, 29-50, 1986.

[132]. G. E Bacon, Neutron diffraction. Clarendon press, Oxford, 1975

[133]. www.ncnr.nist.gov/instruments/bt1/neutron.html.

[134]. H.-R Wenk, Eine photographische Röntgen-Gefügeanalyse, Schweizerische mineralogische und petrographische Mitteilungen 45, 518, 1965

[135]. J. F. H. Clusters, Betrachtungen über Metalltexturen, Philips Techn. Rundschau, 17, p. 13, 1942.

[136]. A. Hammersley http://www.esrf.eu/computing/scientific/FIT2D/

[137]. ASM, Mechanical testing and evaluation Vol. 8, ASM international, 1992.

[138]. M. Hatherly, A. S. Malin and C. M. Carmichael, Proc. of 7th International Conference on Textures of Materials (ICOTOM 7), Netherlands Society for Materials Science, p. 245, 1984.

[139]. ASM, Fractography Vol. 12, ASM international, 1992.

[140]. D. Broek, Elementary engineering fracture mechanics, Sijthoff & Noordhoff International Publisher B.V, Alphen aan den Rijin, The Netherland, 1978.

[141]. http://practicalmaintenance.net/?p=1135

[142]. S. Ivanov and D. Marković, Influence of hard cold working on microstructure and properties of annealing copper tubes, J. of Mining and Metall. 38 (3-4) B, p 163, 2002

[143]. Linssen G., Mengelberg H. D. and Stüwe H.P. Zyklische Texturen in drähten kubisch flächenzentrieter metalle. Z. Metallkd. 55, p. 600, 1964.

[144]. R. Hielscher and H. Schaeben, A novel pole figure inversion method: specification of the MTEX algorithm, J. Appl. Crystallogr. 41, p. 1024, 2008

[145]. F. Bachmann, R. Hielscher and H. Schaeben, Texture Analysis with MTEX – Free and Open Source Software Toolbox, Solid State Phenomena 160, p 63, 2010.

[146]. J. Šaroun, J. Rebelo Kornmeier, M. Hofmann, P. Mikula and M. Vrána, J. Appl. Crystallogr. 46, p. 628, 2013.

[147]. H. Wern and H. Walz, Dependence of X-Ray Elastic Constants on Diffraction Plane, Phys. Status. Solidi B 206, p.545, 1998.

[148]. W. Dahl and H. Mühlenweg, Eigenspannungen und Verfestigung beim Rohrziehen, Stahl u Eisen 84, p. 1250, 1964

[149]. A.Carradò, H.-G. Brokmeier, T. Pirling, R. C. Wimpory, N.schell and H. Palkowski, Development of Residual Stresses and Texture in Drawn Copper Tubes, Adv. Eng. Mat. 15, p. 469 (2013).

[150]. H. Palkowski, S. Brück, T. Pirling and A.Carradò, Investigation on the Residual Stress State of Drawn Tubes by Numerical Simulation and Neutron Diffraction Analysis, Materials 6, p. 5118 (2013).

Appendix 1

Optical Microscope:

1. Microscopic picture at maximum thickness

Microscope picture of DHP-copper tube for axial-radial plane starting from outside diameter to inside diameter

1

2

3

4

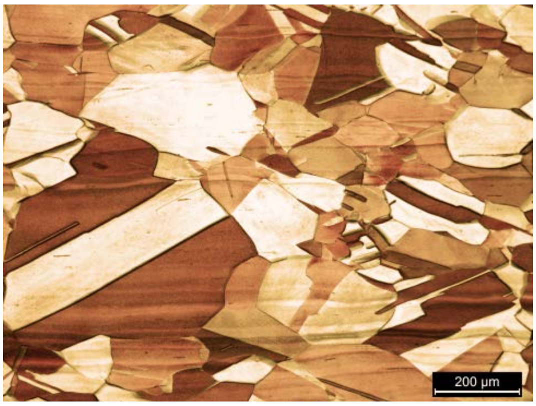

5

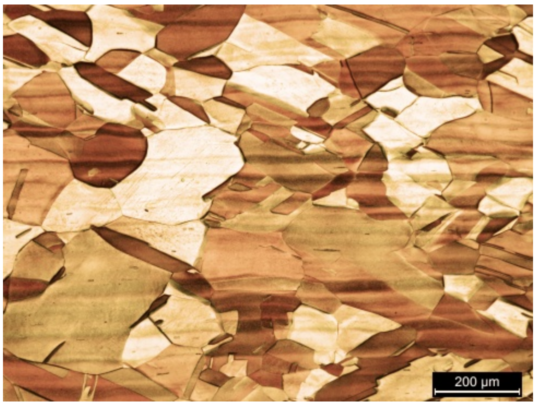

6

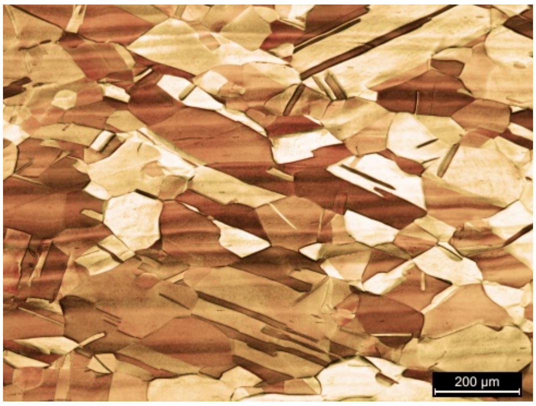

7

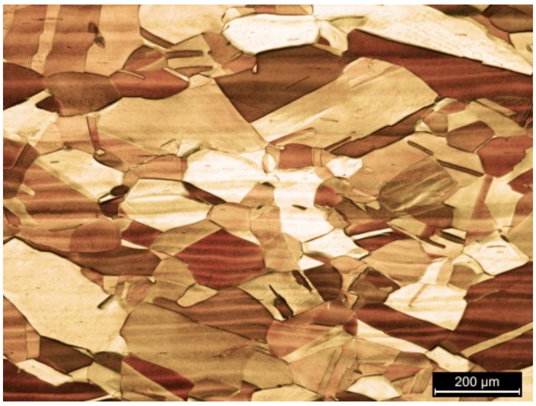

8

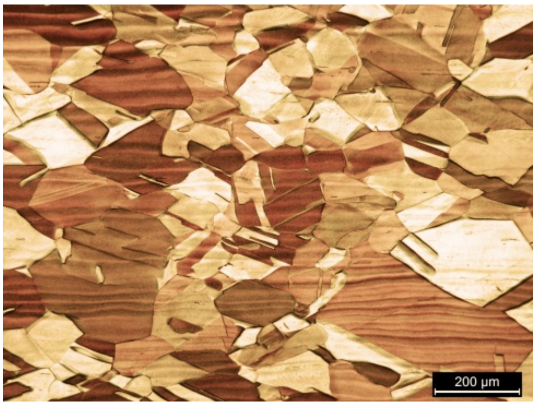

9

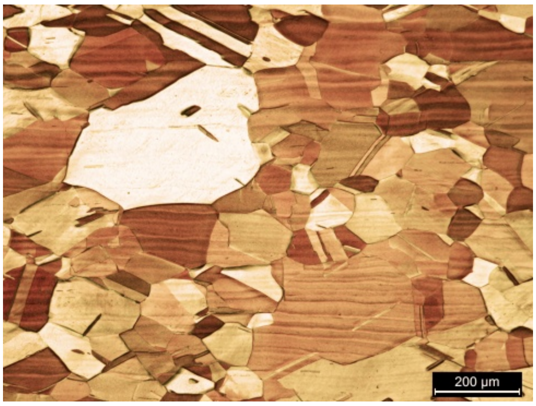

10

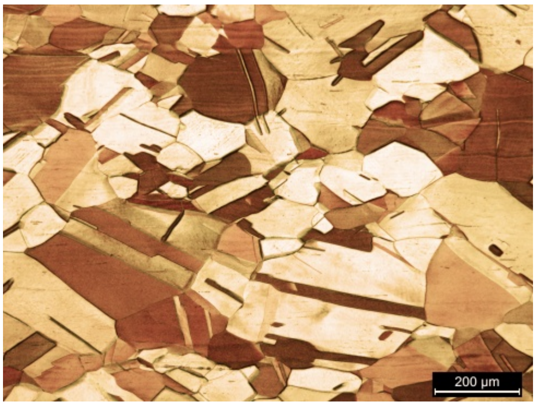

11

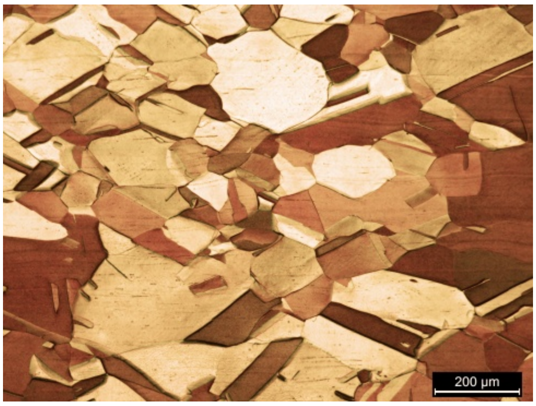

12

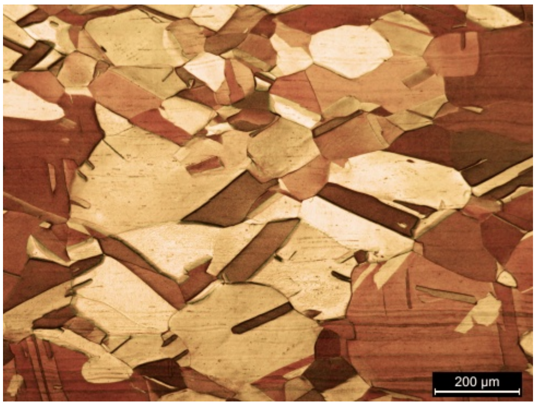

Microscope picture of DHP-copper tube for hoop-radial plane starting from outside diameter to inside diameter

1

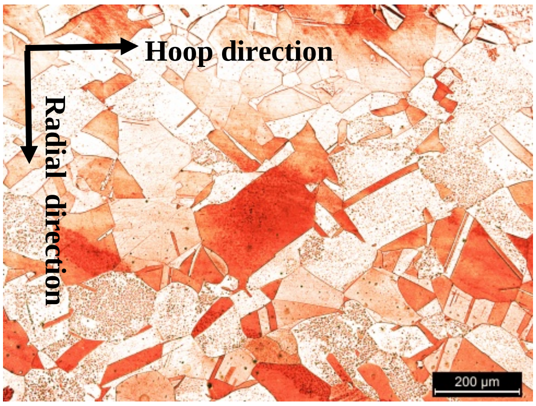

2

3

4

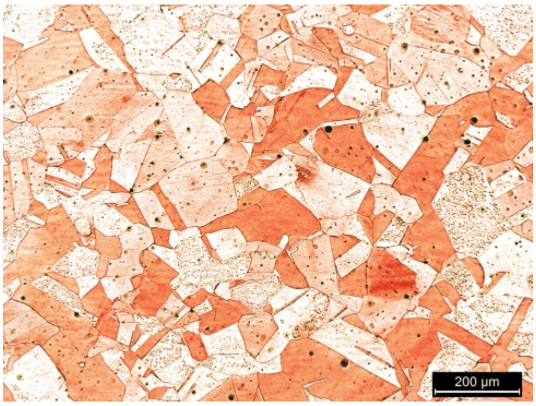

5

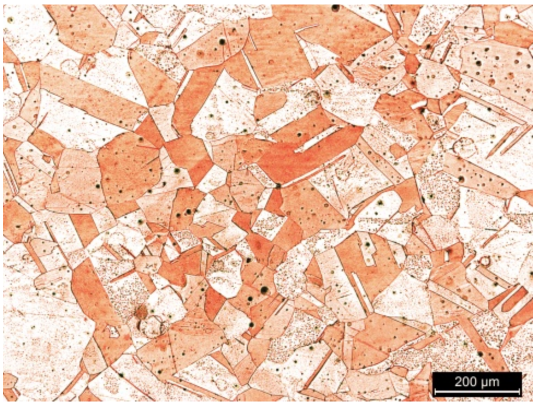

6

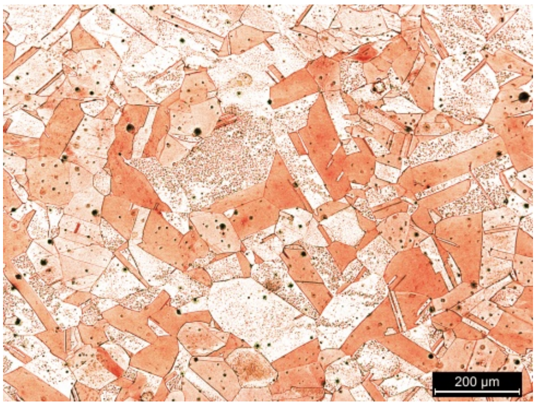

7

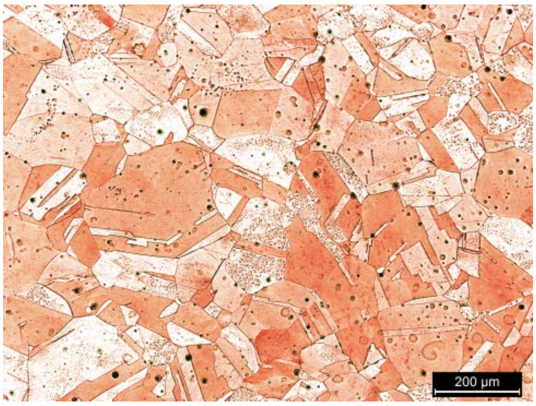

8

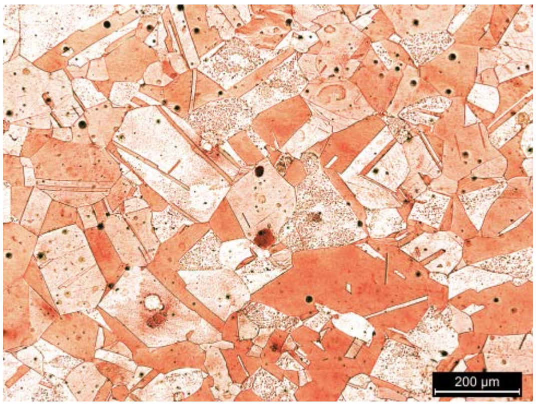

9

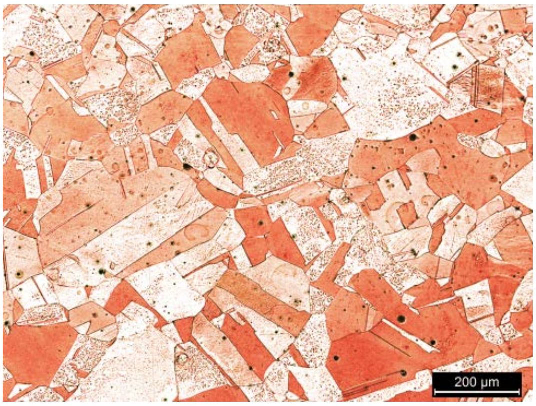

10

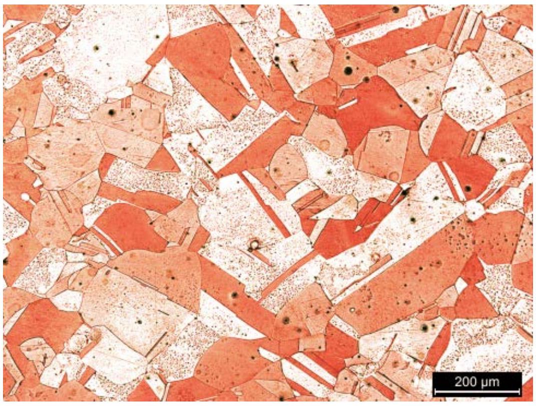

11

12

2. Microscopic picture at middle thickness

Microscope picture of DHP-copper tube for axial-radial plane starting from outside diameter to inside diameter

1

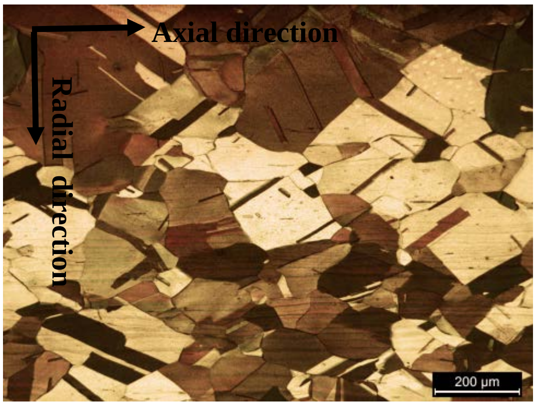

2

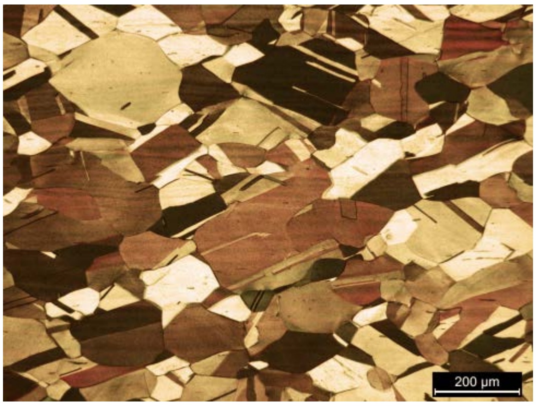

3

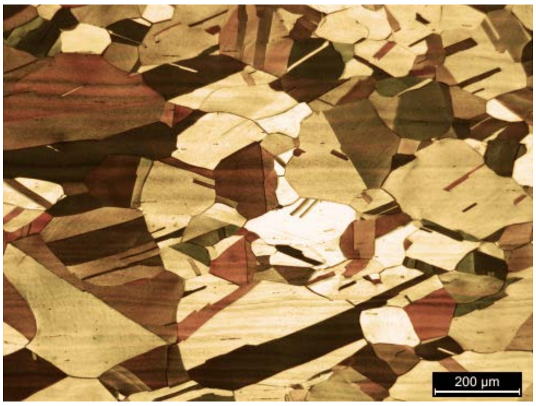

4

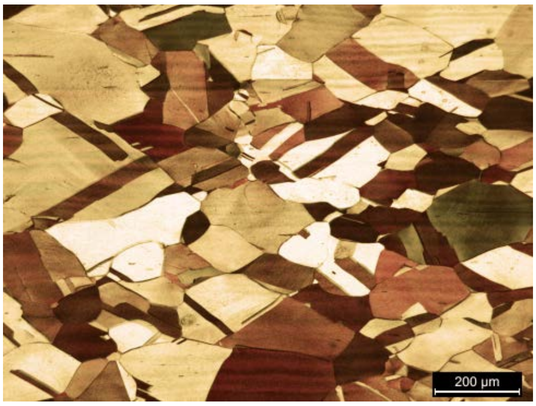

5

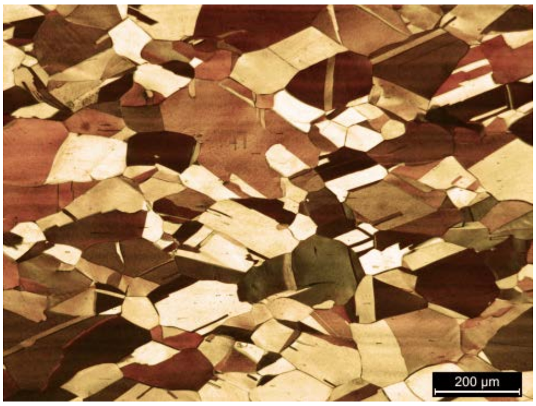

6

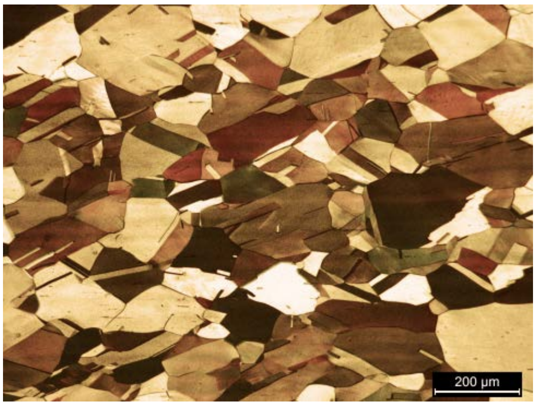

7

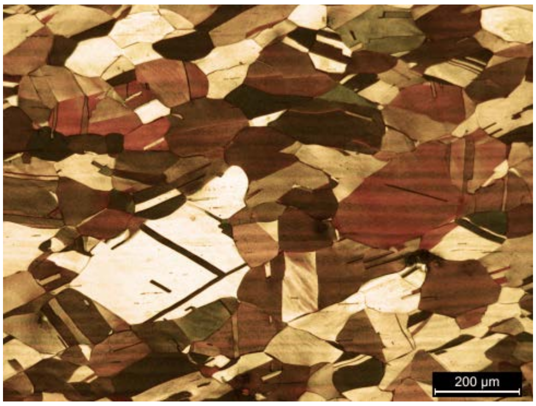

8

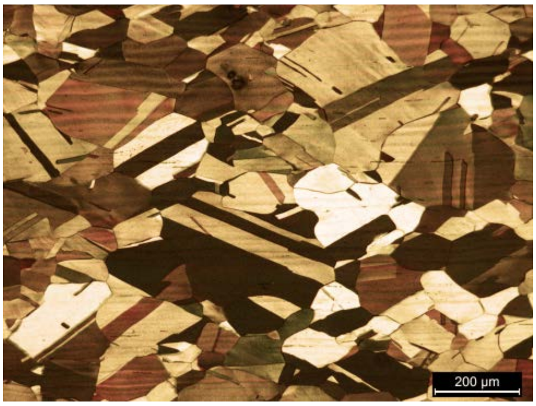

9

10

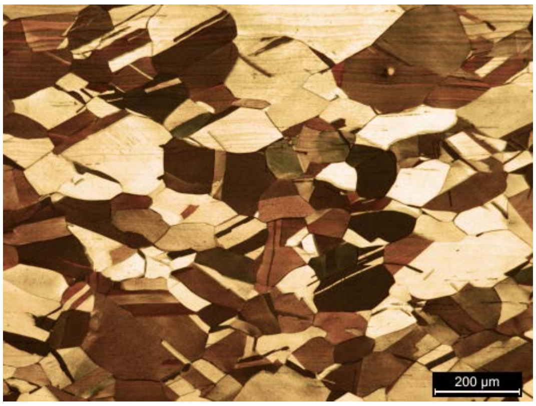

11

Microscope picture of DHP-copper tube for hoop-radial plane starting from outside diameter to inside diameter

1

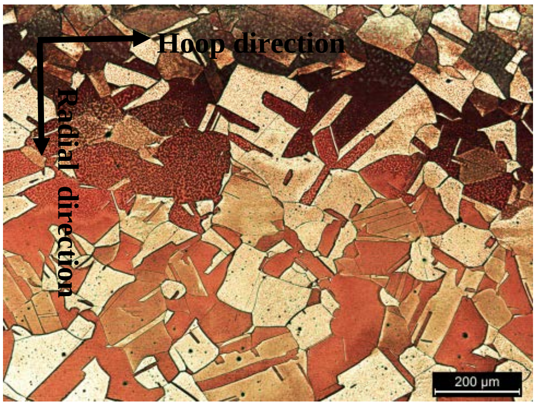

2

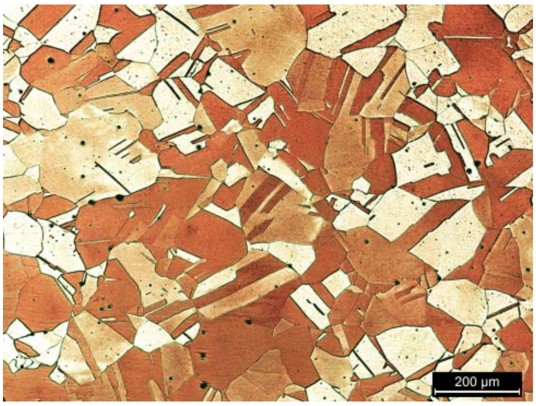

3

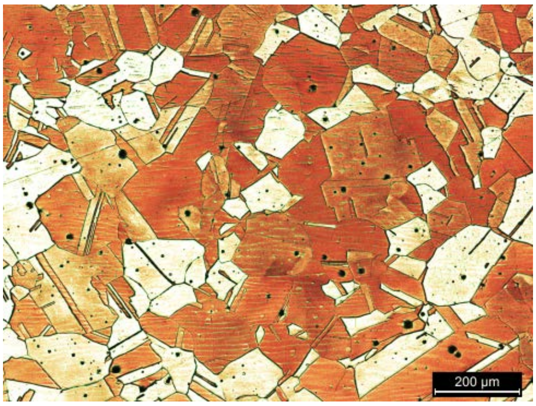

4

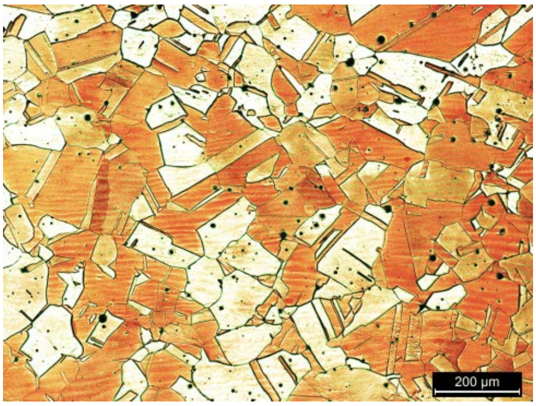

5

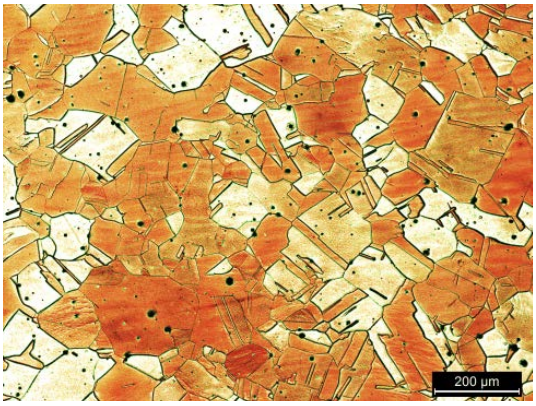

6

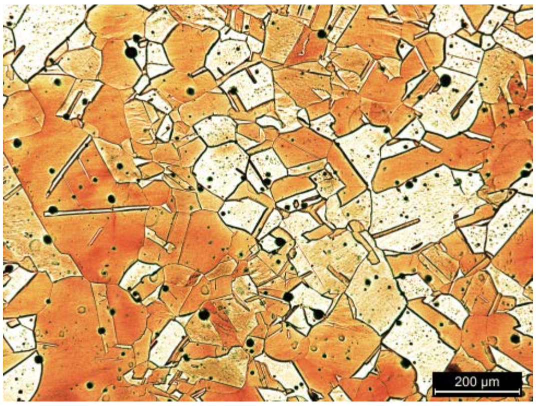

7

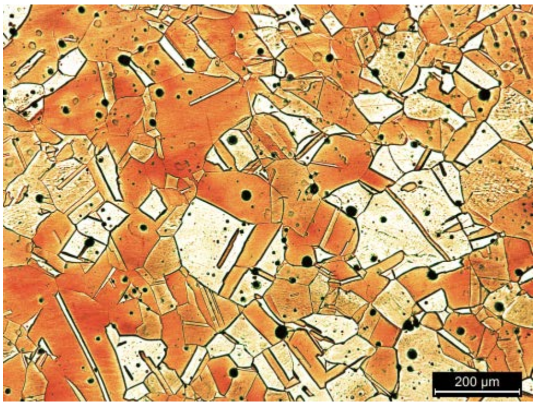

8

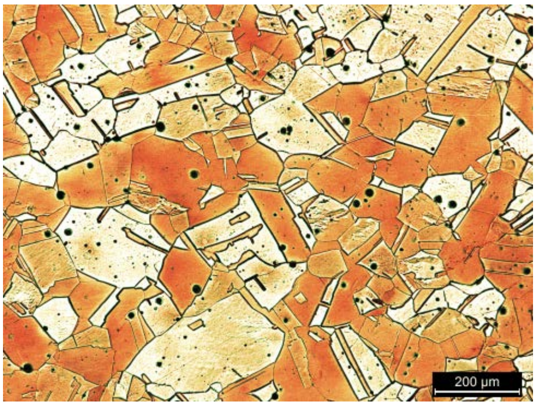

9

10

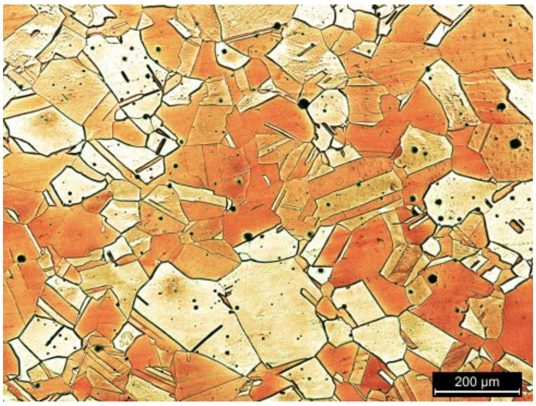

11

3. Microscopic picture at minimum thickness

Microscope picture of DHP-copper tube for axial-radial plane starting from outside diameter to inside diameter

1

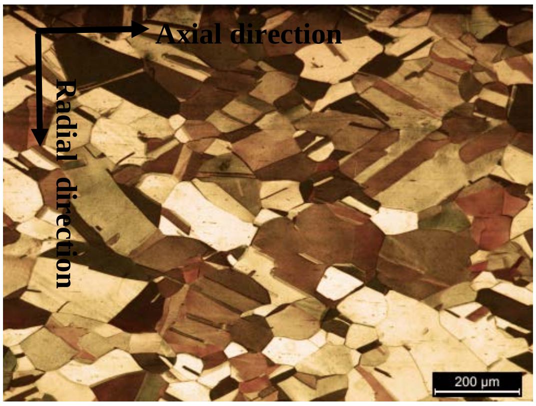

2

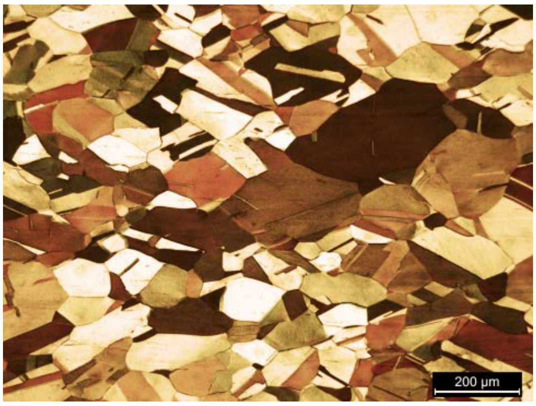

3

4

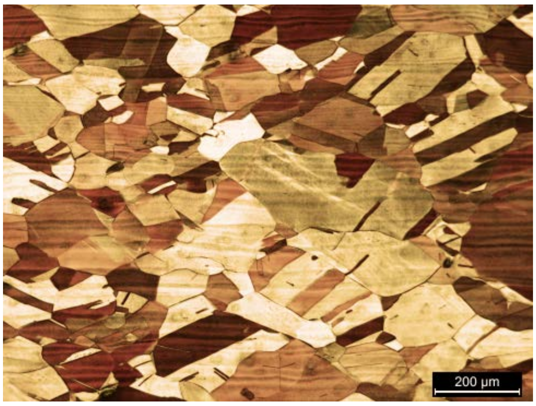

5

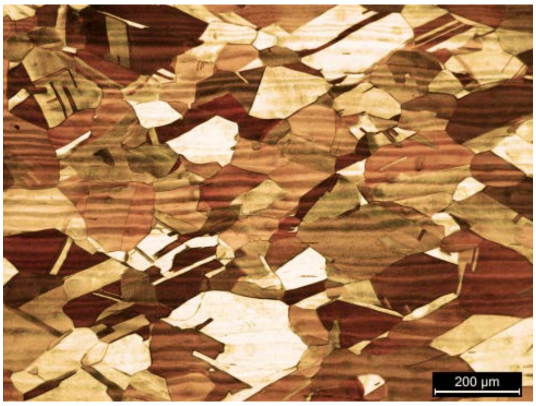

6

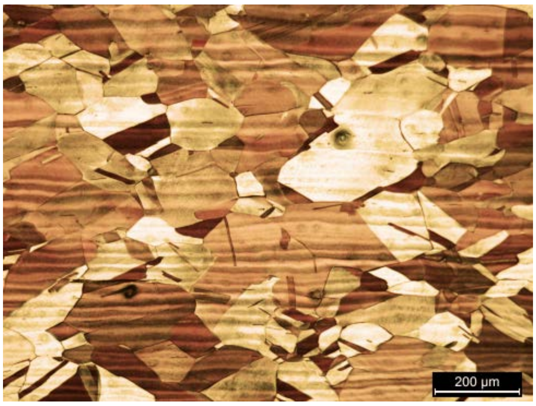

7

8

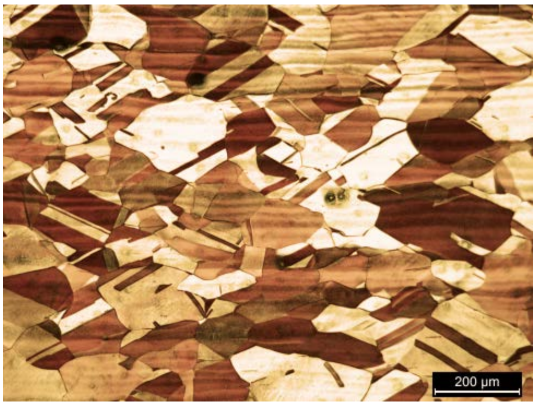

9

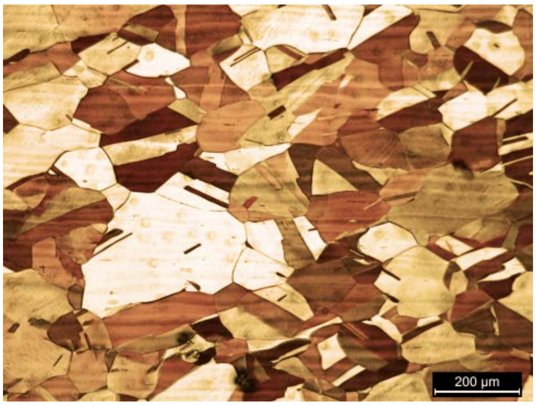

10

11

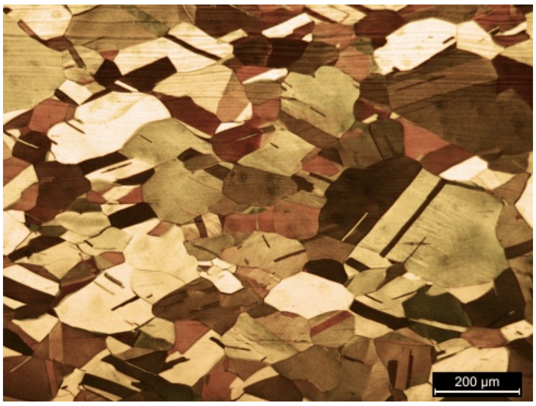

Microscope picture of DHP-copper tube for hoop-radial plane starting from outside diameter to inside diameter

1

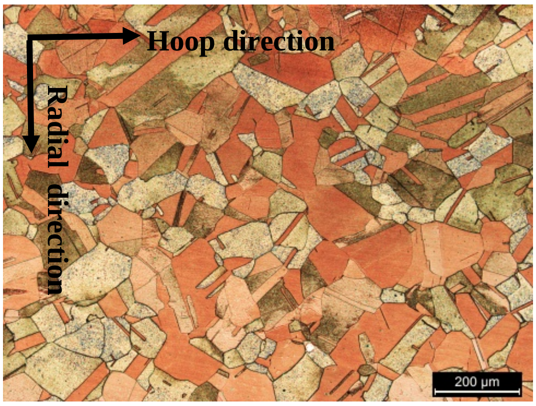

2

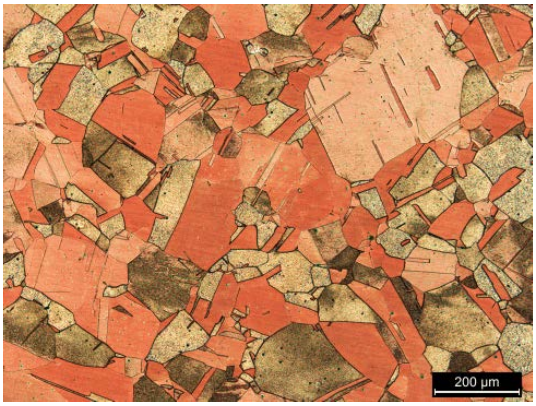

3

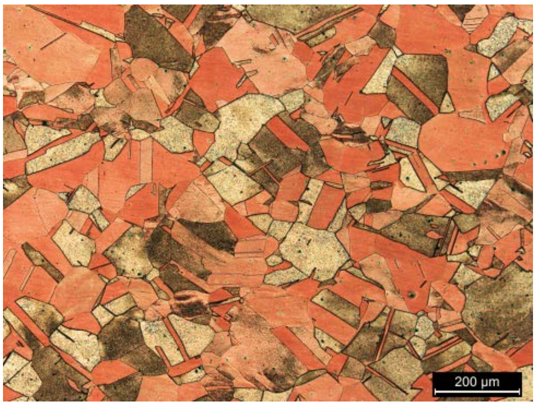

4

5

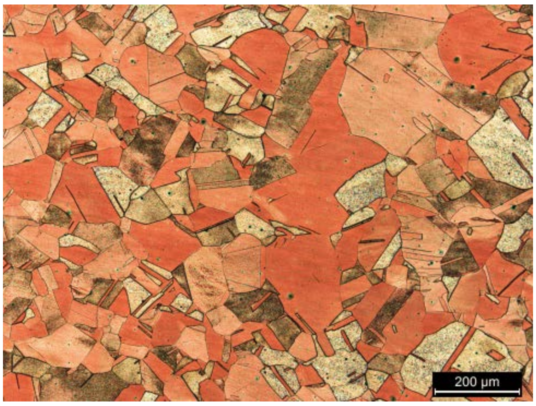

6

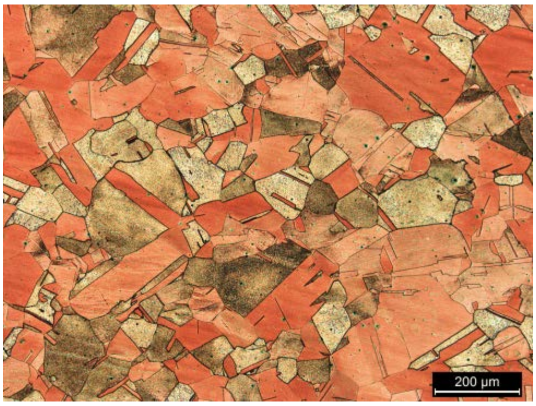

7

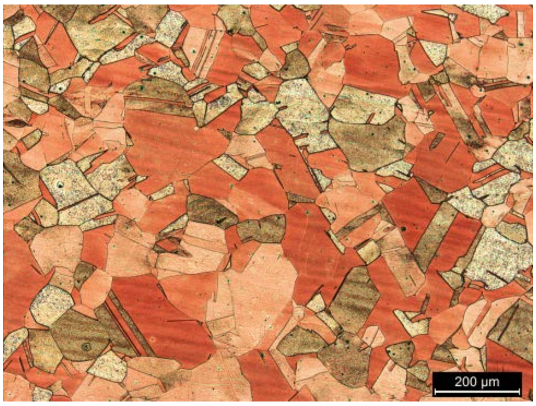

8

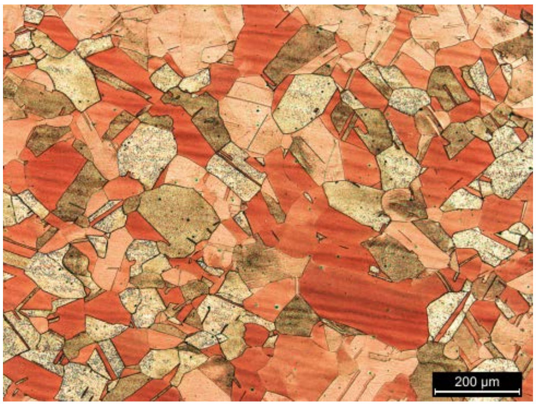

9

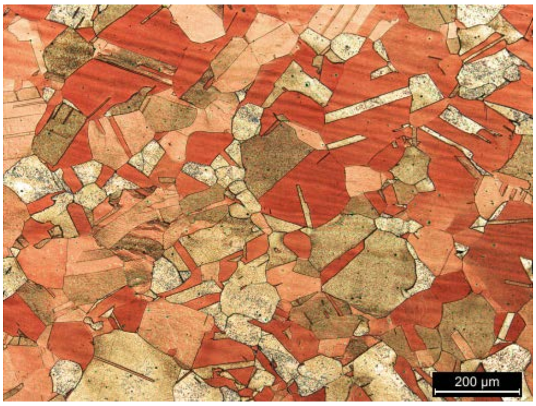

10

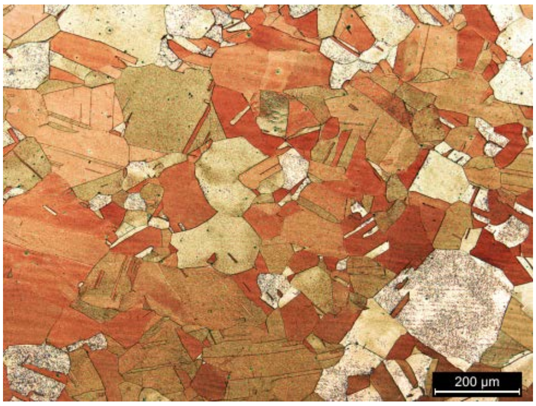

11

Appendix 2

1. Pole figures measured by neutron before correction (all units in mrd)

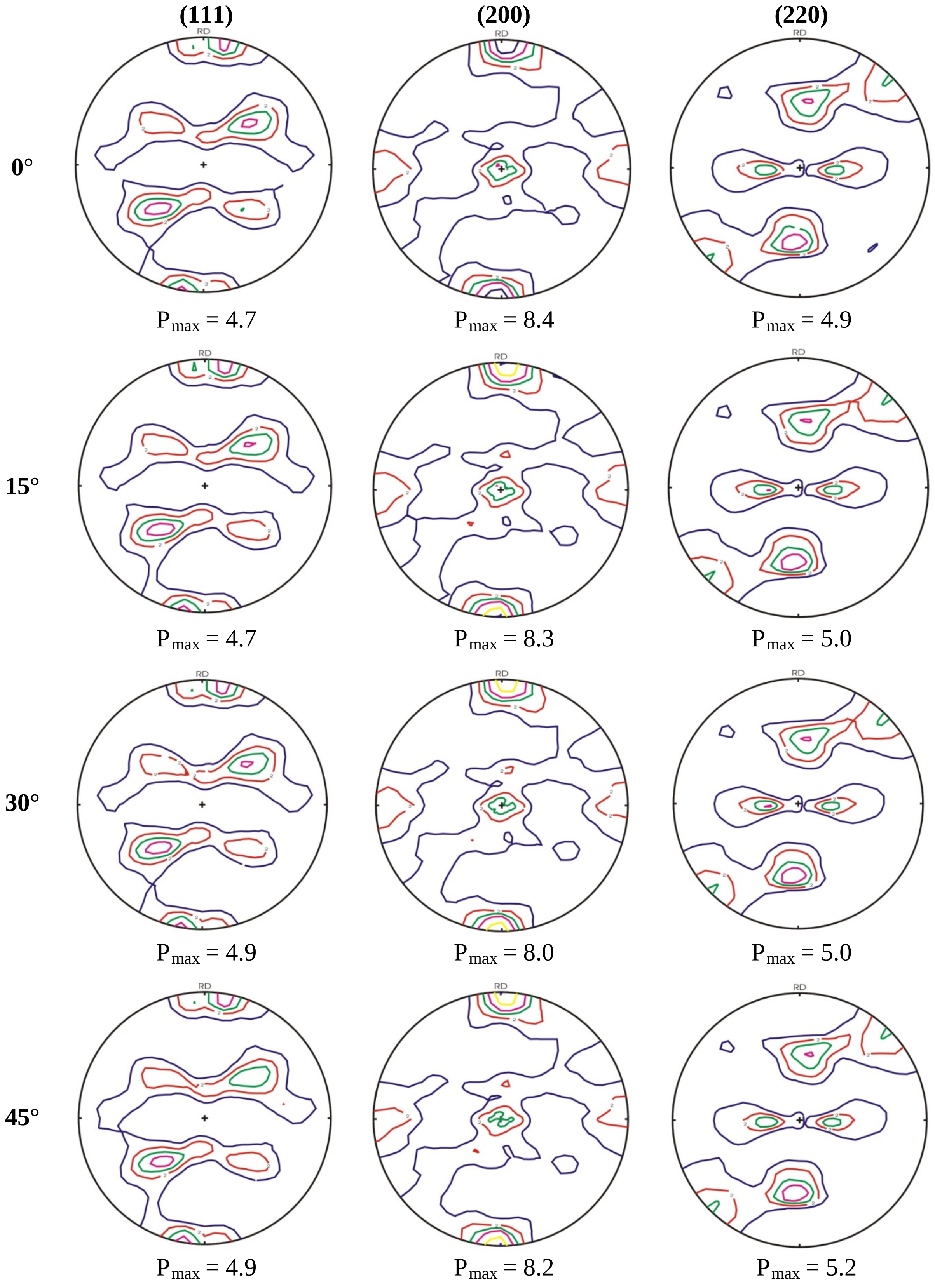

60°

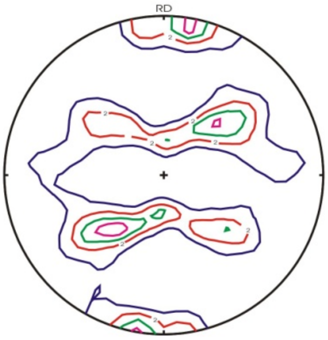

$P_{max} = 4.6$

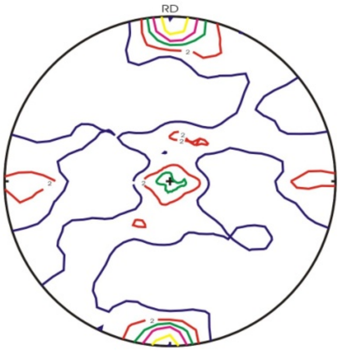

$P_{max} = 8.3$

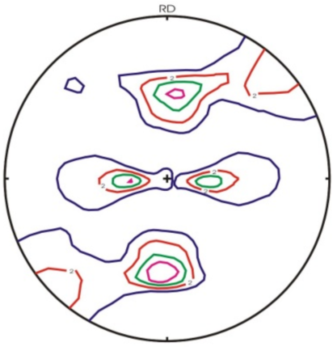

$P_{max} = 5.2$

75°

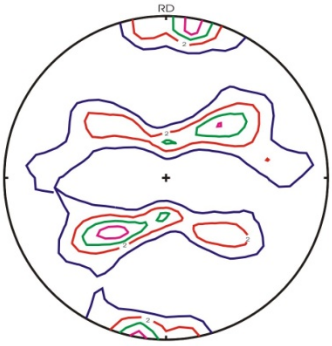

$P_{max} = 4.7$

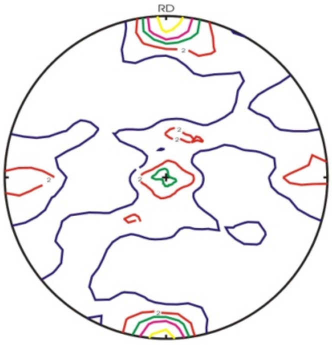

$P_{max} = 7.9$

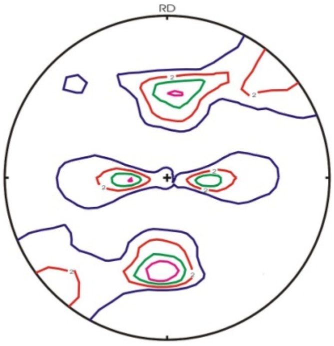

$P_{max} = 5.2$

90°

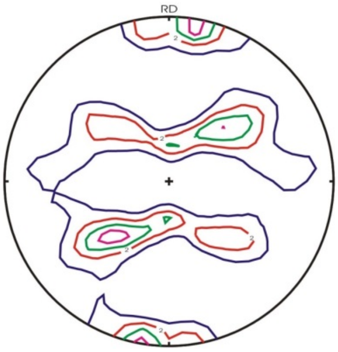

$P_{max} = 4.6$

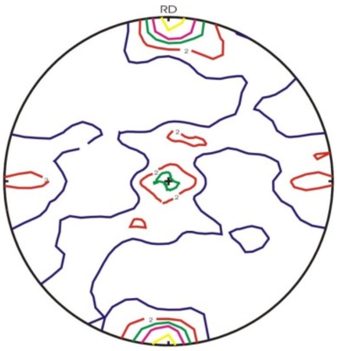

$P_{max} = 7.7$

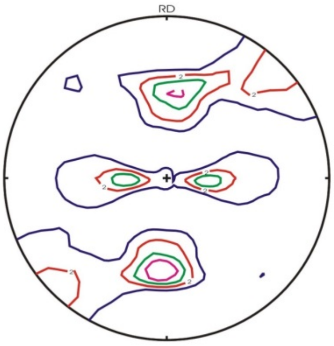

$P_{max} = 5.2$

105°

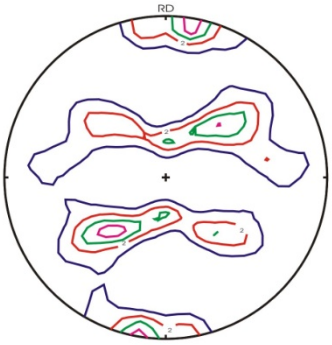

$P_{max} = 4.7$

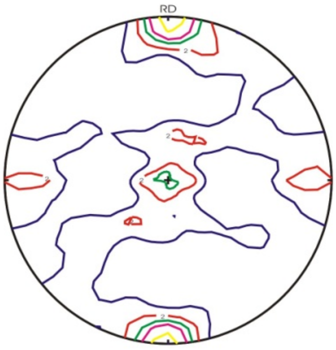

$P_{max} = 7.6$

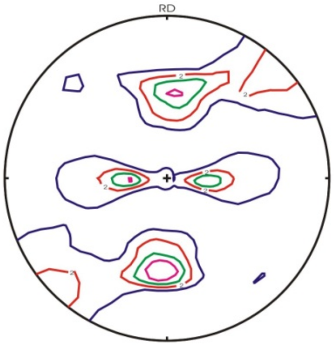

$P_{max} = 5.0$

120°

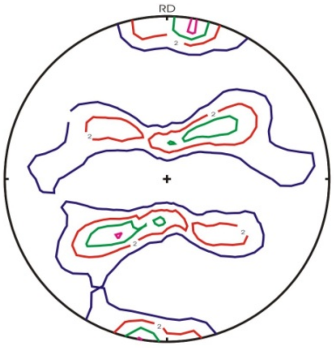

$P_{max} = 4.2$

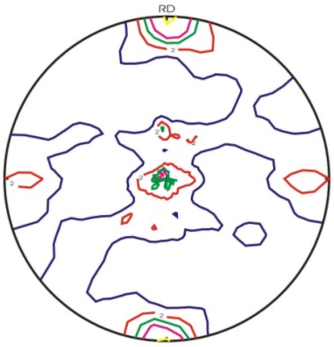

$P_{max} = 6.4$

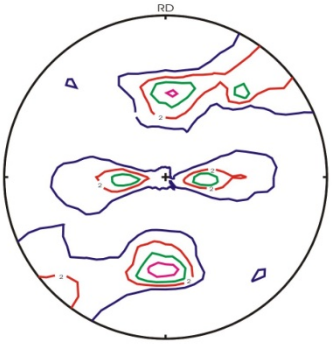

$P_{max} = 4.7$

135°

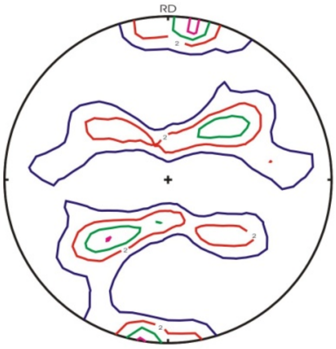

$P_{max} = 4.2$

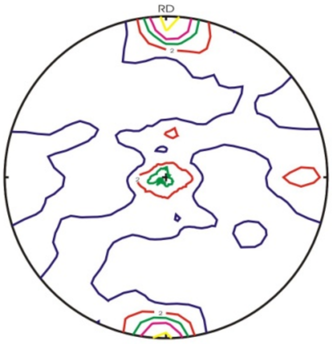

$P_{max} = 7.0$

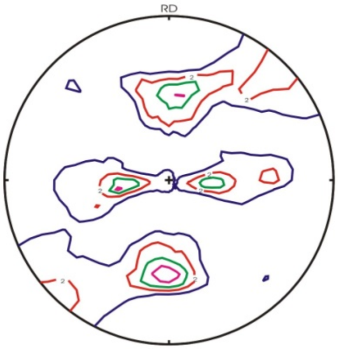

$P_{max} = 4.9$

150°

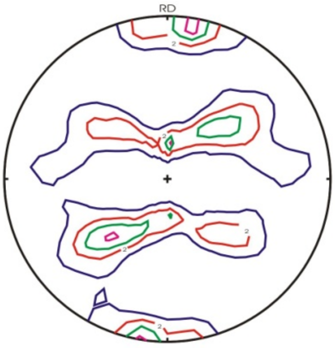

$P_{max} = 4.3$

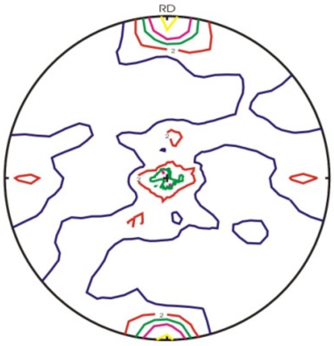

$P_{max} = 6.9$

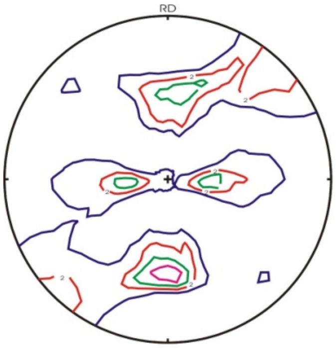

$P_{max} = 4.8$

165°

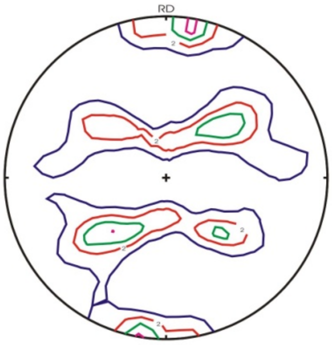

$P_{max} = 4.3$

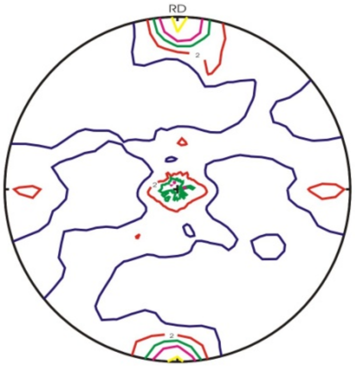

$P_{max} = 6.9$

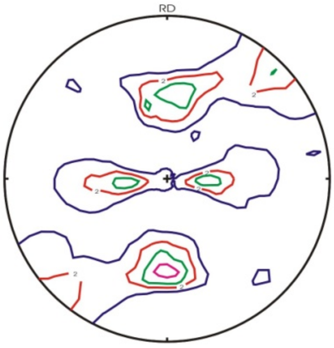

$P_{max} = 4.7$

180°

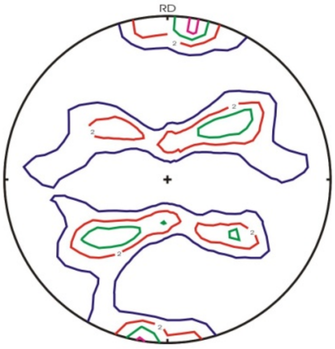

P$_{max}$ = 4.3

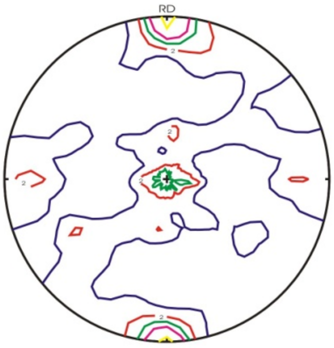

P$_{max}$ = 6.9

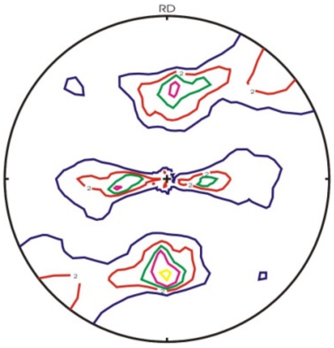

P$_{max}$ = 4.8

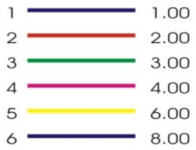

2. Pole figures measured by neutron after correction (all units in mrd)

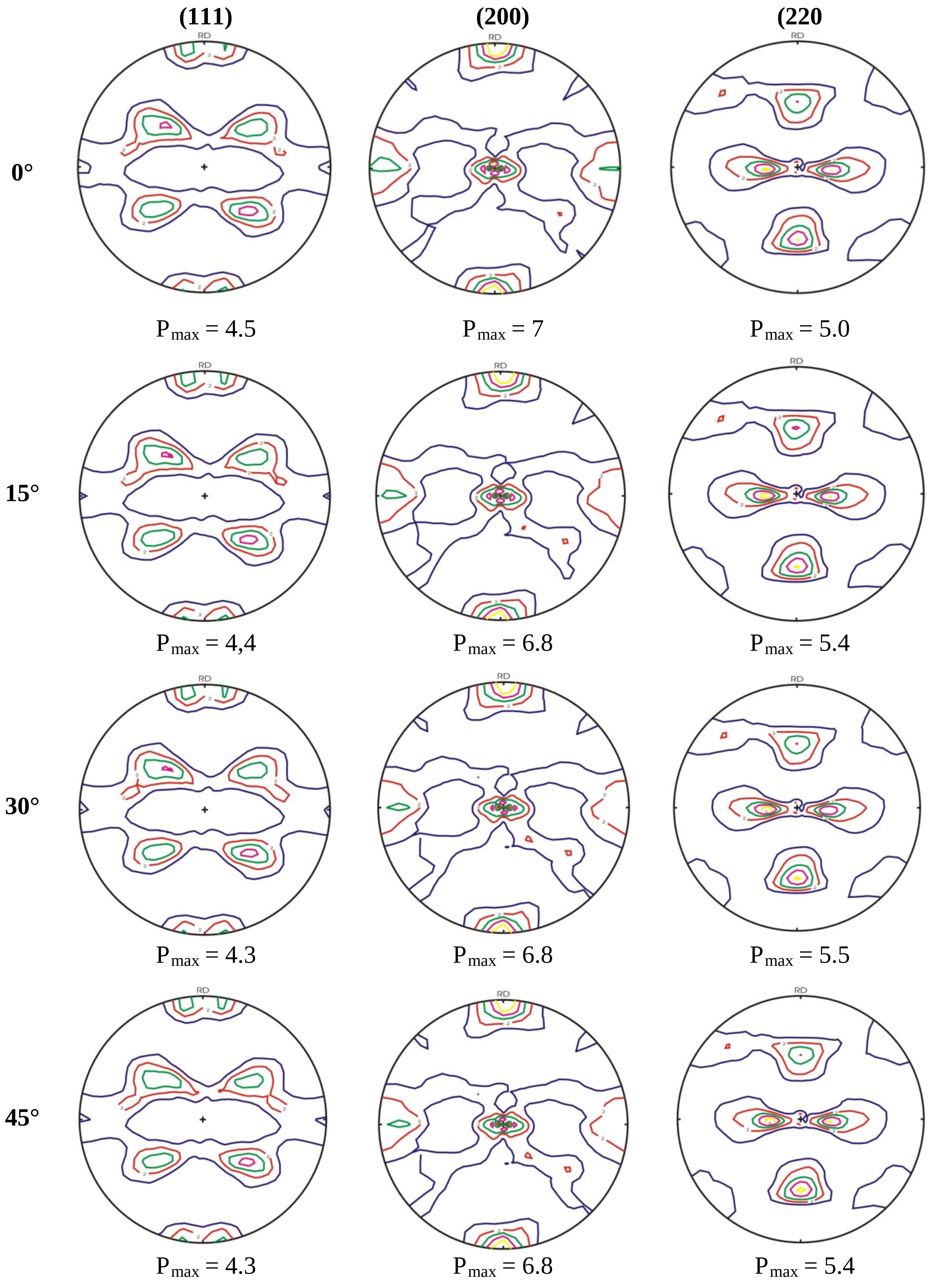

Pmax = 4.5 Pmax = 7 Pmax = 5.0

Pmax = 4,4 Pmax = 6.8 Pmax = 5.4

Pmax = 4.3 Pmax = 6.8 Pmax = 5.5

Pmax = 4.3 Pmax = 6.8 Pmax = 5.4

60°

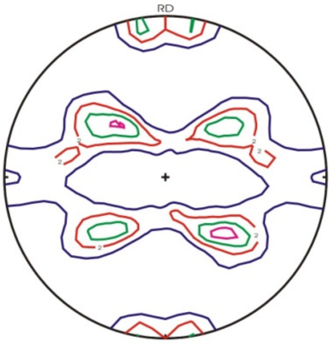

P_{max} = 4.4

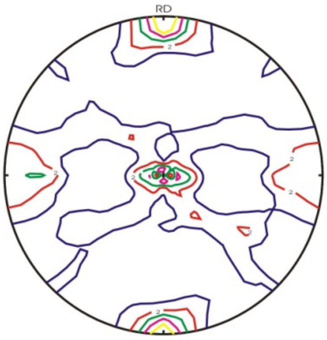

P_{max} = 6.8

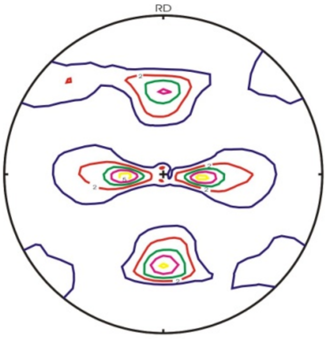

P_{max} = 5.3

75°

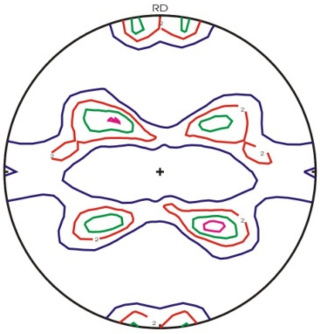

P_{max} = 4.4

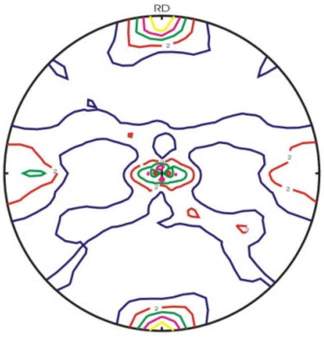

P_{max} = 6.6

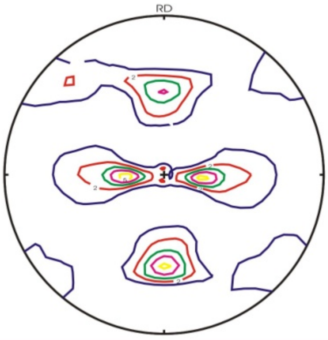

P_{max} = 5.4

90°

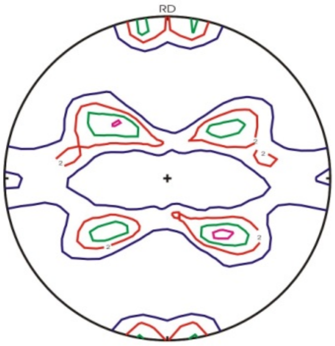

P_{max} = 4.3

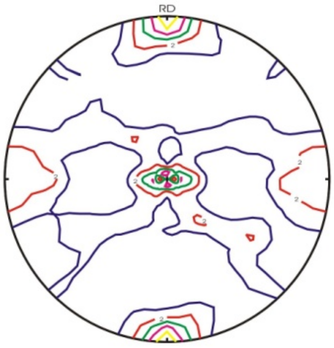

P_{max} = 6.4

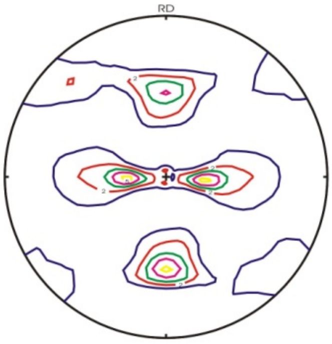

P_{max} = 5.4

105°

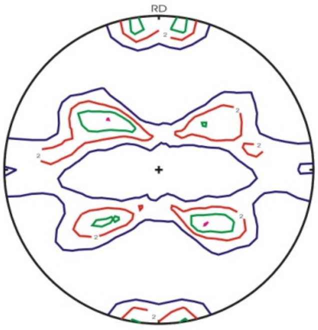

P_{max} = 4.0

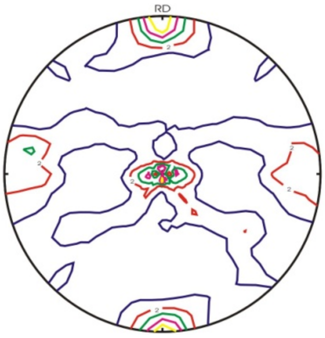

P_{max} = 6.2

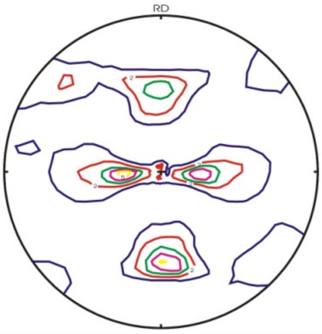

P_{max} = 5.6

120°

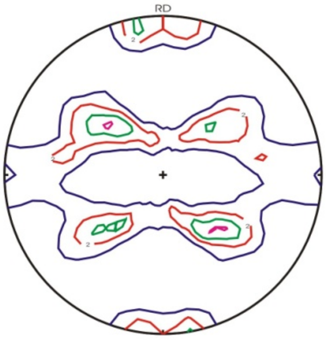

$P_{max} = 4.2$

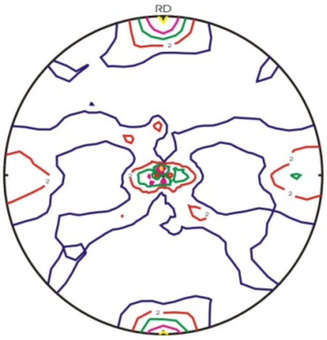

$P_{max} = 5.7$

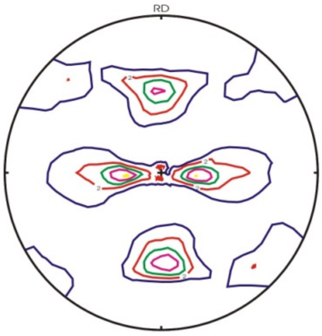

$P_{max} = 5.2$

135°

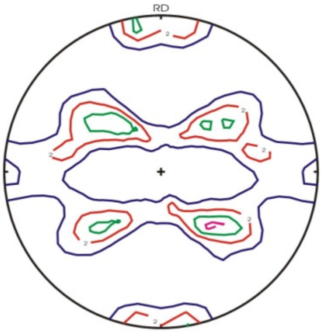

$P_{max} = 4.2$

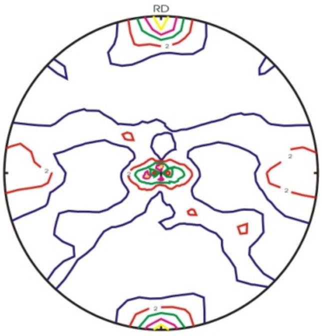

$P_{max} = 5.8$

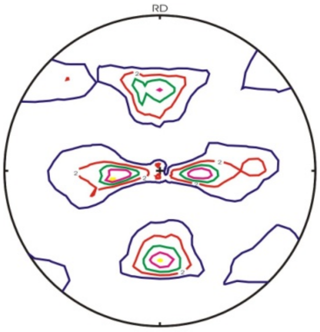

$P_{max} = 5.2$

150°

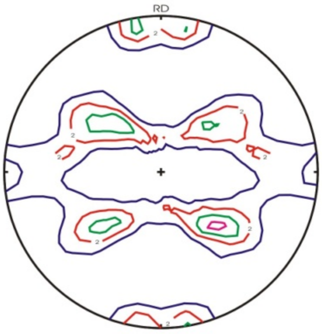

$P_{max} = 4.2$

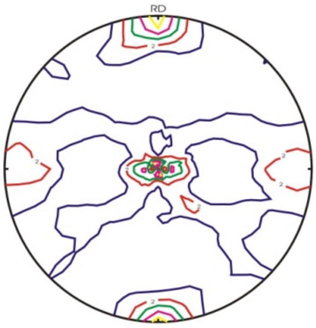

$P_{max} = 5.7$

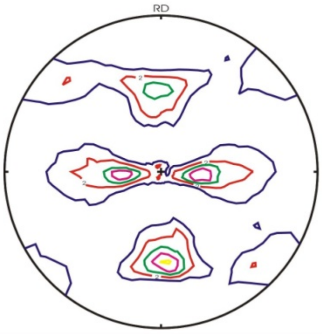

$P_{max} = 5.2$

165°

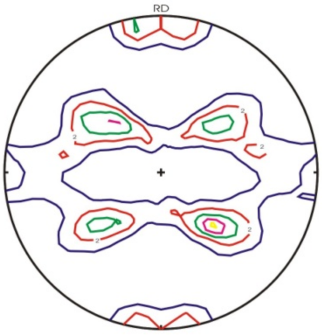

$P_{max} = 5.3$

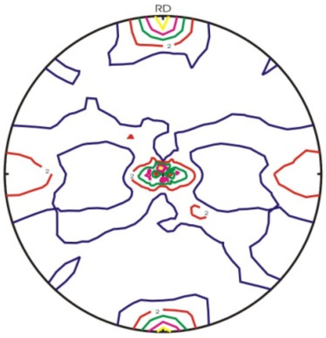

$P_{max} = 5.7$

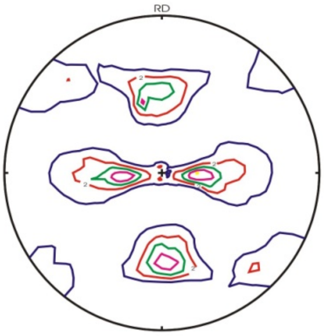

$P_{max} = 5.0$

180°

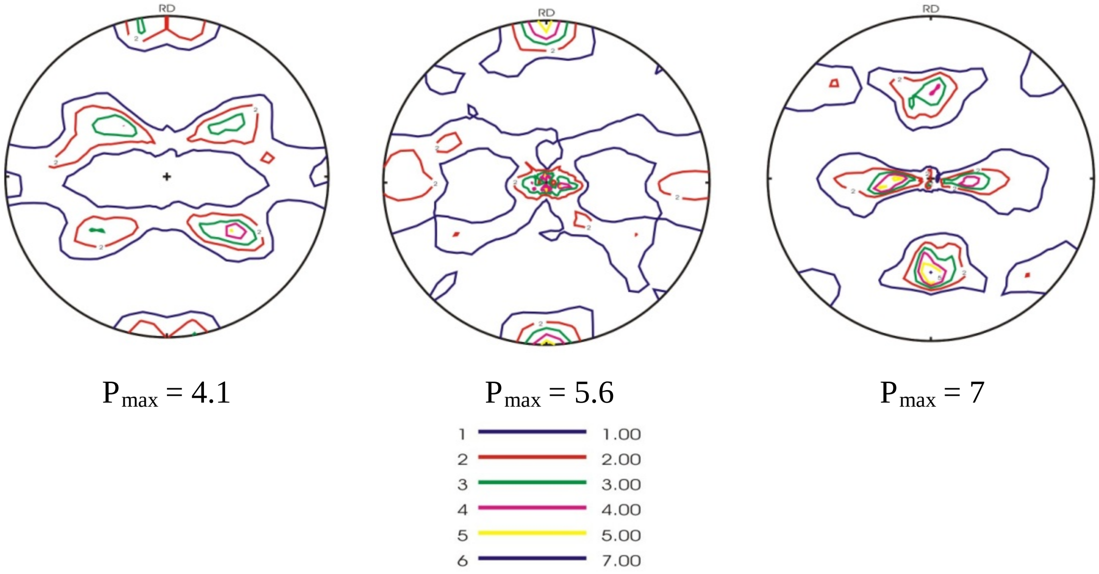

$P_{max} = 4.1$

$P_{max} = 5.6$

$P_{max} = 7$

3. ODF calculation after correction for differt wall thickness

0°

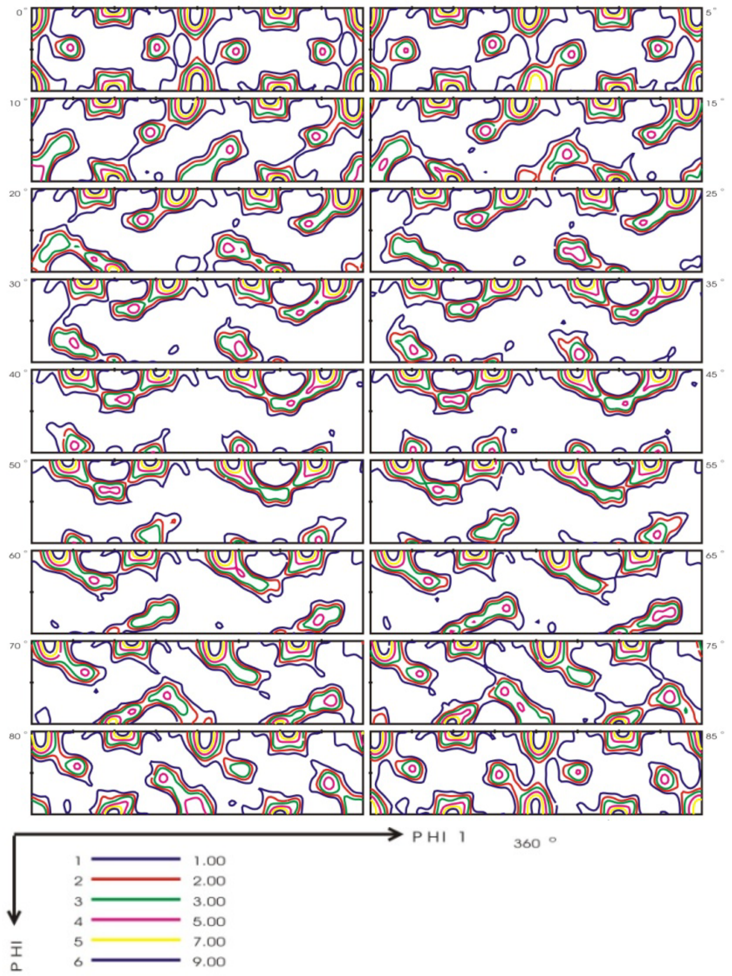

Fmax= 11.7 mrd

15°

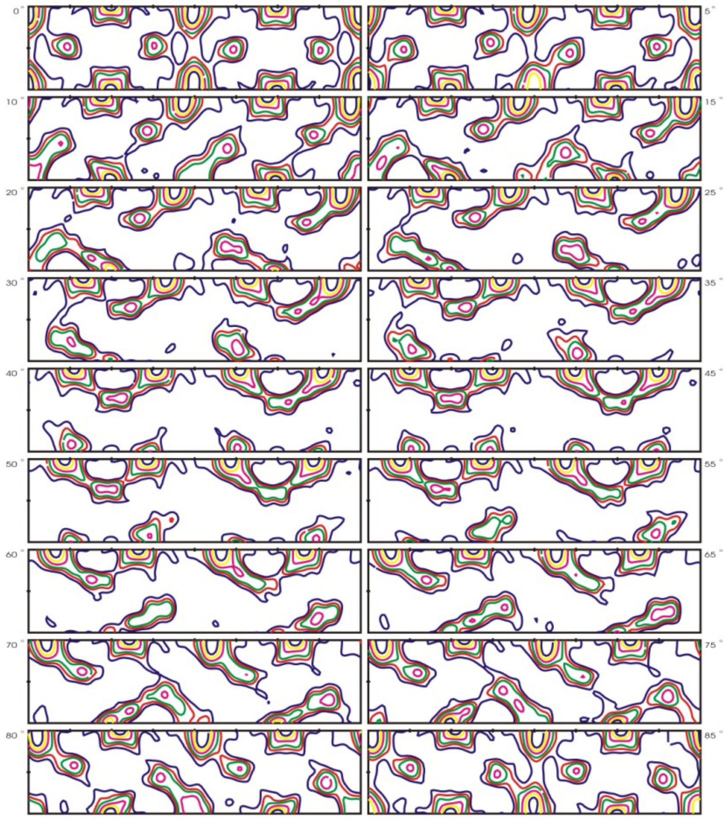

Fmax=11.5 mrd

30°

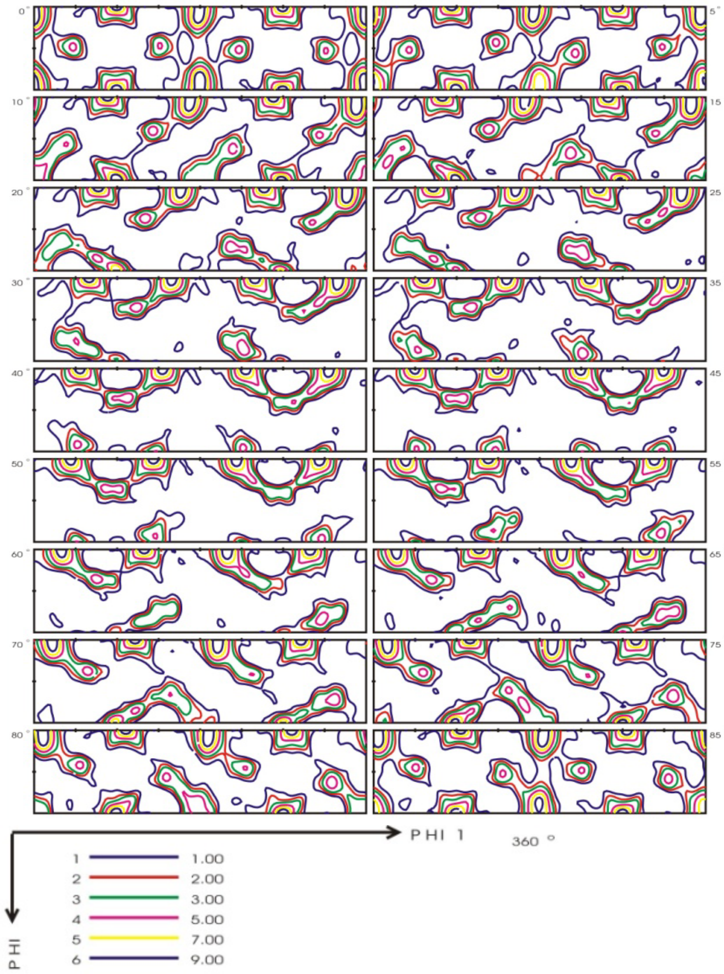

Fmax= 11.4 mrd

45°

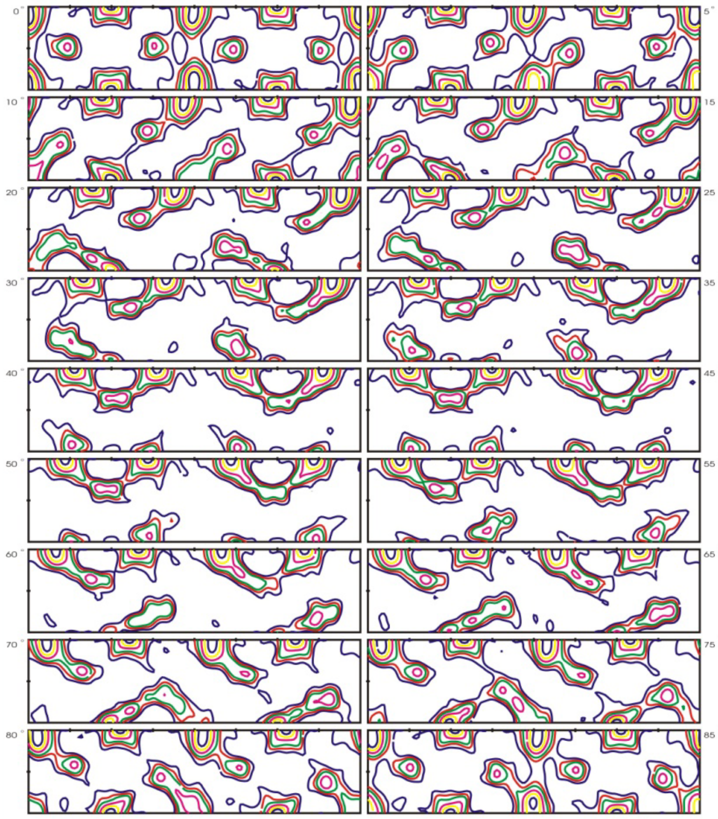

Fmax= 11.3 mrd

60°

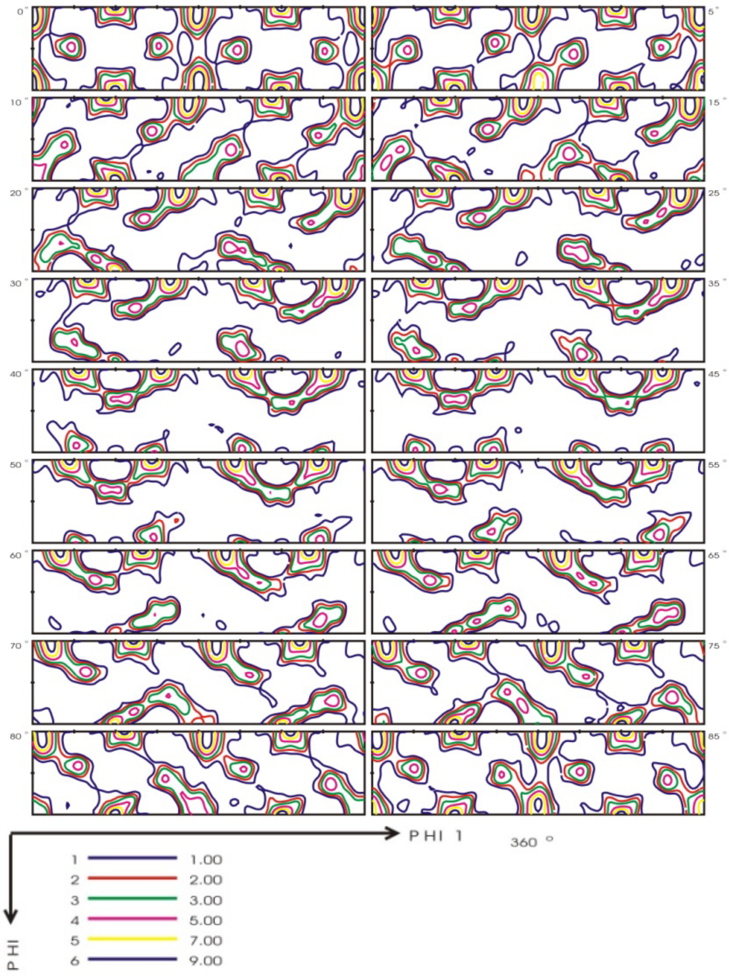

Fmax= 11.3 mrd

75°

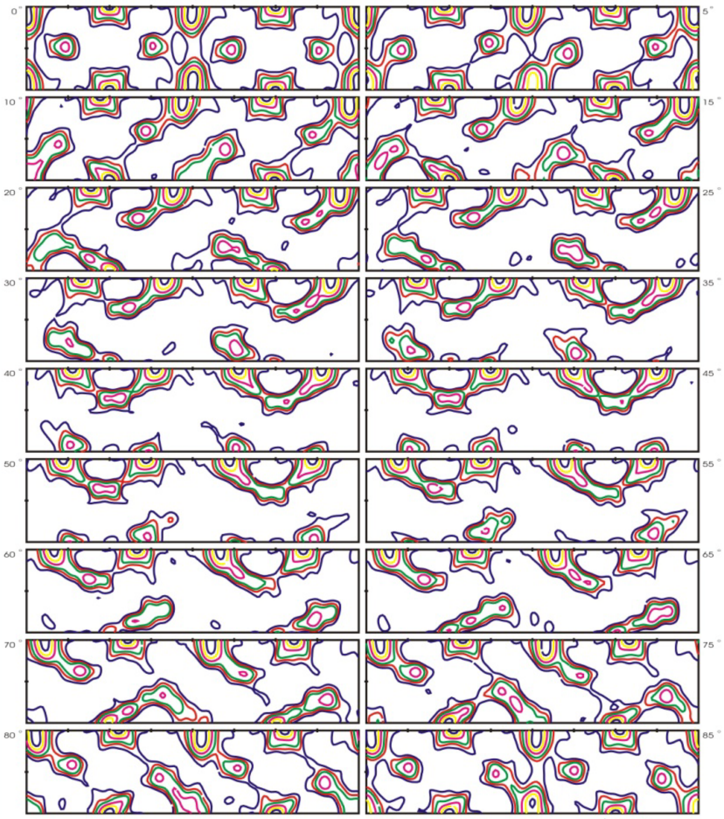

Fmax= 11 mrd

90°

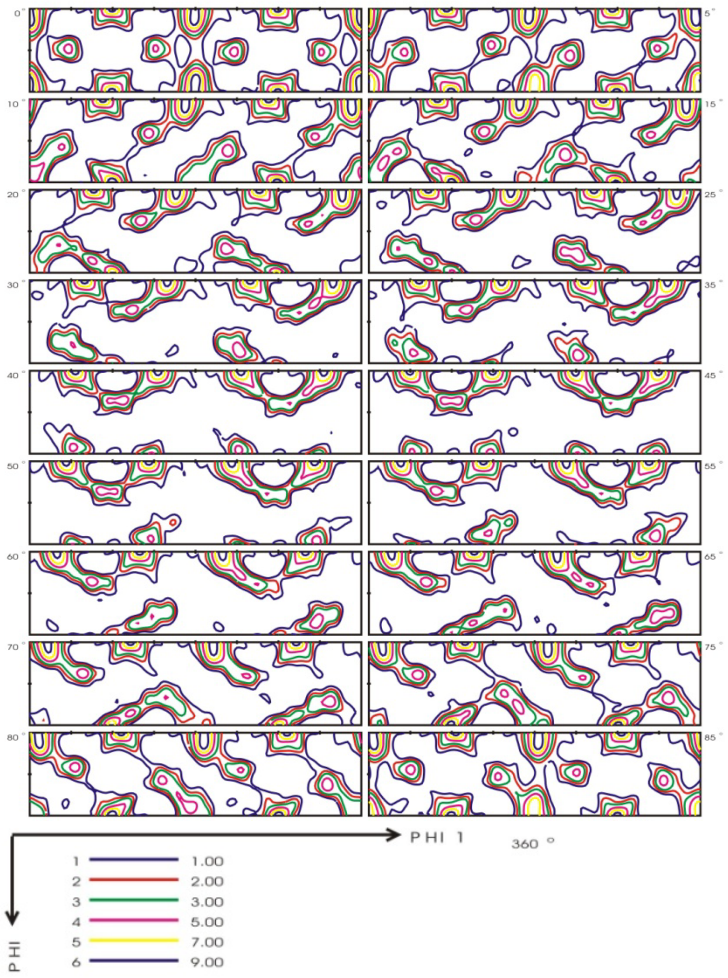

Fmax= 10.5 mrd

105°

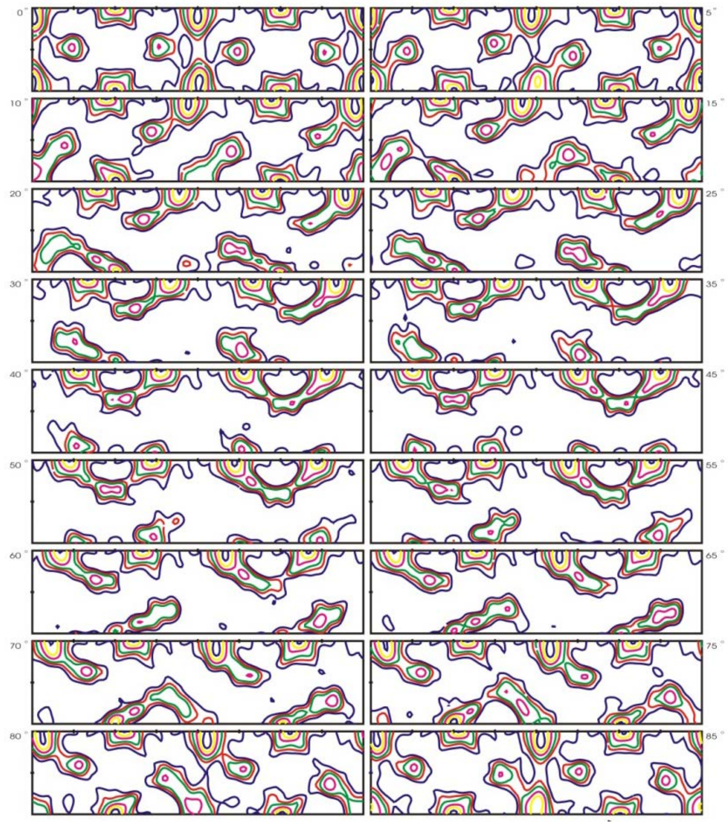

Fmax= 10.3 mrd

120°

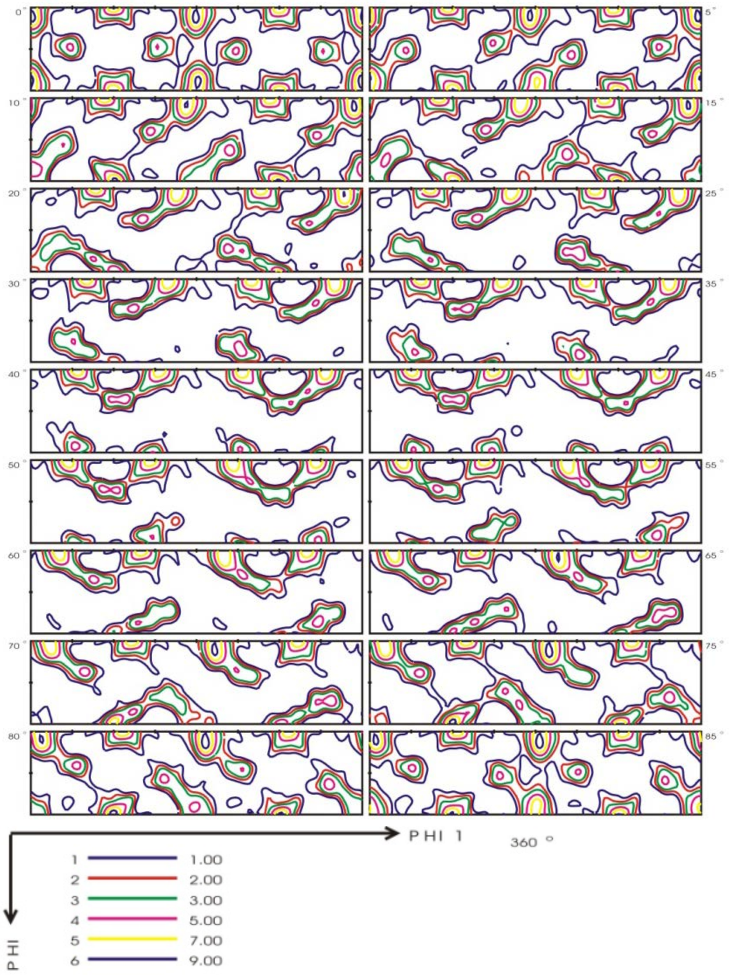

Fmax= 9.9 mrd

135°

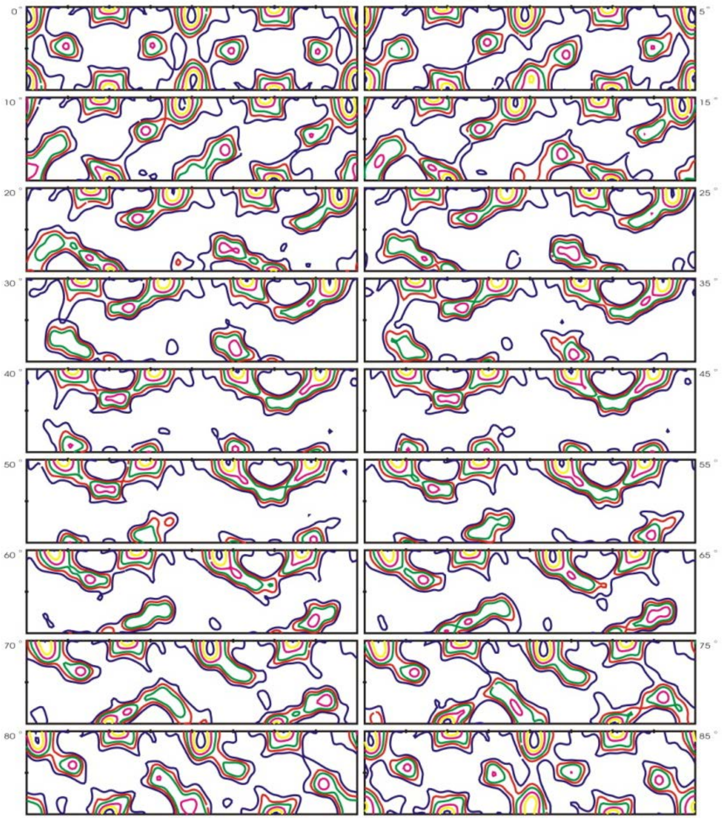

Fmax= 10.3 mrd

150°

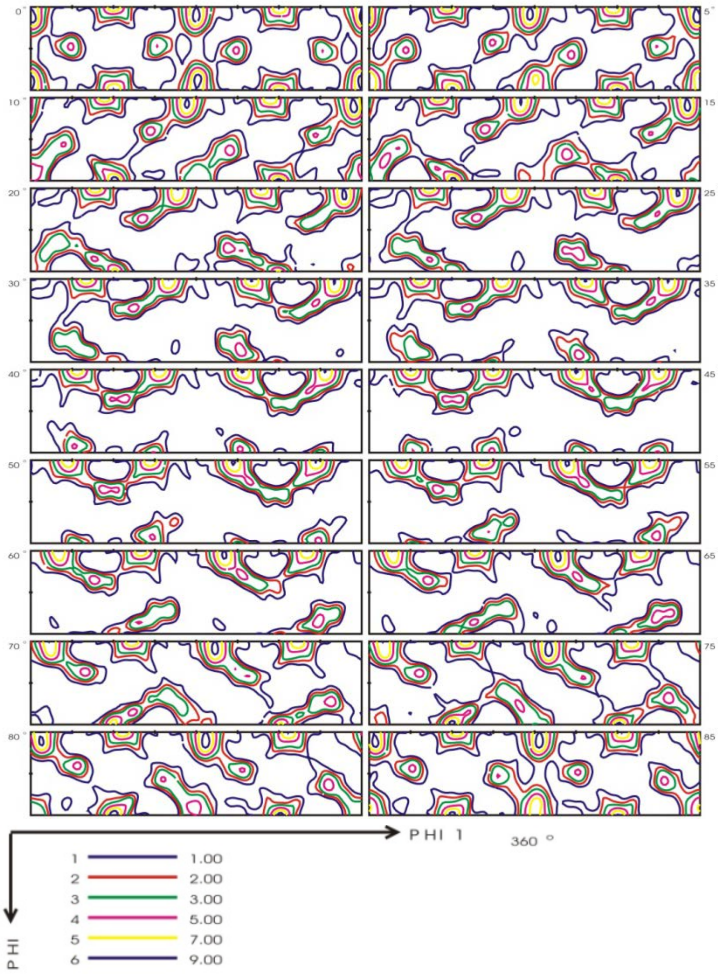

Fmax= 10 mrd

165°

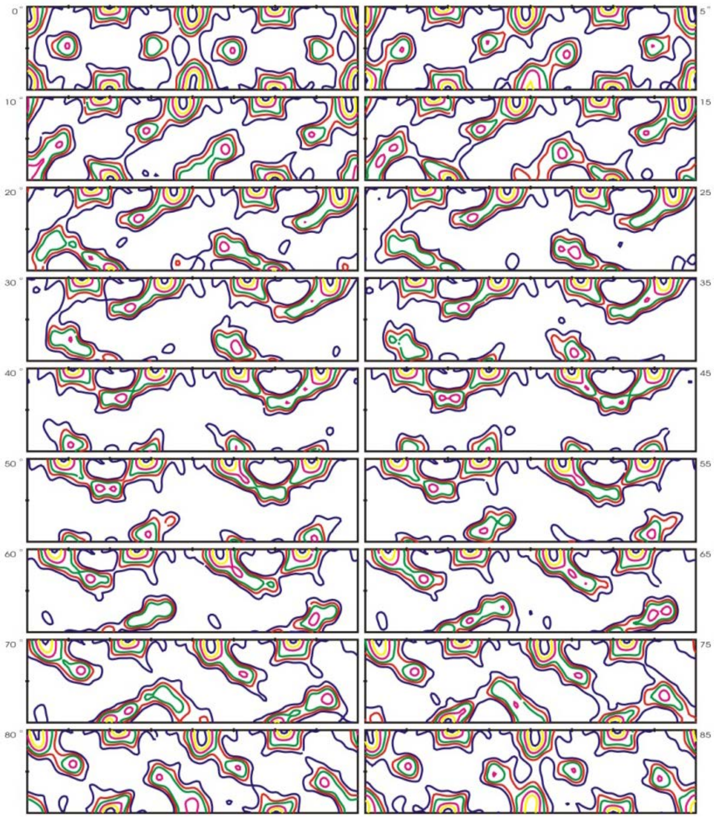

Fmax= 10.4 mrd

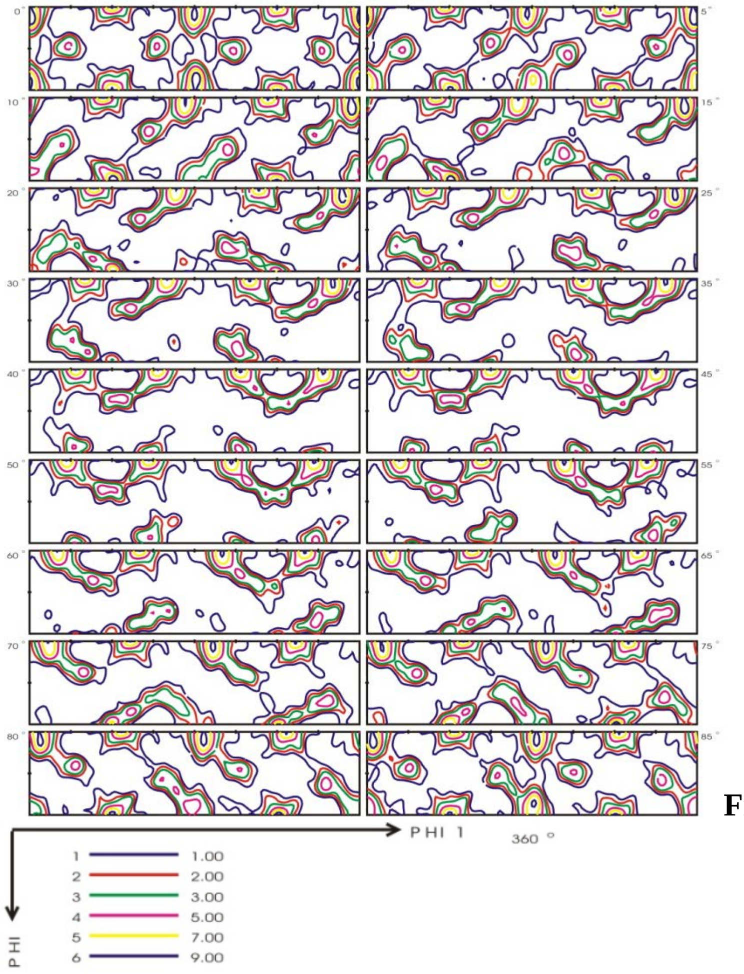

180°

Fmax= 10.6 mrd

4. ODF calculation of Cube sample for differt wall thickness

0°

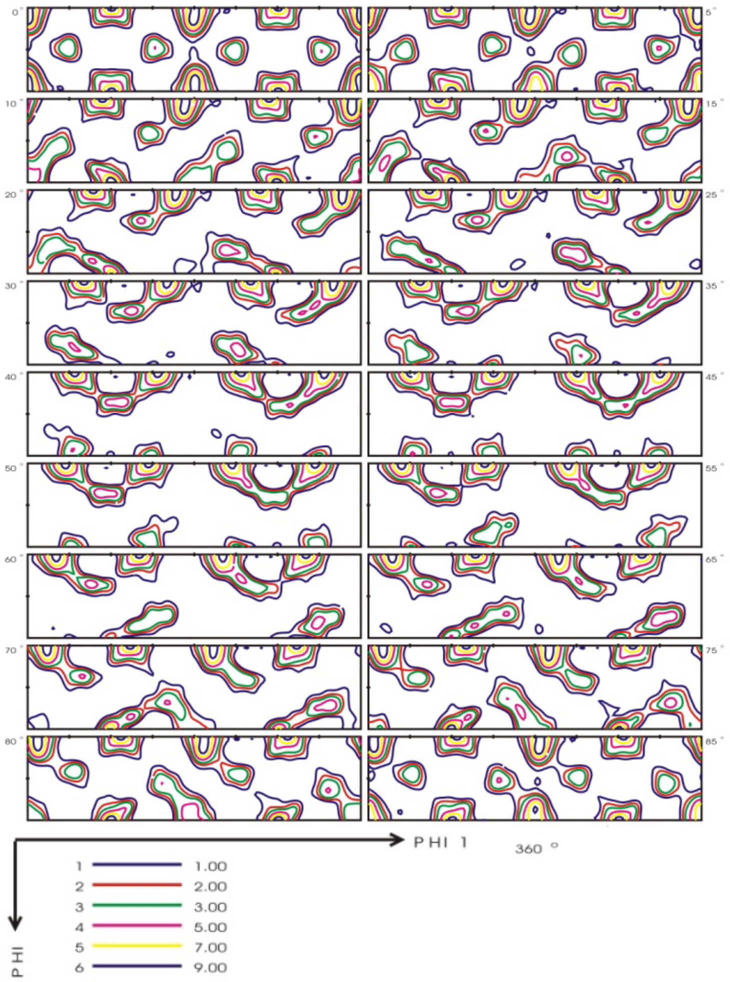

Fmax= 10.6 mrd

90°

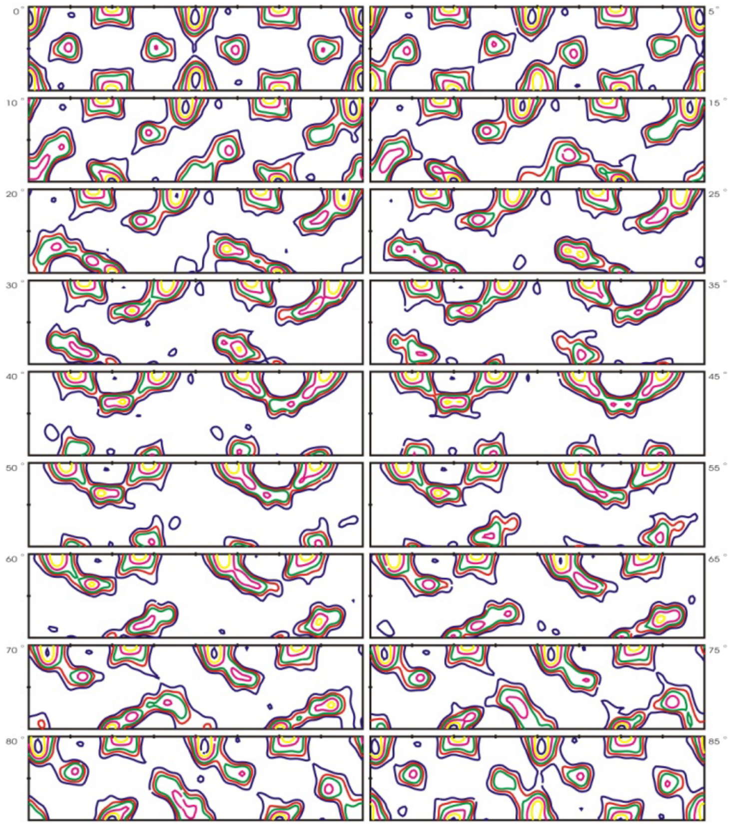

Fmax=10.5 mrd

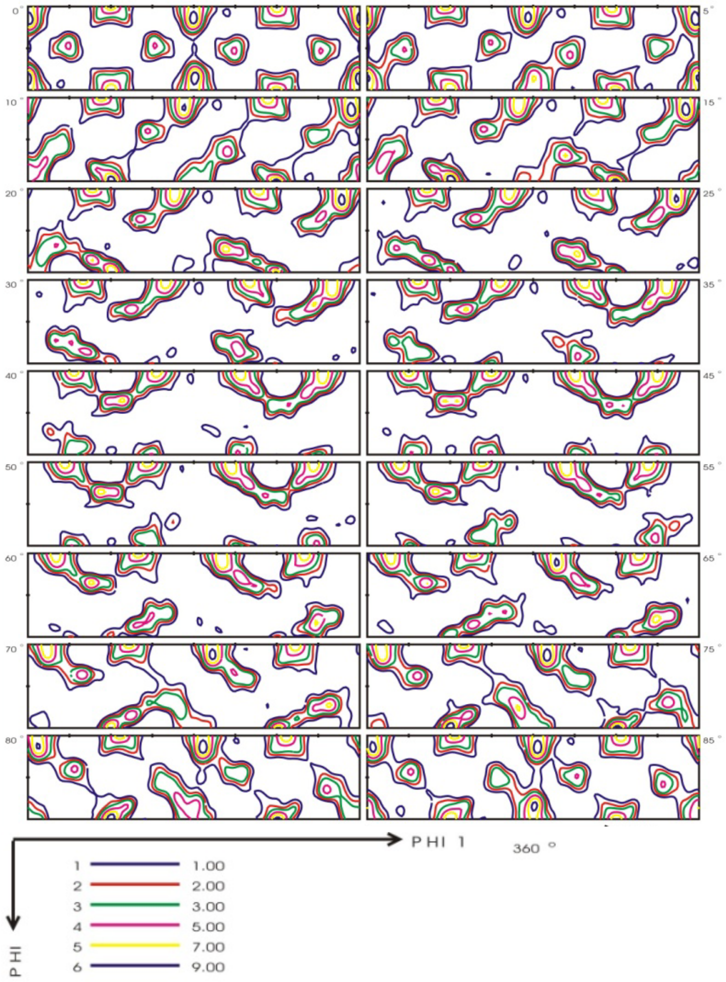

180°

Fmax= 10.5 mrd

Appendix 3

1. Pole figures variations at maximum wall thickness measured by synchrotron (all units in mrd)

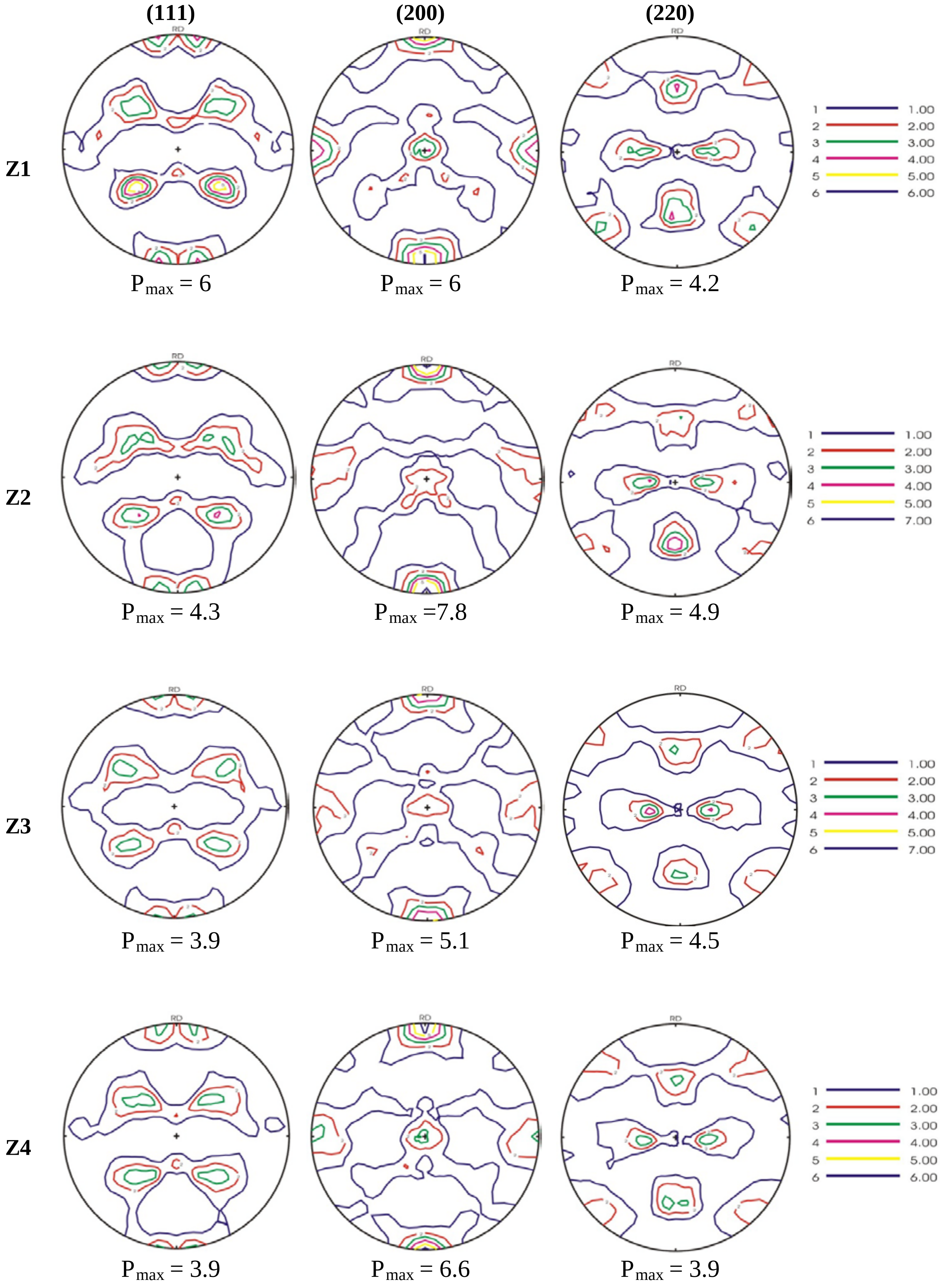

(111) **(200)** **(220)**

Z5

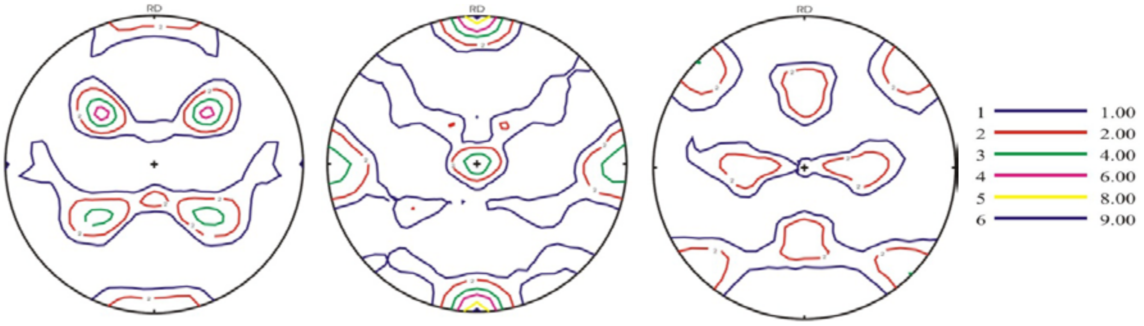

$P_{max} = 6.8$ $P_{max} = 9.5$ $P_{max} = 4.1$

2. Pole figures variations at middle thickness (all units in mrd)

(111) **(200)** **(220)**

Z1

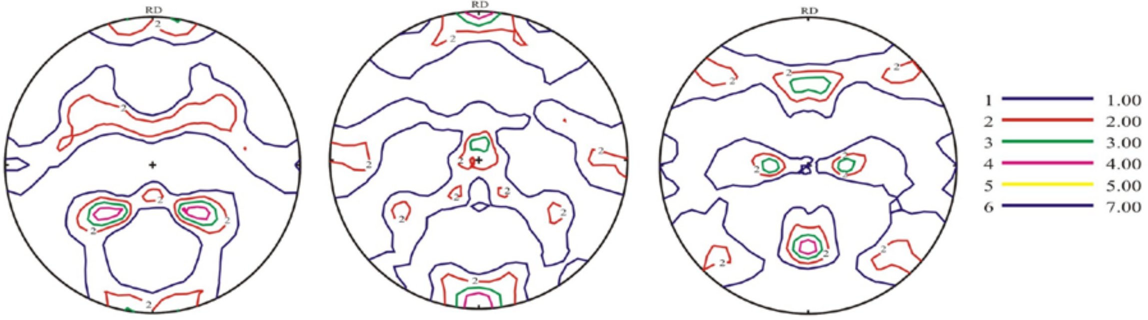

$P_{max} = 5$ $P_{max} = 5$ $P_{max} = 4.6$

Z2

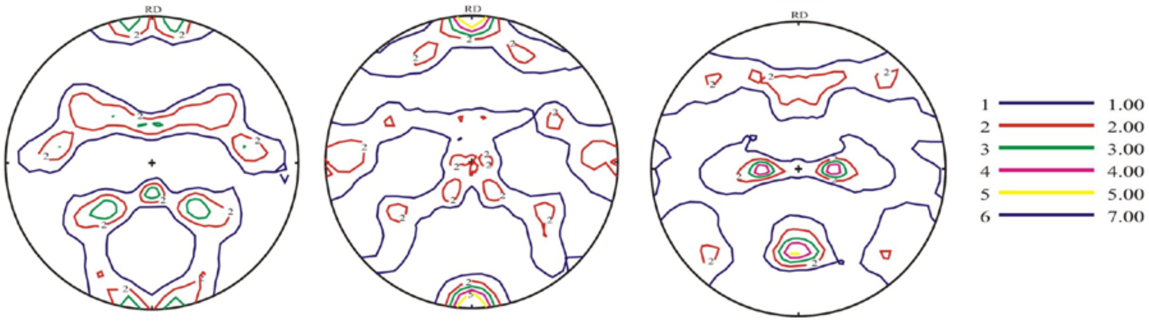

$P_{max} = 4$ $P_{max} = 7.1$ $P_{max} = 5$

Z3

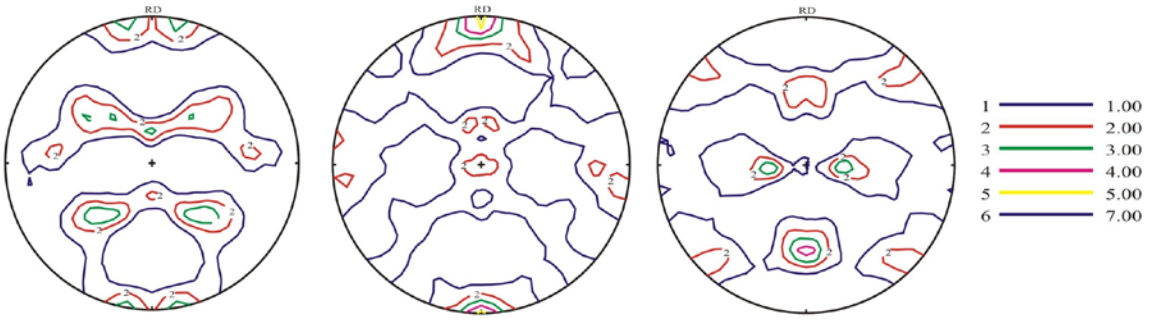

$P_{max} = 3.7$ $P_{max} = 5.3$ $P_{max} = 4.5$

(111) **(200)** **(220)**

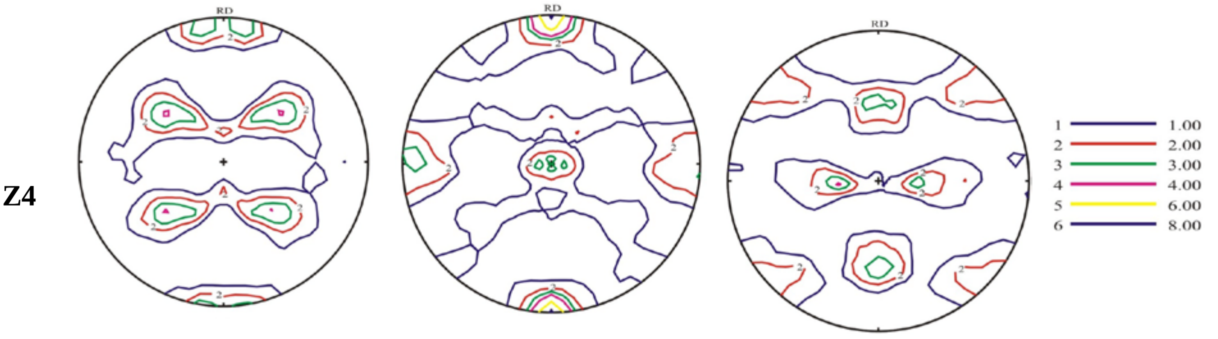

$P_{max} = 4.3$ $P_{max} = 8.4$ $P_{max} = 4.2$

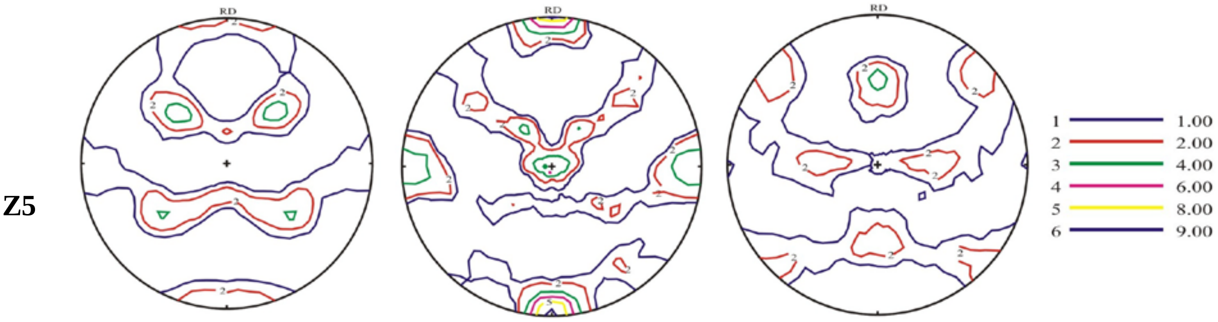

$P_{max} = 5.8$ $P_{max} = 9.2$ $P_{max} = 8.4$

3. Pole figures variations at minimum thickness (all units in mrd)

(111) **(200)** **(220)**

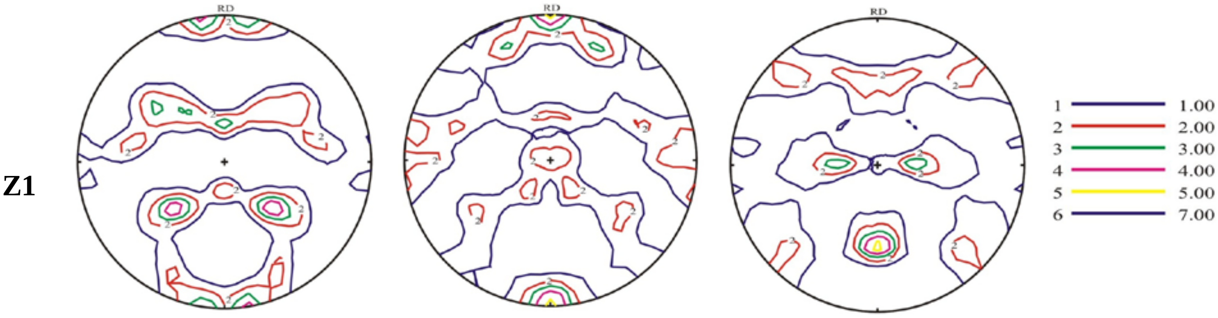

$P_{max} = 5$ $P_{max} = 5.5$ $P_{max} = 5.2$

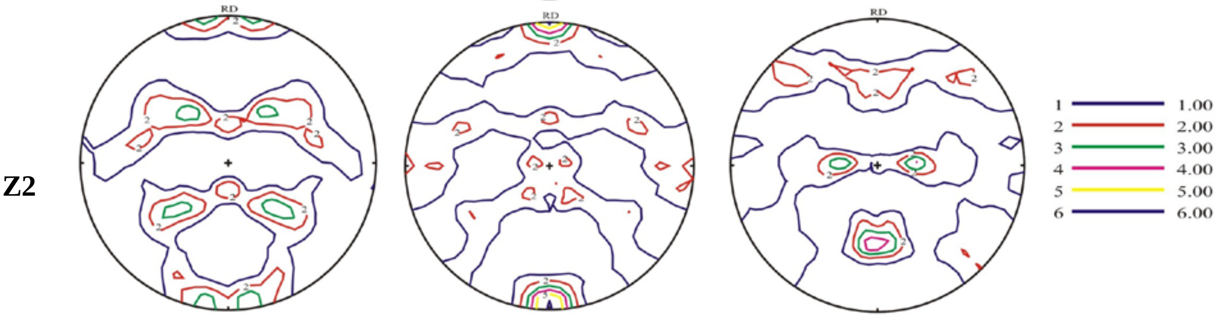

$P_{max} = 3.9$ $P_{max} = 6.3$ $P_{max} = 4.6$

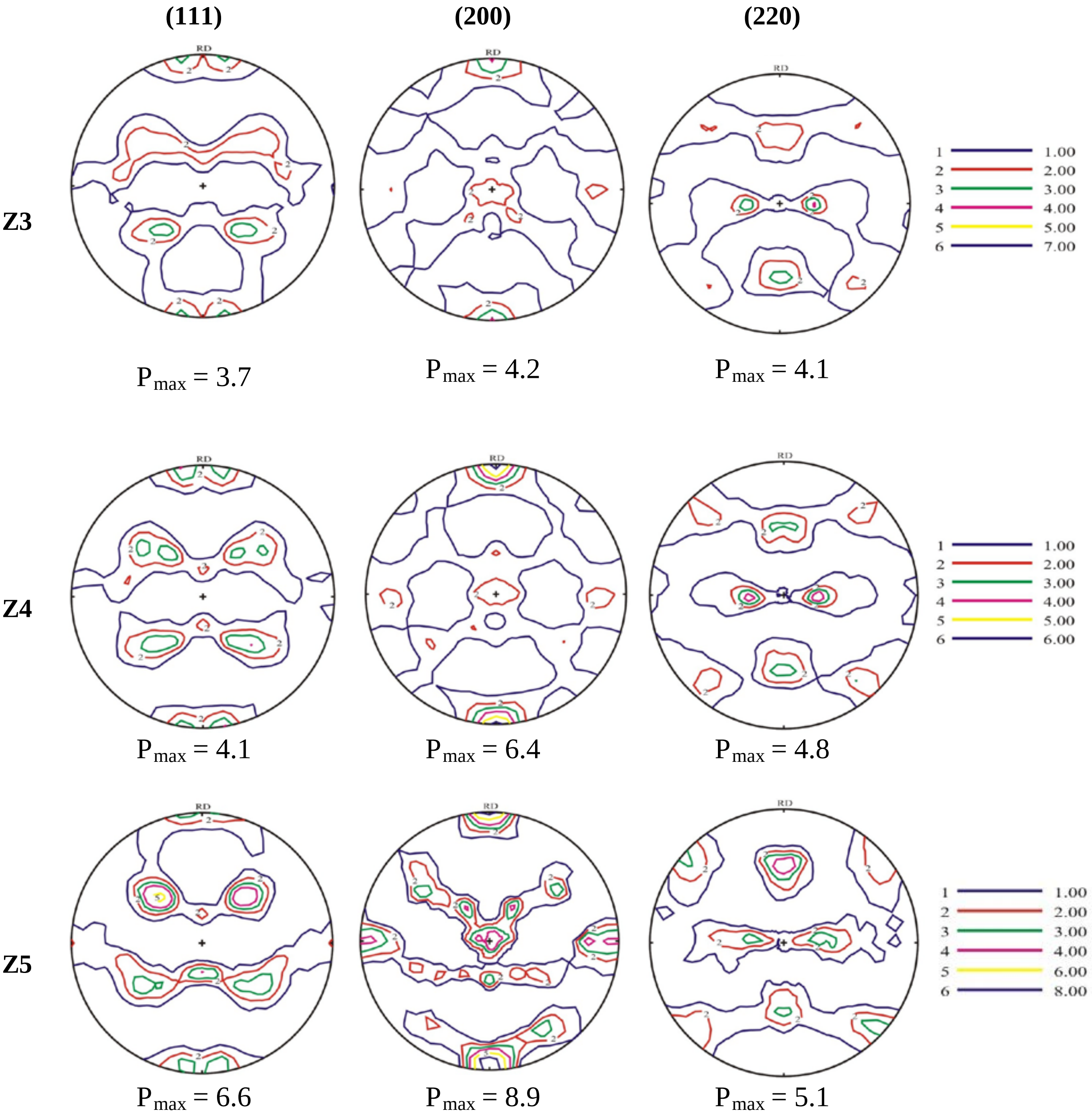
(111)
(200)
(220)
Z3
Z4
Z5
RD
P_{max} = 3.7
P_{max} = 4.2
P_{max} = 4.1
P_{max} = 4.1
P_{max} = 6.4
P_{max} = 4.8
P_{max} = 6.6
P_{max} = 8.9
P_{max} = 5.1
1 1.00
2 2.00
3 3.00
4 4.00
5 5.00
6 7.00
1 1.00
2 2.00
3 3.00
4 4.00
5 5.00
6 6.00
1 1.00
2 2.00
3 3.00
4 4.00
5 6.00
6 8.00

4. ODF variations at maximum wall thickness

Z1

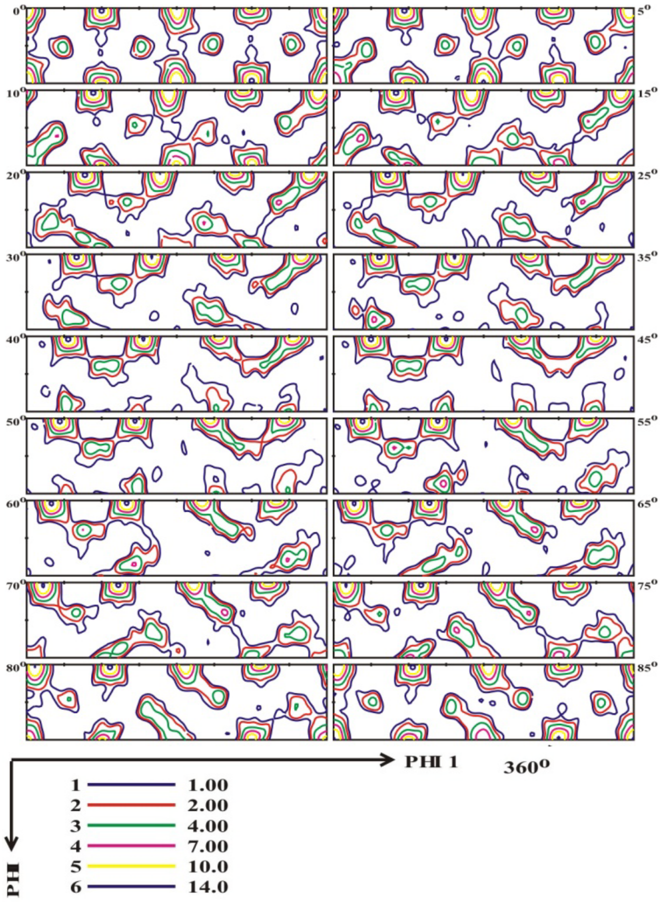

Fmax= 14.7 mrd

Z2

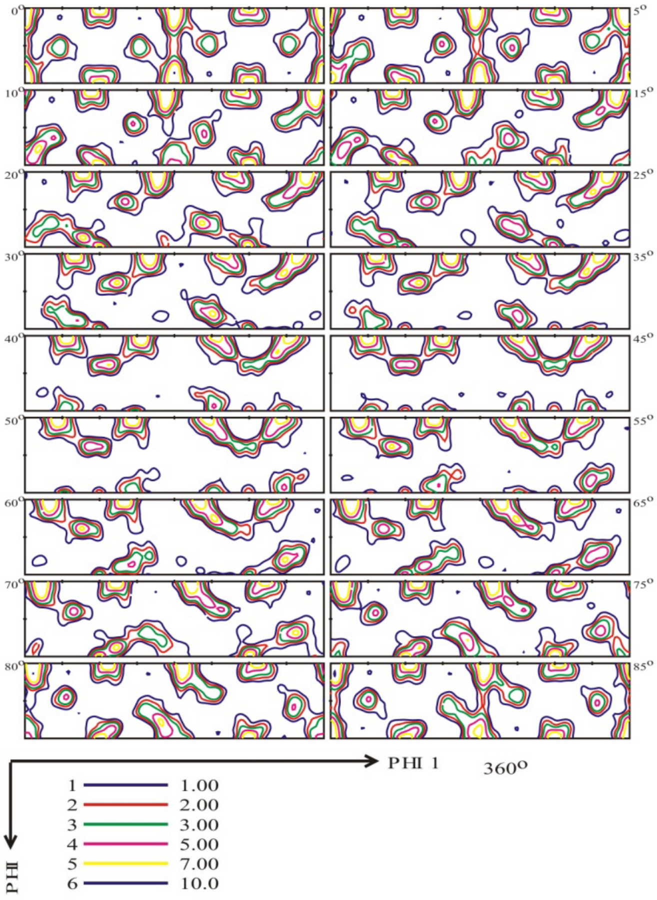

Fmax=10.2 mrd

Z3

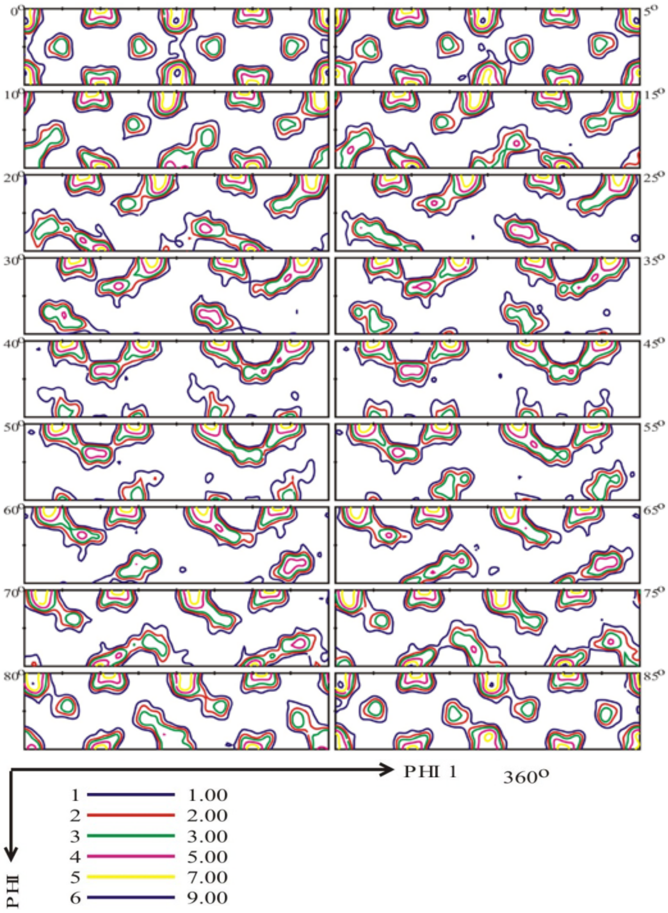

Fmax= 9.5 mrd

Z4

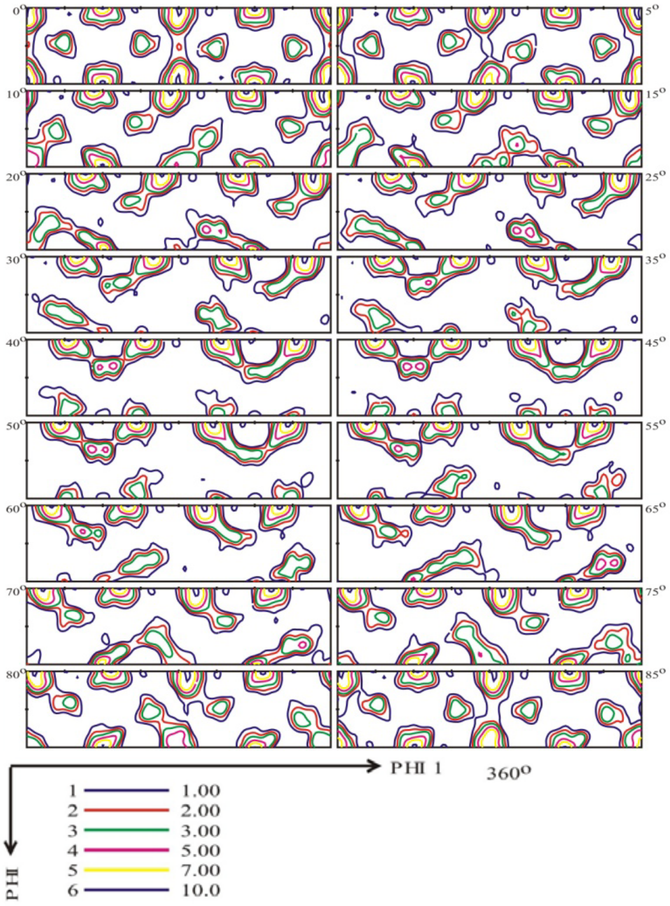

Fmax= 10.6 mrd

Z5

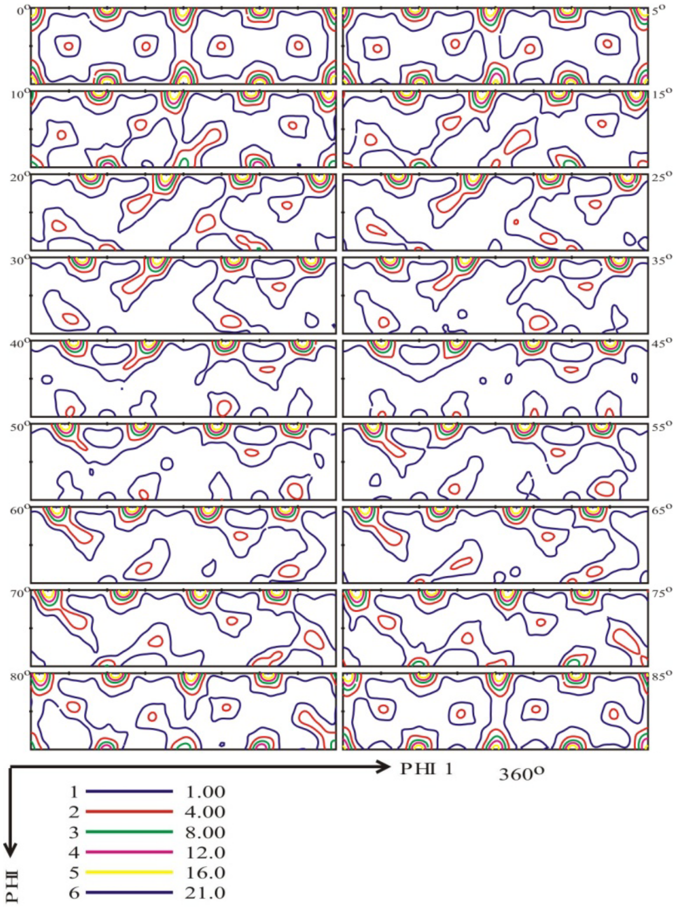

Fmax= 21.1 mrd

5. ODF variations at middle thickness

Z1

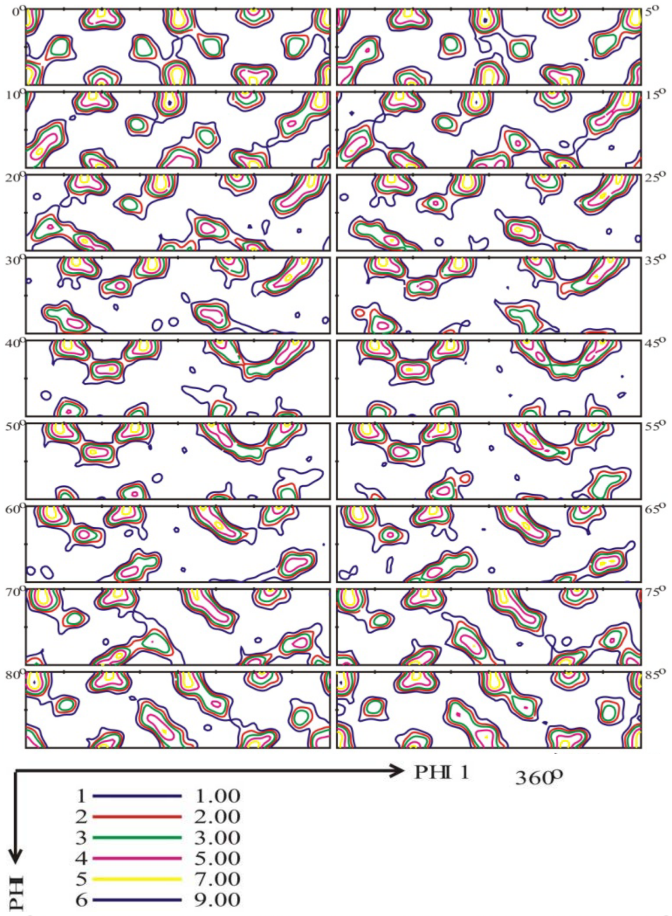

Fmax= 9.2 mrd

Z2

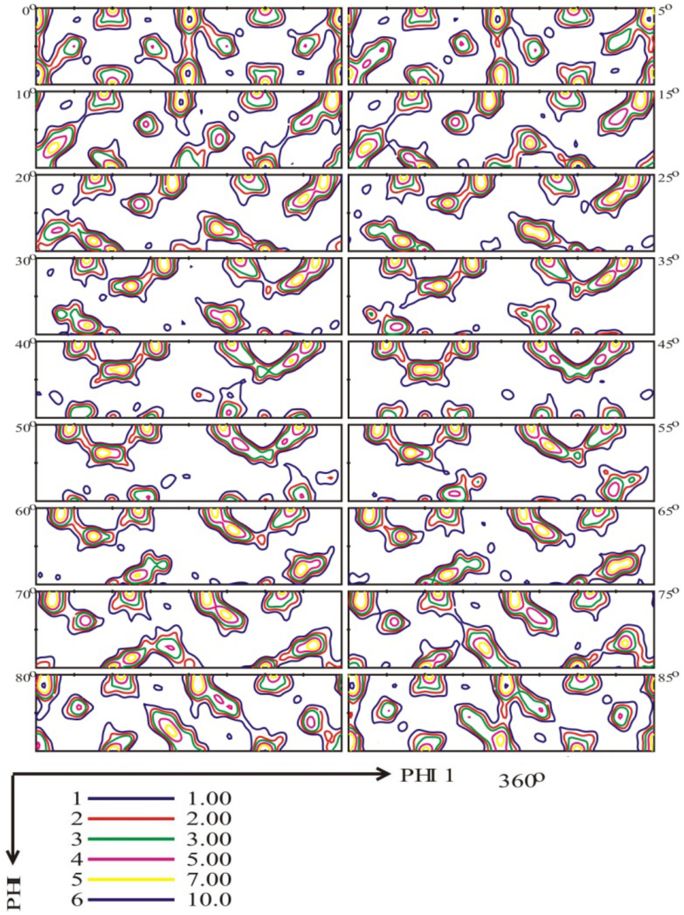

Fmax= 10.6 mrd

Z3

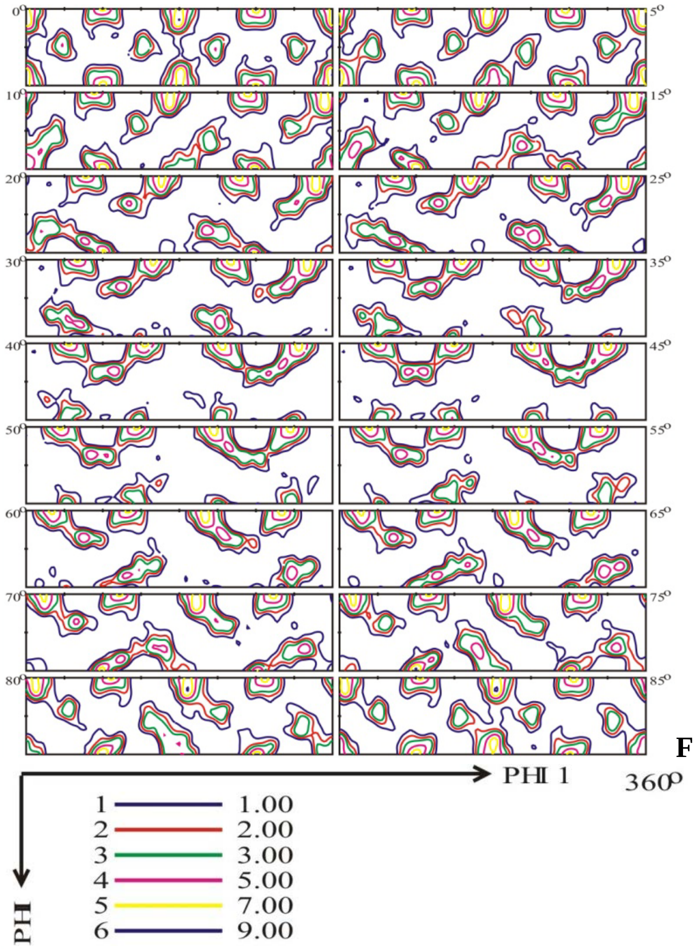

Fmax= 9.2 mrd

Z4

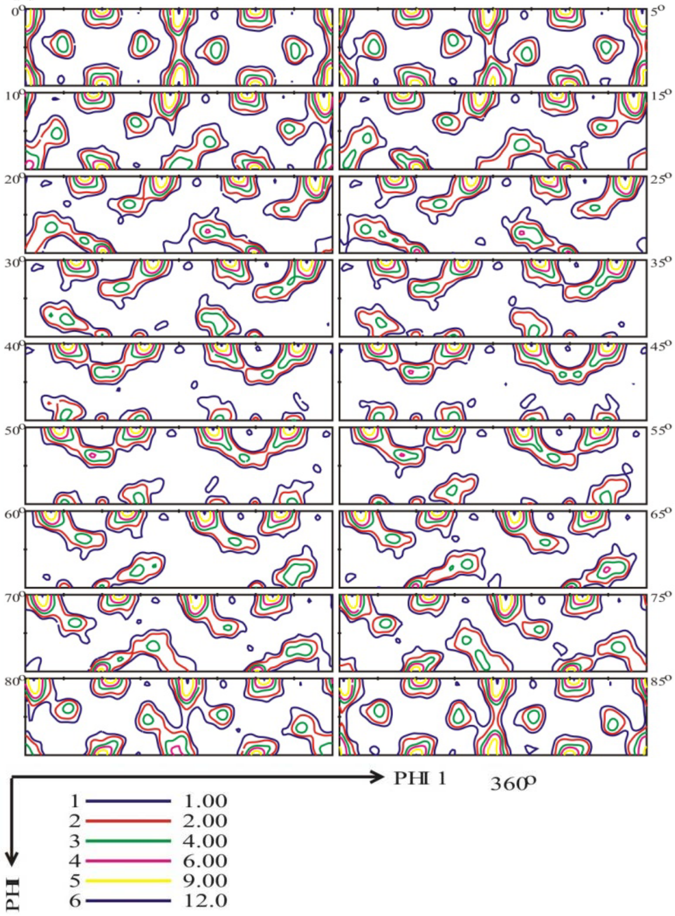

Fmax= 12.2 mrd

Z5

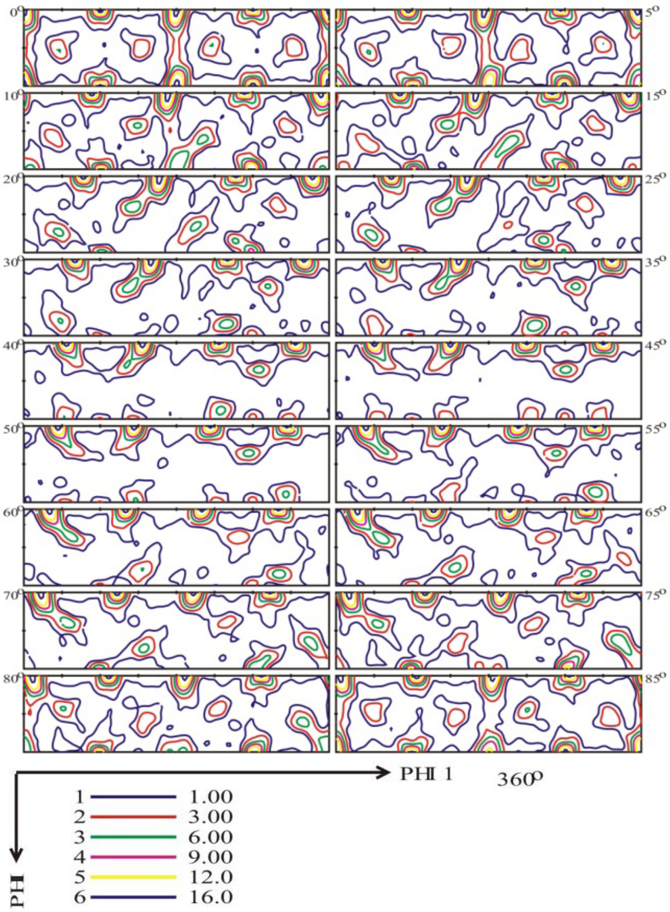

Fmax= 16.9 mrd

6. ODF variations at minimum wall thickness

Z1

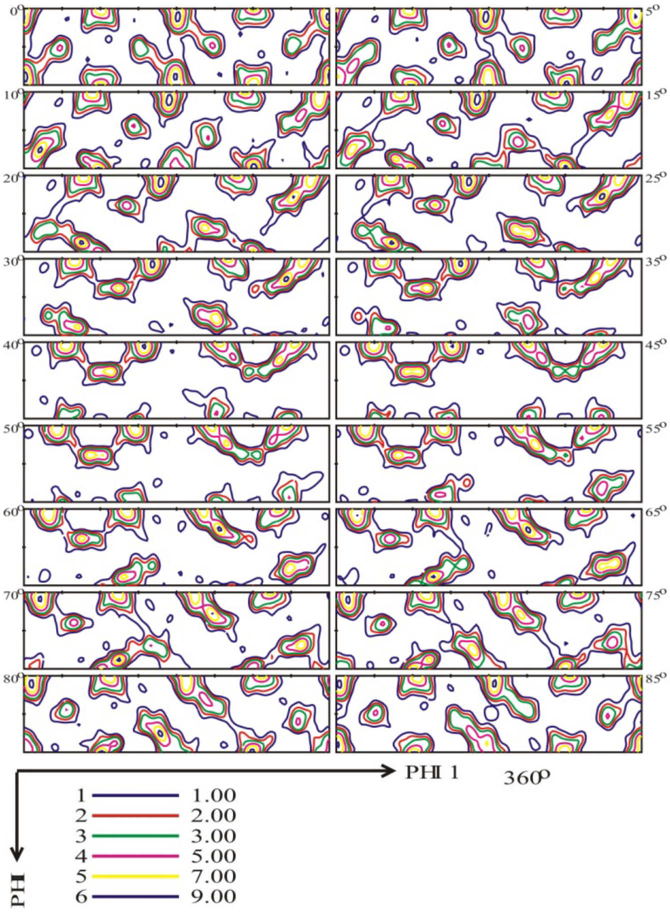

Fmax= 9.8 mrd

Z2

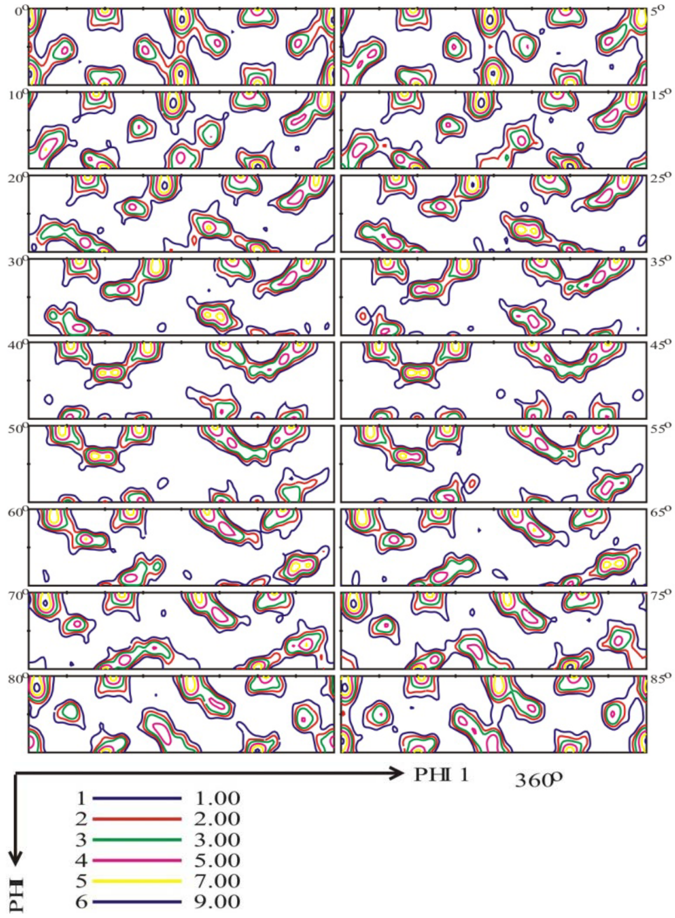

Fmax= 10 mrd

Z3

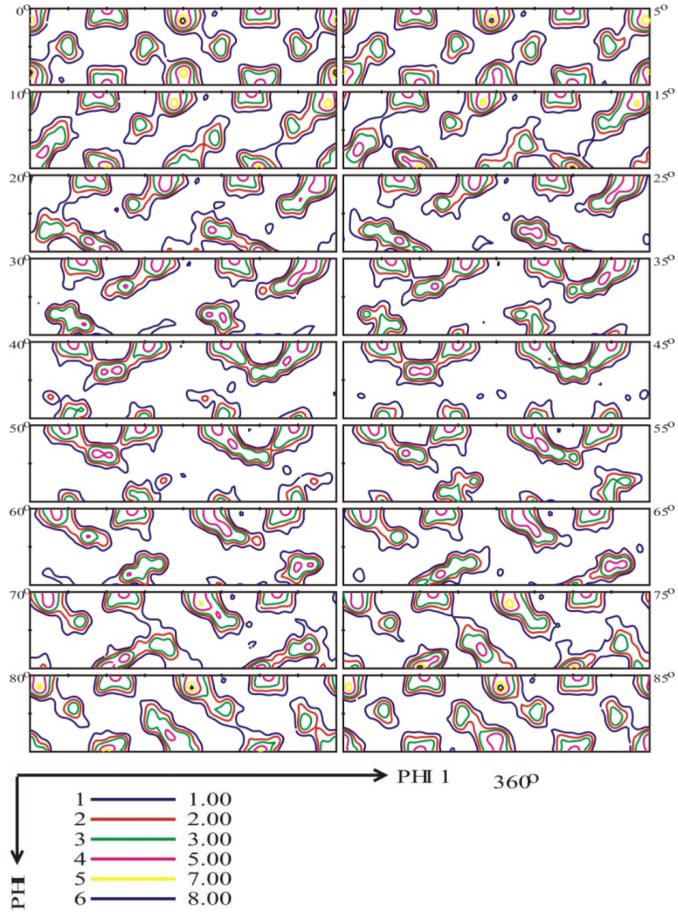

Fmax= 8.5 mrd

Z4

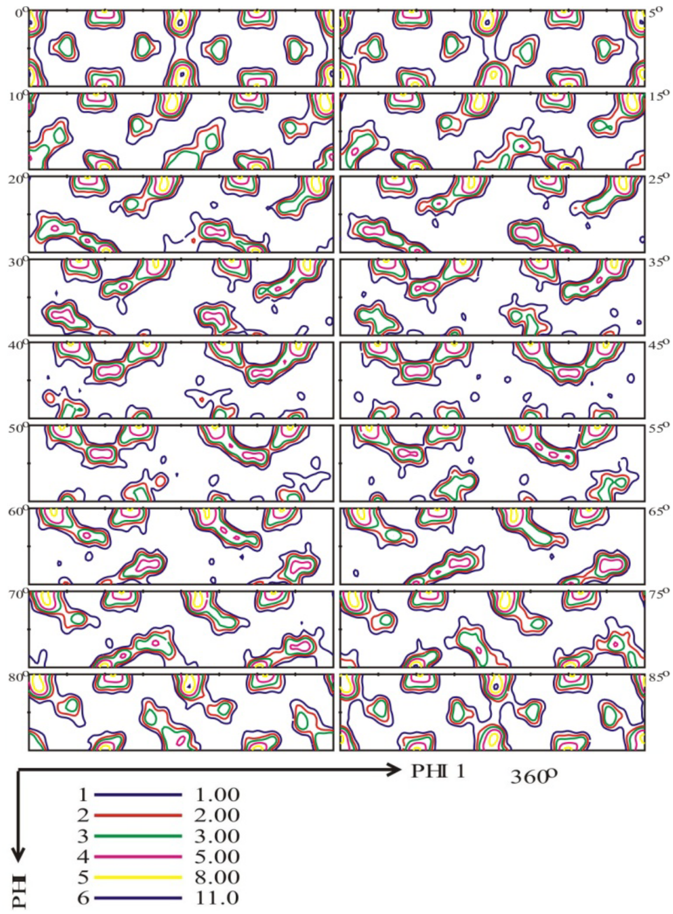

Fmax= 11.6 mrd

Z5

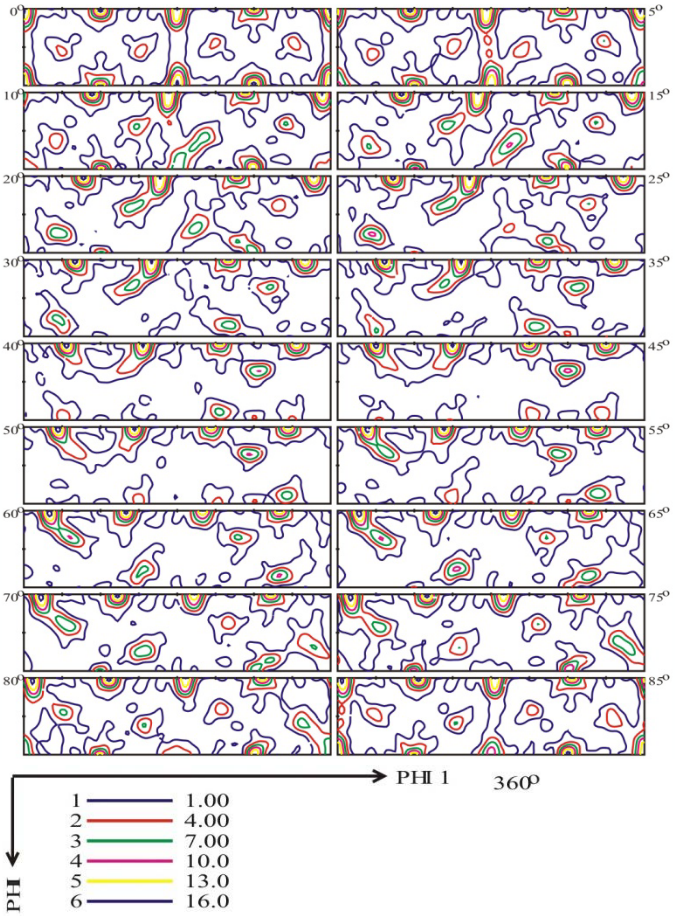

Fmax= 16.9 mrd

Appendix 4

1. EBSD map

Map Nr.

1

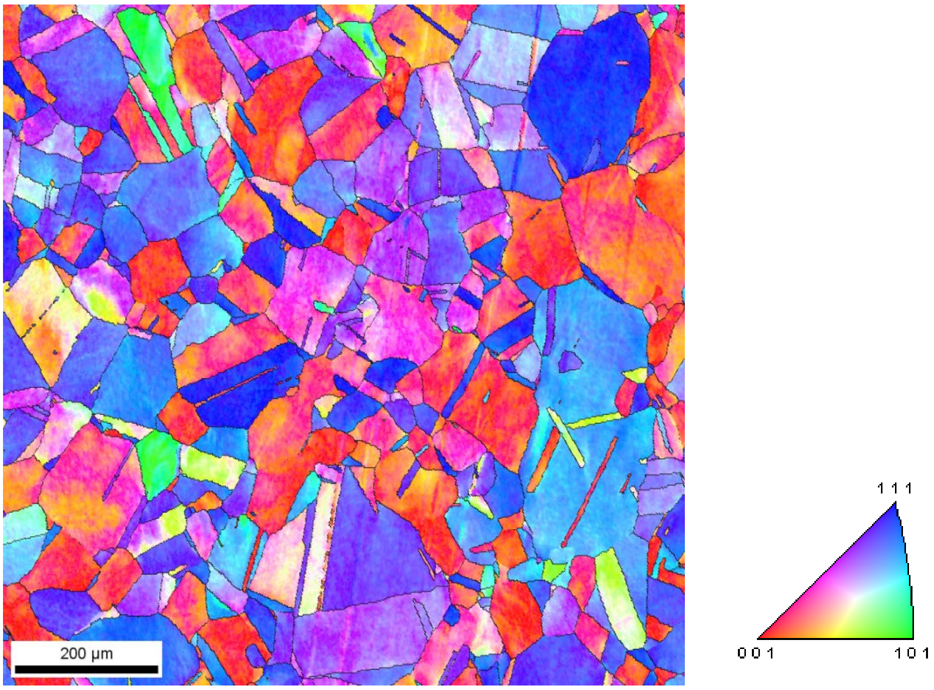

2

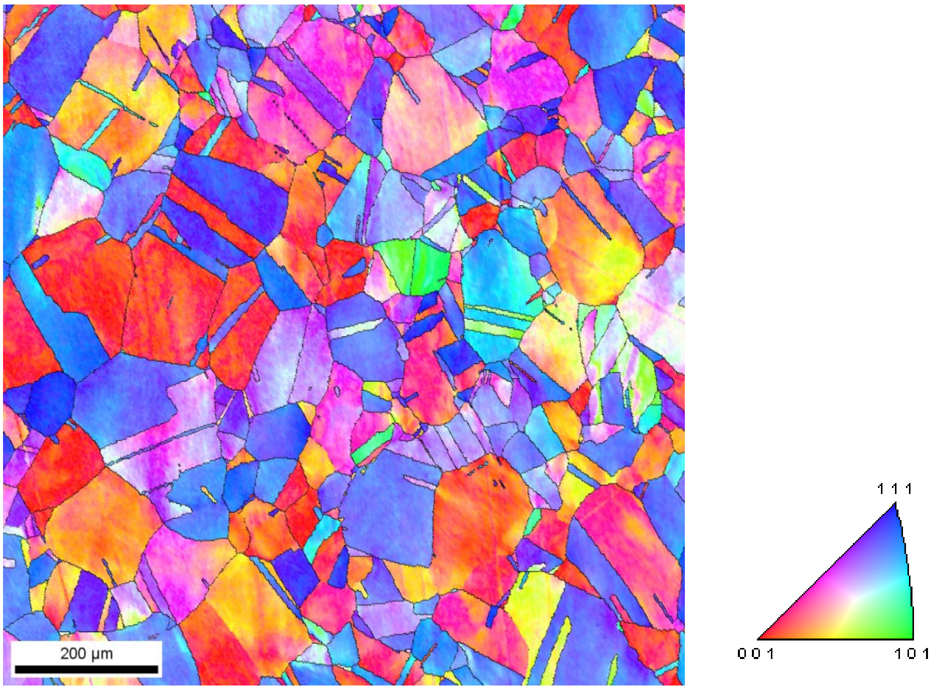

3

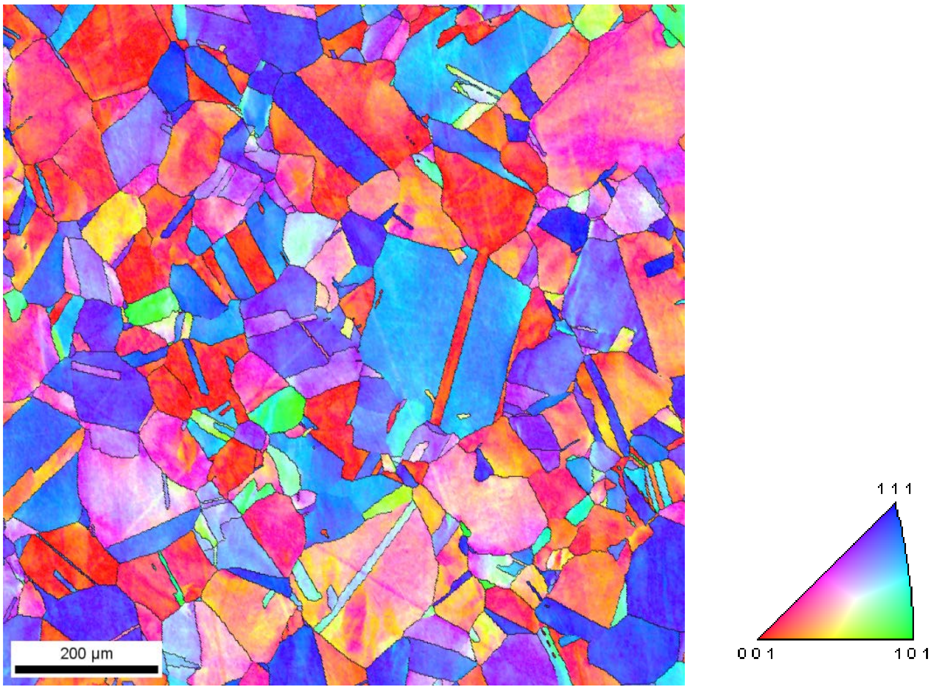

4

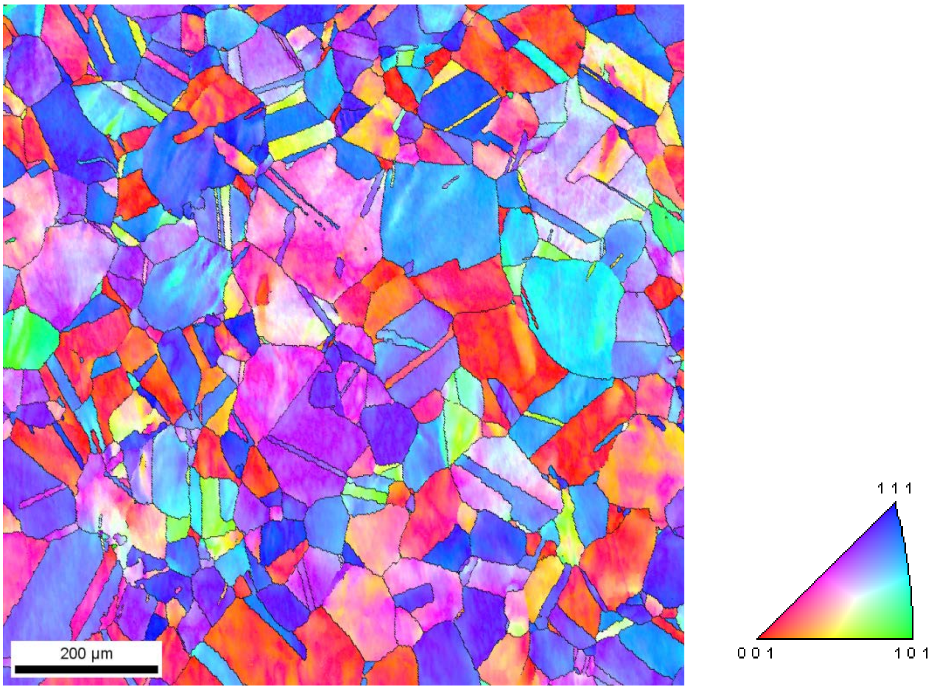

5

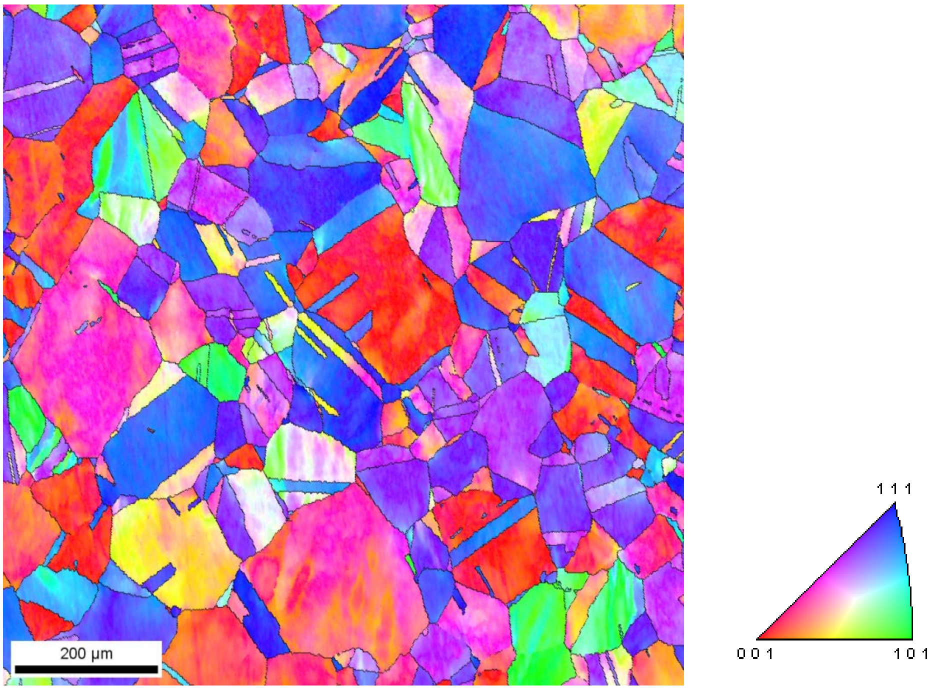

6

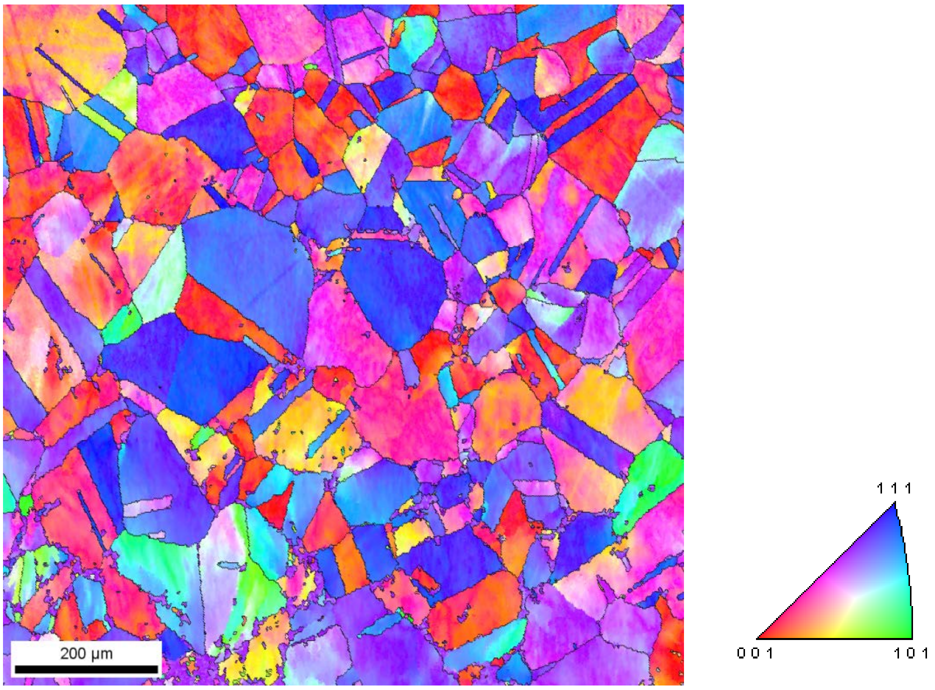

7

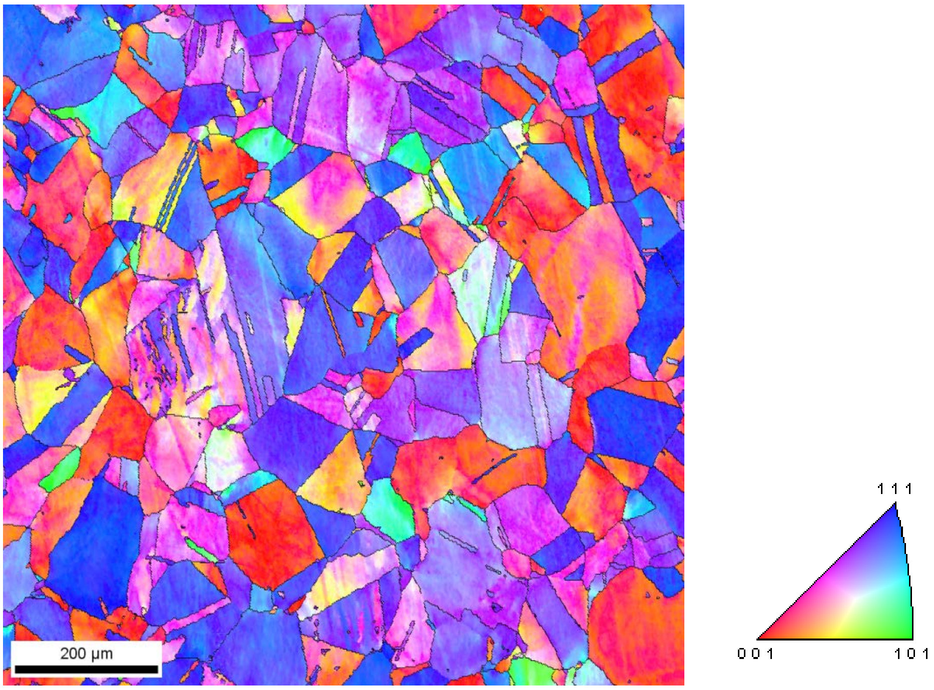

8

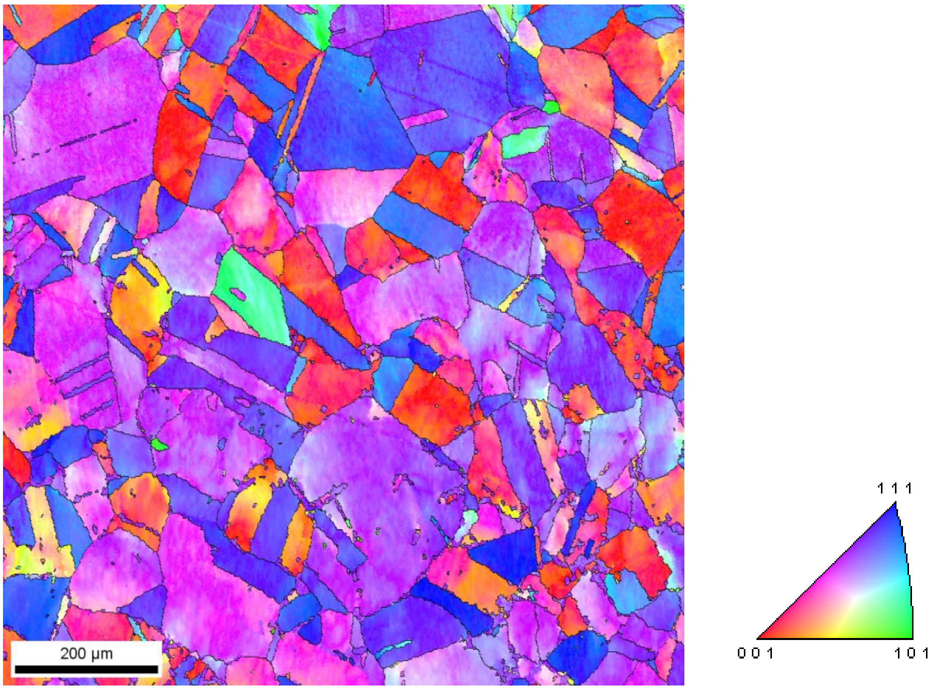

9

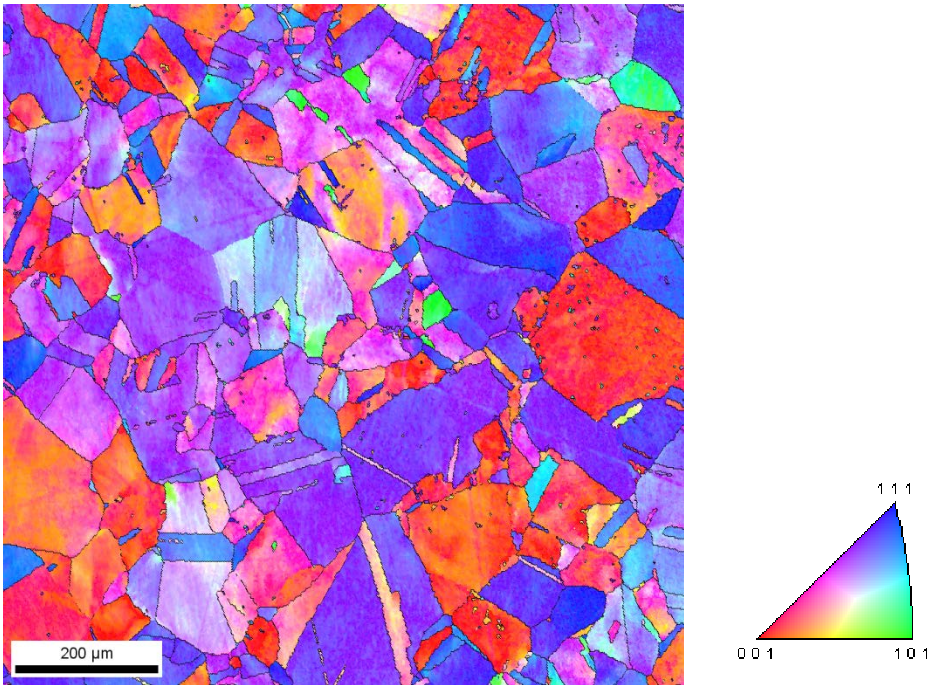

2. ODFs of the EBSD maps

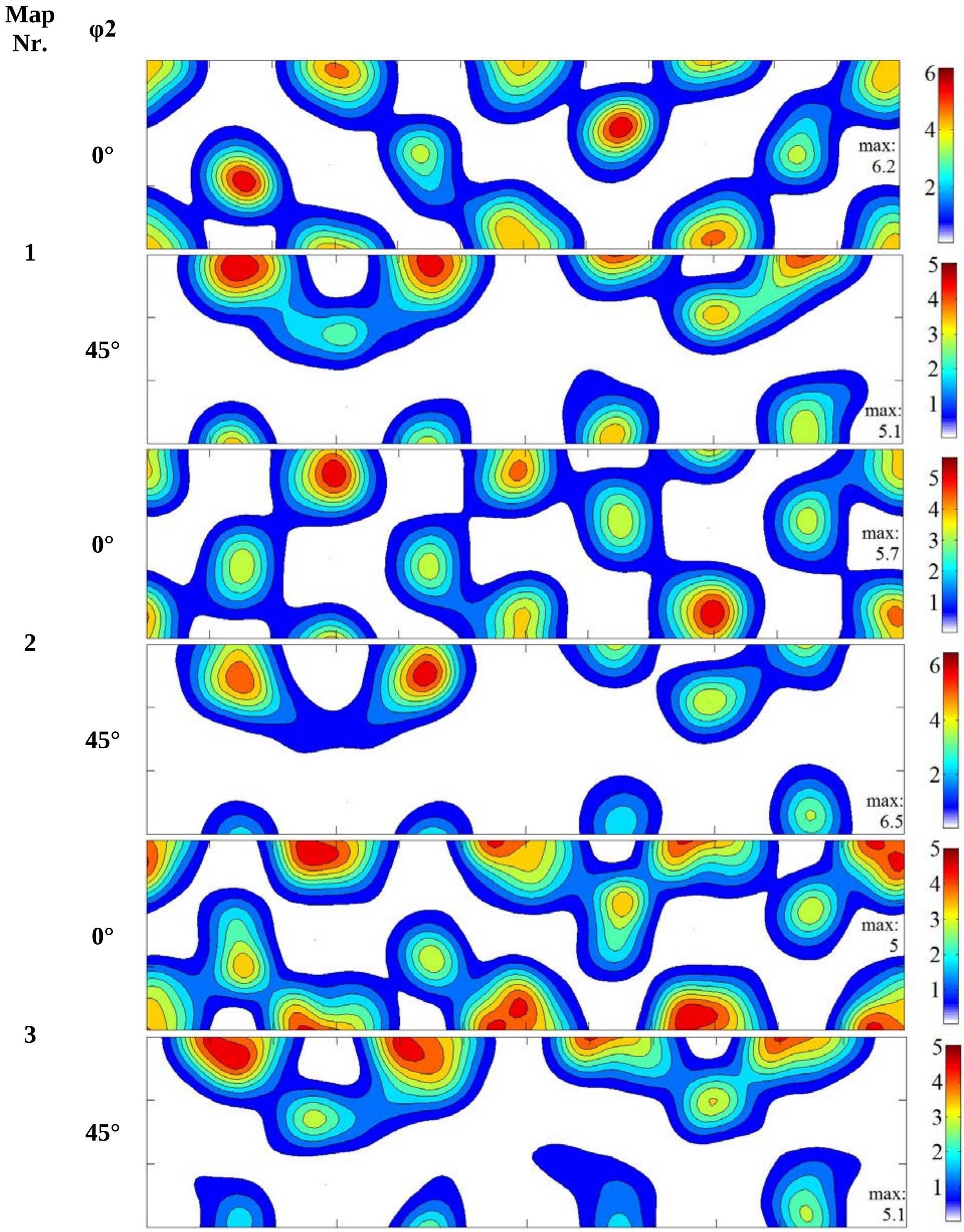

0°

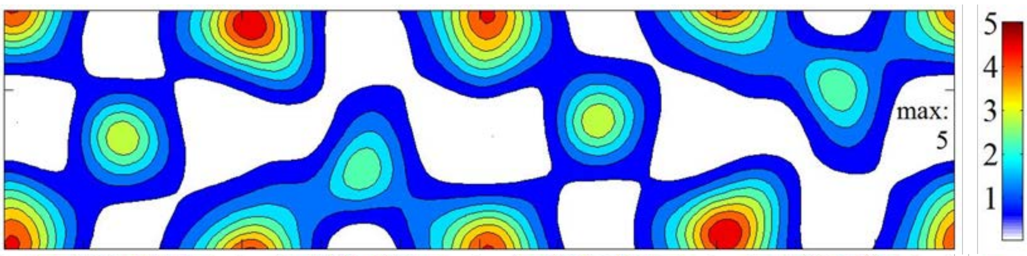

4

45°

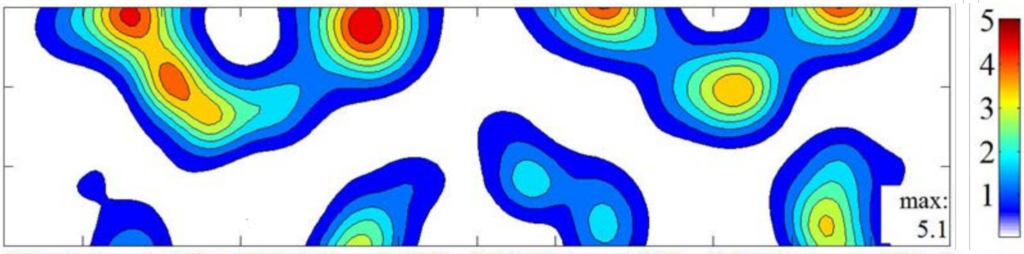

0°

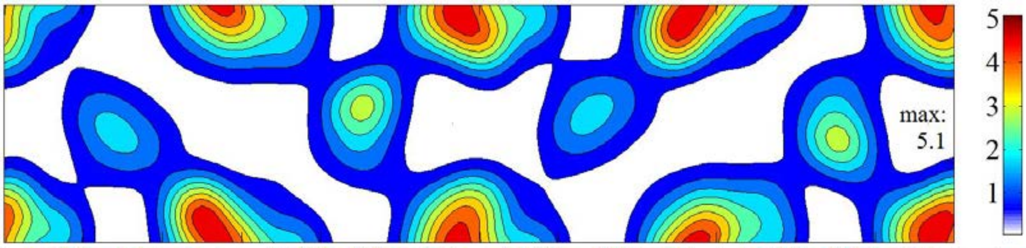

5

45°

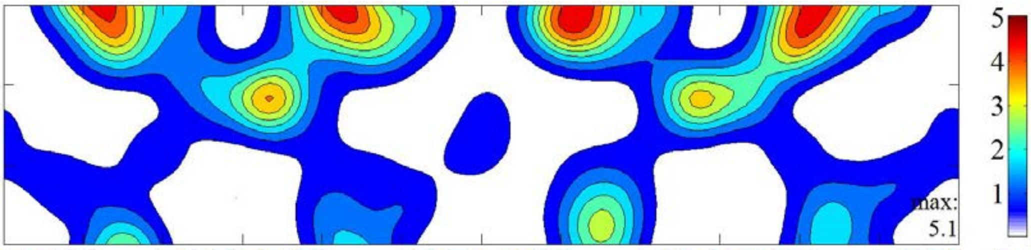

0°

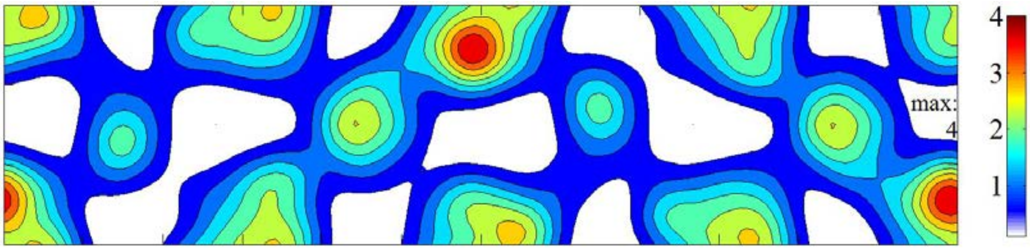

6

45°

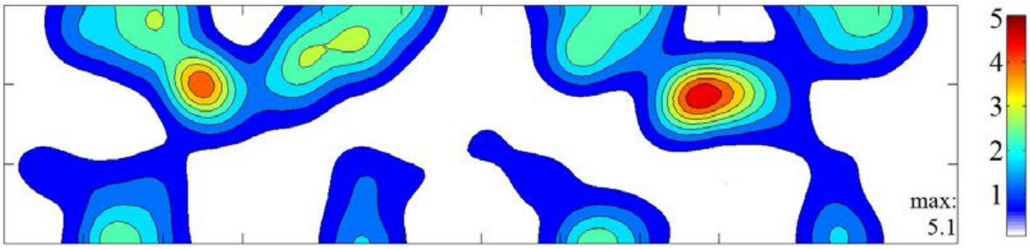

7

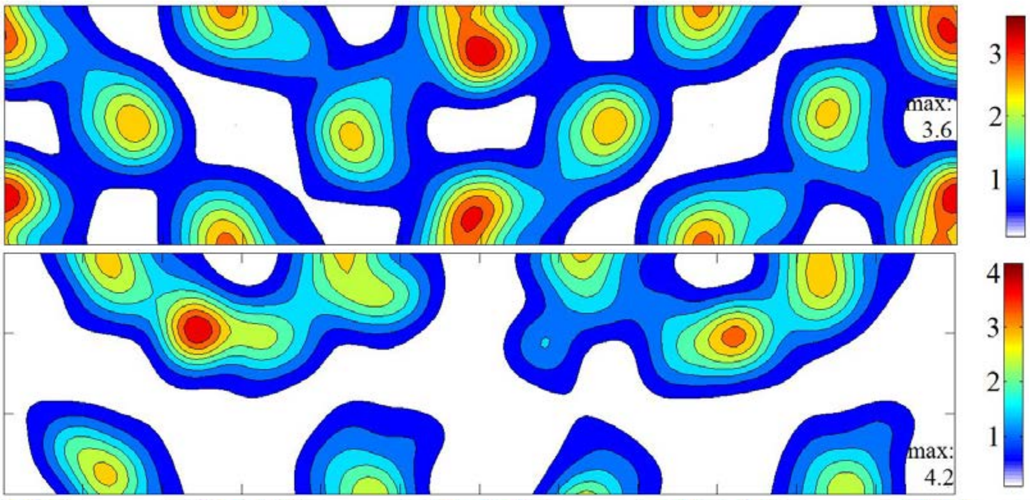

0°

45°

8

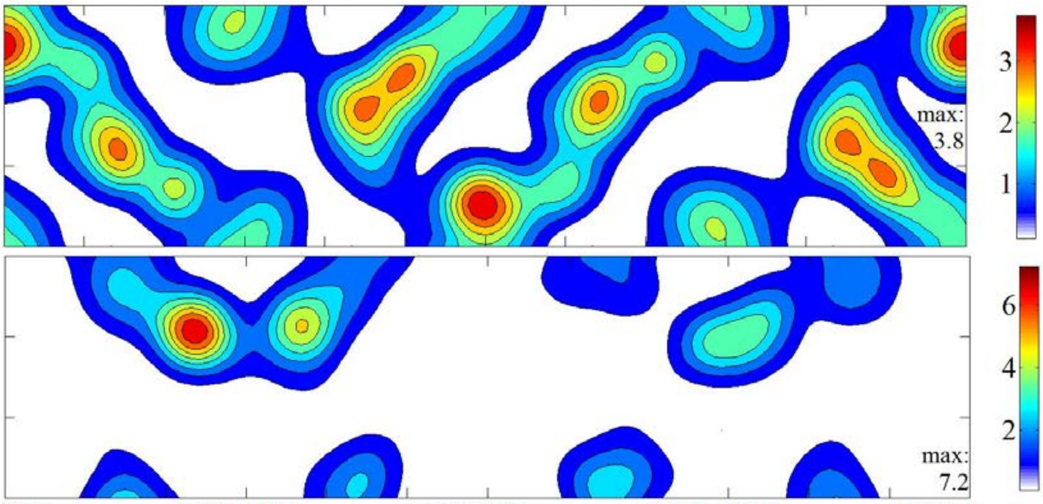

0°

45°

9

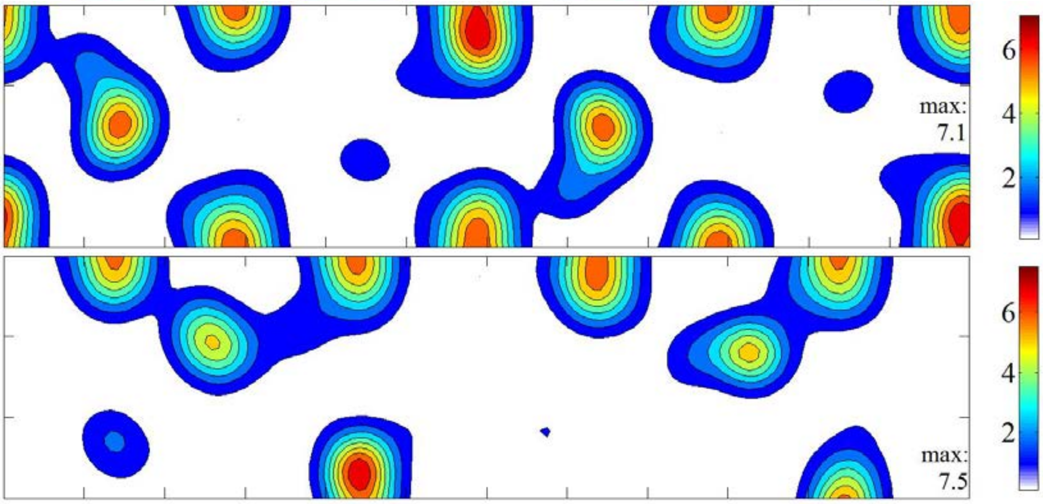

0°

45°

3. The calculated pole figure of the EBSD maps

Map Nr.

1

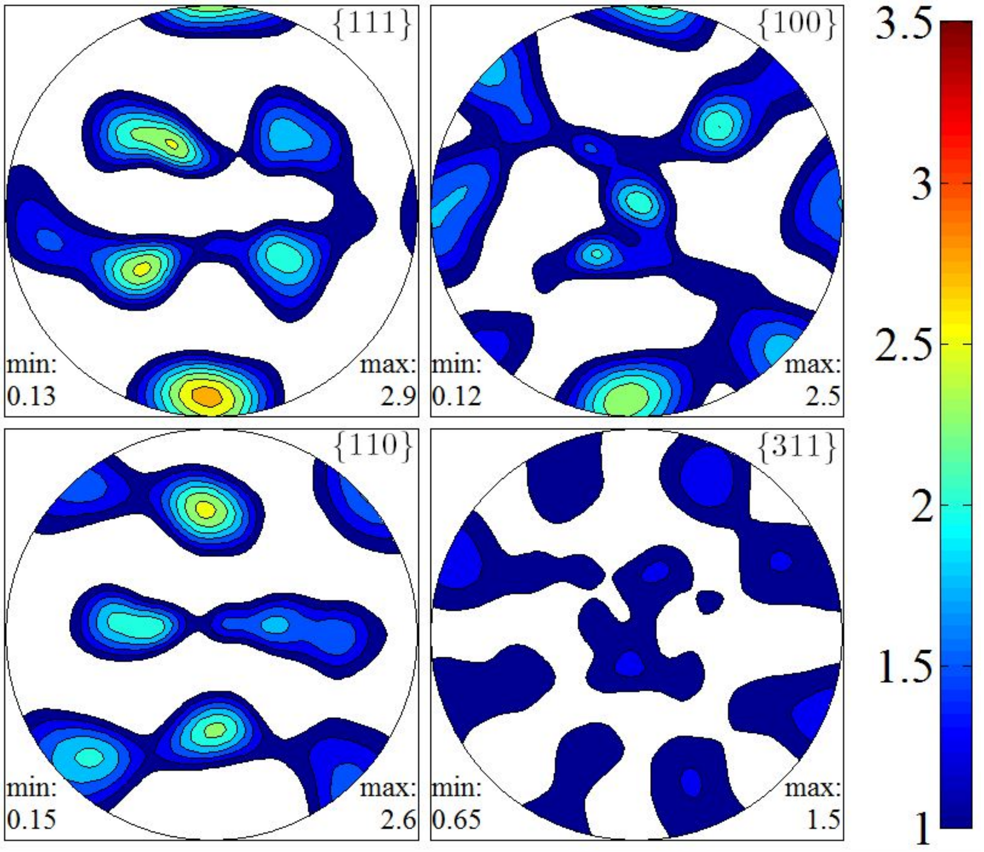

2

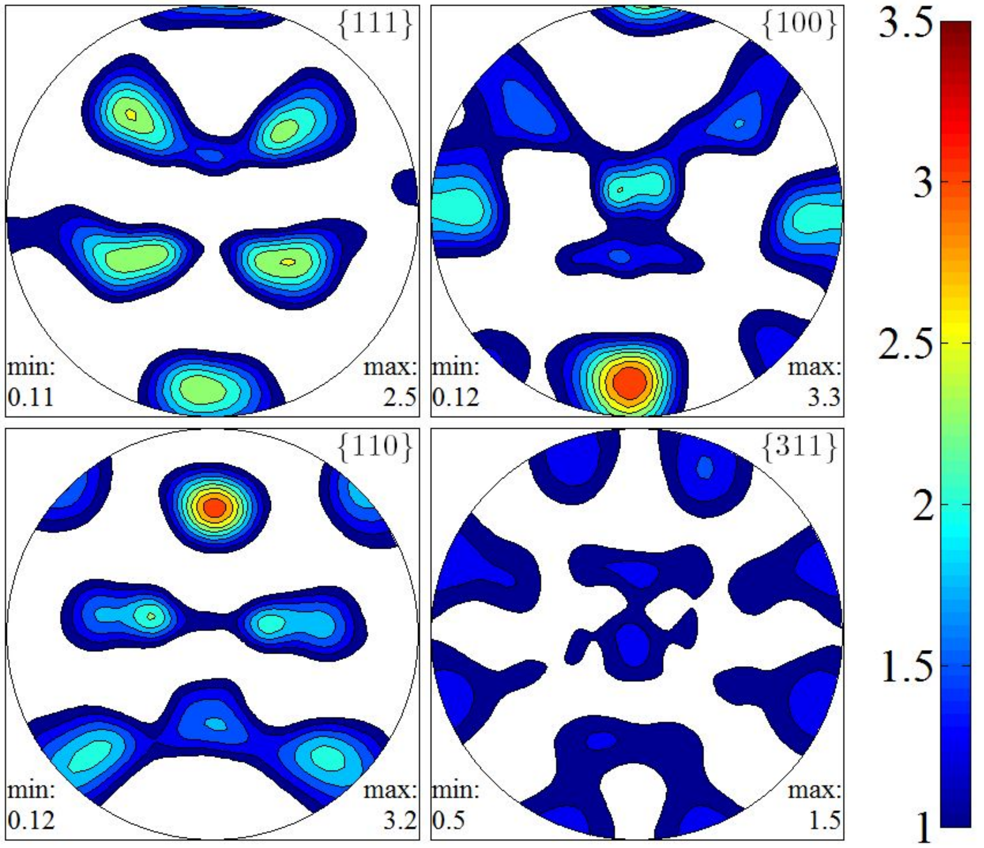

3

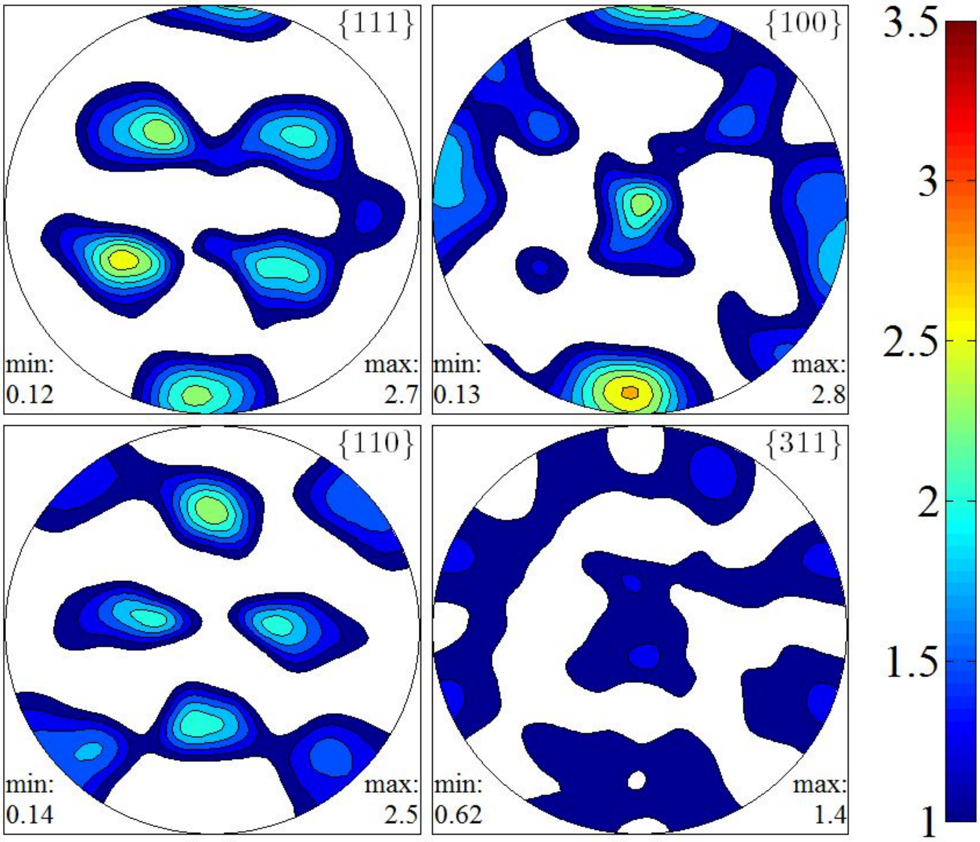
{111}
min:
0.12
max:
2.7
{100}
min:
0.13
max:
2.8
{110}
min:
0.14
max:
2.5
{311}
min:
0.62
max:
1.4
3.5
3
2.5
2
1.5
1

4

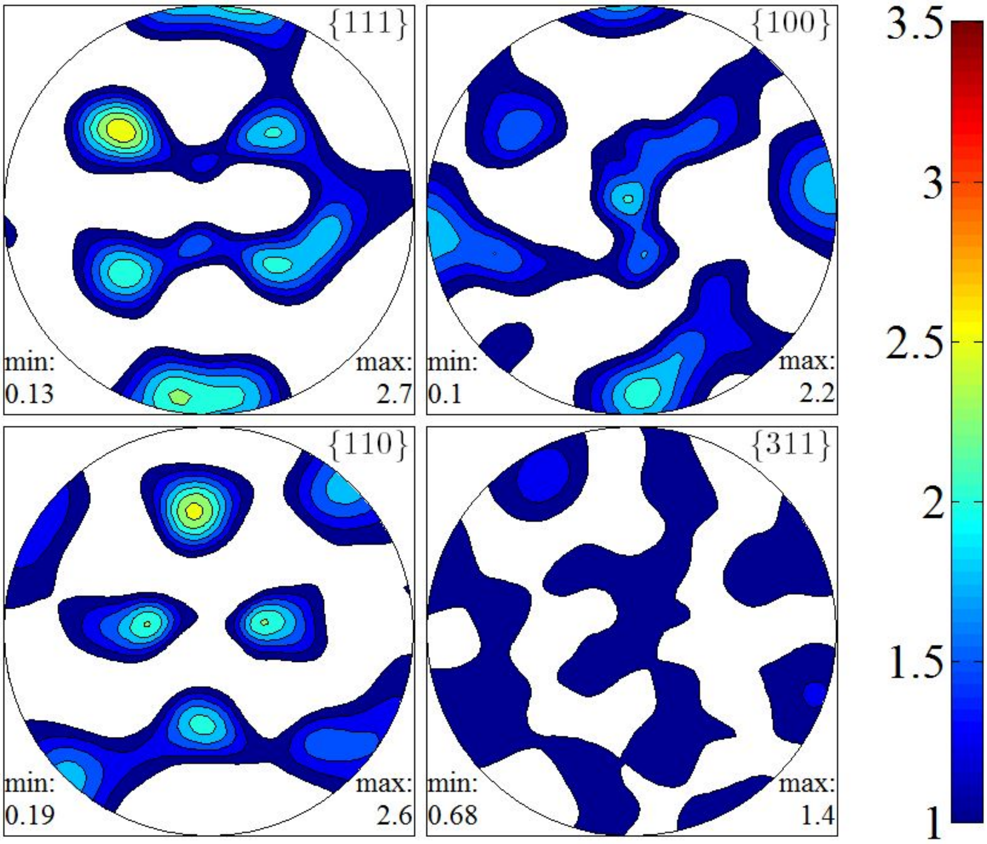
{111}
min:
0.13
max:
2.7
{100}
min:
0.1
max:
2.2
{110}
min:
0.19
max:
2.6
{311}
min:
0.68
max:
1.4
3.5
3
2.5
2
1.5
1

5

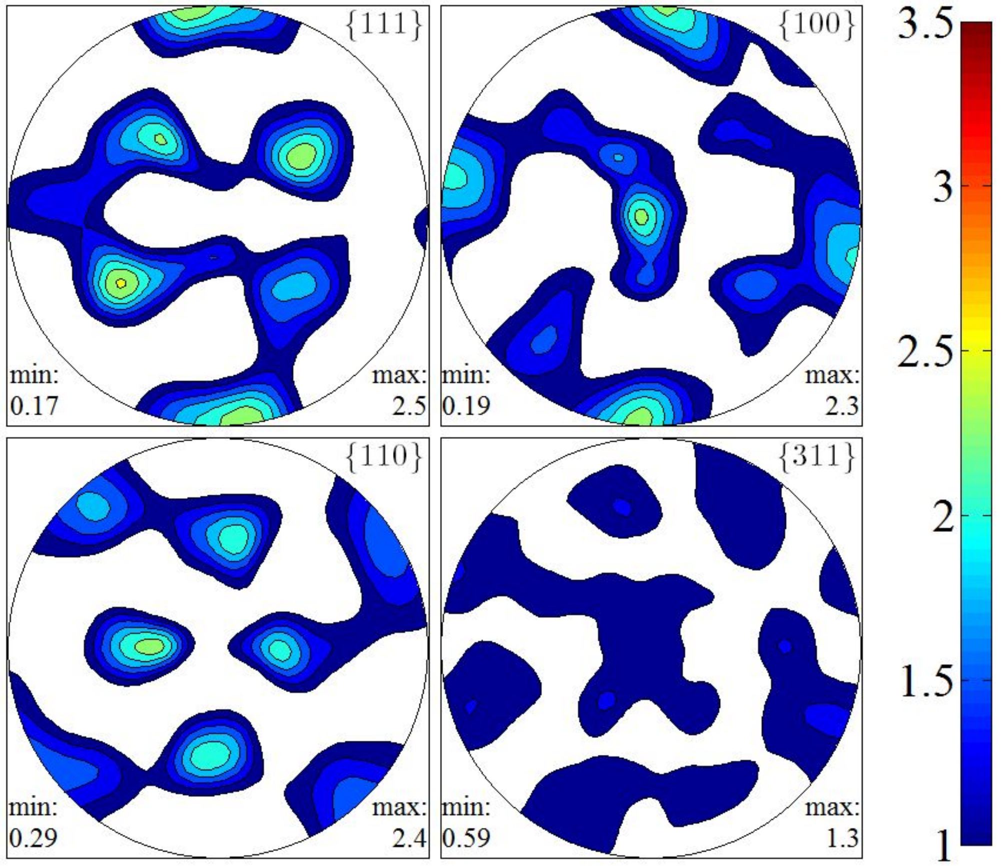
{111}
min:
0.17
max:
2.5
{100}
min:
0.19
max:
2.3
{110}
min:
0.29
max:
2.4
{311}
min:
0.59
max:
1.3
3.5
3
2.5
2
1.5
1

6

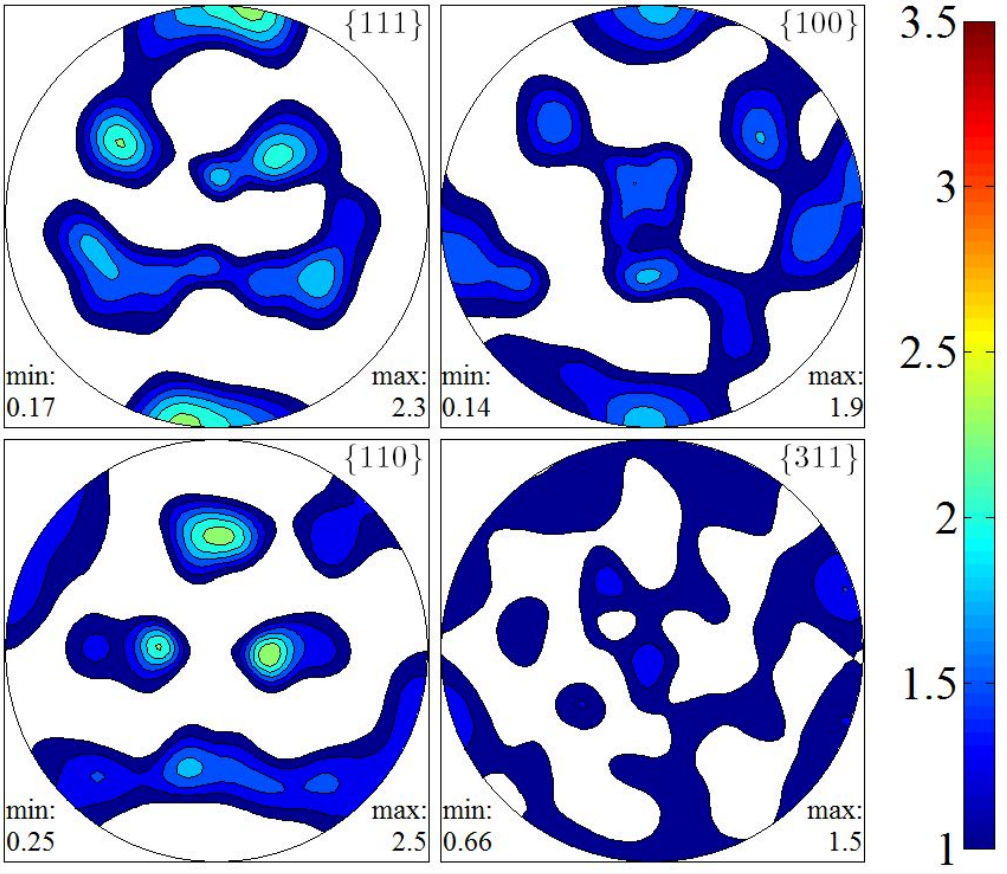
{111}
min:
0.17
max:
2.3
{100}
min:
0.14
max:
1.9
{110}
min:
0.25
max:
2.5
{311}
min:
0.66
max:
1.5
3.5
3
2.5
2
1.5
1

7

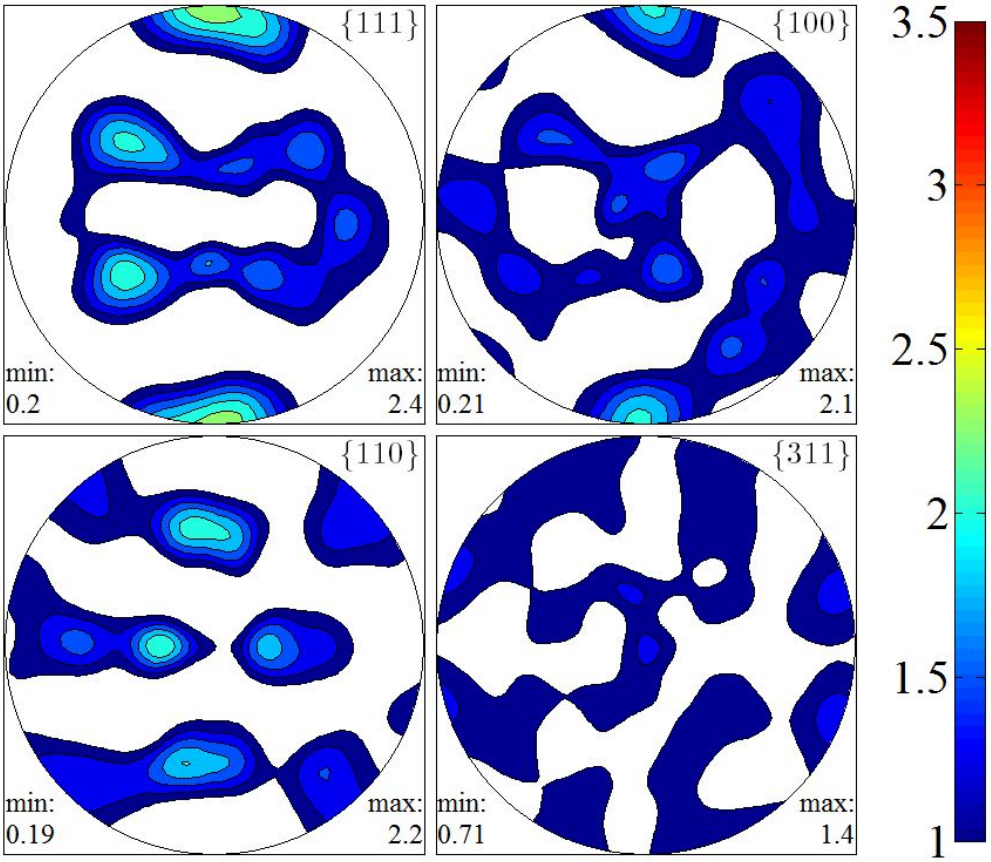
{111}
min:
0.2
max:
2.4
{100}
min:
0.21
max:
2.1
{110}
min:
0.19
max:
2.2
{311}
min:
0.71
max:
1.4
3.5
3
2.5
2
1.5
1

8

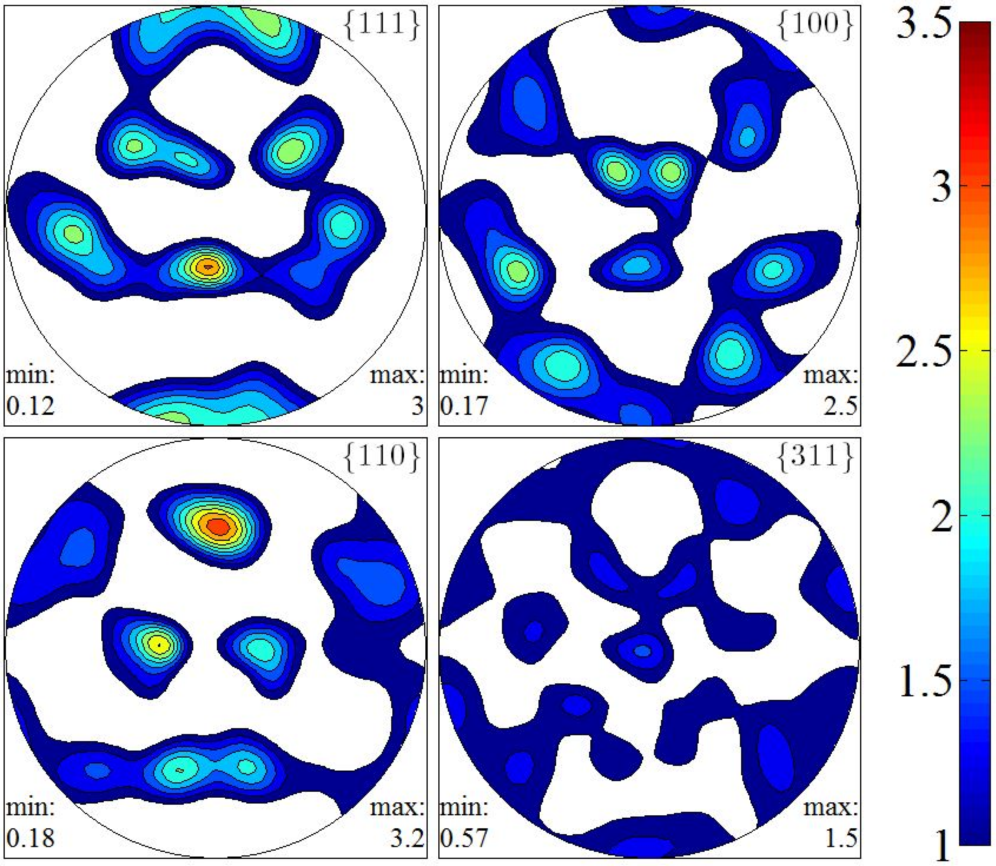
{111}
min:
0.12
max:
3
{100}
min:
0.17
max:
2.5
{110}
min:
0.18
max:
3.2
{311}
min:
0.57
max:
1.5
3.5
3
2.5
2
1.5
1

9

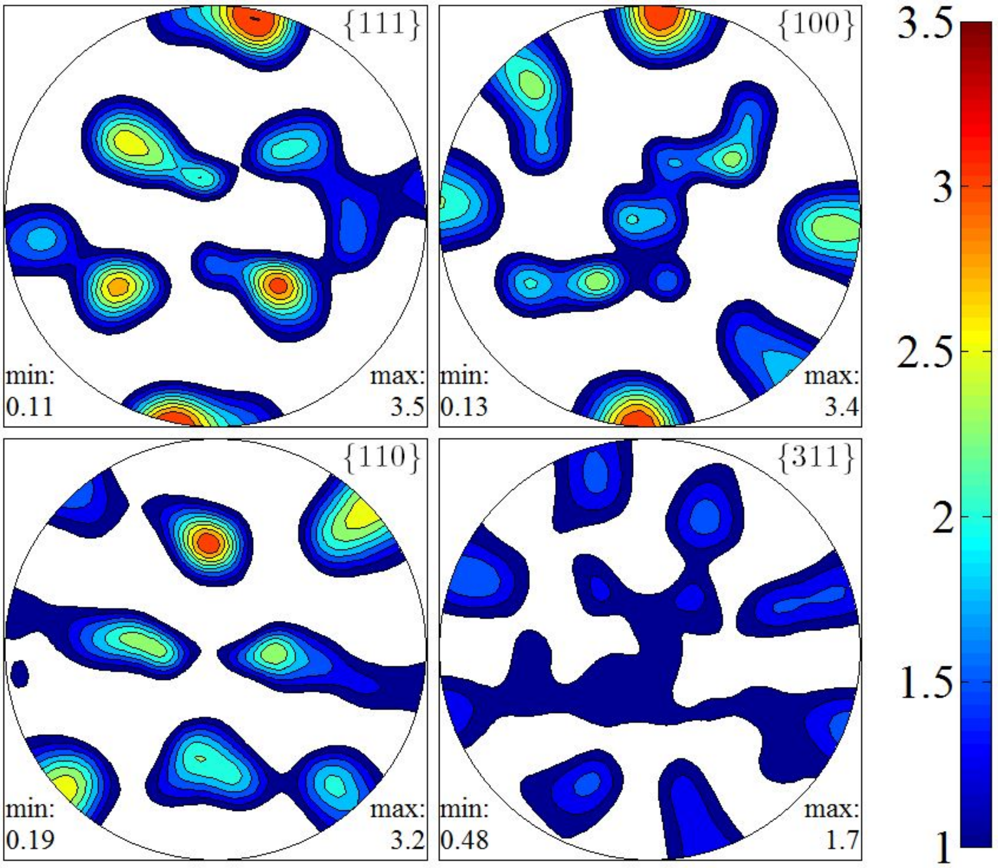
{111}
min:
0.11
max:
3.5
{100}
min:
0.13
max:
3.4
{110}
min:
0.19
max:
3.2
{311}
min:
0.48
max:
1.7
3.5
3
2.5
2
1.5
1

Curriculum Vitae

Al-Hamdany, Nowfal A Abdulrazzag

Personal Details

Name:	Al-Hamdany, Nowfal A Abdulrazzag
Date of birth:	06.05.1983
Place of Birth:	Baghdad/Iraq
Marital Status:	Single
Nationality:	Iraqi
Cell number:	+49 (0) 17684564713
E-Mail:	n.al-hamdany@web.de
Adress:	Otto Hahn Str.1, 21502 Geesthacht

Academic Qualifications

10/2009-04/2015:	**Clausthal University of Technology** **Material Science and Engineering** Ph.D. student
09/2004-02/2008	**Al-Nahrain University/Baghdad, Iraq** **Mechanical Engineering Department** Master of Science
10/2001-09/2004:	**Al-Nahrain University/Baghdad, Iraq** **Mechanical Engineering Department** Bachelor of Science,

Education

10/1995-06/2001:	**Baghdad College School/Baghdad, Iraq** Baccalaureate

Work Experiences

05/2013-present **HZG-WPN, Geesthacht and Hamburg**

Research assistant

- Texture measurement (Synchrotron diffraction)
- Phase analysis (Synchrotron diffraction)
- Elastic lattice constant (In-situ tensile and Synchrotron diffraction)

- X-ray line profile (Synchrotron diffraction)
- Texture measurement (EBSD)
- Supervising new students

09/2010-05/2013: **STRESS-SPEC at MLZ, Garching**

Research assistant

- Texture measurement (Neutron diffraction)
- Residual stress measurement (Neutron diffraction)

10/2009-07/2010: **Tex-2 at HZG (GKSS formerly), Geesthacht**

Research assistant

- Texture measurement (Neutron diffraction)

06/2009-04/2013: **DAAD awarded**

01/2009-05/2009: **Ministry of Oil-Engineering in State Company for Oil Projects(SCOP)/Baghdad, Iraq**

Design engineer

09/2005-09/2008: **Al-Nahrain University- Mechanical Engineering Department**

Assistant lecture:

- Engineering Drawing
- Strength of material Lab
- Metallurgy Lab

31. Mai 2015

Nowfal Al-Hamdany

Publications

Year	Publication
2010	-H.-G. Brokmeier, N. Al-hamdany, C. Randau, W. M. Gan, M. Völler, **Texture and Strain Inhomogeneities of tubes investigated by STRESS-SPEC Robot**, Experimental report FRMII- 2010
2011	-H.-G. Brokmeier, N. Al-hamdany, C. Randau, W. M. Gan, M. Hofmann, **Texture and Strain Inhomogeneities of Tubes investigated by STRESS-SPEC Robot**, Experimental report FRMII- 2011
2012	-N. Al-hamdany, H.-G. Brokmeier, B. Schwebke, Z. Y. Zhong and N. Schell, **Texture inhomogeneity through the thickness for copper tube**, Annual DESY report 2012. -M. Z. Salih, N. Al-hamdany, Z. Y. Zhong, H.-G. Brokmeier, B. Schwebke and N. Schell, **The effect of rolling degree on Fe-2.6%Si**, Annual DESY report 2012.
2013	-M. Z. Salih, H.-G. Brokmeier, M. Uhlarz, B. Weidenfeller, Z. Y. Zhong, N. Al-hamdany, B. Schwebke, N. Schell and W. M. Gan, **The effect of magnetic annealing on crystallographic Texture and microstructure of Fe-2.6%Si**, Annual DESY report 2013. -Z. Y. Zhong, H.-G. Brokmeier, N. Al-hamdany, M. Z. Salih and N. Schell, **Through-thickness texture gradient of a rolled Al7020 plate**. Annual DESY report 2013 -H.-G. Brokmeier, E. Maawad, Z. Zhong, M. Salih, N. Al-Hamdany, B. Schwebke, N. Schell, **Determination of polycrystal diffraction elastic constants of Ti-2.5Cu by using in situ tensile loading and synchrotron radiation**, Annual DESY report 2013
2014	-M. Z. Salih, H.-G. Brokmeier, B.Weidenfeller, Z. Y. Zhong, N. Al-hamdany, B. Schwebke, N. Schell and W. M. Gan, **Magnetic properties and crystallographic texture of Fe-2.6 % Si after different thermo-mechanical treatment**, HASYLAB user meeting 2014. H.-G. Brokmeier, N. Al-hamdany, Z. Y. Zhong, **Texture before and after tensile load of swaged brass**, Experimental report MLZ- 2014. -H.-G. Brokmeier, Z.Y. Zhong, and N. Al-hamdany, **Texture evolution along 45° direction of a textured AA 7020-T6 plate during cyclic loading**, Experimental report MLZ- 2014 -M. Z. Salih, B.Weidenfeller, N. Al-hamdany, H.-G. Brokmeier and W. M. Gan, **Magnetic properties and crystallographic texture of Fe-2.6% Si after 90% cold rolling plus different annealing**, Journal of Magnetism and Magnetic Material, vol 354, pp. 105-111, 2014 -E. Maawad, H.-G. Brokmeier, Z. Y. Zhong, N. Al-hamdany, M. Z. Salih, L. Wagner and N. Schell, **Determination of polycrystalline diffraction elastic constants of Ti-2.5Cu by using in-situ tensile loading and synchrotron**

radiation, Material Science and Engineering A, vol. 594, (2014), pp. 62-67.

-M. Z. Salih, B.Weidenfeller, N. Al-hamdany, H.-G. Brokmeier and W. M. Gan, **The effect of intermediate annealing between cold rolled steps on crystallographic texture and magnetic properties of Fe–2.6% Si**, Journal of Magnetism and Magnetic Material, vol 362, pp. 141-149, 2014

-N. Al-hamdany, H.-G. Brokmeier, C. Randau, W. M. Gan, and M. Völler, **Texture gradient studies of a Cu-tube by the robot at STRESS-SPEC**, Cryst. Res. Technol., 49, p. 888, 2014.

2015 -H.-G. Brokmeier, A. Carradó, N. Al-hamdany,T. Pirling, R.Wimpory, N. Schell and H.Palkowski, **Texture gradient in a copper tube at maximum and minimum wall thickness**, (ICOTOM 17), IOP Conf. Series: Materials Science and Engineering, doi:10.1088/1757-899X/82/1/012102, 2015

-N. Al-hamdany, W. M. Gan, C. Randau, H.-G. Brokmeier and M. Hofmann, **Diffraction on heavy samples at STRESS-SPEC using a robot system** (ICOTOM 17), IOP Conf. Series: Materials Science and Engineering, doi:10.1088/1757-899X/82/1/012105, 2015

-M. Z. Salih, M. Uhlarz, F. Pyczak, H.-G. Brokmeier, B. Weidenfeller, N. Al-hamdany, W. M. Gan, Z. Y. Zhong, N. Schell**, The effect of magnetic annealing on crystallographic texture and magnetic properties of Fe-2.6%Si**, Journal of Magnetism and Magnetic Materials, doi:10.1016/j.jmmm.2015.01.004 (2015)

-C. Randau, H.-G Brokmeier, W. M. Gan, M. Hofmann, M. Völler, W. Tekouo, N. Al-hamdany, Improved sample manipulation at the STRESS-SPEC neutron diffractometer using an industrial 6-axis robot for texture and strain analyses, Nucl. Instrum. and Methods.Phys. Res. Sect. A, doi:10.1016/j.nima.2015.05.014, 2015